EFFECTS OF VARIABLE MAGMA SUPPLY ON MAGMA RESERVOIRS AND ERUPTION CHARACTERISTICS ALONG THE GALÁPAGOS SPREADING CENTER

A DISSERTATION SUBMITTED TO THE GRADUATE DIVISION OF THE UNIVERSITY OF HAWAI‘I AT MĀNOA IN PARTIAL FULFILLMENT OF THE REQUIREMENTS FOR THE DEGREE OF

DOCTOR OF PHILOSOPHY

IN

GEOLOGY AND GEOPHYSICS

AUGUST 2014

By

Alice Colman

Dissertation Committee:

John Sinton, Chairperson
Julia Hammer
Eric Hellebrand
Kenneth Rubin
Michael Mottl

ACKNOWLEDGMENTS

I am happy to thank a number of people who have supported and encouraged me during my time here at UH. First, I would like to express my deep gratitude to my advisor, John Sinton, whose contagious enthusiasm for subjects ranging from phase diagrams to petrography, and from Hawaiian plants to Hawaiian music, have been a continuing source of inspiration over the past five years. I can't imagine a better mentor and companion in the field. Thank you!

A number of other faculty members have contributed perspectives and expertise that have broadened the scope of this work. I am particularly grateful to my committee members, Julia Hammer, Eric Hellebrand, Ken Rubin, and Mike Mottl, for feedback throughout this project. I am also grateful to the many excellent faculty members I have had as professors, including Rob Dunn, Julia Hammer, Eric Hellebrand, Bruce Houghton, John Mahoney, Steve Martel, Scott Rowland, Ken Rubin, John Sinton, Jeff Taylor, and Paul Wessel. Thank you for your time in and out of the classroom! Dorsey Wanless and Brian Monteleone were both integral to the work described in Chapter 3. Thank you also to JoAnn Sinton and Chuck Fraley, for the many hours spent on sample preparation.

The success of this project was dependent on detailed observations made by a talented and diverse group of geologists during research cruise AT15-63. Thank you to the entire GRUVEE crew for your contributions, both onboard and in the ensuing months!

Field trips and applications of theory to real life were what originally drew me to geology, and I am grateful to have had the opportunity to explore Hawai‘i (and beyond!) with an excellent group of fellow graduate students, both on formal trips and on less organized excursions over the past five years. Thank you to everyone with whom I've had the pleasure to hike, climb, camp, and smack rocks, and particularly to my fellow graduate students!

Finally, I am endlessly grateful to my family, who continue to express interest in my research and in geology in general, even on vacation, even when my explanations literally put them to sleep. And to Brian, who has been a constant companion and provided a sounding board and moral support throughout.

Financial support for these research projects was provided by the National Science Foundation, a Denise B. Evans Fellowship, and a Geological Society of America graduate student research grant.

ABSTRACT

This dissertation examines the effects of magma supply on mid-ocean ridge magma reservoirs and eruption characteristics, using mapped lava flow fields erupted at two locations along the Galápagos Spreading Center. Low- and high-magma-supply study areas at 95° and 92°W have similar spreading rates, but differ by 30% in the rate of magma supply due to varying proximity to the Galápagos hotspot.

Detailed geologic maps of each study area incorporate observations of flow contacts and sediment thickness, in addition to sample petrology, geomagnetic paleointensity, and bathymetry data. Mapped lava flow fields are used to compare characteristics of eruptions at the two locations. At the 92°W study area, lava morphologies characteristic of higher effusion rates are more common, and eruptions typically occur along elongated fissures with total eruptive volumes ranging from 0.002–0.13 km^3. In contrast, at the 95°W study area, eruptions typically produce axial seamounts or more irregular clusters of pillow mounds, and eruptive volumes are an order of magnitude larger (0.09 to 1.3 km^3).

Whereas a seismically imaged melt lens exists ~1.7 km below the seafloor at the 92°W study area, no melt lens has been detected at the 95°W study area. Measurements of CO_2 and H_2O in olivine-hosted melt inclusions are used to constrain depths of magma residence at the low-magma-supply study area. Results indicate that prior to three recent eruptions, magma resided at depths of 3.0-3.4 km below the seafloor.

Compositional data were used to compare the characteristics of magmatic systems at the two locations. At 92°W, the rate of magma supply is sufficient to sustain a shallow melt lens (Blacic *et al.*, 2004), within which the competing effects of fractional

crystallization and frequent magmatic recharge result in eruption of lavas with low crystal contents and highly variable MgO. In contrast, melt-rich bodies at 95°W are likely only present intermittently; magmatic evolution at this location appears to be dominated by processes involving crystal-rich mush, which is mixed in varying proportions with hotter, more melt-rich magma during recharge events that closely precede eruptions. Limited residence within melt-rich lenses allows mixing trends to be preserved in erupted lavas.

TABLE OF CONTENTS

LIST OF TABLES

Table **Page**

LIST OF FIGURES

Figure **Page**

CHAPTER 1. INTRODUCTION

1.1. Overview

This dissertation investigates the effects of variable rates of magma supply on the characteristics of eruptions and magmatic systems along the Galápagos Spreading Center (GSC), an intermediate-spreading-rate mid-ocean ridge. Chapter 1 provides background information and describes the structure of the dissertation. Because Chapters 2, 3, and 4 have been or are intended to be published as journal articles, there is significant overlap between background information presented in Chapter 1 and the introductions to Chapters 2, 3, and 4. Chapter 2 describes methods used to map individual eruptive units at two locations along the GSC (95°W and 92°W) with differing rates of magma supply. Mapped eruptive units are then used to compare characteristics of mid-ocean ridge eruptions at the two study areas. Chapter 3 uses measurements of CO_2 and H_2O in olivine-hosted melt inclusions to constrain depths of magma residence at 95°W. Chapter 4 uses analyses of major and trace elements in samples from each eruptive unit (glass, whole rocks, and minerals) to assess the effects of fractional crystallization, crystallization within mush zones, assimilation of altered crust, magma mixing, and recharge events in controlling lava compositions. This analysis is used to place constraints on the characteristics of magmatic systems at the two areas, including crystallinity, temperature, and frequency of magmatic recharge. Chapter 5 summarizes the conclusions of Chapters 2, 3, and 4 and describes potential future work.

1.2. Background

1.2.1. Melt production and supply to the crust at mid-ocean ridges

At mid-ocean ridges, the divergence of lithospheric plates causes passive upwelling of the underlying mantle (see review in McKenzie & Bickle, 1988). Mantle melting begins when the temperature of the adiabatically ascending mantle exceeds its solidus and begins to melt; melting should end when the mantle stops ascending and begins to move laterally away from the ridge axis (e.g., Plank & Langmuir, 1992), when the mantle temperature drops below the solidus as a result of conductive cooling from above (e.g., Niu & Hékinian, 1997), or when clinopyroxene is exhausted. In cross-section, mantle melting occurs within a triangular region beneath the ridge axis (Fig. 1.1)

(e.g., McKenzie & Bickle, 1988; Plank & Langmuir, 1992). In models of pooled, accumulated fractional melting, melts produced throughout the triangular melting region are aggregated and mix before erupting (e.g., O'Hara, 1985; Plank & Langmuir, 1992); the mean extent of mantle melting is the ratio of the total mass of melt produced to the total mass of mantle that passes through the melting region (Plank *et al.*, 1995).

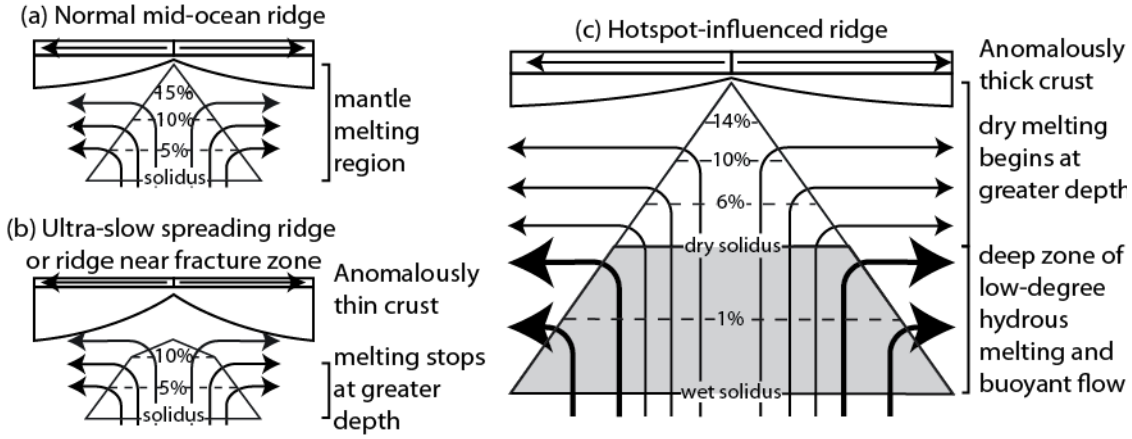

Figure 1.1. Mantle melting regions beneath mid-ocean ridges. Triangle represents region in which mantle melts. Arrows represent flow paths of ascending mantle; size of arrowhead is proportional to rate of flow. Maximum degree of mantle melting is shown as a function of depth; note that the average degree of melting for pooled melts produced throughout the melting regime will be significantly lower than the maximum degree of melting because only a portion of the melting region reaches this maximum degree of melting. (a) Mantle melting beneath a normal mid-ocean ridge. (b) Mantle melting beneath an ultra-slow spreading ridge or near a fracture zone. Melting terminates at greater depth, resulting in thinner crust. (c) Mantle melting in the presence of hydrous mantle, such as along the hotspot-influenced Galápagos Spreading Center. Melting begins at greater depths; elevated water contents may contribute an additional volume of deep, low-degree melts. Flow through this deep, hydrous melting region may be enhanced because of reduced viscosity, leading to the production of even greater volumes of low-degree melts. Modified from figures of Plank & Langmuir (1992); Niu & Hekinian (1997); Robinson *et al.* (2001); Asimow & Langmuir (2003); Cushman *et al.*, (2004); and Ito & Mahoney (2005).

Figure 1.1 illustrates schematically the differences in melt production among different mid-ocean ridge settings (normal, hotspot-influenced, and ultra-slow-spreading ridges). Greater mantle potential temperatures at hotspot-influenced ridges allow melting to begin at greater depths, resulting in a larger total volume of magma being produced (e.g., Schilling, 1973; Klein & Langmuir, 1987). Some hotspots are characterized by elevated water contents; the presence of water in the mantle should increase the depth of

the onset of melting (Gaetani & Grove, 1998; Robinson *et al.*, 2001). Because water behaves highly incompatibly during mantle melting, it is efficiently extracted during melting so that only low-degree melts are produced in the interval between the wet and dry solidi (Asimow & Langmuir, 2003). The combination of the deep, low-degree hydrous melting regime and the expanded dry melting region results in the production of a larger volume of magma, with a lower mean extent of melting, at hotspot-influenced ridges (Asimow & Langmuir, 2003). In contrast, at very slow spreading rates, conduction to the surface becomes more significant, causing the termination of melting at greater depths and correspondingly lower mean melt fractions and smaller total volumes of melt production than at normal mid-ocean ridges (Bown & White, 1994; Niu & Hékinian, 1997; White *et al.*, 2001) (Fig. 1.1). A similar effect is predicted to affect ridges adjacent to fracture zones, due to the presence of relatively old, cold lithosphere (e.g., Detrick *et al.*, 1993).

1.2.2. Variations in magma supply along the global mid-ocean ridge system

The dominant control on magma supply along mid-ocean ridges is spreading rate. Full spreading rates that vary from ~5 mm/yr to 145 mm/yr correspond to variations in magma supply to the crust from 0.03×10^6 to 0.87×10^6 m^3/km/yr, assuming constant crustal thickness of 6 km (Fig. 1.2). Variations in spreading rate along the global mid-ocean ridge system are accompanied by well-documented variations in crustal structure and characteristics of the volcanic eruptions that build the extrusive section of the oceanic crust (see Sections 1.2.3, 1.2.4).

Magma supply can be decoupled locally from spreading rate. At mid-ocean ridges affected by hotspots, elevated rates of melt production within the mantle result in the production of anomalously thick oceanic crust. Such increased melt supply can arise from either temperature anomalies or compositional variations, including increased water contents, in the upwelling mantle. For example, the proximity of the Icelandic plume to the Mid-Atlantic Ridge causes crustal thickness to increase from 7.5 km at 57°45'N (Navin *et al.*, 1998) to 11 km at 62°40'N (Weir *et al.*, 2001) and 19 km at 65°45'N (Staples *et al.*, 1997), and crustal thickness may reach 46 km at the peak of plume influence (Allen *et al.*, 2002); spreading rates remain relatively constant throughout this

region at 18-20 mm/yr (DeMets *et al.*, 2010). Similarly, along the Galápagos Spreading Center, the influence of the Galápagos hotspot causes crustal thickness to increase from ~5.7 km at 97°W to ~7.9 km at 91.5°W (Canales *et al.*, 2002; Detrick *et al.*, 2002), whereas spreading rates vary only from 51 to 55 mm/yr (DeMets *et al.*, 2010).

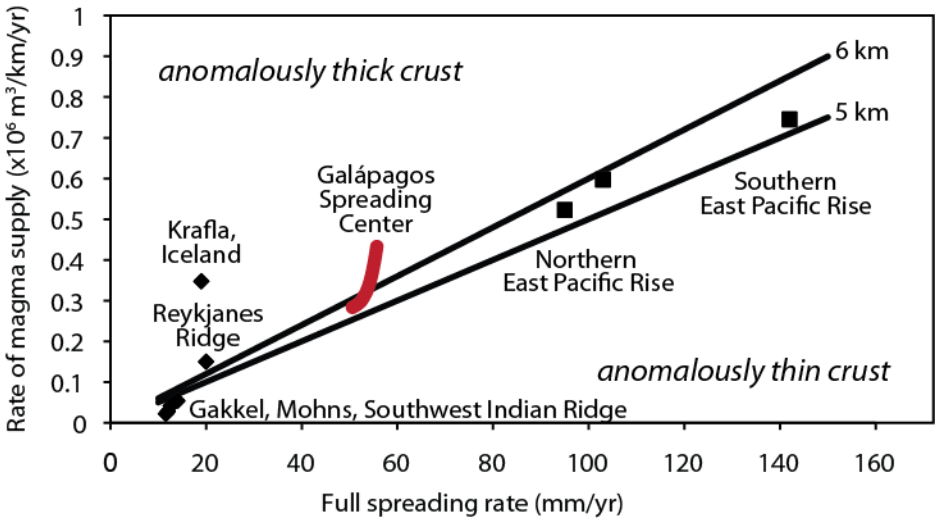

Figure 1.2. Variations in rate of magma supply as a function of spreading rate. Isopleths show variations in rate of magma supply for crust of constant thickness (5 or 6 km). Locations where known spreading rates and crustal thickness can be used to calculate the rate of magma supply are marked by squares (normal ridges) and diamonds (ridges with anomalous rates of magma supply). Red line indicates variations in magma supply along the Galápagos Spreading Center.

Anomalously thin crust is produced at ultra-slow spreading ridges (e.g., 1.9-3.3 km on the Gakkel Ridge (Jokat *et al.*, 2003), 4 km on the Mohns Ridge (Klingenhöfer *et al.*, 2000), 2.5 km on the Southwest Indian Ridge (Muller *et al.*, 1999)), and near fracture zones (e.g., Detrick *et al.*, 1993). These data indicate that rates of magma supply at ultra-slow spreading ridges are ~30-70% lower than those predicted from an assumption of constant 6-km crustal thickness throughout the spreading rate spectrum (Fig. 1.2).

Taken together, the observed ranges in spreading rate and crustal thickness produce two orders of magnitude of variation in the total magmatic flux, or time-averaged rate of crustal production along mid-ocean ridges (Fig. 1.2). Although spreading rate is commonly used as a proxy for the rate of magma supply, there has been no systematic study addressing the effects of variable magma supply, separate from those of spreading rate, on eruptive processes or on the geometry and dynamics of sub-axial magma chambers.

1.2.3. Magma reservoirs within the crust

At fast-spreading ridges, seismic data suggest that a shallow, melt-rich lens overlies a larger, more continuous region of crystal mush along much of the spreading axis (e.g., Sinton & Detrick, 1992; Dunn *et al.*, 2000; Carbotte *et al.*, 2013). Magma residence within shallow crustal magma reservoirs promotes fractionation and homogenization of parental magma compositions, leading to the eruption of dominantly aphyric lavas with widely varying degrees of fractional crystallization (e.g., Sinton & Detrick, 1992; Rubin & Sinton, 2007). With increasing degrees of fractional crystallization, the degree of compositional heterogeneity related to parental magma composition (e.g., variability of incompatible element ratios) decreases, indicating magma homogenization concurrent with fractionation (Rubin & Sinton, 2007; Rubin *et al.*, 2009).

At lower spreading rates, seismic studies typically do not detect axial melt lenses, although low seismic velocities throughout the lower crust indicate the presence of small fractions of melt (e.g., Detrick *et al.*, 1990; Sinton & Detrick, 1992; Dunn *et al.*, 2005). Nevertheless, primary magmas in equilibrium with mantle compositions are exceedingly rare among erupted lava compositions, indicating that even at relatively slow-spreading ridges, magma tends to be modified within the crust prior to eruption (e.g., Stolper, 1980). It is unknown whether this modification occurs during magma ascent through crystal mush, or within melt lenses that are either too small, or too ephemeral, to be seismically imaged (e.g., Sinton & Detrick, 1992; Kelemen & Aharanov, 1998; Lissenberg & Dick, 2007; Rubin & Sinton, 2007).

1.2.4. Eruption characteristics

Although the number of well-documented eruptions along submarine mid-ocean ridges is still relatively small, preliminary observations suggest that those at faster-spreading ridges produce relatively small volumes of lava (Perfit & Chadwick, 1998; Sinton et al., 2002). Because the thickness of the extrusive layer appears to be independent from spreading rate, smaller eruptive volumes and greater rates of crustal

production imply that eruption recurrence intervals must be shorter at faster spreading rates (Perfit & Chadwick, 1998; Sinton *et al.*, 2002).

The greater abundance of sheet flows relative to pillow flows at faster spreading rates suggests that average effusion rates increase with spreading rate (Bonatti & Harrison, 1988; Perfit & Chadwick). McClinton *et al.* (2013) extended these observations to the Galápagos Spreading Center by documenting the relative abundances of lava morphology as a function of the rate of magma supply, and found that effusion rates are also positively correlated with variations in the rate of magma supply (even in the absence of variations in spreading rate). Slower average effusion rates should promote focusing of effusion to point-source eruptions (e.g., Wadge, 1981; Bruce & Huppert, 1989; Whitehead & Helfrich, 1991; Head *et al.*, 1996), consistent with the observation that fissure-fed eruptions are more common at fast-spreading ridges, whereas point-source edifices dominate at slow-spreading ridges (Perfit & Chadwick, 1998).

1.2.5. Eruption-scale studies of mid-ocean ridges

Observations of fissure eruptions along divergent plate boundaries in Iceland's Northern Volcanic Zone (Saemundsson, 1991; Wright *et al*., 2012) and Ethiopia's Dabbahu-Manda Harraro Rift (Ebinger *et al*., 2010; Wright *et al*., 2012), geologic mapping of submarine lava flow fields along the East Pacific Rise (Sinton *et al*., 2002; Soule *et al*., 2007), and radiometric dating of samples from eruptions along the East Pacific Rise (Rubin *et al*., 1994, 2006, 2008; Bergmanis *et al*., 2007) indicate that at least some lava flow fields are the products of multiple, relatively short-lived (hours to weeks) eruptive events, which collectively comprise longer eruptive episodes lasting months to years. For the purposes of this study, we define a lava flow field as the products of a single eruptive episode, which may comprise the products of multiple eruptive events. Whereas it will likely be impossible to distinguish individual lava flows erupted during different eruptive events, greater time intervals between major eruptive episodes should result in distinctions in sediment cover and/ or lava appearance on the composite flow fields that are produced, which should allow them to be distinguished from one another.

Studying individual volcanic eruptions is the most direct way to assess the eruptive and magmatic processes that produce the observed variations in mid-ocean ridge

morphology and lava composition. Petrologic studies of lava flow fields have identified spatial and temporal variations in temperature within magma bodies along the East Pacific Rise (Bergmanis *et al.*, 2007; Goss *et al.*, 2010), and have demonstrated that magma reservoirs can be compositionally heterogeneous as a result of variations in source rock composition, frequency of magmatic recharge and eruption, extent of differentiation, and efficacy and scales of mixing (Rubin *et al.*, 1998; Rubin *et al.*, 2001; Sinton *et al.*, 2002; Bergmanis *et al.*, 2007; Goss *et al.*, 2010). Measurements of eruptive volume place constraints on magma reservoir size and eruption recurrence intervals (Sinton *et al.*, 2002). Variations in lava morphology, lengths of eruptive fissures, and the partitioning of magma between intrusive and eruptive emplacement regimes have implications on the evolution of magmatic transport processes and the local stress fields during an eruptive episode (Bergmanis *et al.*, 2007; Ferguson *et al.*, 2010).

Despite these motivations, relatively few mid-ocean ridge eruptions have been studied in detail (see Rubin *et al.*, 2012 for review). Many studies of mid-ocean ridge eruptions have occurred in response to specific eruptions that were either discovered fortuitously by visual observation on the seafloor (e.g. Haymon *et al.*, 1993), or detected remotely by oceanographic surveys (e.g. Embley *et al.*, 1991) or seismic monitoring (e.g. Dziak *et al.*, 1995). Many of these eruptions happened recently enough that they can be dated with high precision using radiometric techniques (Rubin *et al.*, 1994; 1998; 2006; Bergmanis *et al.*, 2007), providing important constraints on eruptive chronologies and recurrence intervals. The study of very recent eruptions facilitates detailed mapping and characterization of the associated flow fields (Soule *et al.*, 2007; Fundis *et al.*, 2010) because of striking contrasts in flow surfaces and sediment cover that are apparent for very young lava flows.

One disadvantage of the eruption-response approach is that it severely limits the number of eruptions for which we have data. Most flow field mapping in response to perceived "events" has resulted in maps of the products of only the youngest unit in the area. The longer-term eruptive histories for these areas therefore remain unknown, precluding comparisons of successive eruptions along a given stretch of the mid-ocean ridge system. In two cases there have been successive documented events within approximately 15 year intervals: the 1991-2 and 2005 eruptions along the northern East

Pacific Rise near 9°50'N (Soule *et al.*, 2007), and the 1998 and 2011 eruptions of Axial Seamount along the Juan de Fuca Ridge (JdFR) (Embley *et al.*, 1999; Caress *et al.*, 2012). These cases provide insight into the slightly longer-term evolution of magmatic systems.

The alternative approach is to use geologic mapping techniques to reconstruct eruptive histories for segments of the mid-ocean ridge system, whether or not recent eruptions have been observed (e.g., Sinton *et al.*, 2002; Clague *et al.*, 2013), using techniques similar to those used to reconstruct pre-historic eruptive sequences on land. In the field, flow boundaries are identified and relative ages are determined using distinctions in sediment cover, flow direction, fault density, and relationships of superposition (e.g., Sinton *et al.*, 2002). Absolute eruption ages can be determined by radiometric dating (Rubin *et al.*, 1994; 1998; 2006; Bergmanis *et al.*, 2007), geomagnetic paleointensity measurements (Bowles *et al.*, 2005; Bergmanis *et al.*, 2007; Bowles *et al.*, 2014), or radiocarbon dating of foraminifera in sediments overlying lava flows (Clague *et al.*, 2013). Regional geologic mapping campaigns can contribute greatly to our understanding of mid-ocean ridge eruptive processes by providing constraints on the range of eruptive activity that is possible at a given location.

1.3. Geologic setting: Galápagos Spreading Center

The GSC is an east-west-trending, intermediate-spreading-rate ridge that separates the Cocos and Nazca Plates. Seafloor spreading along the GSC began ~25 Ma (Hey *et al*., 1977), and has been strongly influenced by the presence of the Galápagos hot spot, which is currently located ~200 km to the south of the ridge near 91.5°W (e.g., Wilson & Hey, 1995). The average rate of magma supply to the crust (calculated as the product of the spreading rate and crustal thickness along a 1-km segment of ridge, after Sinton *et al.* (2003)) increases with proximity to the hotspot, from 0.26×10^6 m^3/km/yr at 97°W to 0.46×10^6 m^3/km/yr at 91°W. The increase in the rate of magma supply is indicated by the greater crustal thickness near the hotspot (Canales *et al.*, 2002). Other parameters that vary systematically with proximity to the hotspot along the western GSC include the amplitude of the mantle Bouguer anomaly (Canales *et al.*, 2002), depth of the seismically imaged melt lens (Blacic *et al.*, 2004), axial depth (Canales *et al.*, 2002) and

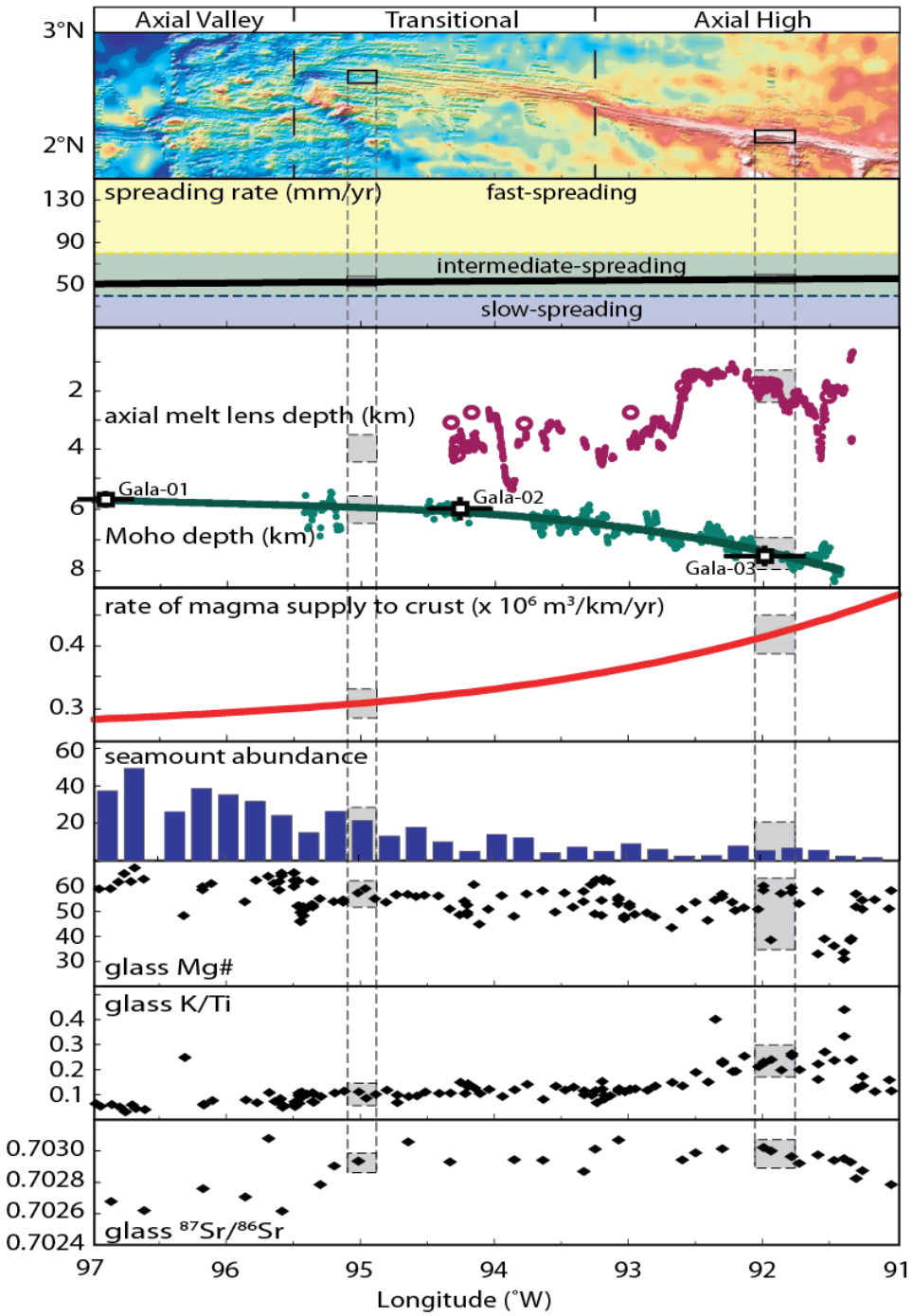

Figure 1.3. Bathymetry of western Galápagos Spreading Center and along-axis variations in: spreading rate (DeMets *et al.*, 2010), melt lens depth (Blacic *et al.*, 2004), Moho depth (Canales *et al.*, 2002), magma supply (Sinton *et al.*, 2003), seamount abundance normalized to surveyed area (Behn *et al.*, 2004), glass Mg# (molar Mg/(Mg+Fe)) (Cushman *et al.*, 2004), glass K/Ti (Cushman et al., 2004), and glass $^{87}Sr/^{86}Sr$ (Ingle *et al.*, 2010). Modified from Detrick *et al.*, 2002. Grey boxes and dashed lines highlight locations of detailed study areas at 95°W (low magma supply) and 92°W (high magma supply).

morphology (Schilling *et al.*, 1982; Sinton *et al.*, 2003; White *et al.*, 2008), topographic roughness in the axial zone (Sinton *et al.*, 2003), seamount abundance (Behn *et al.*, 2004; White *et al.*, 2008), and the chemical and isotopic composition (Schilling *et al.*, 1982, 2003; Cushman *et al.*, 2004; Ingle *et al.*, 2010) and crystallinity (Behn *et al.*, 2004) of erupted lavas.

Surveys of geochemical and isotopic variations along the western GSC have noted increasing enrichments of incompatible elements with proximity to the hotspot, as well as more radiogenic Sr and Pb isotope ratios, and less radiogenic Nd and Hf isotope ratios (Schilling *et al.*, 1982, 2003; Cushman *et al.*, 2004; Ingle *et al.*, 2010). These variations were attributed to mixing of varying amounts of depleted and enriched mantle end-members by Schilling *et al.* (1982, 2003). In contrast, Cushman *et al.* (2004) and Ingle *et al.* (2010) attributed these variations to lower mean extents of mantle melting near the hotspot caused by a deep zone of low-degree hydrous melting. Superimposed on variations in parental magma composition along the length of the GSC are variations in the degree of fractionation reached prior to eruption (as indicated by, e.g., MgO content or magnitude of Sr anomaly in glass samples), with more variable and greater maximum degrees of fractionation occurring near the hotspot (Schilling *et al.*, 1982; Cushman *et al.*, 2004; Ingle *et al.*, 2010). In addition, propagating rifts are associated with local variations in mantle melting and magmatic differentiation (Christie & Sinton, 1981; Schilling *et al.*, 1982; Sinton *et al.*, 1983; Christie & Sinton, 1986; Rotella *et al.*, 2009).

1.4. Structure of the dissertation

Chapter 2 describes methods used to produce geologic maps of lava flow fields emplaced during individual eruptive episodes at two locations along the Galápagos Spreading Center (92°W and 95°W) with differing time-averaged rates of magma supply. Sequences of mapped eruptions at each study area are then used to compare eruptive characteristics such as eruptive edifice morphology, eruptive volume, eruptive frequency, and effusion rate. Results of this portion of the dissertation indicate that eruptions are typically smaller, but occur more frequently, and have higher average effusion rates, at relatively high rates of magma supply. Effusion along eruptive fissures typically persists

throughout eruptions at high rates of magma supply, whereas effusion more commonly focuses to a point source during eruptions at lower magma supply. Chapter 2 was published in *Geochemistry, Geophysics, Geosystems* in August, 2012 (Colman *et al.*, 2012).

The depths of shallow magma reservoirs at intermediate- to high-magma-supply mid-ocean ridges are well constrained by seismic reflection studies. Although magma is likely to reside within the crust prior to erupting at slower-spreading ridges, shallow magma reservoirs have rarely been detected by seismic studies at lower rates of magma supply. Chapter 3 uses a petrologic approach to constraining depths of magma residence prior to eruption wherein the CO_2 and H_2O contents of olivine-hosted melt inclusions are used to constrain pressures (and thereby depths) of melt inclusion entrapment at 95°W, where a melt lens has not been seismically imaged. Samples for this study were selected from three of the recent eruptive units at 95°W, allowing temporal variations in the depths of magma residence to be documented. An additional sample from 94.2°W was used to compare the depth of the seismically imaged melt lens to the depths of melt inclusion entrapment. Chapter 3 was submitted to *Earth and Planetary Science Letters* in April, 2014.

Chapter 4 uses compositional variations among samples from individual eruptive units at each study area to constrain the relative importance of different magmatic processes within shallow magma reservoirs prior to eruption. This study uses major and trace element compositions of lava samples, as well as major element compositions of mineral phases and observations of mineral textures. At the high-magma-supply study area, the combination of efficient crystal fractionation within melt-rich magma reservoirs and frequent eruptions results in the eruption of lavas with widely varying degrees of fractionation. Assimilation of hydrothermally altered crust causes Cl contents to increase with increasing degrees of fractionation, although effects on other major and trace elements are not observed. At the low-magma-supply study area, magmatic recharge appears to precede each eruption, so that lavas are mixtures of varying proportions of relatively primitive and more evolved magmas, and erupted lavas do not reach the same degrees of differentiation achieved at the high-magma-supply study area. Between eruptions, the presence of mush-dominated magmatic systems causes magmatic

differentiation to occur via a process akin to *in situ* crystallization, so that erupted lavas are the products of mixing between primitive magmas and magmas that have been modified by evolution within a largely crystalline mush.

Finally, Chapter 5 summarizes the conclusions of these studies, and describes plans for future work that would build on these results.

CHAPTER 2. EFFECTS OF VARIABLE MAGMA SUPPLY ON MID-OCEAN RIDGE ERUPTIONS: CONSTRAINTS FROM MAPPED LAVA FLOW FIELDS ALONG THE GALÁPAGOS SPREADING CENTER

2.1 Abstract

Mapping and sampling of 18 eruptive units in two study areas along the Galápagos Spreading Center (GSC) provide insight into how magma supply affects mid-ocean ridge (MOR) volcanic eruptions. The two study areas have similar spreading rates (53 versus 55 mm/yr), but differ by 30% in the time-averaged rate of magma supply (0.3×10^6 versus 0.4×10^6 m^3/km/yr). Detailed geologic maps of each study area incorporate observations of flow contacts and sediment thickness, in addition to sample petrology, geomagnetic paleointensity, and inferences from high-resolution bathymetry data. At the lower-magma-supply study area, eruptions typically produce irregularly shaped clusters of pillow mounds with total eruptive volumes ranging from 0.09 to 1.3 km^3. At the higher-magma-supply study area, lava morphologies characteristic of higher effusion rates are more common, eruptions typically occur along elongated fissures, and eruptive volumes are an order of magnitude smaller (0.002–0.13 km^3). At this site, glass MgO contents (2.7–8.4 wt. %) and corresponding liquidus temperatures are lower on average, and more variable, than those at the lower-magma-supply study area (6.2–9.1 wt. % MgO). The differences in eruptive volume, lava temperature, morphology, and inferred eruption rates observed between the two areas along the GSC are similar to those that have previously been related to variable spreading rates on the global MOR system. Importantly, the documentation of multiple sequences of eruptions at each study area, representing hundreds to thousands of years, provides constraints on the variability in eruptive style at a given magma supply and spreading rate.

2.2. Introduction

Although mid-ocean ridge (MOR) magmatism is estimated to account for 75 % of the recent global magmatic budget (Crisp, 1984), volcanic eruptions on submarine MORs are notoriously difficult to observe directly, and their study necessitates a variety of unconventional approaches. Along the global MOR system, the products of only about two-dozen submarine eruptions have been mapped previously (Sinton *et al.*, 2002 and

references therein; Soule *et al.*, 2007; Caress *et al.*, 2012; Rubin *et al*., 2012). Among these examples, observed and inferred variations in eruption rate, size, and frequency correlate reasonably well with variations in spreading rate (Perfit & Chadwick, 1998; Sinton *et al.*, 2002). For most ridges, where crustal thickness is relatively constant, spreading rate and magma supply necessarily co-vary over thousand to million year timescales (Canales *et al.*, 2000; Bonatti *et al.*, 2003), although shorter-term fluctuations about the steady value are also known (Sinton *et al.*, 2002; Stakes *et al*., 2006). Along the Galápagos Spreading Center (GSC), however, the Galápagos hotspot causes a significant increase in magma supply to the crust at roughly constant spreading rate, relative to non-hotspot influenced ridges. The GSC thus provides a rare opportunity to study the effects of magma supply on MOR eruptions, independent of variations in spreading rate.

Many models proposed for MOR evolution based on field observations and geologic mapping (e.g., Ballard & van Andel, 1977; van Andel & Ballard, 1979; Perfit & Chadwick, 1998), bathymetry (e.g., Kappel & Ryan, 1986), and numerical modeling (e.g., Ito & Behn, 2008) suggest that activity along individual ridges might alternate between predominantly tectonic and magmatic phases. As such, a given ridge segment is likely to be constructed of eruptive units emplaced at a variety of crustal stress states, and fed by magmatic systems that might vary in reservoir volume, crystallinity, temperature, depth, and connectivity. The products of individual volcanic eruptions provide snapshots of magmatic systems and eruptive processes at specific times in the evolution of a spreading center.

Chemically heterogeneous lava flow fields from individual eruptions along the East Pacific Rise (EPR) (e.g., Bergmanis *et al.*, 2007; Goss *et al*., 2010) have been interpreted to reflect spatial variations in temperature within magma bodies, which could arise from variations in parental magma composition, the frequency of magmatic recharge and eruption, the extent of differentiation, and/ or the efficacy and scales of magmatic mixing (Rubin *et al*., 1998, 2001; Sinton *et al*., 2002; Bergmanis *et al*., 2007; Goss *et al*., 2010). Measurements of eruptive volume have been used to place constraints on magma reservoir size and eruption recurrence intervals (Perfit & Chadwick, 1998; Sinton *et al*., 2002). Variations in lava morphology (e.g., Fundis *et al*., 2010), lengths of eruptive fissures (Gregg *et al*., 1996; Sinton *et al*., 2002; Ferguson *et al*., 2010), and the

partitioning of magma between intrusive and extrusive emplacement regimes (e.g., Ferguson *et al*., 2010) have been used to understand the evolution of magmatic transport processes and local stress fields during the course of individual eruptive episodes.

Relatively few MOR eruptions have been studied in detail (Rubin *et al*., 2012). Most studies have occurred in response to evidence acquired during the course of seafloor investigations (e.g., Haymon *et al*., 1993; Auzende *et al*., 1996, Caress *et al*., 2012), or detected remotely by oceanographic surveys (e.g., Embley *et al*., 1991; Chadwick *et al*., 1995) or seismic monitoring (Fox *et al*., 1995; Dziak & Fox, 1999; Fox, 1999). Lavas sampled from these eruptions are generally young enough that they can be dated with high-precision radiometric techniques, providing constraints on eruptive chronologies and recurrence intervals (Rubin *et al*., 1994; 1998; Bergmanis *et al.*, 2007; Rubin *et al.*, 2012). The study of very recent eruptions also facilitates detailed mapping and characterization of the associated flow fields because of striking contrasts in flow surfaces and sediment cover between newly erupted and older lavas (Soule *et al*., 2007; Fundis *et al*., 2010). Targeted mapping of individual detected eruptions has proven particularly effective along MOR segments with short eruption recurrence intervals (e.g., Embley *et al.*, 1991; Chadwick *et al.*, 1998; Embley *et al*., 2000; Soule *et al*., 2007; Caress *et al.*, 2012).

One disadvantage of the eruption-response approach is that it results in few well-characterized eruptions in a given area (Rubin *et al.*, 2012). Most flow field mapping in response to detected events has resulted in maps of only the youngest one or two units in the area. The longer-term eruptive histories for these areas therefore remain unknown, precluding comparisons of successive eruptions along a given length of the MOR system. In two cases there have been successive documented volcanic events at approximately 15 year intervals: the 1991-2 and 2005-6 eruptions along the northern EPR near 9°50'N (Haymon *et al*., 1993; Tolstoy *et al.*, 2006), and the 1998 and 2011 eruptions of Axial Seamount along the Juan de Fuca Ridge (JdFR) (Embley *et al*., 1999; Caress *et al*., 2012). These cases provide glimpses of the slightly longer-term evolution of magmatic systems.

Regional mapping campaigns can contribute greatly to our understanding of MOR eruptive processes by documenting the variations in eruptive activity that occur at a given

location, even in the absence of "historic" eruptions (Sinton *et al*., 2002). For example, Bergmanis *et al*. (2007) identified the five most recent eruptive units along a portion of the southern EPR near 17°30'S and showed that significant variations in mantle source composition and the extent of mixing in sub-axial magma reservoirs occurred over only a few hundred years. Here, we present the results of geologic mapping investigations in two areas of the GSC (Fig. 2.1) that differ in time-averaged crustal production rates (Sinton *et al.*, 2003) and volcanic morphology (Behn *et al*., 2004; White *et al*., 2008). Our results allow us to constrain the effects of magma supply on the size, frequency, and characteristics of individual eruptive episodes representing hundreds to thousands of years of volcanic activity at each site.

2.3. Geologic setting: Galápagos Spreading Center

The western GSC is an east-west-trending, intermediate-spreading-rate ridge that separates the Cocos and Nazca Plates (Fig. 2.1). The history and morphology of the GSC have been strongly influenced by the presence of the Galápagos hotspot (e.g., Wilson & Hey, 1995), which is located ~200 km to the south of the ridge near 91°30'W. Spreading rates along the GSC increase from 48 mm/yr at 100°W to 61 mm/yr at 85°W (Fig. 2.1b) (Argus *et al*., 2011). Crustal thickness increases with proximity to the hotspot, reaching ~8 km near 91°30'W (Fig. 2.1c) (Canales *et al*., 2002). The seismically imaged axial magma chamber (AMC) deepens away from the hotspot, with no AMC detected west of 94.7°W (Fig. 2.1c) (Blacic *et al*., 2004). Other parameters that vary systematically with proximity to the hotspot include axial depth (Canales *et al*., 2002), axial morphology (Sinton *et al.*, 2003; White *et al.*, 2008), topographic roughness in the axial zone (Sinton *et al.*, 2003), seamount abundance (Behn *et al.*, 2004; White *et al.*, 2008), and the chemical composition (Cushman *et al.*, 2004; Ingle *et al*., 2010) and crystallinity (Behn *et al*., 2004) of erupted lavas.

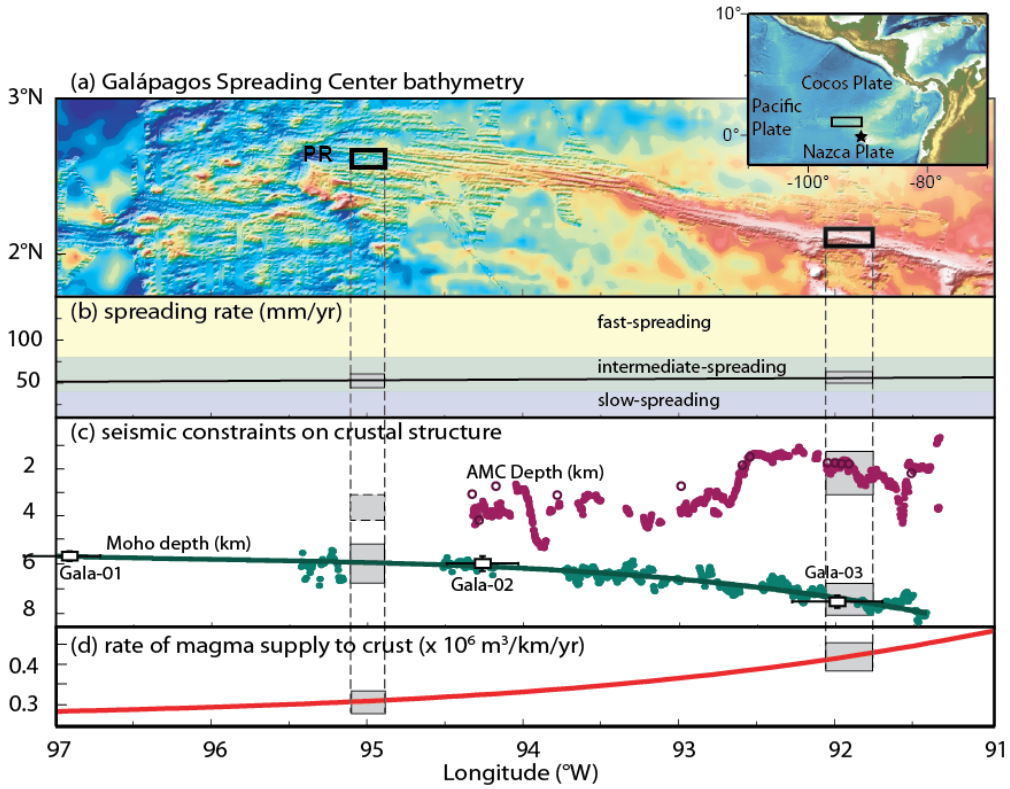

Figure 2.1. Regional setting and along-axis variations on the western Galápagos Spreading Center (GSC). Inset shows location of study areas relative to Central and South America. Star marks presumed location of Galápagos hotspot. (a) Regional bathymetry based on global compilation of multi-beam data merged with satellite-derived bathymetry data (Ryan *et al*., 2009). Black boxes outline locations of study areas, shown in Figure 2.2. PR, propagating rift. (b) Spreading rate (Argus *et al*., 2011). (c) Depths of axial magma chamber (AMC) seismic reflector (Blacic *et al*., 2004) and Moho (Canales *et al*., 2002). Solid circles, data from along-axis multichannel seismic (MCS) profiles; open circles, data from cross-axis MCS profiles. Gala-01, Gala-02, Gala-03, data from ocean bottom seismic refraction experiments (Canales *et al*., 2002). (d) Crustal production rate calculated as crustal thickness (from Canales *et al*., 2002) × spreading rate (Argus *et al*. (2011), after Sinton *et al*. (2003).

Two study areas with contrasting time-averaged rates of magma supply were selected for detailed geologic mapping of individual lava flow fields in order to investigate the effects of magma supply on MOR volcanic eruptions. The low- and high-magma-supply study areas are located 330 km apart at 95°W and 92°W, respectively (Figs. 2.1, 2.2). Over this distance, the average crustal magma supply (calculated as the product of the spreading rate and crustal thickness, after Sinton *et al.* (2003)) increases by

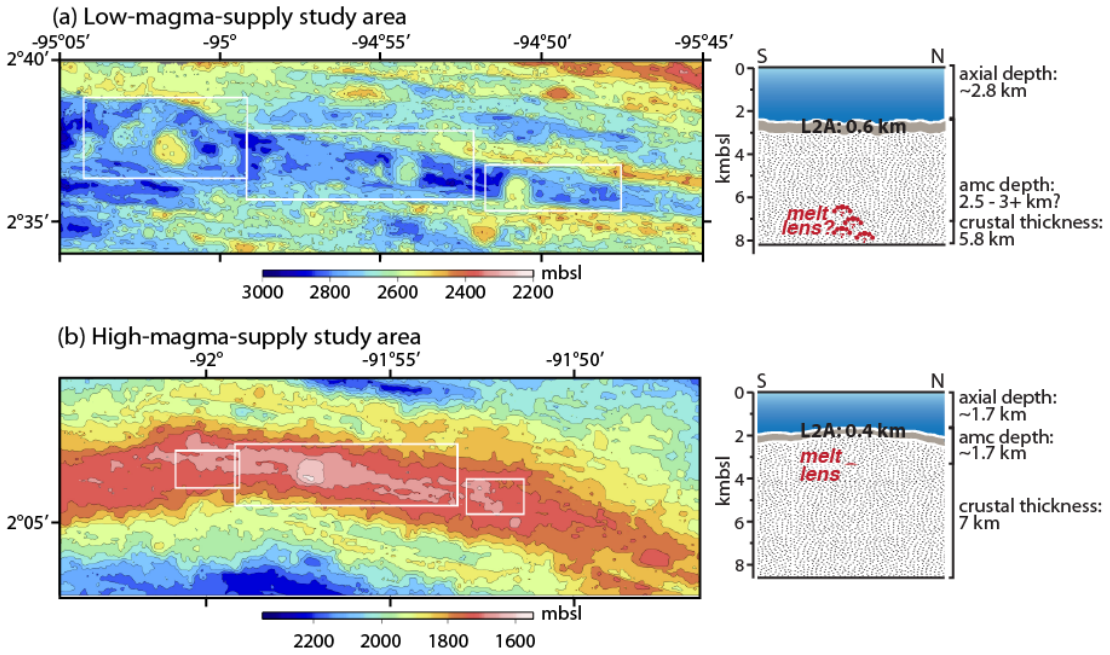

Figure 2.2. Bathymetric maps and schematic cross-sections of low- and high-magma-supply study areas. Cross-sections summarize structural differences as defined by seismic data (Blacic *et al*., 2004; Canales *et al*., 2002). At low magma supply, the seafloor is deeper, seismic layer 2A (L2A) is thicker, the crust is thinner, and no melt lens was imaged. White rectangles outline locations of geologic maps presented in Figures 2.4-2.9. Mbsl, meters below sealevel; kmbsl, kilometers below sealevel. (a) Low-magma-supply study area. (b) High-magma-supply study area.

roughly one third, from 0.3 × 10^6 m^3/km/yr to 0.4 ×10^6 m^3/km/yr (Fig. 2.1d). Short-term spatial and temporal variations in magma supply likely affect both areas, but are unknown in the absence of time-series seafloor deformation data or other constraints.

The low-magma-supply study area makes up the western half of the third-order spreading segment M5 of Sinton *et al.* (2003). A multi-channel seismic survey did not detect an axial melt lens in this region; ~35 km to the east, at 94.7°W, a magma lens is 3-4 km deep (Blacic *et al.*, 2004). A well-defined axial graben at least 2 km wide and 200 m deep is present throughout the 95°W study area (Fig. 2.2a). The axial graben widens to 6 km at the western end of the study area, as it approaches the tip of a westward-propagating rift (Fig. 2.2a) (e.g., Hey *et al*., 1986; Sinton *et al.*, 2003).

The high-magma-supply study area is roughly centered within the third-order spreading segment E5 of Sinton *et al*. (2003). A seismically detected melt lens is present at 1.6 km below the seafloor near the center of the segment, deepening to 2 km and 2.4

km at the western and eastern segment ends, respectively (Blacic *et al*., 2004). Within this area, the spreading center forms an axial rise that is cut by a shallow axial graben 10-40 m deep (Fig. 2.2b). Differences in axial morphology and crustal structure between the two study areas are summarized in Figure 2.2.

2.4. Eruptive unit definition and mapping

Observations of fissure eruptions along divergent plate boundaries in Iceland's Northern Volcanic Zone (Saemundsson, 1991; Wright *et al*., 2012) and Ethiopia's Dabbahu-Manda Harraro Rift (Ebinger *et al*., 2010; Wright *et al*., 2012), geologic mapping of submarine lava flow fields along the EPR (Sinton *et al*., 2002; Soule *et al*., 2007), and radiometric dating of samples from eruptions along the EPR (Rubin *et al*., 1994; 2006; Bergmanis *et al*., 2007; Rubin *et al.*, 2008) indicate that at least some lava flow fields are the products of multiple, relatively short-lived (hours to weeks) eruptive events, which collectively comprise longer eruptive episodes lasting months to years. For the purposes of this study, we define a lava flow field as the products of a single eruptive episode, which may comprise the products of multiple eruptive events. Lavas within a mapped flow field should be similar in age, have erupted from a spatially related set of vents, and display petrologic variations that represent co-magmatic evolution (non-random compositional variation that may reflect variable degrees of fractionation or magmatic mixing). With knowledge of eruption recurrence intervals and sedimentation rates, distinctions can be made among lavas erupted during different eruptive episodes from the past several hundred years, but not necessarily among eruptive events within a single eruptive episode.

In the field, the relative ages of submarine lavas can be assessed using observations of superposition and cross-cutting relationships, flow surface preservation, and sediment cover. Freshly erupted lava flows have lustrous, glassy surfaces, on which sediment begins to accumulate immediately (e.g., Haymon *et al.*, 1993). Sedimentation patterns vary depending on regional slope (steep flanks of mounds tend to shed sediment, which accumulates at their bases) and flow morphology (for high-relief flow morphologies, sediment accumulates first in low-lying pockets, which eventually fill and coalesce) (van Andel & Ballard, 1979). Additionally, hydrothermal activity can locally

enhance sedimentation rates (e.g., Chadwick *et al.*, 1998), and bottom currents can redistribute sediment. Bearing in mind these complications, sediment cover on submarine lava flows should be a reasonable proxy for relative age (van Andel & Ballard, 1979). Sediment accumulates relatively quickly along the GSC (1 mm/20-30 years) (Kleinrock & Hey, 1989; Mix *et al.*, 1991; Mitchell, 1998), allowing distinctions to be made among multiple eruptive episodes within the last several hundred years. Similarly, side-scan sonar data can be used to identify cross-cutting relationships between lava flows and fault scarps, and backscatter intensity can be used to assess sediment cover and aspects of flow surface roughness.

Radiometric and geomagnetic paleointensity dating techniques can be used to determine the relative and absolute ages of lava flow fields. Although these techniques are not available in the field, they have been used successfully to confirm that mapped flow fields comprise lavas that are similar in age, and to constrain eruption recurrence intervals (Bowles *et al.*, 2006; Bergmanis *et al.*, 2007) and the chronology of eruptive events within eruptive episodes (Rubin *et al.*, 1994, 1998, 2006).

Lavas erupted during a single eruptive episode are typically delivered to the seafloor via a set of spatially related eruptive fissures, although they need not be contiguous. In some cases, eruptive fissures are visible (Gregg *et al.*, 1996; Sinton *et al.*, 2002; Soule *et al.*, 2007), but elsewhere they are obscured by low effusion-rate lavas and/ or later eruptions (e.g., Chadwick & Embley, 1994; Embley *et al.*, 2000; Sinton *et al.*, 2002). Individual eruptive episodes may include effusion from multiple distinct fissure segments (e.g., Chadwick *et al.*, 1995; Soule *et al.*, 2007). In the absence of mappable eruptive fissures, vent location can be inferred from lava flow directions (e.g., Ballard & van Andel, 1977) and topographic considerations.

At divergent plate boundaries, lavas erupted during individual eruptive episodes commonly have a limited range in modal mineralogy and phenocryst content, and define coherent trends in chemical variation (Rubin *et al.*, 1998; 2001; Sinton *et al.*, 2002). The variations, however, can be more complicated than those associated with simple fractionation, as exemplified by the N1 eruption at 17°30'S on the EPR, where magma mixing-controlled variations in magmatic temperature coincide with a third-order discontinuity in the ridge (Bergmanis *et al.*, 2007). Similarly, the major and trace element

compositions of lavas erupted during the 2005-6 eruption at 9°50'N on the EPR vary along the length of an eruptive fissure system spanning several 3rd and 4th order offsets (Goss *et al.*, 2010). Although many MOR eruptions in Iceland also show coherent spatial-compositional trends (Sinton *et al.*, 2005), complicated magmatic processes appear to be more common in hotspot-affected regions with anomalously thick crust (e.g., Maclennan *et al.*, 2008; Grönvold *et al.*, 2008; Eason & Sinton, 2009).

2.5. Methods

2.5.1. Field investigations: AT15-63 shipboard operations

In March-April 2010, the Galápagos Ridge Undersea Volcanic Eruptions Expedition (AT15-63, *R/V Atlantis*) carried out geologic mapping at two study areas along the GSC (Figs. 2.1, 2.2; see also www.soest.hawaii.edu/gruvee). Observations of the seafloor were made during thirteen dives at each study area (twenty-six total), using the human-occupied submersible *Alvin* (operated by the Woods Hole Oceanographic Institution, WHOI). *Alvin* dive tracks averaged 3.6 km in length, covering a total of ~46 km at each study area. Individual dives visited targets identified from bathymetric maps and previously collected DSL 120A acoustic backscatter data (White *et al.*, 2008). Divers used relationships of superposition between lava flows and changes in sediment cover, lava flow direction, and lava morphology to infer boundaries between eruptive units. In addition, 300 rock samples were collected for petrologic study. The submersible was navigated using gyro-compass measurements of heading and Doppler-derived speeds in conjunction with ultra-short baseline (USBL) navigation fixes. Because this navigation system is dependent on communication with the ship, error is accumulated when the submersible loses contact with the ship, for example in close proximity to fault scarps. After the cruise, dive tracks were adjusted manually, where necessary, so that measured depths and diver observations of prominent features were consistent with bathymetric maps.

Night programs during the cruise included photographic surveys and sampling with the deep-towed camera sled *TowCam* (Fornari, 2003), and bathymetric surveys using the autonomous underwater vehicle (AUV) *Sentry* (both operated by WHOI). *TowCam* deployments covered 40 km of seafloor (average 2.5 km per tow), and were

used both for reconnaissance over potential dive targets, and to visit lower priority locations, frequently farther off-axis. The camera system was towed 5-8 m above the seafloor at a speed of 0.25-0.5 knots, taking color digital photographs of regions ~3-5 m across at 10 s intervals. The camera was connected to the ship via a fiber-optic cable, allowing real-time selection of sampling sites and classification of lava morphology and age relationships. A total of 47 glass samples (wax cores) and 3 rock samples were retrieved with *TowCam*.

Sentry was used to map the seafloor at high resolution (1-2 m spatial; < 0.5 m vertical) (McClinton *et al.*, 2012). *Sentry* was equipped with a Reson 7125 400 kHz multi-beam sonar system, and operated concurrently with *TowCam*. Flying at 60-80 m above the seafloor, *Sentry* mapped 38 km^2 and 47 km^2 of seafloor at the low- and high-magma-supply study areas, respectively. Mapping of the seafloor at this high resolution reveals morphological details including mounds from which larger volcanic edifices are constructed, lava channels, collapse pits, inflated regions, and even individual hydrothermal chimneys. High-resolution bathymetry data were used to plan *Alvin* and *TowCam* deployments, and to extrapolate observed contacts to regions of the seafloor that were not visited by *Alvin* or *TowCam*.

2.5.2. Shore-based investigations

2.5.2.1. Lava composition

Where rock samples were available, they were characterized in hand sample; thin sections were made of selected samples from each eruptive unit. Major element compositions of volcanic glass from 331 samples (including rock samples from *Alvin* and glass chips from *TowCam*) were determined using the University of Hawai‘i JEOL JXA-8500F, five-spectrometer electron microprobe. Average compositions and typical mineralogy of samples from each flow field are presented in Table 2.1. Analytical procedures and the full dataset of glass microprobe analyses are available in the supplementary materials.

Table 2.1. Average chemical composition and sample descriptions for lavas from GSC eruptive units

		SiO_2	TiO_2	Al_2O_3	FeO*	MnO	MgO	CaO	Na_2O	K_2O	P_2O_5	S	Sum	Temp (°C)	Sample mineralogy
Low magma supply	Frijoles	50.3	1.42	14.1	11.3	0.20	7.48	12.2	2.25	0.13	0.13	0.13	99.6	1175	15-20% plag-phyric;
	n = 17 σ	0.4	0.07	0.2	0.2	0.01	0.18	0.2	0.03	0.01	0.01	0.00			2-5% ol-phyric
	Del Norte	49.8	1.27	14.8	10.4	0.18	8.28	12.6	2.11	0.11	0.11	0.12	99.6	1187	<5-15% plag-phyric,
	n = 25 σ	0.3	0.03	0.1	0.1	0.01	0.07	0.1	0.02	0.00	0.01	0.00			1-2% ol-phyric
	Buho	49.9	1.45	14.7	11.0	0.19	8.27	11.9	2.25	0.13	0.13	0.13	100.1	1192	< 2 % ol-phyric
	n = 28 σ	0.5	0.03	0.2	0.1	0.01	0.22	0.1	0.06	0.00	0.01	0.00			
	Tortuga	50.5	1.23	14.7	10.6	0.19	8.13	12.7	2.25	0.08	0.10	0.12	100.8	1189	15-20% plag-phyric;
	n = 6 σ	0.1	0.03	0.1	0.1	0.00	0.08	0.0	0.02	0.00	0.00	0.00			< 2% ol-phyric
	Dragón	49.6	1.26	14.6	10.6	0.18	8.26	12.3	2.12	0.10	0.10	0.12	99.2	1189	3-5% plag-phyric
	n = 15 σ	0.3	0.02	0.1	0.1	0.01	0.07	0.0	0.03	0.00	0.01	0.00			
	Pulgár	50.6	1.28	14.2	10.8	0.19	7.95	12.6	2.10	0.08	0.10	0.12	100.1	1183	10-15% plag-phyric;
	n = 9 σ	0.3	0.02	0.1	0.1	0.01	0.06	0.0	0.02	0.00	0.01	0.00			< 2% ol-phyric
	Pinguino	51.0	1.38	14.2	11.3	0.19	7.63	12.2	2.15	0.11	0.12	0.13	100.7	1176	< 3% ol- and plag-
	n = 4 σ	0.3	0.04	0.1	0.2	0.00	0.11	0.1	0.02	0.00	0.01	0.00			phyric
	Altares	51.4	1.51	14.4	11.5	0.20	7.42	12.0	2.41	0.14	0.14	0.13	101.3	1171	5-15% plag; < 2% ol
	n = 10 σ	0.3	0.10	0.1	0.2	0.01	0.21	0.2	0.09	0.02	0.02	0.00			
High magma supply	Ninos	50.5	2.93	13.1	14.9	0.25	4.36	8.8	3.38	0.64	0.41	0.18	99.4	1105	aphyric
	n = 29 σ	0.6	0.04	0.1	0.2	0.01	0.10	0.2	0.06	0.02	0.01	0.00			
	Calór	50.4	2.04	14.0	12.2	0.20	6.26	10.9	2.75	0.45	0.24	0.14	99.6	1144	aphyric
	n = 30 σ	1.4	0.17	0.3	0.3	0.05	0.08	0.2	0.12	0.04	0.06	0.01			
	Empanada	50.3	2.79	13.4	14.4	0.24	4.81	9.3	3.27	0.56	0.36	0.17	99.6	1114	aphyric
	n = 11 σ	1.5	0.18	0.4	0.6	0.02	0.42	0.4	0.10	0.05	0.03	0.01			
	Dulces	53.0	2.52	13.3	13.8	0.24	3.33	7.5	3.55	0.86	0.54	0.14	98.8	1084	aphyric
	n = 4 σ	1.1	0.18	0.2	0.1	0.01	0.49	0.6	0.21	0.08	0.04	0.01			
	Gusanos	48.8	1.94	14.9	11.2	0.19	7.00	11.9	2.76	0.34	0.22	0.13	99.5	1156	aphyric
	n = 3 σ	0.7	0.04	0.2	0.2	0.01	0.16	0.3	0.01	0.01	0.01	0.00			
	Iguana	50.6	2.04	14.1	12.2	0.20	6.10	10.9	2.77	0.50	0.25	0.14	99.7	1144	aphyric
	n = 11 σ	0.4	0.02	0.1	0.1	0.01	0.08	0.1	0.02	0.01	0.01	0.00			
	Cocodrilo	50.6	2.04	14.1	12.2	0.20	6.10	10.9	2.77	0.50	0.25	0.14	99.7	1139	aphyric
	n = 11 σ	0.8	0.04	0.2	0.3	0.01	0.16	0.2	0.05	0.02	0.01	0.00			
	Lobo del Mar	50.0	2.29	14.6	12.2	0.20	5.98	10.5	3.01	0.41	0.27	0.15	99.6	1139	< 1 % plag-phyric
	n = 5 σ	0.8	0.04	0.1	0.2	0.00	0.14	0.1	0.06	0.01	0.01	0.00			
	Lagarto	48.1	1.71	16.2	10.2	0.17	7.99	11.9	2.56	0.32	0.20	0.11	99.5	1183	aphyric
	n = 7 σ	0.3	0.03	0.1	0.1	0.00	0.10	0.1	0.02	0.01	0.00	0.00			
	Cobija	49.3	1.89	14.6	11.3	0.19	6.92	11.8	2.71	0.37	0.21	0.13	99.3	1155	aphyric
	n = 11 σ	0.6	0.13	0.4	0.5	0.01	0.19	0.4	0.13	0.03	0.03	0.00			

2.5.2.2. Geologic interpretation

Following each *Alvin* dive and *TowCam* deployment, preliminary geologic maps were prepared showing the locations of apparent flow contacts and other features such as faults, fissures, collapse structures, and flow directions. *TowCam* images and screen shots from *Alvin* dive video were assigned locations and geo-referenced. After the conclusion of the cruise, the preliminary geologic maps were used in conjunction with dive videos and transcripts to draw inferred flow boundaries. DSL 120A side-scan sonar data from a December 2005 survey (White *et al.*, 2008) and the high-resolution bathymetry from *Sentry* were used to extend unit boundaries beyond the visually observed contacts, and to help constrain relative ages. Glass composition and sample descriptions were also used to refine flow field boundaries, and to correlate noncontiguous segments of lava flow fields, where consistent with observations of sediment cover.

2.6. Eruptive edifice morphology

Eruptive unit morphologies at the two study areas can be classified on the basis of vertical relief and plan-view basal elongation. We use the four edifice morphologies (smooth flows, hummocky ridges, hummocky mounds, seamounts) described by Head *et al*. (1996) along the Mid-Atlantic Ridge (MAR), but note that the sizes of the features observed within our study areas are somewhat different (see below). Both smooth flows and hummocky ridges are elongated parallel to the spreading axis (Head *et al.*, 1996). Smooth flows are low-relief lava flow fields that typically occur within topographic lows, and may be composed of pillows or sheet flows (Fig. 2.3a) (Head *et al.*, 1996). The inferred eruptive vents feeding these flow fields are aligned along fissures that are up to several kilometers long. Lava is efficiently transported away from the vents via lava channels and inflated lobate lava flows, producing laterally extensive (up to 2.2 km wide) fields. Hummocky ridges have greater relief than smooth flows (maximum 40-50 m tall, except where flow is focused) (Fig. 2.3d). All hummocky ridges observed within our study areas are discontinuous along axis. Several of the hummocky ridges are

significantly longer than those observed along the MAR (2-11 km long within our study areas, vs. 1-2.5 km long along the MAR) (Head *et al*., 1996) .

Unlike smooth flows and hummocky ridges, hummocky mounds and seamounts are essentially equi-dimensional (Head *et al*., 1996). Hummocky mounds are made up of clusters of smaller mounds that may be conical or have small summit plateaus (Fig. 2.3b). The hummocky mounds along the GSC are generally larger than those observed along the MAR (1.5-3 km diameter; 90-200 m tall within our study areas, vs. 0.05-0.5 km diameter; < 50 m tall along the MAR). Seamounts are more regular in shape, with plateau-like summit regions (Fig. 2.3c); these edifices are associated with the largest-volume eruptions at each study area, and are similar in size to those observed along the MAR (2-2.7 km diameter; 150-300 m tall at our study areas, vs. 0.5-3 km diameter; 50-350 m tall along the MAR). Collapse craters are locally present within the summit regions.

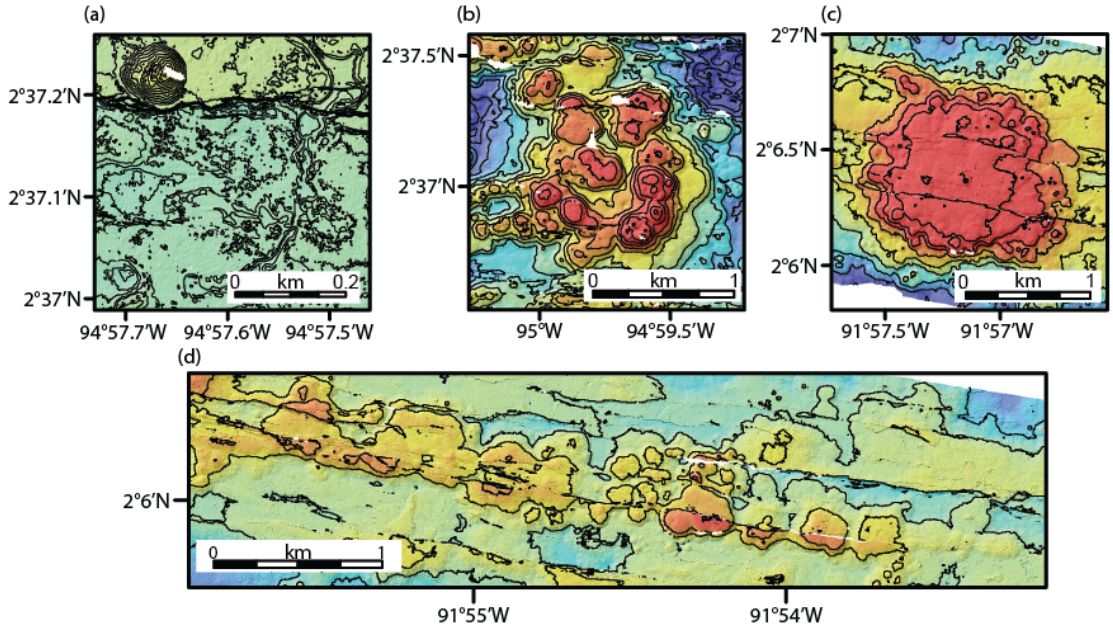

Figure 2.3. Representative maps of eruptive morphology classifications, after Head *et al.* (1996). Morphologies are shown as seen in < 1 m resolution Sentry data (McClinton *et al*., 2012). Contour interval: 20 m, except 2 m for smooth flows. (a) Smooth flows. (b) Hummocky mounds. (c) Seamount. (d) Hummocky ridge.

2.7. Eruptive Units

Each study area has been divided into three geographic sub-regions (western, central, and eastern), within which we can constrain relative age relationships among

mapped units. Within each sub-region, eruptive units are presented from oldest to youngest. Eruptive units were named based on their appearance in map view or defining characteristics. Three common sediment cover classifications are used (e.g., Fox *et al*., 1988): light, moderate, or heavy. Light sediment cover consists of a dusting of sediment on flow surfaces, with slight accumulations in pockets between pillows; sheet flow morphology and details such as striations on pillow lobes are easily discerned. With moderate sediment cover, pockets between pillows contain significant accumulations of sediment (but are not filled); jumbled sheet flow surfaces are partially obscured. Under heavy sediment cover, sediment-filled pockets between pillows are coalescing; lobate and sheet flows are blanketed with sediment such that flow morphology is obscured. The mapped unit boundaries, major element compositions, and representative outcrop photos are presented in Figs. 2.4-2.9. A table describing observed hydrothermal features is provided in the supplementary materials.

Samples collected at both study areas are predominantly basalts (less than 52 wt. % SiO_2 (LeBas & Streckeisen, 1991)). Fractionation of olivine, plagioclase, and clinopyroxene drives melt compositions to higher FeO* (total iron) and TiO_2 contents until Fe-Ti- oxides become stable at ~4 wt % MgO; basalts with greater than 12 wt. % FeO* and 2 wt. % TiO_2 are classified as FeTi basalts, after Byerly *et al.* (1976). At the low-magma-supply study area, FeTi basalts are rare (2 % of samples), whereas at the high-magma-supply study area, they account for half of all samples. Small volumes of basaltic andesite (greater than 52 wt. % SiO_2 (LeBas & Streckeisen, 1991)) are present in the eastern sub-region of the high-magma–supply study area (see Section 2.7.2.3, below).

2.7.1. Low-magma-supply study area

2.7.1.1 Western region (95°04’W-94°59’W) (Figure 2.4)

Two eruptive units, Buho and Pulgar, were mapped in the northern half of the axial graben shown in Figure 2.2a. The Pulgar flow field is made up of a cluster of hummocky mounds. The flanks of the mounds are constructed of unornamented, elongate pillows, whereas lobate flows are more common at the summit plateaus of individual hummocks. Samples from Pulgar have 10-15 vol. % plagioclase phenocrysts and less than 2 vol. % olivine phenocrysts, and cluster tightly in composition (7.9-8.0 wt. %

MgO). Pulgar has moderate to heavy sediment cover (somewhat heavier at the nearly flat summits of mounds), but heavier sediment and greater fault density on the surrounding seafloor indicate that Pulgar is younger than the regions surrounding it.

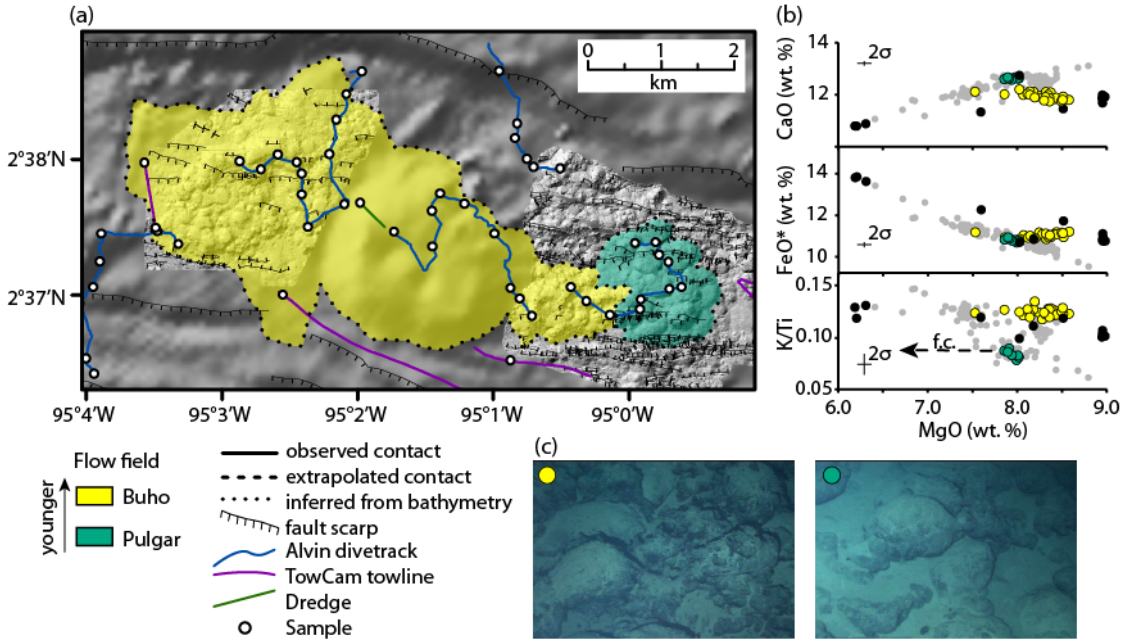

Figure 2.4. Western region, low-magma-supply study area. (a) Geologic map of region; see legend for symbols. Unit boundaries are symbolized according to how well constrained they are. (b) Compositional fields for eruptive units within the central region. Colors correspond to those used in the geologic map: yellow, Buho; teal, Pulgar; black, older units from western region; grey, other low-magma-supply samples. Dashed line labeled "f.c." on plot of MgO vs. K/Ti shows liquid line of descent predicted by MELTS for fractional crystallization at 500 bars, with oxygen fugacity two log units below the fayalite-magnetite-quartz buffer (Ghiorso & Sack, 1995; Asimow & Ghiorso, 1998). (c) Photos of seafloor within each eruptive unit showing typical sediment cover and lava morphology; colors same as in compositional plots.

The Buho flow field is the largest mapped eruptive unit, and comprises an axial seamount 2.6 km in diameter and smaller clusters of hummocky mounds to the east and west. The plateau-like summit region of Buho's central seamount has undulating topography, broken by two collapse craters each 400 m in diameter and greater than 50 m deep. Lavas throughout the flow field have highly ornamented pillow morphology, with abundant cm-scale buds protruding from 1-2 m-diameter pillow lobes. Samples are basalts with less than 2 vol. % olivine phenocrysts and greater intra-flow compositional variation than Pulgar (7.5-8.6 wt. % MgO). Similar mineralogy and geomagnetic paleointensity of samples collected throughout Buho (J. Bowles, unpublished data)

support mapping this large flow field as a single eruptive unit. Buho's light to moderate sediment cover and lower fault density indicate that Buho is younger than Pulgar. At the same MgO content, samples from Pulgar and Buho have different K/Ti ratios (0.09-0.10 and 0.12-0.13, respectively), indicating that they were derived from different parental magmas.

2.7.1.2. Central region (94°59'W-94°52'W) (Figure 2.5)

A sequence of four mapped lava flow fields in the central region of the low-magma-supply study area exhibits considerable variability in eruptive style. The most prominent eruptive edifice in the central region is Pinguino, an axial seamount 1.7 km in diameter that rises ~200 m above the adjacent graben floor. The northern and southern flanks of Pinguino are cut by east-west-trending faults, and are partially obscured by talus. Side-scan sonar and *TowCam* imagery of the summit region reveal several partially collapsed tumuli; lobate lavas are more abundant at the summit than on the flanks. Samples from Pinguino have 7.5-7.8 wt. % MgO and less than 3 vol. % olivine and plagioclase phenocrysts. The heavy sediment cover observed throughout the summit plateau indicates that Pinguino is the oldest eruptive unit in this sub-region.

The next oldest flow field in the region is Dragón, a relatively small cluster of hummocky mounds that is slightly elongated parallel to the spreading axis, and centered within the axial graben. Dragón's steep flanks are constructed of ornamented pillow lavas. Samples from Dragón define a tight compositional field with 8.2-8.4 wt. % MgO, and have 3-5 vol. % plagioclase phenocrysts. Sediment cover is moderate to heavy even on the steep flanks.

Much of the floor of the axial graben in this sub-region is covered by the broad, gently south-sloping Del Norte flow field, which was erupted from a series of vents near the northern wall of the axial graben and flowed predominantly to the south, where it ponded within the inner axial graben. The areal distribution of Del Norte lava suggests eruption from a fissure at least 3 km long; the eruptive fissures cut through older, compositionally distinct pillow mounds, which are now surrounded by Del Norte lavas. Predominantly north-south-trending lava channels apparently dispersed lava across the

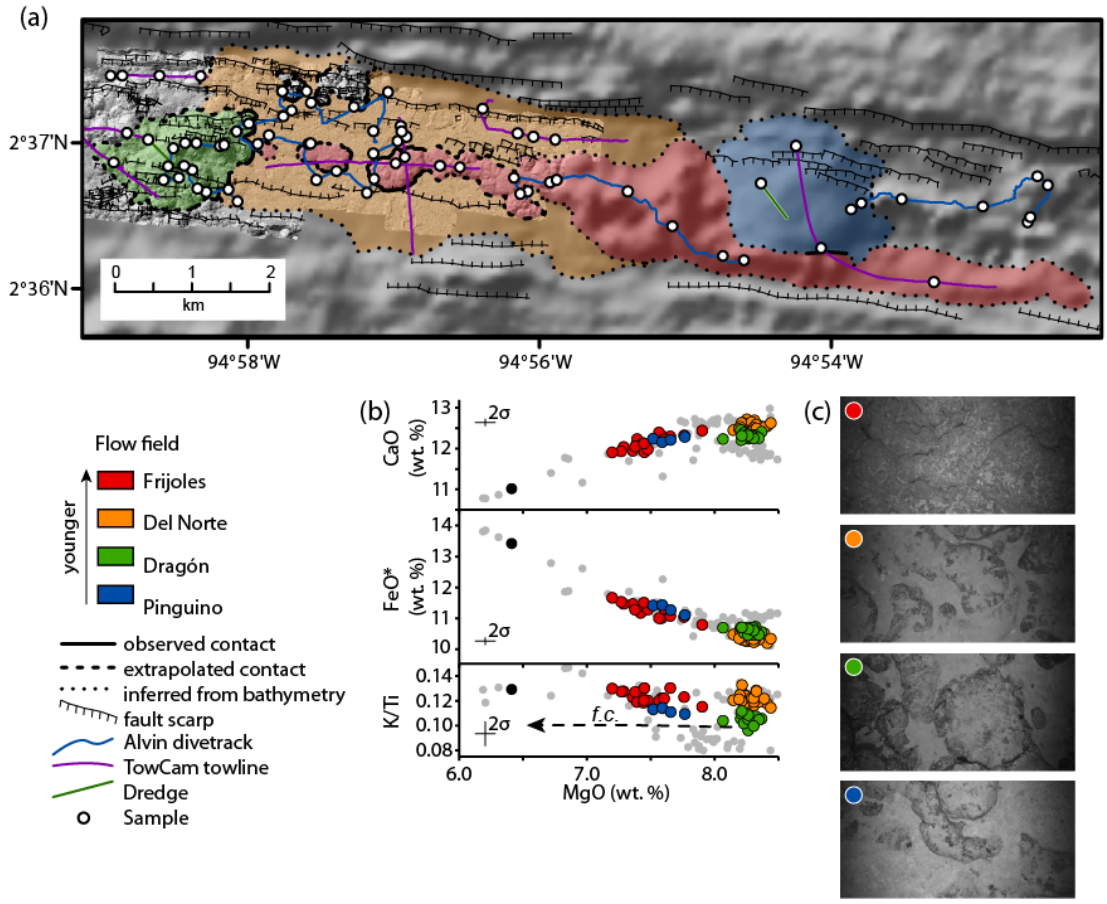

Figure 2.5. Central region, low-magma-supply study area. (a) Geologic map of region; see legend for symbols. Unit boundaries are symbolized according to how well constrained they are. (b) Compositional fields for eruptive units within the central region. Colors correspond to those used in the geologic map: red, Frijoles; orange, Del Norte; green, Dragón; blue, Pinguino; black, older mound crosscut by Del Norte eruptive fissures; grey, other low-magma-supply samples. Dashed line labeled "f.c." on plot of MgO vs. K/Ti shows liquid line of descent predicted by MELTS for fractional crystallization at 500 bars, with oxygen fugacity two log units below the fayalite-magnetite-quartz buffer (Ghiorso & Sack, 1995; Asimow & Ghiorso, 1998). (c) Photos of seafloor within each eruptive unit showing typical sediment cover and lava morphology; colors same as in compositional plots.

axial graben floor. A characteristic stratigraphic sequence of basal sheet flows overlain by lobate flows and small pillow mounds was observed in several locations within this unit, likely indicating decreasing effusion rates as the eruption progressed. Samples from Del Norte are basalts with 5-15 vol. % plagioclase phenocrysts and 1-2 vol. % olivine phenocrysts, and 8.3-8.4 wt. % MgO. In contrast, a sample from the older mound that is cut by Del Norte's eruptive fissures has lower MgO (6.5 wt. %) and is more phenocryst-

rich. Del Norte is younger than Dragón, as shown by a high-lava mark (post-drainout feature (Fornari *et al.*, 2004)) of Del Norte lavas ~10 m above the surrounding flow surface on the eastern flank of Dragón, and Del Norte lavas that bury small-offset faults cutting Dragón. Del Norte flows are cut by 10-15 m-high fault scarps at both sides of the graben, indicating that at least some major tectonic event(s) post-dates Del Norte emplacement.

The youngest lavas mapped in the low-magma-supply study area are the Frijoles pillow mounds, which form a discontinuous hummocky ridge centered within the axial graben, ~800 m south of the fissures inferred to have fed the Del Norte eruption. The eastern extent of the Frijoles unit deviates to the south along the flank of the axial graben where Pinguino blocks the middle of the graben. The Frijoles pillow mounds were erupted along a 10.6 km-long eruptive fissure, unlike the more equi-dimensional eruptions that predominate in the study area. *Sentry* bathymetry of the mounds shows that the western mounds have relatively low relief, with broad, nearly horizontal summit plateaus. The eruption appears to have focused near the center of the eruptive fissure, where a large, steep-sided cluster of hummocky pillow mounds reaches heights of nearly 200 m above the surrounding seafloor. Samples range from 7.2 to 7.9 wt. % MgO and contain 15-20 vol. % plagioclase phenocrysts, 2-5 vol. % olivine phenocrysts, and sparse clinopyroxene phenocrysts. The relative age of this youngest unit in the sub-region is confirmed by direct observation of contacts between lightly sedimented Frijoles lavas overlying more heavily sedimented Del Norte lavas in several locations. In addition, *Sentry* bathymetry provides multiple examples of Frijoles mounds that bury Del Norte lava channels and tumuli, and faults that crosscut Del Norte lavas. Yellowish sediment in the summit region of some of the mounds suggests the previous occurrence of diffuse flow hydrothermal activity nearby, similar to stains and coatings observed by Embley *et al*. (2000) on the CoAxial segment of the JdFR.

The major and minor element compositions of the four most recent eruptive units in the central subregion of the low-magma-supply study area require at least two parental magmas (Fig. 2.5). Based on these data, it is possible that Frijoles and Del Norte could be related by fractionation of a single parental melt composition. However, the difference in K/Ti between Dragón and Del Norte (0.10-0.11 and 0.12-0.13, respectively) at the same

MgO content requires that they were derived from different parental magmas. Variations in the major and minor element compositions within each of these eruptions appear to be consistent with fractional crystallization.

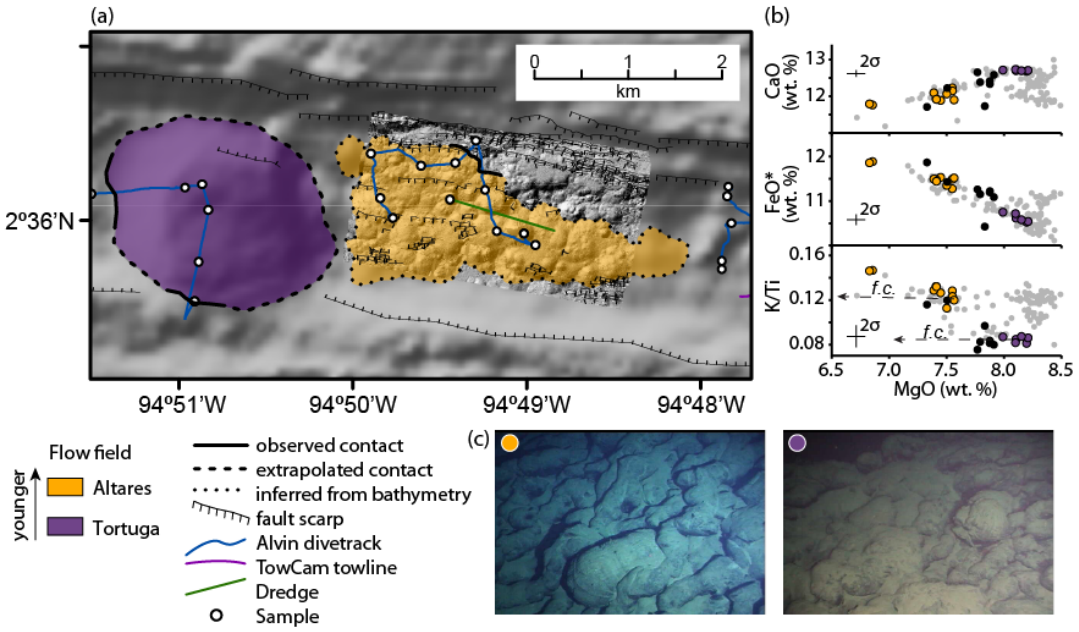

Figure 2.6. Eastern region, low-magma-supply study area. (a) Geologic map of region; see legend for symbols. Unit boundaries are symbolized according to how well constrained they are. (b) Compositional fields for eruptive units within the central region. Colors correspond to those used in the geologic map: orange, Altares; purple, Tortuga; black, other eastern sub-region lavas older than Altares; grey, other low-magma-supply samples. Dashed line labeled "f.c." on plot of MgO vs. K/Ti shows liquid line of descent predicted by MELTS for fractional crystallization at 500 bars, with oxygen fugacity two log units below the fayalite-magnetite-quartz buffer (Ghiorso & Sack, 1995; Asimow & Ghiorso, 1998). (c) Photos of seafloor within each eruptive unit showing typical sediment cover and lava morphology; colors same as in compositional plots.

2.7.1.3. Eastern region (94°51.5'W-94°48'W) (Figure 2.6)

A third axial seamount, Tortuga, is located in the eastern region of the low-magma-supply study area. As with the other axial seamounts that were visited, its lower flanks are obscured by an apron of pillow talus. The summit plateau has a mixture of pillow flows and inflated lobate flows similar to features at Pinguino. Deep, east-west trending fissures dissect the summit plateau, exposing pillow and lobate flows. Samples from Tortuga have 15-20 vol. % plagioclase phenocrysts and less than 2 vol. % olivine

phenocrysts, with 8.0-8.2 wt. % MgO. Heavy sediment cover suggests that Tortuga is similar in age to Pinguino, Dragón, and Pulgar.

The Altares flow field is the easternmost mapped eruptive unit in the low-magma-supply study area, and consists of a cluster of hummocky mounds that is somewhat elongated along a trend oblique to the spreading axis. The flanks of the mounds are mantled with elongate pillow lavas, and lobate flows are more common at the plateau-like summit regions. Samples from Altares have 5-15 vol. % plagioclase and less than 2 vol. % olivine, and contain 7.4-7.6 wt. % MgO. Sediment cover is light to moderate. Near the center of the flow field, a pinnacle built of elongate pillows (apparently erupted at very slow effusion rate) rises ~100 m above the summit plateau. Despite being more evolved compositionally (6.8-6.9 wt. % MgO) than the remainder of the flow field, this pinnacle does not exhibit a significant difference in sediment cover from the rest of Altares. If the pinnacle formed during a later eruptive event, it must have occurred soon after the end of the Altares eruption. K/Ti increases with decreasing MgO in Altares samples, suggesting that compositional variation in this flow field is dominated by magma mixing between at least two variably fractionated batches of magma. The difference in K/Ti between Altares and Tortuga requires different parental magmas for these two units.

2.7.2. High-magma-supply study area

2.7.2.1. Western Region (92°0.5'W-91°59'W) (Figure 2.7)

The western region of the high-magma-supply study area is intensely faulted, and lacks prominent mounds and ridges, making the identification of flow boundaries difficult. In addition, submersible dives experienced stronger currents throughout the 92°W study area, suggesting that sediment redistribution may be more significant here. Two eruptive units within the western sub-region, Lagarto and Lobo del Mar, are distinguishable mainly on the basis of compositional differences. A third eruptive unit, Calor, is mapped as the westernmost extent of one of the eruptive units in the central region of the high-magma-supply study area (see Section 2.7.2.2, below) based on similarities in composition and sediment cover. The Lobo del Mar flow field erupted from a series of vents aligned along an eruptive fissure near the center of the axial

graben. A network of lava channels connects these fissures to a partially collapsed lava lake slightly south of the axis. Samples from this flow field are FeTi basalts with 5.8 to 6.2 wt. % MgO. Notably, samples from the Lobo del Mar flow field are slightly (≤1 %) plagioclase-phyric; samples from every other eruptive unit sampled in the high-magma supply-study area are aphyric.

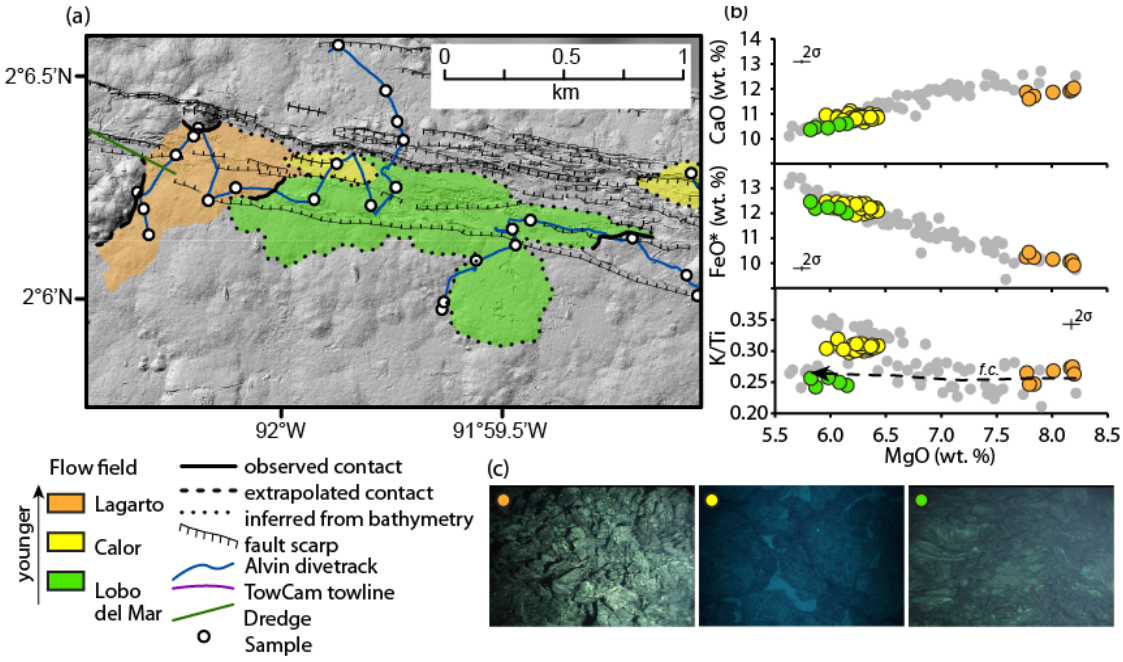

Figure 2.7. Western region, high-magma-supply study area. (a) Geologic map of region; see legend for symbols. Unit boundaries are symbolized according to how well constrained they are. (b) Compositional fields for eruptive units within the central region. Colors correspond to those used in the geologic map: yellow, Calor; peach, Lagarto; green, Lobo del Mar; grey, other high-magma-supply samples. Dashed line labeled "f.c." on plot of MgO vs. K/Ti shows liquid line of descent predicted by MELTS for fractional crystallization at 500 bars, with oxygen fugacity one log unit below the fayalite-magnetite-quartz buffer (Ghiorso & Sack, 1995; Asimow & Ghiorso, 1998). (c) Photos of seafloor within each eruptive unit showing typical sediment cover and lava morphology; colors same as in compositional plots.

The westernmost mapped flow field in the high-magma-supply study area is the Lagarto flow field, which includes jumbled sheet flows and more laterally extensive regions made up of lobate flows and pillows. In the eastern region of the flow field, there is a north-south-trending channel system within the inner axial graben. Samples from the Lagarto flow field have much higher MgO (7.8 to 8.2 wt. %) than those from Lobo del

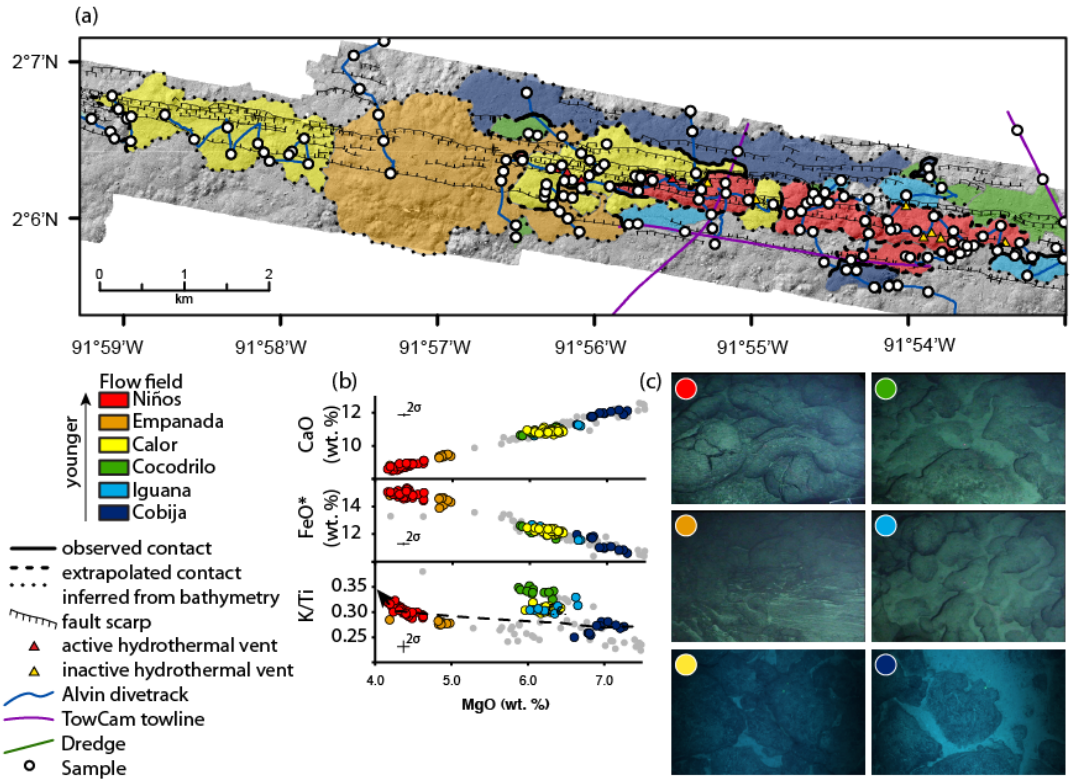

Figure 2.8. Central region, high-magma-supply study area. (a) Geologic map of region; see legend for symbols. Unit boundaries are symbolized according to how well constrained they are. (b) Compositional fields for eruptive units within the central region. Colors correspond to those used in the geologic map: red, Niños; orange, Empanada; yellow, Calor; green, Cocodrilo; blue, Iguana; purple, Cobija; grey, other high-magma-supply samples. Dashed line labeled "f.c." on plot of MgO vs. K/Ti shows liquid line of descent predicted by MELTS for fractional crystallization at 500 bars, with oxygen fugacity one log unit below the fayalite-magnetite-quartz buffer (Ghiorso & Sack, 1995; Asimow & Ghiorso, 1998). (c) Photos of seafloor within each eruptive unit showing typical sediment cover and lava morphology; colors same as in compositional plots.

Mar, although their major and minor element compositions are consistent with derivation from a common parental magma by fractional crystallization. Sediment cover on the two eruptive units is not sufficiently different to assign relative ages.

2.7.2.2. Central region (91°59'W-91°53'W) (Figure 2.8)

Of the six eruptive units that were mapped in the central sub-region of the high-magma-supply study area, Cobija extends the farthest off-axis. Cobija is a smooth lava

flow field that consists of a mixture of low-lying pillow, lobate and sheet lavas. Samples from Cobija are aphyric basalts with 6.6-7.3 wt. % MgO. Cobija has heavy sediment cover, and preliminary geomagnetic paleointensity data indicate an eruptive age of ~400 years (Bowles *et al.*, 2011). Lavas with similar sediment cover and composition are observed both to the north and south of the axis, and likely belong to the same eruptive episode, with intervening areas buried by more recent eruptive activity.

Moving inward toward the spreading axis in the central region, there are two younger flow fields, Cocodrilo and Iguana. Both flow fields contain a mixture of pillow, lobate, and sheet lavas. Samples from both Cocodrilo and Iguana range from basalts to FeTi basalts (5.9-6.3 and 6.0-6.7 wt. % MgO, respectively), but the two flow fields have different K/Ti ratios (0.33-0.35 and 0.30-0.33), indicating that they either evolved from, or mixed with, different parental magmas. Differences in sediment cover at the boundaries between the two flow fields demonstrate that Cocodrilo is slightly younger than Iguana. Significant portions of these eruptive units appear to have been buried by younger flows.

Calor is a hummocky ridge that stretches 8.3 km along axis. The off-axis boundaries of the western half of the Calor flow field were not observed, but are presumed to be similar in width to the more extensively-mapped eastern half (1 km wide). Calor is less sedimented than Cocodrilo and Iguana, and preliminary geomagnetic paleointensity measurements indicate that they are less than ~200 years old (Bowles *et al*., 2011). Samples from Calor are FeTi basalts that are compositionally similar to those from Iguana (6.0-6.4 wt. % MgO; 0.30-0.32 K/Ti). In April 2010, several high-temperature hydrothermal chimneys were active near Calor's eastern boundary.

The Empanada flow field comprises a broad, 100 m-tall axial seamount and a series of associated sheet flows to the east. The seamount, located near 92°W, is the only relatively large, point-source flow field mapped within the high-magma-supply study area. The flanks of the seamount consist of pillow lavas, whereas lavas at the summit plateau are lobate, with some large, collapsed tumuli that rise 5-10 m above the surrounding flow surfaces. The low-lying sheet flows were erupted from vents just south of the axial graben, apparently during a high-effusion-rate phase before effusion along the eruptive fissure focused to the seamount itself. Samples from both the seamount and

the adjacent sheet flows are FeTi basalts (4.2-5.0 wt. % MgO; 0.28-0.29 K/Ti). Although there is not a significant difference in sediment cover between Empanada and Calor and preliminary geomagnetic paleointensity measurements of the two units are indistinguishable (Bowles *et al*., 2011), Empanada is less faulted than Calor and appears to have buried the middle of the Calor ridge, suggesting that it is younger.

To the east of Empanada and Calor, the Niños flow field forms a discontinuous pillow ridge up to 40 m tall along the spreading axis. The ridge is widest (~650 m) between 91°54'W-91°55'W, and narrows along axis to both the east and west. The majority of the flow field is composed of pillow lavas. An inflated region and sheet flow extending to the south of the ridge near 91°54'W likely represents the earliest exposed phase of the eruption. Samples from the Niños ridge are FeTi basalts that range from 4.2 to 4.6 wt. % MgO, while those from the sheet flow have 4.5-4.6 wt. % MgO. Niños is only lightly sedimented and is probably the most recent eruptive unit in the central sub-region, although the geomagnetic paleointensity of samples is indistinguishable within error from those of Calor and Empanada (Bowles *et al*., 2011). Inward-facing faults with scarps 10-20 m high cut the Niños field, indicating post-emplacement tectonic activity. Evidence of recent hydrothermal activity abounds within the Niños flow field. Temperatures greater than 300°C were measured in fluids emanating from a cluster of active hydrothermal chimneys (two 9-10 m high, and one smaller chimney) in the western region of the Niños flow field. Extinct chimneys up to 15 m tall, and beds of clam and mussel shells where diffuse venting presumably occurred, occur along fissures and fault scarps throughout the eruptive unit.

2.7.2.3. Eastern Region (91°53'W-91°51'W) (Figure 2.9)

Two relatively young eruptive units (Dulces and Gusanos) bury a series of fault scarps that dissect much of the eastern region of the study area. The Gusanos flow field consists of two narrow hummocky ridges (~150 m wide), aligned along the spreading axis. Samples from this unit are aphyric basalts (6.8-7.1 wt. % MgO). Sediment cover is light throughout the unit. Inactive hydrothermal chimneys are present within, and to the north of, the western Gusanos ridge.

At either end of each Gusanos ridge are small (~0.2 km in diameter), equi-dimensional hummocky mounds belonging to the Dulces flow field. The pillows that make up these mounds are large (~1 m in diameter). Samples from Dulces are FeTi basalts and basaltic andesites that are the most fractionated compositions in either study area (2.7-4.0 wt. % MgO) (Table 2.1), and thin sections contain abundant plagioclase, clinopyroxene, and olivine microphenocrysts. The Dulces mounds appear to postdate the Gusanos ridges, but both units were apparently emplaced relatively recently. A portion of the Cocodrilo flow field extends into the eastern sub-region, but substantially thicker sediment cover and greater fault density (including faults that are buried by Gusanos and Dulces flows) indicate that the Gusanos and Dulces flow fields are younger than Cocodrilo. Lack of flow contacts precludes a more precise definition of the ages of these units relative to the others in the central high-magma-supply study area.

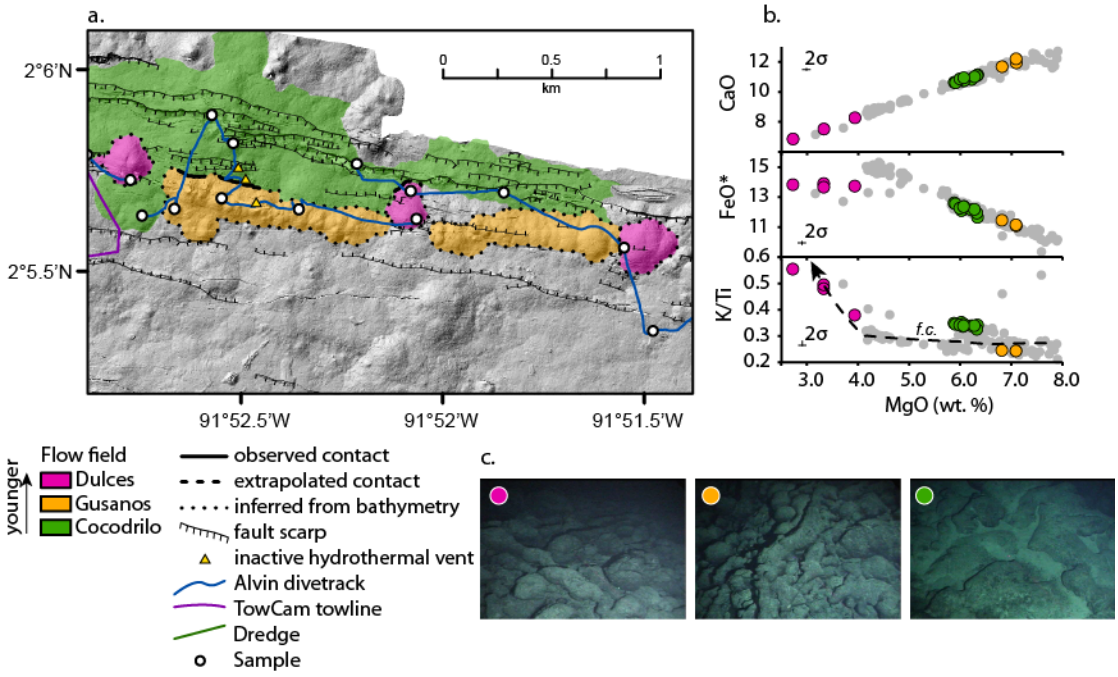

Figure 2.9. Eastern region, high-magma-supply study area. (a) Geologic map of region; see legend for symbols. Unit boundaries are symbolized according to how well constrained they are. (b) Compositional fields for eruptive units within the central region. Colors correspond to those used in the geologic map: pink, Dulces; orange, Gusanos; green, Cocodrilo; grey, other high-magma-supply samples. Dashed line labeled "f.c." on plot of MgO vs. K/Ti shows liquid line of descent predicted by MELTS for fractional crystallization at 500 bars, with oxygen fugacity 1 log unit below the fayalite-magnetite-quartz buffer (Ghiorso & Sack, 1995; Asimow & Ghiorso, 1998). (c) Photos of seafloor within each eruptive unit showing typical sediment cover and lava morphology; colors same as in compositional plots.

2.8. Eruption characteristics

2.8.1. Lava composition

Samples from the low-magma-supply study area consistently have higher phenocryst contents than those from the high-magma-supply study area, where phenocrysts were only observed in samples from the Lobo del Mar flow field (Table 2.1). This observation is consistent with eruption from the seismically imaged melt lens at the high-magma-supply study area, which is expected to contain crystal-poor magma, and from crystal-rich magma reservoirs at lower magma supply, in agreement with the global systematics of MORs (Sinton & Detrick, 1992). It is notable, however, that the largest flow field in the low-magma-supply area, the Buho flow field, is nearly aphyric. It is presently unclear whether this anomalous eruption was fed from a large, melt-rich magma reservoir or rather from a smaller reservoir that was replenished during the course of the eruption.

At both study areas, mapped eruptive units exhibit only limited compositional heterogeneity with compositional trends that can largely be explained by moderate degrees of fractional crystallization (except within the Altares flow field, where variable K/Ti requires multiple parental magmas). Only two mapped flow fields (Dulces and Buho) have ranges in MgO greater than 1 wt. %. The limited variability of MgO content within individual eruptive units suggests that melt reservoirs are relatively well-mixed, even at low magma supply. For example, the Frijoles flow field extends 10.8 km along axis at the low-magma-supply study area, with only 0.7 wt. % range in MgO and 0.01 in K/Ti, despite previous eruptions in the same region with different MgO and K/Ti contents.

In contrast to the limited compositional variation within eruptive units, there are striking compositional differences between successive eruptions. The common juxtaposition of successive flow fields with compositions that cannot be related by fractional crystallization requires either eruption from separate melt reservoirs within the crust, or magma recharge to the same reservoir(s) occurring at time scales similar to eruption intervals. This observation is consistent with those in Bergmanis *et al*. (2007) for the very-fast-spreading southern EPR.

2.8.2. Lava temperature

Lava compositions in the high-magma-supply study area have lower average MgO with a wider compositional range than those at low magma supply (average MgO = 6.2 wt. %, range = 5.7 wt. % at high magma supply, compared to 8.0 wt. % and 2.9 wt. % at low magma supply). MgO content decreases with decreasing temperature in basaltic magmas crystallizing olivine + plagioclase ± clinopyroxene. Liquidus temperatures of glass samples from each eruptive unit calculated using MELTS (Ghiorso & Sack, 1995; Asimow & Ghiorso, 1998) confirm that eruption temperatures of lavas at the high-magma-supply study area are more variable, but cooler on average (1080-1180°C), than those at low magma supply (1170-1210°C) (Table 2.1; Fig. 2.10). A similar relationship has been observed with spreading rate along the global MOR system, i.e., that lavas from fast-spreading ridges (high magma supply) have cooler eruption temperatures than lavas from slow-spreading ridges (Sinton & Detrick, 1992). Rubin & Sinton (2007) emphasized the correlation between eruption temperature and magma chamber depth, and attributed this result to low but variable crustal temperatures at shallow depths where melt lenses reside at relatively fast spreading rates. Magma reservoirs are predicted to exist at greater depths at our low-magma-supply study area (Blacic *et al*., 2004), where erupted lavas are generally hotter but less variable in eruption temperature, presumably because the mid- to lower crust is farther removed from the effects of vigorous hydrothermal cooling.

Variations in MgO content (and calculated liquidus temperatures) are also documented within some of the most densely sampled individual eruptive units. Along the Frijoles eruptive fissure, the region with the greatest eruptive volume does not coincide with the highest temperatures (Fig. 2.11). This result is similar to that for the N1 eruption along the SEPR, where Bergmanis *et al*. (2007, Fig. 8) noted that the maximum erupted volume along axis corresponded with relatively low eruption temperatures and a local minimum in the AMC depth. In the case of the Frijoles eruption, it is unclear whether the variation in MgO records a spatial or temporal variation in lava temperatures and we lack data on the along-axis depths of the reservoir feeding the eruption. Cooler lava temperatures could be erupted from regions where the AMC is shallower, or

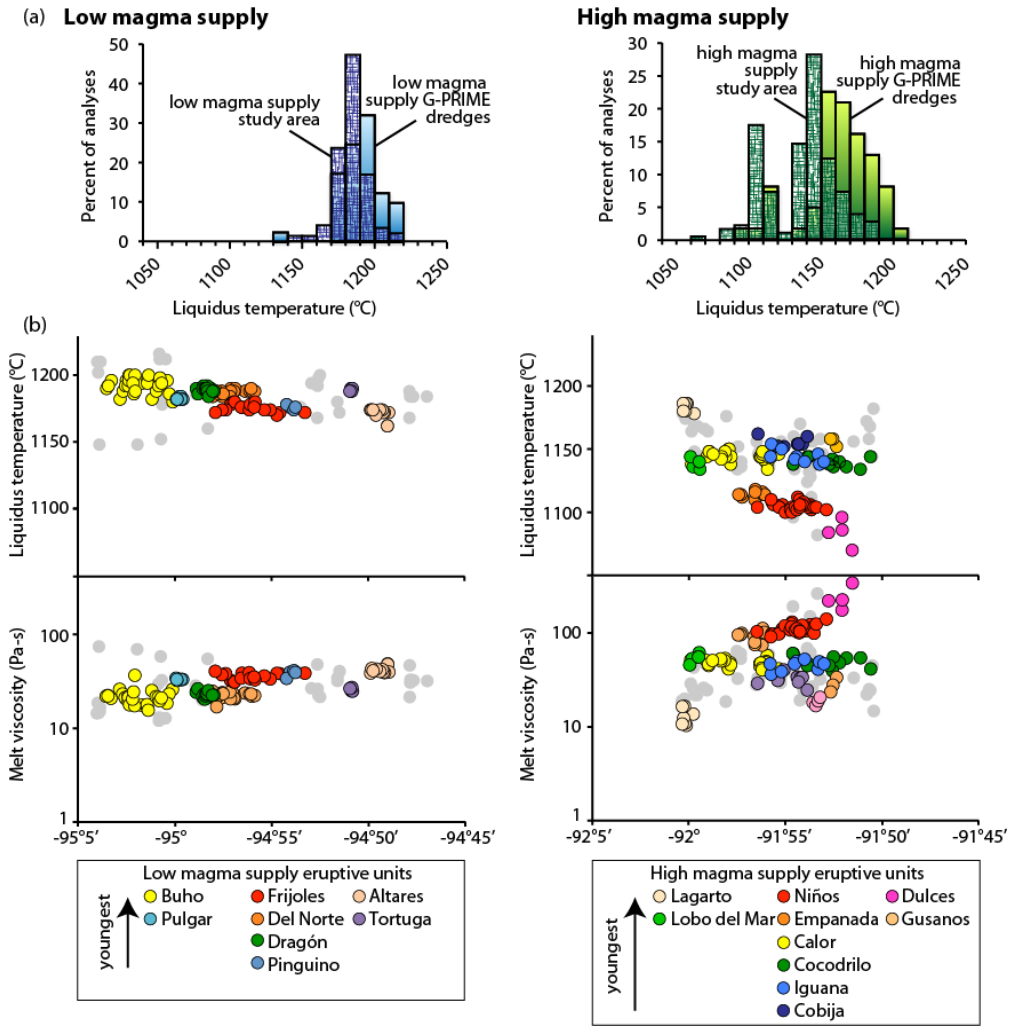

Figure 2.10. Lava liquidus temperatures calculated using MELTS (Ghiorso & Sack, 1995; Asimow & Ghiorso, 1998). (a) Histograms of lava liquidus temperatures at low and high magma supply along the GSC. Patterned bars are samples from low (n=151) and high (n=178) magma supply study areas, this study. Solid bars are dredge samples from G-PRIME cruise; low magma supply (n=40) is taken as west of 94.4°W, where magma supply is $< 0.3\times10^6$ m^3/km/yr; high magma supply (n=62) is taken as east of 94.4°W. (b) Liquidus temperature (upper panel) and liquidus melt viscosity (calculated using method of Giordano *et al*. (2008)) of rock samples along axis for low (left) and high (right) magma supply study areas. Colors of dots correspond to eruptive units (see legend at bottom).

conceivably from the cooler edges or ends of the melt reservoir, although the latter seems unlikely to coincide with high eruption volumes. Alternatively, it is possible that lava temperatures along the length of the eruptive fissure were initially high, and cooled progressively during the course of the eruption. In this case, one might find the lowest temperatures where effusion continued the longest (see Section 2.8.5).

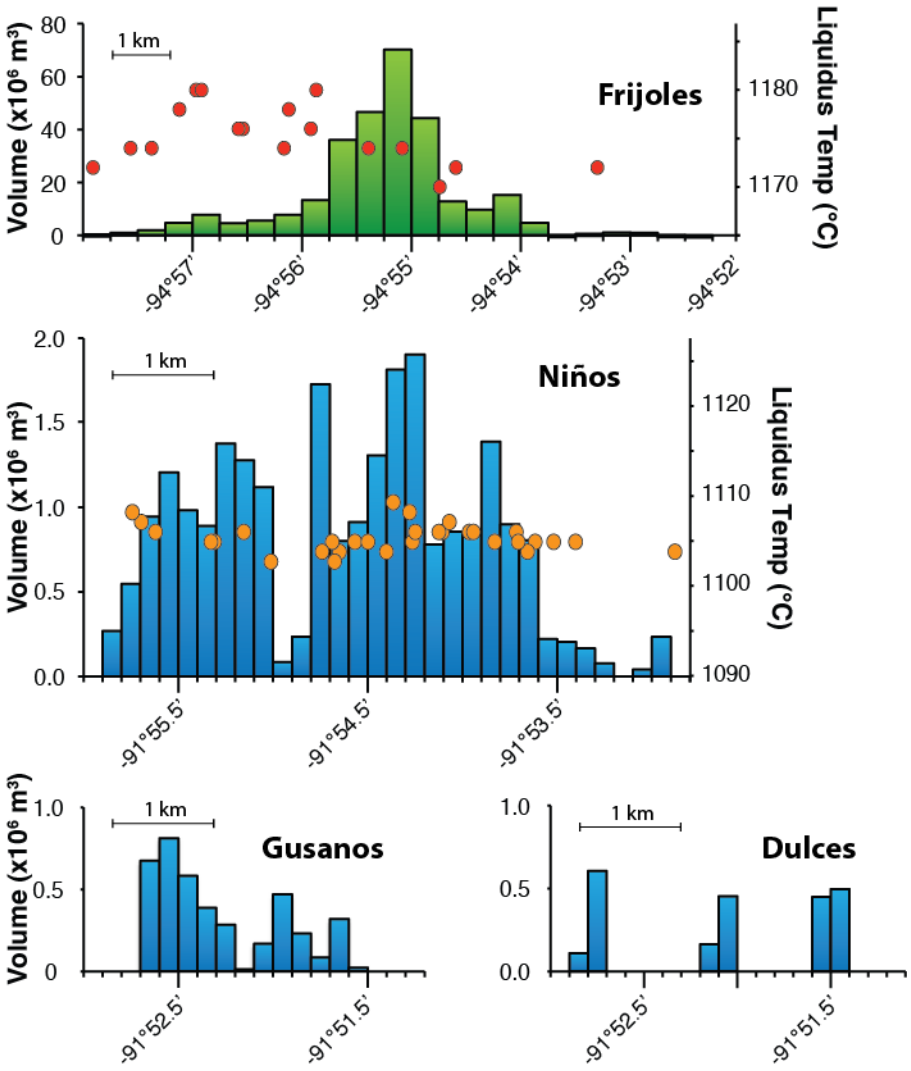

Figure 2.11. Along-axis variation in eruptive volume for fissure eruptions at low (Frijoles) and high (Niños, Gusanos, and Dulces) magma supply study areas. Eruptive units were binned by latitude (0.25 arc minute bins for Frijoles; 0.1 arc minute bins for other units) and volumes calculated as for unit volumes, using bathymetry and a horizontal basal surface. Red and orange dots in Frijoles and Niños plots show along-axis variations in liquidus temperatures (calculated using MELTS (Ghiorso & Sack, 1995; Asimow & Ghiorso, 1998)) for samples collected in each flow field. For both the Frijoles and Niños eruptions, the highest liquidus temperatures correspond to what are thought to be the earlier parts of the eruptions (see text for discussion).

2.8.3. Eruptive volume

Eruptive volumes of low-relief units (smooth flows) and higher-relief units (hummocky mounds and ridges and seamounts) within our study areas were estimated using two different methods. For relatively high-relief units, we assume a pre-existing horizontal basal surface at the average depth of the unit's boundary, and calculate the volume between this surface and the mapped seafloor depth. The assumption of a horizontal basal surface results in an overestimate of unit volumes if the mapped unit buried pre-existing edifices, and an underestimate if the flow unit filled pre-existing depressions.

For the low-relief Del Norte flow field, we multiplied the mapped lava flow area by an average thickness of 15 m (based on observed collapse depths, flow front heights, and the thicknesses of flows exposed on fault scarps) to obtain a flow unit volume, similar to methods of Gregg *et al*. (1996), Sinton *et al*. (2002), and Soule *et al*. (2007) for low-relief units along the EPR. The 15-m thickness that we estimate is significantly greater than the 1-2 m used by Soule *et al*. (2007) for the latest eruption at 9°50' N along the EPR, but is similar to the maximum thickness of the 2011 Axial volcano flow field (as measured by repeat bathymetric surveys) where it "filled a shallow depression and inflated" (Caress *et al.*, 2012). The Del Norte flow field occurs within a similar confining structure, provided by the axial graben, and appears to have had a similar emplacement history.

The areas and estimated volumes of mapped flow fields are presented in Table 2.2. For Del Norte and Calor, each of which was partially buried by successive eruptions, we present an additional estimate of the total (original) area and eruptive volume. In several other cases (Cobija, Cocodrilo, Iguana, Lagarto, Lobo del Mar), there has been too much post-eruptive faulting and/ or burial to make reasonable estimates of original flow field areas and hence, eruptive volumes. Additionally, we have not attempted to account for the possibility that some eruptions (particularly those located near the boundaries of each study area) extended along axis outside the study areas.

Bearing in mind the uncertainties associated with the estimation of flow field thicknesses and original outcrop areas, our results indicate that erupted volumes range over one to two orders of magnitude at each study area, similar to the variation in

Table 2.2. GSC lava flows: dimensions and descriptions

	Flow field name	Mapped unit length (km)	Mapped outcrop area (km^2)	Volume (km^3)	Comments
Low magma supply	Frijoles	10.8	6.2	0.28	youngest mapped unit at low magma supply study area: discontinuous chain of pillow mounds
	Del Norte	6	8.2 (9.4)[a]	0.12 (0.14)[a]	predominantly sheet and lobate flows erupted from north of axial graben; locally, small pillow mounds
	Buho	7.1	14.6	1.31	axial seamount with summit collapse craters flanked by smaller, clusters of highly ornamented pillow mounds
	Tortuga	2.3	3.9	0.36	axial seamount; summit region predominantly inflated, partially collapsed flows
	Dragón	2	1.8	0.09	irregular, steep-sided cluster of slightly ornamented pillow mounds, roughly centered within axial graben
	Pulgar	1.8	2	0.12	cluster of unornamented pillow mounds; most mounds have summit plateaus where lobate flows predominate
	Pinguino	2.1	3	0.24	axial seamount; summit region predominantly inflated, partially collapsed flows
	Altares	3.7	3.5	0.1	irregularly shaped cluster of pillow mounds; 100-m tall pinnacle rises from summit plateau of largest mound
High magma supply	Niños	6.1	2	0.03	youngest unit in DSA2: pillow ridge with recently active hydrothermal activity
	Calor	8.3	3.46 (5.25)[a]	.03 (.03)[a]	intermediate-aged pillow ridge hosting several actively venting hydrothermal chimneys
	Empanada	3.5	3.9	0.13	small axial seamount and associated low-lying sheet flows
	Dulces	2.7	0.1	0.002	discontinuous chain of small pillow mounds
	Gusanos	2.1	0.3	0.005	discontinuous pillow ridges aligned along spreading axis
	Iguana	5.5	0.7	--	pillows, lobate flows, and jumbled to hackly sheet flows, partially buried by more recent units
	Cocodrilo	9.6	2.2	--	broad mounds made up mostly of pilllow and lobate flows, partially buried by more recent units
	Lobo del Mar	1.7	0.6	--	chain of eruptive vents, channels, and associated off-axis lava lake (partially collapsed)
	Lagarto	--	0.3	--	pillow, lobate, and channelized sheet flows.
	Cobija	5.6	2.4	--	oldest mapped flow field: low-relief pillow, lobate, and sheet flows

-- Units for which sufficient outcrop does not exist to make reasonable estimates of volume.

[a] Areas and volumes in parentheses include regions presumed to have been buried by later eruptive activity (Del Norte; Calor)

eruptive volume documented at other locations along the MOR system (Perfit & Chadwick, 1998; Sinton *et al.*, 2002).

Mapped eruptive volumes at the low-magma-supply study area are greater on average, and range to significantly greater values (0.091-1.3 km^3) than those at the high-magma-supply-study area (0.0022-0.13 km^3). The inverse correlation between magma supply and average eruptive volume along the GSC agrees with that between spreading rate and eruptive volume proposed for the global MOR system (Perfit & Chadwick, 1998; Sinton *et al*., 2002). We show here, however, that significant variations in average eruptive volume can arise from variations in magma supply, independent of spreading rate (Fig. 2.12).

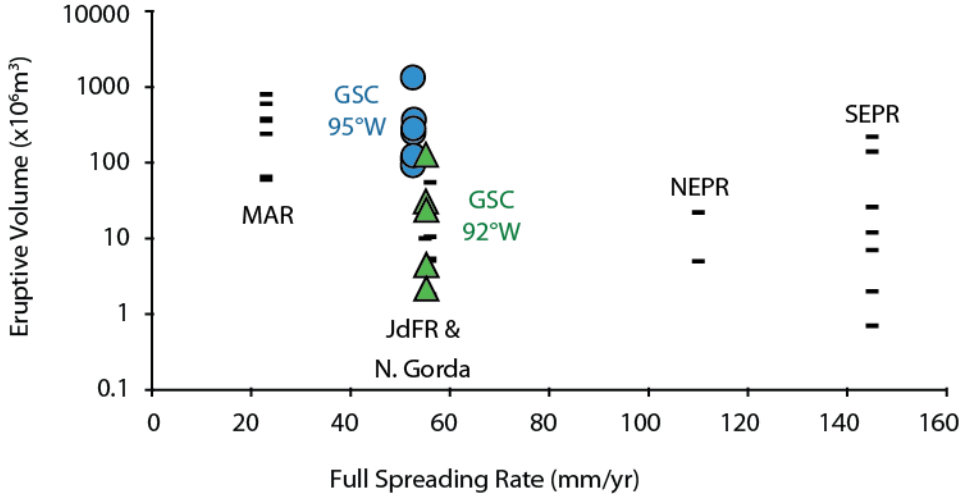

Figure 2.12. Eruptive volume variations versus spreading rate. Variability in eruptive volume for eruptions on most ridges is at least an order of magnitude (exception is northern East Pacific Rise, for which there are only two documented eruptions). GSC eruptive volumes demonstrate non-spreading rate-related variation in eruptive volume. GSC volumes are reported in this paper. Those from other ridges are from Sinton *et al*. (2002), Soule *et al*. (2007), and references therein. MAR, Mid-Atlantic Ridge; JdFR & N. Gorda, Juan de Fuca and North Gorda Ridges; NEPR, northern East Pacific Rise; SEPR, southern East Pacific Rise.

Axial seamounts with broad summit plateaus are consistently the largest eruptive units at both study areas; these features are larger and more common at the low-magma-supply study area. Empanada is the only axial seamount within the high-magma-supply study area. Smith & Cann (1992) used a magmastatic model to argue that the height of eruptive edifices with large summit plateaus is limited by the depth of the magma reservoir feeding the eruption, with greater depths required to produce tall seamounts.

Empanada's height (~100 m) agrees remarkably well with the prediction of the Smith & Cann model for an AMC depth of 1.7 km (the depth of the seismically imaged melt lens at high magma supply). If this model holds for the low-magma-supply study area, where we lack seismic imaging of an AMC, the magma reservoirs feeding the Buho, Pinguino, and Tortuga eruptions should have been 2.5-3 km deep.

Both the Buho and Empanada seamounts represent high-standing parts of eruptive units that are surrounded by co-eruptive, lower relief smooth flows or hummocks. Although we do not have temporal resolution within these eruptive sequences, a likely scenario is that the eruptions began as longer fissures that progressively closed down to long-lived centers at the location of the seamounts (e.g., Wadge, 1981). Thus at least some MOR axial seamounts represent only parts of more extensive eruptive sequences. Buho and Empanada are relatively young features and their flanks have not been completely obscured by later activity. Whether or not other axial seamounts, including older features like Pinguino or Tortuga, might also represent the high-standing remnants of more extensive lava sequences is unclear.

2.8.4. Eruption recurrence intervals

There are three submarine locations where multiple eruptions have been observed (9°50'N EPR, Axial Seamount (JdFR), and the Coaxial segment of the JdFR) (see Rubin *et al*., 2012 for review). Eruption recurrence intervals are 10-20 years in each of these locations, although it is unclear how representative the associated eruption recurrence intervals are of eruptive activity over longer time periods (Rubin *et al*., 2012). In the absence of repeat eruptions, three general approaches have been used to calculate eruption recurrence intervals along other MORs: calculating the number of meter-wide diking events needed to accommodate seafloor spreading (e.g., Hooft *et al*., 1996; Curewitz & Karson, 1998); dating sequences of lava flows, using one or a combination of radiometric techniques, geomagnetic paleointensity, and sediment thickness (Bergmanis *et al*., 2007); and using the average eruptive volume and time-averaged rate of production of extrusive lavas (Perfit & Chadwick, 1998; Sinton *et al*., 2002).

Simple estimates based on meter-wide dikes overestimate eruptive frequencies because not all intruded dikes reach the surface (25-50 % in Hawai'i and Iceland (e.g.,

Hooft *et al.*, 1996)). Furthermore, there could be systematic variations in the fraction of dikes that erupt depending on, for example, the rate of magma supply, regional stress state, and depth of the reservoirs from which dikes initiate (Behn *et al*., 2006; Buck *et al*., 2006; Bialas *et al*., 2010). In addition, the percent of spreading accommodated by faulting (as opposed to diking) appears to vary systematically with spreading rate; estimates presented by Cowie *et al*. (1993) suggest that at the slow-spreading MAR, 10-20% of spreading is accommodated by faulting, compared with 5-10% along the fast-spreading EPR. The spreading rates of 53 and 55 mm/yr at our study areas (Argus *et al*., 2011) generate essentially indistinguishable diking recurrence intervals of 19 and 18 years for 1-m wide dikes at the low-and high-magma-supply study areas, respectively, assuming steady state diking behavior.

Constraints from geomagnetic paleointensity measurements at the high-magma-supply study area suggest that there have been at least six eruptions along one 10 km-long ridge segment in the past 400 years (Bowles *et al*., 2011), yielding an average eruption recurrence interval of 67 years. The paleointensity data suggest that eruptions within this region might be episodic, with hundreds of years of relative quiescence in the interval between the 400year-old eruption and several more recent eruptions that appear to cluster more closely in time (Bowles *et al*., 2011). A several-hundred-year period between eruptive episodes approaches the recurrence intervals of recent rifting phases along slow-spreading subaerial ridges in Iceland and Ethiopia (e.g., Wright *et al*., 2012). Qualitative observations of sediment thickness at the two GSC study areas suggest that the intervals between eruptions are longer at low magma supply, where there are greater differences in sediment cover between successive eruptive units.

Using the spreading rate (Argus *et al*., 2011), thickness of seismic layer 2A (Blacic *et al*., 2004), and estimated eruptive volumes, we can generate a third estimate for the eruption recurrence interval required to build the extrusive layer at each study area. Layer 2A is thicker at the low-magma-supply area (0.6 km and 0.4 km at low- and high-magma-supply study areas, respectively) (Blacic *et al*., 2004), so the volumetric rate of production of layer 2A is actually greater there. Because the median eruptive volume is also greater at low magma supply, the calculated median eruption recurrence interval is

~4 times longer near 95°W (183 years along a 25 km-long ridge segment vs. 46 years at high magma supply).

2.8.5. Average effusion rates

Analog modeling studies have shown that submarine lava morphology is controlled by the relative rates of heat loss and lateral advection of a flow, with efficiently cooled or slowly-moving flows producing pillow lavas, inefficiently cooled or quickly-moving flows producing sheet flows (e.g., Griffiths & Fink, 1992; Gregg & Fink, 1995), and lobate flows having intermediate characteristics. At a given location, the rate of cooling is unlikely to vary greatly, but there may be significant variation in the rate of advection caused by differences in effusion rate, slope, and lava viscosity. Flow morphology in submarine lava flow fields has been used as a proxy for eruption rate (e.g., Gregg *et al*., 1996), but to derive actual rates, reasonable estimates of lava viscosity and pre-existing slopes must be employed.

Along the GSC, we can use observed lava morphologies to qualitatively compare effusion rates within eruptive units and more generally between the two study areas (Table 2.2). Pillow lavas are the most common lava morphology at both study areas, but lobate and sheet flows account for a larger proportion of flows at high magma supply. Using an automated seafloor classification system, McClinton *et al*. (2012) mapped lava morphology within the high-magma-supply study area, and found 47% pillows, 31% lobates, and 12% sheets. Similar work in the low-magma-supply study area found 85% pillows, 5% lobates, and 5% sheets (J. McClinton, personal communication, 2011). These estimates are consistent with observations during dives and camera tows, which indicated that sheet flows were rare in the low-magma-supply study area, with the exception of parts of the Del Norte flow field, and that lobate flows were generally restricted to the summits of hummocks and seamounts. Correlations between lava morphology and spreading rate (and, thus, magma supply) have been observed elsewhere (e.g., Bonatti & Harrison, 1988; Perfit & Chadwick, 1998; Meyer & White, 2007). Similarly, studies of lava morphology within individual spreading center segments at 9°N and 16-19°S along the EPR indicate that low-effusion rate eruptions are more common at discontinuities in

the ridge axis, where eruptive activity is distributed over a wider region across axis (White *et al*., 2002, 2009).

Our lava morphology observations suggest that effusion rates are, on average, greater at the high-magma-supply study area, despite evidence that eruptions with a range of effusion rates have occurred in both study areas. Analog models predict that decreasing viscosity will also cause lava morphology to transition from pillow to lobate to sheet flows, even at a constant effusion rate (e.g., Gregg & Fink, 1995). Melt viscosity is affected by temperature, major element composition, and volatile content (e.g., Giordano *et al*., 2008). Although the lower silica and higher alkali and water contents of glasses from the high-magma-supply study area (Cushman *et al.*, 2004) would tend to lower lava viscosity there for a given temperature and MgO content, the higher degrees of fractionation and lower liquidus temperatures at the high-magma-supply study area have a counter-balancing effect. Viscosity calculations using the method of Giordano *et al*. (2008) yield liquidus melt viscosities ranging up to 340 Pa-s at high magma supply, compared to a maximum liquidus melt viscosity of 70 Pa-s at low magma supply (Fig. 2.10).

Using viscosity and lava morphology to estimate actual effusion rates for each eruption (or for different phases of individual eruptions) requires consideration of crystallinity and crystal morphology, which can increase the bulk viscosity by orders of magnitude (e.g., Costa *et al*., 2009; Vona *et al*., 2011). Quantification of these parameters is beyond the scope of the present discussion, but several examples demonstrate that to first order, the observed variations in lava morphology are not simply a function of bulk magma viscosity. The Buho eruption in the low-magma-supply study area has one of the lowest liquidus melt viscosities (averaging 22 Pa-s), and is essentially aphyric, but all mapped regions of the flow field contain ornamented pillow lavas indicative of low effusion rates, even on steep seamount flanks. In contrast, Del Norte has the same liquidus melt viscosity and slightly higher crystallinity, but flow morphologies range from pillows to sheets. These observations require variations in effusion rate that are independent of lava viscosity.

Observations of eruptive edifice morphologies at each study area provide additional constraints on effusion rates. Laboratory experiments and models of magma

flow within a dike indicate that high flow rates are required to maintain effusion along the length of a fissure (e.g., Wadge, 1981; Bruce & Huppert, 1989; Whitehead & Helfrich, 1991; Head *et al*., 1996). Magma flowing through a dike is cooled by conduction through the dike walls, causing increased viscosity and consequently decreased velocity. Conduit widths decrease where magma freezes along the dike walls; conversely, in regions of greater flow, thermal erosion of the dike walls is possible (Wadge, 1981). If the effusion rate is not sufficient to maintain an open channel within the dike, flow will cease. The prevalence of moderately long fissure eruptions (Fig. 2.13) at the high-magma-supply study area supports the interpretation that effusion rates are generally higher there than at the low-magma-supply study area, since high effusion rates should allow more of the fissure length to remain active for longer durations. It is notable, however, that the longest eruptive fissure recognized in either area is the Frijoles eruption in the low-magma-supply area. Prolonged effusion along a fissure could effectively decrease the elongation of the associated flow field (the ratio of the flow field's length to its width), as lavas are emplaced away from the fissure itself, but the length of the fissure along which lava is erupted should still reflect the effusion rate at the time the fissure was active, assuming the entire length of the fissure was active at once.

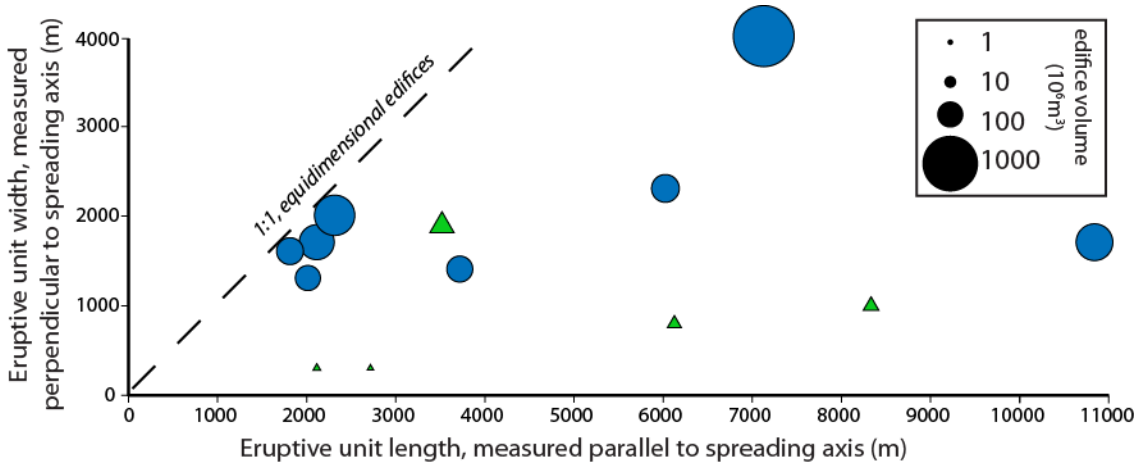

Figure 2.13. Plan-view geometry of mapped eruptive units. Symbol size corresponds to flow field volume. Blue circles, low-magma-supply study area; green triangles, high-magma-supply study area.

Variations in lava morphology and eruptive edifice morphology within several of the mapped lava flow fields indicate spatial and temporal variations in effusion rate over the course of individual eruptive episodes. The Del Norte, Niños, and Empanada flow

fields each include extensive low-lying regions where sheet flows predominate, overlain by localized pillow mounds; these sequences suggest an initial high effusion rate phase after which effusion rates waned (McClinton *et al*., 2011). Similarly, the along-axis distribution of lava along the Frijoles, Buho and Empanada flow fields indicates a focusing of flow near the center of what were probably the initial eruptive fissures (Fig. 2.11). These eruptive histories are consistent with decreasing effusion rates and localization of flow observed during subaerial basaltic fissure eruptions in Iceland (Thorarinsson *et al*., 1973; Wadge, 1981; Harris *et al.*, 2001) and Hawai‘i (Richter *et al*., 1973; Lockwood *et al*., 1987), and inferred from seafloor observations on the MAR (Ballard & van Andel, 1977). Other hummocky ridges, such as the Gusanos and Niños eruptive units at the high-magma-supply study area, appear to have less flow localization (Fig. 2.11).

Despite the evidence for variable eruption rates within some eruptions, the combined flow morphology and eruptive edifice morphology observations strongly suggest that average effusion rates are higher at the high-magma-supply site, and that the observed variations cannot be attributed to differences in magma viscosity. The high effusion rates at high magma supply could be caused by higher average magma driving pressures in the high supply magma reservoirs. The declining eruption rates and flow localization of several units during the course of the eruptions may have been driven by declining magma driving pressures late in the eruptive episodes.

2.9. Relevance to other mid-ocean ridges

The increase in magma supply along the GSC is associated with proximity to the Galápagos hotspot, which affects magma chemistry and crustal structure in ways that would not be expected at MORs unaffected by hotspots. Despite this abnormality, the increased magma supply near the hotspot allows a melt lens to persist at shallow depths within the crust, and the higher average degrees of fractionation observed along the GSC associated with this shallow melt lens are entirely consistent with global ridge systematics (e.g., Rubin & Sinton, 2007). However, hotspot-related enrichments in H_2O and incompatible elements at a given MgO content in our high-magma-supply area (e.g., Cushman *et al*., 2004; Ingle *et al*., 2010) are not typical of most fast-spreading ridges.

The elevated H_2O content, in particular, should decrease melt viscosity, with potential increases in effusion rates and the abundance of sheet flows relative to pillow lavas. Nevertheless, an increase in fissure eruptions at our high-magma-supply study area is consistent with the observed trend with increasing magma supply normally associated with spreading rate (Sinton *et al*., 2002), even though it may be augmented by differences in melt viscosity that are uncharacteristic of melt supply at "normal" ridges.

Although the GSC provides a rare opportunity to isolate the effects of variable magma supply from those of spreading rate, these two parameters are coupled along most of the global MOR system. To facilitate comparison with other ridges, we calculate the equivalent "normal" MOR spreading rate for each study area as the product of crustal thickness and spreading rate, assuming a uniform, 6 km-thick crust. The equivalent spreading rates are 50 and 67 mm/yr for the low and high-magma-supply study areas, respectively, both within the range of intermediate spreading rates. Thus the difference in spreading rates (and rates of magma supply) considered here is only about 10 % of the total range in spreading rates in the global MOR system. It is therefore perhaps surprising that our observations indicate profound differences in eruption characteristics over such a small difference in overall supply. But eruption characteristics correlate well with magma chamber depth along the GSC, illustrating the sensitivity of magma chamber depth to small variations in magma supply at intermediate spreading rates (e.g., Small & Sandwell, 1989; Purdy *et al*., 1992; Sinton & Detrick, 1992).

2.10. Conclusions

Detailed mapping of eruptive units at low- and high-magma-supply study areas along the GSC allows us to quantify the range in eruption characteristics within each study area. At both study areas, the frequent juxtaposition of different flow fields with compositions that cannot be related by simple fractional crystallization is consistent with melt reservoirs that are either discontinuous or poorly mixed along axis, or replenished with compositionally distinct magmas at time scales that approach the eruption recurrence interval. Systematic variations in average lava temperature, eruptive volume, lava morphology, and eruptive unit morphology with increasing magma supply are generally consistent with those observed globally with increasing spreading rate.

Eruptions within our high-magma-supply study area commonly have magma ascent rates sufficient to sustain eruptions along fissures greater than 5 kilometers in length (assuming entire fissure lengths are active simultaneously). Lava temperatures within the study area vary by over ~100°C, and moderate to high degrees of fractionation are typical. The vast majority of these eruptions appear to be fed by the seismically imaged, mid-crustal AMC, which is thought to be a persistent feature at the high-magma-supply study area. Preliminary constraints suggest that the average repose period between highly episodic major rifting and eruption episodes is on the order of several decades.

At our lower-magma-supply study area, eruptions tend to be larger in volume and less frequent (with repose periods of hundreds of years), have lower average effusion rates, and are more likely to focus to a point source. Magma chambers at low magma supply are thought to reside deeper within the crust, although a melt lens has not been seismically imaged at the low-magma-supply study area, and erupted lava temperatures are correspondingly hotter and more uniform. Long-lived, slow eruptions of large volumes of crystal-bearing lava (less than 15 % phenocrysts) have built much of the upper oceanic crust in this region.

Whereas the variation in typical eruptive activity between the two study areas provides insight into the dependence of MOR eruptive processes on magma supply and consequent depths of magma reservoirs, the variability in eruptive characteristics can be used to place constraints on the range of conditions that are possible at each study area. Uncommon high-effusion-rate fissure eruptions of low-viscosity lava occur in the low-magma-supply area, and point-source edifices can form in the high-magma-supply area. These observations indicate that a range of stress states and magma chamber conditions are possible at a given location. Several individual eruptive units exhibit a range of edifice and lava morphologies that suggest eruption rates declined during the course of on-going eruptions.

This study demonstrates the variability of eruptive processes within two areas characterized by quantified differences in long-term magma supply that are not associated with changes in spreading rate. It is only because we have multiple examples within each area that systematic differences between areas become evident. Although the differences in average characteristics between areas generally accord with our present

understanding of the effect of variable magma supply on magma chamber depths and attendant magmatic processes, the variability within areas has not been previously documented. It is clear that similar systematic investigations over a wide range of other ridges will be required to better understand the fundamental processes controlling the variability of eruptive processes, within and between eruptions, and to constrain the effects of larger variations in magma supply on eruptive processes.

Acknowledgments

We are grateful to the *Alvin*, *Sentry*, and *TowCam* teams and to the crew of *R/V Atlantis* Cruise AT15–63 for their assistance with data acquisition at sea. We especially acknowledge Captain A. D. Colburn and Expedition Leader Bruce Strickrott for their contributions to this cruise. We thank the Ecuadorian government and the Parque Nacional Galápagos for permission to work in their territorial waters, and the staff of the Charles Darwin Research Foundation for help with logistics. Dan Fornari helped immensely with pre- and post-cruise logistics and ensured the readiness of the *TowCam* system. Mike Perfit and David Ferguson provided thorough and helpful reviews that improved the manuscript, and Scott Rowland is thanked for comments on an earlier version. JoAnn Sinton, Mary Tardona, and Eric Hellebrand helped with sample preparation and micro- probe analyses. This work was supported by the National Science Foundation grants OCE08–49813, OCE08–50052, and OCE08– 49711. This is SOEST contribution 8718.

CHAPTER 3. CONSTRAINTS FROM MELT INCLUSIONS ON DEPTHS OF MAGMA RESIDENCE AT INTERMEDIATE MAGMA SUPPLY ALONG THE GALÁPAGOS SPREADING CENTER

3.1. Abstract

Shallow, seismically imaged melt lenses are a ubiquitous feature of mid-ocean ridges with high magma supply; melt lenses deepen and become less continuous along-axis as the rate of magma supply decreases. Despite compelling evidence for evolution of magma within the crust prior to eruption at lower magma supply, melt lenses are rarely detected along ridge segments with rates of magma supply lower than 0.3×10^6 m^3/yr/km, and the depths of magma residence prior to eruption are therefore unknown. We use ion microprobe measurements of H_2O and CO_2 concentrations of olivine-hosted melt inclusions to calculate vapor saturation pressures that constrain crystallization depths at two locations along the Galápagos Spreading Center (95°W and 94.2°W). These sites were chosen to examine crystallization pressures in the presence (94.2°W) and absence (95°W) of a seismically imaged melt lens. At 95°W, where magma supply is too low to sustain a seismically resolvable melt lens, samples were selected from each of the three most recent eruptive units, allowing us to document temporal variations in the depth of magma residence at this location. Clusters in melt inclusion entrapment depths for these eruptions range from 3.0 to 3.4 km below the seafloor, indicating that magmas at 95°W resided at a narrow range of mid-crustal depths prior to eruption, generally consistent with the global trend of increasing melt lens depth with decreasing rate of magma supply. A discrepancy between seismic data and the peak in melt inclusion entrapment depths at 94.2°W may reflect temporal variability of magmatic systems at this location. This study demonstrates the potential for using measurements of the concentrations of H_2O and CO_2 in olivine-hosted melt inclusions to determine the depths of crustal magmatic systems that feed mid-ocean ridge eruptions, even in locations where seismic studies have not detected melt lenses.

3.2. Introduction

Along fast-spreading mid-ocean ridges, relatively high rates of magma supply promote the formation of quasi-steady-state, shallow, axial magma reservoirs (e.g.,

Phipps Morgan & Chen, 1993a; Sinton & Detrick, 1992). Seismic reflectors interpreted as melt-dominated lenses overlying low-seismic-velocity zones of crystal mush are nearly ubiquitous along fast-spreading ridges; with decreasing spreading rates, melt lenses deepen and become less continuous along axis (see review in Dunn & Forsyth, 2007). Hooft & Detrick (1993) showed that the depth of the seismic melt lens along the East Pacific Rise is significantly deeper than the magma's level of neutral buoyancy in the crust. Rather, melt lens depths along fast-spreading ridges appear to be controlled by the thermal structure of the crust (e.g., Carbotte *et al*., 2013; Hooft *et al*., 1997; Phipps Morgan & Chen, 1993a; Purdy, 1992).

Despite compelling petrological evidence for evolution of magma within the crust prior to eruption at slower spreading rates, melt lens reflectors have rarely been imaged at full spreading rates less than ~50 mm/yr (e.g., Sinton & Detrick, 1992), and comparatively little is known about the locations or longevity of magma reservoirs that feed eruptions in these settings. Modeling by Phipps Morgan & Chen (1993a) suggests that a threshold exists at intermediate spreading rates, below which rates of magma supply are not high enough to overcome cooling by robust hydrothermal systems in the upper crust, and shallow melt bodies cannot be sustained. With no persistent shallow melt body, is there still a preferred depth for magma reservoirs at slower spreading rates, or do lower rates of magma supply promote the creation of ephemeral melt lenses at multiple levels within the crust?

Enhanced melt production along the Galápagos Spreading Center (GSC) near the Galápagos hotspot (located ~200 km south of the ridge near 91.5°W) generates trends in axial depth and morphology, eruptive style, degree of magma fractionation, and depth of seismically detected melt lenses that mimic variations with spreading rate along the global mid-ocean ridge system (Canales *et al*., 2002; Detrick *et al*., 2002; Sinton *et al*., 2003; Behn *et al*., 2004; Blacic *et al*., 2004). Between 98°W and 91.5°W along the GSC, the time-averaged rate of magma supply to the crust (calculated as the product of spreading rate (DeMets *et al*., 2010) and crustal thickness (Canales *et al*., 2002), after Sinton *et al*. (2003)) increases by ~50 percent, making the GSC an ideal location to assess the influence of magma supply on mid-ocean ridge magmatic systems (Fig. 3.1b).

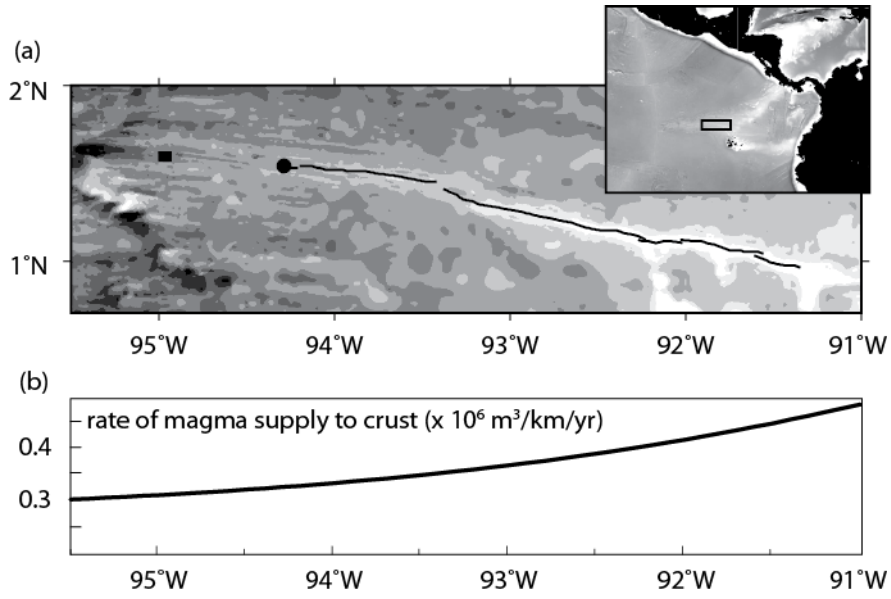

Figure 3.1. Bathymetry and rate of magma supply along Galápagos Spreading Center. (a) Bathymetric map of western Galápagos Spreading Center (GSC); lighter shading indicates shallower depths. Black line, regions of the GSC where an axial melt lens was seismically detected during the G-PRIME research cruise (Blacic *et al.*, 2004). Black circle, dredge sample EW56D (Cushman *et al*., 2004). Black rectangle, 95°W study site. Inset, location of GSC in the eastern equatorial Pacific Ocean; black rectangle, location of bathymetric map of western GSC. (b) Variation in rate of magma supply along the GSC, calculated as product of spreading rate (DeMets *et al*., 2010) and crustal thickness (Canales *et al*., 2002), after Sinton *et al*. (2003).

The 2000 G-PRIME research cruise documented along-axis variations in the depth of the seismic melt lens reflector between 91.3°W and 94.3°W. Close to the Galápagos hotspot, where the rate of magma supply is relatively high, the melt lens is imaged as a nearly continuous, high-amplitude reflector 1-2 km below the seafloor (bsf) (Blacic *et al*., 2004). West of 92.5°W, coincident with a change from an axial high to a transitional axial morphology, the melt lens deepens rapidly and becomes less continuous; depths of 2.5-4.0 km bsf were recorded by cross-axis multichannel seismic lines (Blacic *et al*., 2004). West of 94.4°W, no melt lens has been detected seismically, despite running cross-axis seismic lines at 94.7°W and 95.1°W (Blacic *et al*., 2004), and the depths of magma residence in the crust prior to erupting therefore are unknown.

Because the solubilities of H_2O and CO_2 are pressure-dependent, measurements of their concentrations in volatile-saturated glass can be used to determine the melt equilibration pressure (Dixon *et al*., 1995). Volatile contents of selvage glasses from the

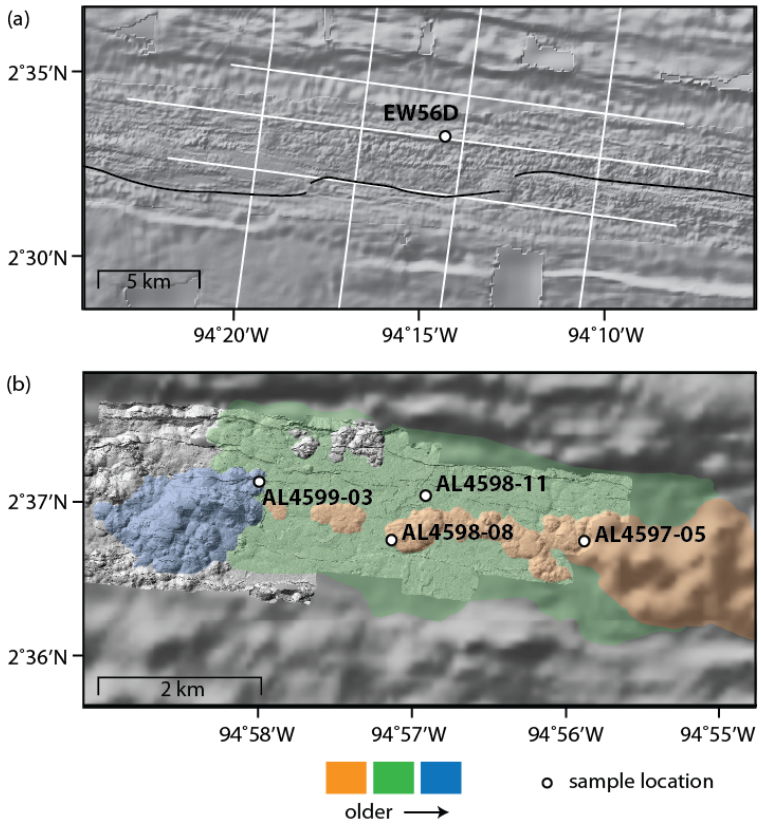

Figure 3.2. Bathymetric maps of study sites and sample locations. (a) Shaded relief map of 94.2°W study site showing locations of dredge sample EW56D and seismic reflection lines (white lines) constraining axial melt lens depth (Blacic *et al*., 2004). Black lines, axis location from Sinton *et al*. (2003). Bathymetry is global compilation of multi-beam sonar data merged with satellite-derived bathymetry data (Ryan *et al*., 2009) (b) Shaded relief map of 95°W study site showing lava flow fields for three most recent eruptive units (Colman *et al*., 2012). White circles, locations of samples used in this study. Bathymetry is multi-beam sonar data (higher resolution data obtained from the autonomous underwater vehicle *Sentry*).

chilled exteriors of submarine lava flows commonly reflect partial degassing during or after the magma's ascent to the surface, with equilibration pressures intermediate between those of the seafloor and the magma reservoir (Dixon & Stolper, 1995; le Roux *et al*., 2006; Shaw *et al*., 2010; Soule *et al*., 2012; Wanless & Shaw, 2012). However, the volatile contents of olivine-hosted melt inclusions can preserve the pressures at which the melt inclusions were trapped (Saal *et al*., 2002; Shaw *et al*., 2010; Wanless & Shaw, 2012).

Detailed submersible-based geologic mapping at 95°W along the GSC has identified lava flow fields emplaced during a sequence of three recent eruptions with

known relative ages (Fig. 3.2b) (Colman *et al*., 2012). At that location, no melt lens has been seismically observed (Blacic *et al*., 2004). Here, we use CO_2 and H_2O concentrations of naturally glassy, olivine-hosted melt inclusions from this sequence of eruptions to determine the depths at which the melt inclusions were trapped. In addition, we have measured CO_2 and H_2O in melt inclusions from a sample dredged near the ridge axis at 94.2°W, close to the western-most seismically imaged melt lens; this provides a comparison with the depth of the seismically detected melt lens at that location (Fig. 3.2a).

3.3. Study locations

3.3.1. 94.2°W

A G-PRIME dredge near 94.2°W (sample EW56D) was located roughly 3 km north of the spreading axis shown by Sinton *et al*. (2003) (Fig. 3.2a). Because the seafloor in that region has not been mapped at the scale of individual eruptive units and the sample was not observed in situ, its age is unknown. It could have been erupted recently from a slightly off-axis vent, or erupted on axis and flowed off axis. Alternatively, based on the spreading rate and distance from the eruptive axis, it could be as much as ~100,000 years old.

3.3.2. 95°W

Using visual observations, sample compositions, and high-resolution bathymetry data (McClinton *et al*., 2012), Colman *et al*. (2012) identified and mapped lava flow fields produced during eight recent eruptive episodes at 95°W (Fig. 3.2b). This study uses samples collected by the submersible *Alvin* from three of these mapped eruptive units (described as the Dragón, Del Norte, and Frijoles flow fields in Colman *et al*. (2012); referred to henceforth as the oldest, intermediate-aged, and youngest eruptive units, respectively). The oldest of these eruptions produced a small cluster of pillow mounds roughly centered within the axial graben. The intermediate-aged flow field erupted from fissures to the north of the inner axial graben; flows traveled south and ponded on the axial graben floor. Flow morphologies in this eruptive unit range from sheets to pillow lavas (Colman *et al*., 2012; McClinton *et al*., 2013), indicating that effusion rates were

high, at least at the onset of the eruption. Collapses in lobate flows within this flow field reveal large lava tubes. The youngest flow field was erupted from a fissure near the center of the inner axial graben and comprises a 10.8-km-long, discontinuous chain of pillow mounds. Observed flow contacts and differences in sediment thickness and fault density confirm that these eruptions were separated in time (likely spanning roughly two thousand years), in addition to being compositionally distinct (Colman *et al*., 2012). Samples AL4597-05 (IGSN: JMS000041) and AL4598-08 (IGSN: JMS000053) were collected from the youngest mapped eruptive unit at 95°W, AL4598-11 (IGSN: JMS000056) is from the intermediate-aged unit, and AL4599-03 (IGSN: JMS000059) is from the oldest unit (Fig. 3.2b).

3.4. Methods

3.4.1. Volatile and major element concentrations

We measured the concentrations of volatiles (H_2O, CO_2, Cl, F, S) and major elements in 83 naturally glassy, olivine-hosted melt inclusions from five samples. After crushing and sieving selvage glass from the exterior of each sample, olivine crystals with fully enclosed glassy melt inclusions were hand-picked for analysis. Melt inclusions were exposed following methods described by Shaw *et al*. (2010). Prior to exposing melt inclusions, they were visually inspected for the presence of vapor bubbles using a binocular microscope. Only one of the analyzed melt inclusions contained a vapor bubble, although the sample set contained additional melt inclusions with bubbles. When present, vapor bubbles were exposed, measured, and corrected for following the procedure described by Shaw *et al*. (2010) (Table 3.3). Reflected light images of polished, exposed melt inclusions and host olivines are included in the supplemental data.

Volatile concentrations were measured using the Cameca 1280 ion microprobe at Woods Hole Oceanographic Institution (Table 3.3). Major element compositions of the melt inclusions (Table 3.3) and their host olivines (Table 3.5) were measured using the JEOL JXA-8500F electron microprobe at the University of Hawai‘i. Analytical conditions are provided in the appendix (Section 3.11.1), in addition to average values and reproducibility for standards during repeat analyses (Table 3.2). Analytical uncertainty on H_2O and CO_2 measurements is ~10 % relative (2σ).

3.4.2. Saturation pressures

Saturation pressures were calculated from H_2O and CO_2 concentrations using VolatileCalc (Newman & Lowenstern, 2002), which is based on the solubility model of Dixon *et al*. (1995) and is well calibrated for normal mid-ocean ridge basalts at pressures less than 3 kbar. Similar to the approach of Wanless & Shaw (2012), the saturation pressures were converted to depths of entrapment using a depth-dependent average crustal density and accounting for the depth of the seafloor. A crustal density profile was calculated based on the seismic velocity structure of the crust (Canales *et al*., 2002) and the relationship between density and seismic velocity (Carlson & Herrick, 1990). We then used this profile to calculate the average density of overlying crust as a function of depth (see Appendix, Section 3.11.3 for details and uncertainty analysis).

3.5. Modification of melt composition during and after melt inclusion entrapment

Melt inclusion compositions can be modified after entrapment by continued crystallization on, or diffusion through, the melt inclusion walls (see review in Kent, 2008). Before using melt inclusion data to constrain the conditions of melt inclusion entrapment, we assess whether their compositions are representative of the magmas from which they were trapped. Here, we are specifically concerned with the CO_2 and H_2O concentrations of melt inclusions.

3.5.1. Boundary layer effects

Boundary layers form at the edges of rapidly growing olivine crystals when the crystallization rate exceeds the diffusion rate of a given element, progressively enriching the boundary layer in incompatible elements and depleting it in compatible elements (see review in Kent, 2008). These boundary layers are most enriched in the most slowly diffusing incompatible elements. If the boundary layer is trapped within a rapidly growing olivine crystal, the composition of the resulting melt inclusion will not be representative of the parental melt. Because diffusion rates for CO_2 in basaltic melts are relatively slow (comparable to that of Al (Zhang & Ni, 2010; Zhang *et al*., 2010)), we

might expect CO_2 concentrations to be elevated in melt inclusions that trapped boundary layers.

In a study of natural basalts and picrites, Kuzmin & Sobolev (2004) documented 1-3 μm-wide boundary layers enriched in incompatible elements, but did not detect boundary layer effects in melt inclusions larger than 20 μm. All melt inclusions measured in our study were greater than 20 μm in diameter (Table 3.3). Because CaO diffuses more rapidly than Al_2O_3 in basaltic melt, Faure & Schiano (2005) noted that boundary layer development results in elevated Al_2O_3/CaO ratios, compared to melts affected only by simple fractional crystallization. In our samples, both the inclusion size and the lack of anomalous Al_2O_3/CaO indicates that the majority of melt inclusions are not affected by boundary layer effects. The CO_2 and H_2O concentrations of melt inclusions with apparent over-enrichments in Al_2O_3 relative to CaO are within the range defined by melt inclusions that do not exhibit potential boundary-layer effects.

3.5.2. Post-entrapment crystallization

Post-entrapment crystallization of olivine on melt inclusion walls can modify melt inclusion compositions (see review in Kent, 2008). Diffusive equilibration between the melt inclusion rim and host olivine, and between the host olivine and carrier melt, can make it difficult to determine how much post-entrapment equilibration has occurred (Gaetani & Watson, 2000; 2002; Danyushevsky *et al*., 2002; Laubier *et al.*, 2012). Fortunately, low degrees of post-entrapment crystallization have little effect on incompatible element concentrations (e.g., Laubier *et al*., 2012).

To quantify the magnitude of effects related to post-entrapment crystallization on CO_2 concentrations, we have followed the procedure used by Shaw *et al*. (2010) to correct melt inclusion compositions. We assumed no diffusive equilibration and incrementally added (or subtracted) olivine in equilibrium with the melt inclusion to the melt inclusion glass composition until it reached compositional equilibrium with the olivine near the melt inclusion rim. We used an olivine-melt distribution coefficient of 0.308 to calculate the composition in equilibrium with the melt at each step, as predicted by the olivine-melt equilibrium model of Toplis (2005), assuming that the fraction of total iron present as Fe^{3+} is 0.15 (Cottrell & Kelley, 2011). In all cases, the amount of

olivine added was less than 11 wt. %. Depths of entrapment for post-entrapment-crystallization-corrected melt inclusions are provided in Table 3.4; the difference between depths calculated from corrected and raw melt inclusion compositions is less than 10 percent except in five melt inclusions with relatively low pressures of entrapment (< 400 bars). Recognizing uncertainties in the extent to which melt inclusions and host olivines have been affected by diffusive equilibration in addition to post-entrapment crystallization (e.g., Gaetani & Watson, 2000; 2002; Danyushevsky *et al*., 2002), and noting that the effects of small amounts of olivine crystallization on H_2O and CO_2 concentrations are minimal, we use pressures of entrapment calculated using raw H_2O and CO_2 concentrations in the following discussion.

3.5.3. Diffusive exchange of volatiles with carrier melt

Diffusive loss (or gain) of H_2O from melt inclusions can occur where a gradient in H_2O concentration exists between melt inclusion and carrier melt (e.g., Portnyagin *et al*., 2008; Lloyd et al., 2012; Bucholz *et al*., 2013; Hartley *et al*., 2014; Le Voyer *et al*., 2014). Such a gradient is unlikely to develop at the moderate confining pressures found on the seafloor (~250-280 bars in our study area) and relatively low volatile contents of normal mid-ocean ridge basalts (< 0.3 wt. % H_2O in our samples). Under these conditions, H_2O behaves essentially as an incompatible element (e.g., Cushman *et al*., 2004; Ingle *et al*., 2010), and gradients in H_2O concentration between melt inclusions and carrier melts are not observed. Furthermore, at the low H_2O concentrations that are typical of mid-ocean ridge magmas, loss (or gain) of H_2O due to diffusion will not affect the pressure estimates (Wanless & Shaw, 2012).

Due to the relatively low solubility of CO_2 in basaltic melt, strong gradients in CO_2 concentration develop between melt inclusions and their carrier melts during magma ascent and eruption as CO_2 exsolves from the carrier melt. A simple, one-dimensional, radially symmetric diffusion model (e.g., Cottrell *et al.*, 2002; Qin *et al*., 1992) can be used to assess the timescales relevant to diffusive loss of CO_2 from melt inclusions (see Appendix Section 3.11.4 for discussion and more detailed results of diffusion models). Small melt inclusions close to the rims of their host olivine crystals are modified most rapidly (Cottrell *et al.*, 2002; Qin *et al.*, 1992). For a conservative case considering the

smallest melt inclusions we analyzed (10 μm radius) with only 5 μm olivine separating the melt inclusion from the carrier melt, it takes two years to decrease the CO_2 concentration of melt inclusion by even one percent at magmatic temperatures. Thus, it is highly unlikely that melt inclusion CO_2 compositions would be modified on the timescales of eruptions by diffusive equilibration with carrier melts.

Having demonstrated that the H_2O and CO_2 concentrations in this suite of melt inclusions are representative of magma compositions at the time of entrapment, we can use melt inclusion saturation pressures to calculate depths of entrapment (Table 3.3).

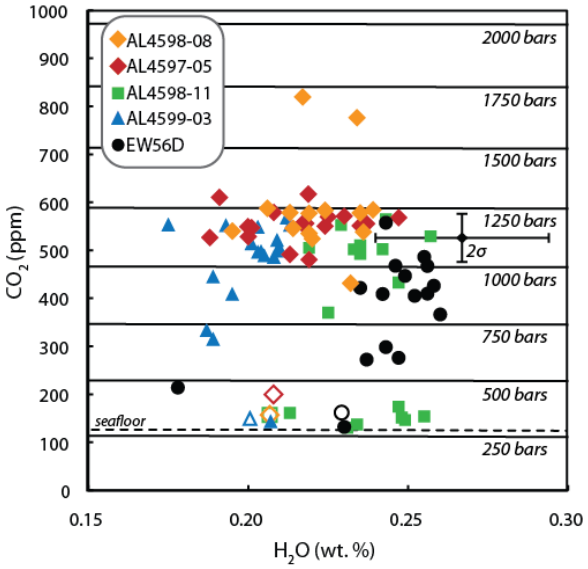

Figure 3.3. H_2O and CO_2 concentrations of melt inclusions and selvage glasses. Circles, samples from 94.2°W. Diamonds, most recent eruption at 95°W; squares, intermediate-aged eruption; triangles, oldest eruption. Hollow symbols, selvage glasses; solid symbols, melt inclusions. Isobars were calculated using VolatileCalc (Newman & Lowenstern, 2002).

3.6. Results

3.6.1. Volatile concentrations

Selvage glasses at 94.2°W and 95°W have volatile concentrations similar to those reported by Cushman *et al*. (2004) at those locations (0.23 wt. % H_2O, 163 ppm CO_2 at 94.2°W; 0.20-0.24 wt. % H_2O, 150-200 ppm CO_2 at 95°W). Melt inclusions have similar H_2O concentrations to selvage glasses at each location (0.18-0.26 wt. % at both 94.2°W and 95°W) but range to significantly higher CO_2 concentrations (132-557 ppm at 94.2°W; 130-819 ppm at 95°W) (Fig. 3.3), indicating melt inclusion entrapment within the crust prior to eruption.

3.6.2. Saturation pressures and entrapment depths

Saturation pressures in selvage glasses at both locations are somewhat greater than seafloor pressure (selvage glass saturation pressures are 330-438 bars, compared to seafloor pressures of 251-281 bars), indicating that magmas are super-saturated with volatiles when erupted. Selvage glass samples collected along the length of the GSC have similar degrees of super-saturation (Fig. 3.4). Interestingly, the degree of super-saturation increases to the east, despite decreasing depths of magma residence. This trend could reflect more rapid average eruption rates at relatively high rates of magma supply (le Roux *et al*., 2006), consistent with along-axis variations in lava morphology (McClinton *et al*., 2013; White *et al*., 2008) and eruptive style (Behn *et al*., 2004; Colman *et al*., 2012).

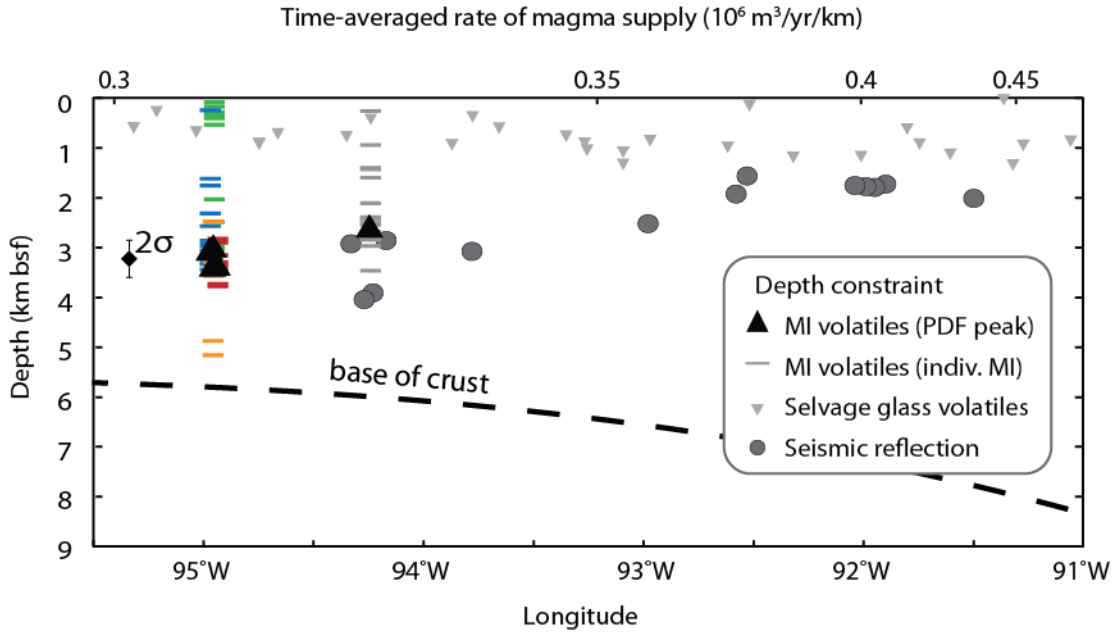

Figure 3.4. Along-axis variations in axial magma reservoir depths and other features of the Galápagos Spreading Center (GSC), 91°-95.5°W. Bars, saturation depths of individual melt inclusions (MIs); colors as in Fig. 3.3. Error bar indicates uncertainty on individual MI depth determinations. Black triangles, peaks in probability density functions (PDFs) for MIs from individual samples, interpreted as depths of magma residence prior to each eruption. Gray circles, seismic reflection constraints on axial melt lens depths from cross-axis multichannel seismic lines; uncertainty smaller than size of symbols (±110 m) (Blacic *et al.*, 2004). Inverted gray triangles are saturation depths for GSC selvage glasses, demonstrating volatile super-saturation of erupted lavas (Cushman *et al.*, 2004).

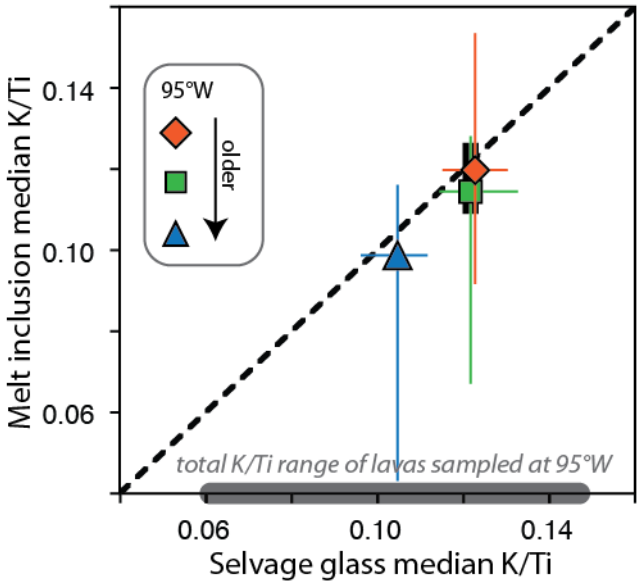

Figure 3.5. Comparison of median K/Ti of melt inclusions and selvage glasses from each eruptive unit. Melt inclusions show greater K/Ti variation than their host lavas, but have the same median composition within uncertainty; range of compositions for samples from each population indicated by colored lines. Diamond, most recent eruption (AL4598-08 and AL4597-05); square, intermediate-aged eruption (AL4598-11); triangle, oldest eruption (AL4599-03). Dashed line represents identical median compositions in melt inclusions and pillow rims. Vertical black bar denotes range in compositions of melt inclusions from intermediate-aged eruption with near-seafloor pressures of entrapment. Median K/Ti of flow fields and total range in K/Ti of lavas sampled at 95°W from Colman *et al*. (2012).

At 94.2°W, saturation pressures of melt inclusions range from 292 to 1180 bars (Fig. 3.3), corresponding to entrapment depths of 0.2-3.5 km bsf (Fig. 3.4). At 95°W, most saturation pressures of melt inclusions are between 288 to 1298 bars (0-3.8 km bsf). Two melt inclusions from the most recent eruption record higher crystallization pressures of 1612 and 1695 bars (4.9 and 5.2 km bsf).

3.6.3. Melt inclusion and carrier lava K/Ti

Unlike most major elements, the incompatible element ratio K/Ti should be essentially unchanged by post-entrapment crystallization (e.g., Kent, 2008), and is therefore a useful monitor of compositional variation among melt inclusions from each eruptive unit. Compositional variations among lavas from each eruptive unit at 95°W are well characterized (Colman *et al.*, 2012). Within each of these eruptive units, the range

and standard deviation of K/Ti of melt inclusions is greater than that of the carrier melt, but the median value of the melt inclusions is the same as that of the carrier melt within uncertainty (Fig. 3.5). Lava compositions typically have reduced variability relative to melt inclusions at a given location, consistent with mixing of melts prior to eruption (e.g., Maclennan, 2008; Laubier, 2012).

Variations in K/Ti and other incompatible element ratios within the most recent eruptive unit suggest that it is the product of mixing between a relatively evolved, high-K/Ti magma and a relatively primitive, low-K/Ti magma prior to eruption. Melt inclusions from this eruptive unit span a greater compositional range than selvage glasses, but the median K/Ti of melt inclusions is the same as that of the carrier melt within uncertainty (Fig. 3.5), consistent with melt inclusions being trapped concurrent with magma mixing. Evidence for recent mixing within the two previous eruptions at 95°W is less compelling. Differences in K/Ti between samples from the intermediate-aged and oldest eruptive unit at the same MgO content are inconsistent with derivation from a single parental magma, and indicate that magmatic recharge occurred between the two eruptions (Colman *et al.*, 2012).

3.7. Preferred depths of melt inclusion formation

In each of the samples studied, melt inclusion depths of entrapment cluster about a given depth (or depths) rather than being evenly distributed over the range of values measured (Fig. 3.3). Wanless & Shaw (2012) noted clusters in depths of entrapment in suites of melt inclusions from 9°N and 13°N on the East Pacific Rise and from the Cleft and Vance segments of the Juan de Fuca Ridge, despite large overall ranges in entrapment depths. In both locations along the East Pacific Rise, the peaks in melt inclusion entrapment depths were within uncertainty of the seismically imaged melt lenses; along the Juan de Fuca Ridge, where the seismically imaged melt lens is deeper, the peaks in the melt inclusion entrapment depths were also deeper (Wanless & Shaw, 2012). In order to interpret the clusters in entrapment depth from our study areas, we consider the conditions likely to create preferential entrapment of melt inclusions at certain depths.

3.7.1. Generation of peaks in melt inclusion entrapment depths

Experimental studies indicate that melt inclusions can form from two-stage cooling sequences, wherein early, rapid cooling promotes skeletal growth, followed by slower cooling that allows polyhedral crystal faces to develop, trapping enclosed melt to form inclusions (Kohut & Nielsen, 2004; Faure & Schiano, 2005; Goldstein & Luth, 2006). Faure & Schiano (2005) noted that melt inclusions also can form from embayments in polyhedral olivine crystals at constant, low cooling rates of 1-2°C/hr in the absence of a rapid-cooling-rate period. However, at the same slow cooling rates, Goldstein & Luth (2006) did not observe melt inclusion formation. In experiments with uniformly high cooling rates, dendrites are produced but fully enclosed melt inclusions are rare (Kohut & Nielsen, 2004; Faure & Schiano, 2005; Goldstein & Luth, 2006).
In a mid-ocean ridge setting, the variable crystal growth rates required by the two-stage mechanism for melt inclusion formation are most likely to occur within crustal magma reservoirs. Crystals subjected to higher degrees of undercooling at magma chamber margins may develop skeletal morphologies; subsequent transport to the warmer interior of the magma body (e.g., by convection) could allow polyhedral growth, trapping melt inclusions (Colin *et al.*, 2012; Faure & Schiano, 2004; Kohut & Nielsen, 2004). Melt inclusions from the Mid-Atlantic Ridge have been interpreted in this context (Colin *et al.*, 2012; Faure & Schiano, 2004). Skeletal morphologies can also develop during recharge of a magma reservoir as a result of magma mixing between primitive and evolved magmas (Faure & Schiano, 2004; Kohut & Nielsen, 2004). In this case, initially rapid crystal growth rates within the more primitive magma slow as the magmas equilibrate, allowing melt inclusion entrapment.

Melt inclusions formed at uniformly low slow cooling rates (as in low-cooling rate experiments of Faure & Schiano, (2005)) can likely form throughout the lower crust, as well as in the interior of magma reservoirs. If melt inclusions form over a broad range of depths within the crust during magma ascent from the mantle, peaks in the distribution of their entrapment depths should occur when magma stalls at a certain depth, i.e., in magma reservoirs, as observed in melt inclusion studies from higher-magma-supply ridges (e.g., Wanless & Shaw, 2012). Thus populations of melt inclusions formed by either one or both of the experimentally identified mechanisms (one-step or two-step

cooling) should have peaks in the distribution of entrapment depths corresponding to magma reservoir depths. If magma ascends through multiple magma reservoirs en route to the surface (e.g., Kelemen & Aharanov, 1998), olivine crystals that crystallized at greater depths may be left behind, so that shallower entrapment depths would be sampled preferentially (Wanless & Shaw, 2012). In this case, we may only see a peak in entrapment depths from the shallowest reservoir in which the magma resided prior to eruption.

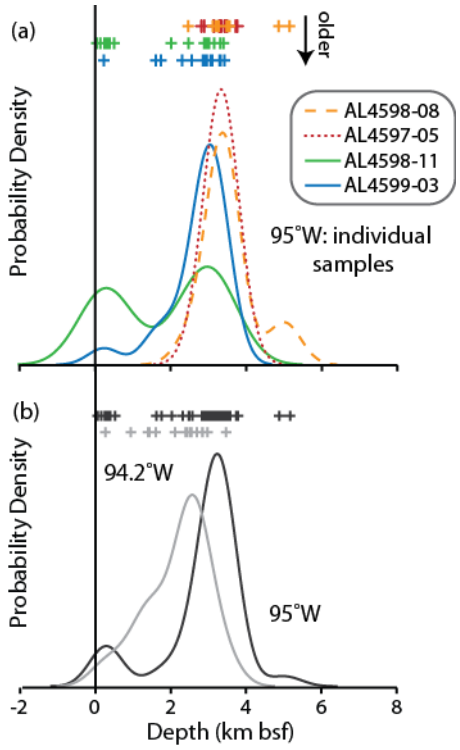

Figure 3.6. Probability density functions (PDFs) for melt inclusion entrapment depths; bsf, below seafloor. Crosses mark depths calculated from individual melt inclusion analyses. (a) PDFs for individual samples at 95°W; colors as in Figure 3.3. (b) PDFs for all samples from 95°W and 94.2°W study areas.

3.7.2. Identification of peaks in depths of entrapment

To identify peaks in the distribution of entrapment depths for each eruptive unit, probability density functions (PDFs) were generated for each sample (see Rudge, 2008 for discussion). Bandwidths used to generate each PDF are given in Table 3.5.

3.7.3. Peaks in melt inclusion entrapment depths at 94.2°W

For the 94.2°W sample, the melt inclusion PDF peak is at 2.6 km bsf (Fig. 3.6b). At that location, the seismically imaged melt lens is significantly deeper, at 3.9 ± 0.11 km bsf (Blacic *et al.*, 2004) (see Fig. 3.2a for locations of seismic lines relative to sample

location). In fact, only one analyzed melt inclusion from 94.2°W has an entrapment depth within uncertainty of the seismic melt lens at that location. We consider two possibilities for the discrepancy between melt lens depth and the peak in the PDF: (1) significant crystallization occurs above the melt lens at this location and (2) this sample erupted at a time in the past when the melt lens was located at a shallower depth. If this lava was erupted recently, the discrepancy between the seismic melt lens depth and the peak in the distribution of melt inclusion entrapment depths suggests that a significant amount of crystallization occurred more than one km above the seismic melt lens. Perhaps magma stalled within the shallow crust during its ascent, allowing for significant melt inclusion entrapment at that depth. For this scenario to be consistent with the seismic data, the shallow magma reservoir within which the melt inclusions formed must have been ephemeral, perhaps present only shortly prior to eruption, or too small to be seismically detected.

Alternatively, this sample may not be related to the currently imaged melt lens. Observations from ophiolites and tectonic exposures through the oceanic crust (Pito and Hess Deep) suggest that fluctuations in melt lens depth through time may be common (e.g., Gillis & Coogan, 2002; Coogan *et al*., 2003; Gillis, 2008). Since this sample was collected ~3 km north of the ridge axis, the age and location of eruption with respect to the ridge axis are unknown. If the depth of the melt lens at this location is temporally variable, the difference in depths could reflect changes in the depth of the melt lens at that location between the time when the sample was erupted and the time when the seismic survey was done.

Within 10 km to the east and west of 94.2°W, at similar time-averaged rates of magma supply, seismically imaged melt lenses exist at shallower depths (2.9 ± 0.11 km bsf) (Blacic *et al*., 2004), which are within uncertainty of the 94.2°W melt inclusion PDF peak. If the difference in melt lens depth between these locations were a persistent feature, we might expect the extrusive layer to be thicker at 94.2°W, where the seismic melt lens is deeper (Buck *et al*., 1997). Instead, there does not appear to be a systematic relationship between the thickness of seismic layer 2A (interpreted as the extrusive layer) and the depth of the seismic melt lens at this scale (layer 2A thickness is 497-514 m where the melt lens depth is 3.9-4.0 km bsf, compared with 430-505 m where the melt

lens depth is 2.9 km bsf (Blacic *et al*., 2004)). In contrast, along the length of the GSC, there is a general trend of increasing layer 2A thickness with deepening of the melt lens (Blacic *et al*., 2004), consistent with co-variations in these parameters over longer time periods. Thus an alternative explanation would be that the peak in the PDF for the sample from 94.2°W reflects a shallower depth of the melt lens at the time in the past when the sample was erupted.

3.7.4. Peaks in melt inclusion entrapment depths at 95°W

At 95°W, the melt inclusion PDF peaks for the three most recent eruptions are at depths of (from oldest to most recent eruption) 3.0 km bsf, 3.0 km bsf, and 3.4 km bsf (Fig. 3.6a). Despite the common depth of magma residence between the oldest and intermediate-aged eruption, differences in K/Ti at the same MgO content require that they had different parental magmas, indicating either that recharge occurred between eruptions or that they were fed from separate magma reservoirs at similar depths (Colman *et al*., 2012). The two samples from different locations in the youngest eruptive unit yield indistinguishable PDF peaks that are ~0.4 km deeper than those of the earlier two eruptions. The limited range of melt inclusion entrapment depths associated with these three eruptions suggests that there is a preferred depth of magma residence at this lower rate of magma supply, at least over the time period represented by this eruptive sequence (roughly two thousand years (Colman *et al*., 2012)).

Sample AL4598-11 has an additional cluster of melt inclusions with near-seafloor entrapment depths (Fig. 3.6a). This sample was collected ~560 m from its eruptive fissure. In contrast, samples AL4598-08 and AL4597-05 were collected within 200 m of their eruptive fissures and do not contain melt inclusions with near-seafloor saturation pressures. The melt inclusions with shallow entrapment depths have decreased variability in K/Ti relative to the other melt inclusions from this eruption and cluster more tightly about the average lava composition for the flow field (Fig. 3.5), suggesting that they were trapped after the parental magma had been homogenized. Additionally, the degrees of volatile super-saturation of these melt inclusions relative to the seafloor are similar to those of selvage glasses along the GSC. We hypothesize that low-pressure melt inclusions in sample AL4598-11 were trapped after eruption during a relatively low-

cooling-rate-period (several hours), possibly during transport across the seafloor within lava tubes such as those observed in collapses within the flow field (Gregg & Fornari, 1998; Soule et al., 2012). This scenario is consistent with the experimentally observed mechanisms for melt inclusion formation; cooling rates may be elevated during eruption, followed by a low-cooling-rate period during tube-fed flow (Gregg & Fornari, 1998) when melt inclusions can be formed. Thus, our results suggest that melt inclusions can form over a range of conditions; samples collected close to eruptive vents will be least likely to contain melt inclusions that were trapped after eruption.

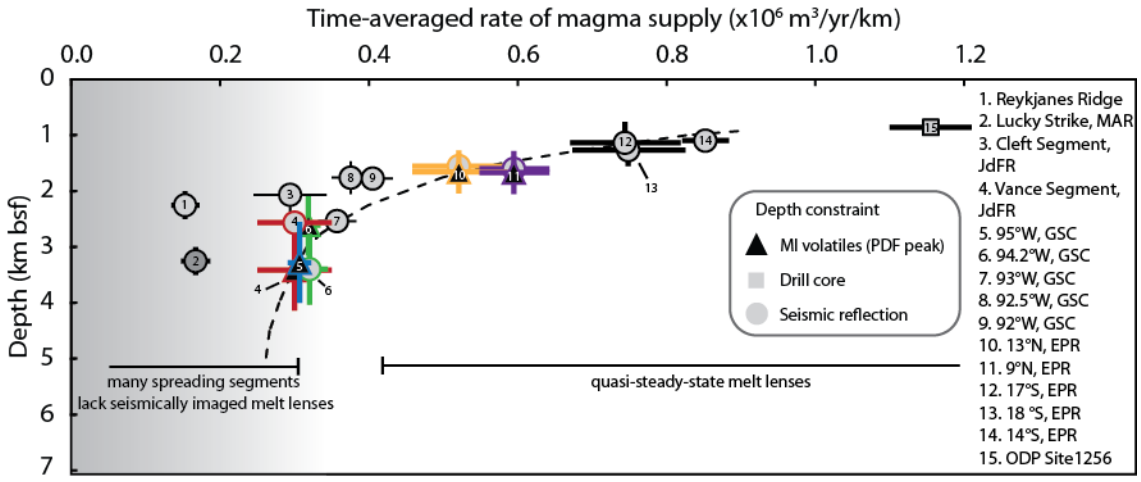

Figure 3.7. Depths of axial magma reservoirs along the global mid-ocean ridge system. Rate of magma supply per km of ridge is calculated as the product of spreading rate and crustal thickness, after Sinton *et al*. (2003). See Table 3.7 for compilation of seismic data and spreading rates used in magma supply calculations. Circles, seismic reflection constraints on magma reservoir depths (Reykjanes, Sinha *et al*., 1997; Lucky Strike segment of Mid-Atlantic Ridge (MAR), Seher *et al*., 2010; 94.2°W Galápagos Spreading Center (GSC), 93°W GSC, 92.5°W GSC, 92°W GSC, Blacic *et al*., 2004; Cleft Segment of Juan de Fuca Ridge (JdFR), Vance Segment of JdFR, Canales *et al*., 2005; 13°N East Pacific Rise (EPR), Detrick *et al*., 1987; 9°N EPR, Carbotte *et al*., 2013; 14°S EPR, 17°S EPR, 20°S EPR, Hooft *et al*., 1997). Seismic reflection depths are average and range of cross-axis seismic data as reported by authors, except where cross-axis lines were not available or where along-axis lines detected shallower melt lens depths. Triangles, peaks in probability functions for melt inclusion depths (data for EPR and JdFR from Wanless & Shaw, 2012); error bars represent 2σ uncertainty on individual melt inclusion depth determinations. Square, drill core constraints on magma reservoir depth at super-fast spreading rates (ODP Site 1256, Wilson *et al*., 2006). Dashed line, magma reservoir depths predicted by thermal model of Phipps Morgan & Chen (1993a), with spreading rate converted to rate of magma supply assuming 6 km crustal thickness.

3.8. Global perspective on depths of seismically detected axial melt lenses

Because crustal thickness is relatively invariant over much of the world's spreading system (e.g., White *et al*., 1992), global rates of magma supply are dominated by the approximately 20-fold variation in spreading rate. Nevertheless, crustal thickness and the rate of magma supply can vary independently from spreading rate (e.g., Carbotte *et al*., 1998; Detrick *et al*., 2002; Hooft *et al*., 1997; Phipps Morgan & Chen, 1993b). Here, we have calculated time-averaged rates of magma supply for those mid-ocean ridges where there are constraints on magma reservoir depths (Fig. 3.7), following Sinton *et al*. (2003). Note that on-axis crustal thickness along the Juan de Fuca Ridge has not been measured, and the rates of magma supply calculated at that location assume 5-7 km thick crust. By comparing magma residence depths as a function of magma supply, instead of spreading rate, we can explicitly compare hotspot-affected mid-ocean ridges, where the oceanic crust is anomalously thick (e.g., Galápagos Spreading Center, Reykjanes Ridge), to "normal" mid-ocean ridges.

At rates of magma supply greater than 0.4×10^6 m^3/yr/km, there is strong geophysical evidence for the existence of quasi-steady-state axial melt lenses at shallow crustal depths (~1-2 km bsf) (e.g., Dunn & Forsyth, 2007). Data shown in Figure 3.7 (Carbotte *et al*., 2013; Detrick *et al*., 1987; Hooft *et al.*, 1997) indicate that melt lenses monotonically shoal by ~1 km as the rate of magma supply triples from 0.4×10^6-1.2×10^6 m^3/yr/km. The decrease in magma chamber depth with increasing rates of magma supply is consistent with models where the depths of shallow magma reservoirs are thermally controlled (e.g., Hooft & Detrick, 1993; Phipps Morgan & Chen, 1993a). Axial melt lens depths are consistently greater, but also more variable at low time-averaged magma supply rates (0.1×10^6-0.4×10^6 m^3/yr/km) (Fig. 3.7) (Blacic *et al*., 2004; Canales *et al*., 2005). Along relatively low-magma-supply regions of the GSC (e.g., 94.2°W), melt lens depths range from 2.9-4.0 km bsf over an along-axis distance of less than 10 km, in the absence of large offsets in the spreading axis (Fig. 3.4) (Blacic *et al*., 2004).

At rates of magma supply less than 0.3×10^6 m^3/yr/km, seismic reflections from axial melt lenses are absent along most ridge segments studied (e.g., Detrick *et al*., 1990; Sinton & Detrick, 1992; Peirce *et al*., 2005), although two studies that specifically targeted ridge segments thought to be magmatically active did detect melt lenses (Sinha

et al., 1997; Singh *et al*., 2006). At these lower rates of magma supply, there does not appear to be a global correlation between the time-averaged rate of magma supply and the depth of magma residence, although magma reservoir depths are consistently greater than at high-magma-supply ridges. There currently is no evidence for the presence of magma reservoirs at depths shallower than ~2 km bsf, even intermittently, below low-magma-supply ridge segments (Fig. 3.7).

3.9. Reconciling seismically detected melt lenses with peaks in melt inclusion entrapment depths

Consideration of mechanisms for melt inclusion entrapment indicates that peaks in entrapment depth PDFs are likely to be related to crustal magma reservoirs (see section 6.1). If these crustal magma reservoirs are the melt lenses imaged by seismic reflection studies, melt inclusion entrapment depth PDF peaks should coincide with seismic melt lens depths (Wanless & Shaw, 2012). Indeed, Wanless & Shaw (2012) found that for recently erupted samples from the East Pacific Rise, the clusters in entrapment depths are remarkably similar to the melt lens depth (Fig. 3.7). At 94.2°W along the GSC, however, the melt inclusion PDF peak is significantly shallower than the nearest seismic melt lens depth, and on the Vance segment of the Juan de Fuca Ridge, the PDF peak is deeper than (though within error of) the seismic melt lens depth. We suggest that these discrepancies could reflect temporal variations in the depths of the melt lens at these locations.

Seismic studies constrain spatial variations in the depth of the melt lens along axis at the time of the study, but not temporal variations in the depth of the melt lens at a given location. Melt inclusion entrapment depth determinations provide an opportunity to determine the variability in magma residence depths at a given location. For example, the increased depth of the peak in melt inclusion entrapment depth in the most recent eruption at 95°W suggests that depths of magma residence were deeper by ~0.4 km prior to that eruption than for the previous two eruptions at that location.

An important test of whether melt inclusion PDF peaks are created within the same magma reservoirs that are detected by seismic studies will be to compare melt inclusion entrapment depths to seismic melt lens depths in other locations (preferably at intermediate rates of magma supply) where recent eruptions have occurred. In order to

avoid uncertainties associated with temporal variability of melt lens depth, it is important to compare melt inclusions from recently erupted lavas to the results of recent seismic studies. There are surprisingly few locations on the mid-ocean ridge system where recent eruptions have been identified and even fewer where they have been sampled (Rubin *et al*., 2012), but seismic reflection studies have documented the depths of axial melt lenses in nearly all of them.

3.10. Conclusions

This study demonstrates the potential for using measurements of the concentrations of H_2O and CO_2 in olivine-hosted melt inclusions to determine the depths of magma residence prior to eruption along mid-ocean ridges in locations where multi-channel seismic studies have not detected axial melt lens reflectors. This technique can be used most effectively when near-vent samples are collected from mapped lava flow fields at submarine mid-ocean ridges. When coupled with geologic mapping, studies of melt inclusion entrapment depths offer the unique opportunity to constrain temporal variations in magma residence at a given location. At our study sites at 94.2°W and 95°W along the GSC, magmas resided at depths of 2.6 and 3.0-3.4 km bsf, respectively, prior to eruption. Despite magmatic recharge between the oldest and intermediate-aged eruptions at 95°W, magma resided at similar depths prior to each eruption (~3.0 km bsf). In contrast, the most recent eruption tapped magma from a slightly deeper reservoir lying ~3.4 km bsf. Along the global mid-ocean ridge system, ridges with time-averaged rates of magma supply greater than 0.4×10^6 m^3/yr/km host persistent shallow melt lenses whose depths increase slightly with decreasing magma supply. In contrast, at lower-magma-supply ridges, magma reservoirs exist intermittently at more variable, but consistently greater depths beneath the axis. Additional work is needed to confirm whether the magma reservoirs sampled by melt inclusions are the same as seismically imaged melt lenses.

3.11. Appendix

3.11.1. Analytical methods

3.11.1.1. Ion microprobe

A total of 83 melt inclusions and five selvage glasses were analyzed for H_2O, CO_2, F, S, and Cl concentrations using the Cameca 1280 ion microprobe at Woods Hole Oceanographic Institution. All analyses were run during a one-week period in March 2013 using a Cs^+ beam, following methods described by Shaw *et al.* (2008). A mid-ocean ridge basalt glass standard (ALV-519-4-1) with composition similar to our melt inclusions was run routinely throughout the analyses to monitor instrumental drift. The species measured were ^{12}C, $^{16}O^1H$, ^{19}F, ^{32}S, and ^{35}Cl; each intensity measured was normalized to ^{30}Si and converted to weight concentrations using calibration curves made from a set of natural and artificial glasses measured at the beginning of the week. Several standards were run again at the end of the week to confirm that the calibration was still valid. The background signal for $^{16}O^1H$ converted to H_2O was 0.08 wt. % (and background ^{12}C converted to CO_2 was 27 ppm) as measured on nominally anhydrous synthetic forsterite phenocrysts. The ion microprobe measurements of H_2O (0.23 wt. %) and CO_2 (163 ppm) in sample EW56D accord well with measurements of 0.23 wt. % and 155 ppm for the same sample made previously by Fourier transform infrared spectroscopy (FTIR) (Cushman *et al.*, 2004).

3.11.1.2. Electron microprobe

Major elements of melt inclusions and selvage glasses were analyzed using the five-spectrometer JEOL JXA-8500F electron microprobe at the University of Hawaii in May, 2013. These data were collected with an accelerating voltage of 15 keV, 10 nA beam current, 10 μm beam diameter, and Probe for EPMA software. A ZAF matrix correction was applied to all analyses. As space allowed, up to three points were measured on each melt inclusion, and the results were averaged. Peak and background counting times were 60 seconds for S; 50 seconds for Al, K, and Mg; 40 seconds for Si and Ca; 30 seconds for Ti, Na, Fe, and P; and 20 seconds for Mn. Samples were calibrated using Makaopuhi glass standard A-99 (Si, Al, Ca, Mg), Juan de Fuca glass standard VG-2 (Fe), and mineral standards Amelia albite (Na), sphene glass (Ti),

orthoclase (K), Verma garnet (Mn), fluorapatite (P), and troilite (S). Glass standards VG-2 and A-99 were run as unknowns throughout the analyses to monitor instrumental drift (see Table 3.2 for reproducibility and average values).

Major elements of host olivines were also analyzed by electron microprobe at the University of Hawai‘i in May 2013. These data were collected with an accelerating voltage of 20 keV, 200 nA beam current, and 10 μm beam diameter. Olivines were analyzed adjacent to each melt inclusion, and in transects running perpendicular to the olivine rim. Peak counting times were 100 seconds for Si, Ni, Mg, and Ca; 60 seconds for Mn; and 30 seconds for Fe. Background counting times were 90 seconds for Si, Ni, Mg, and Ca ; 60 seconds for Mn; and 30 seconds for Fe. Samples were calibrated using mineral standards San Carlos olivine (Si, Fe, Ni, Mg), Kakanui augite (Ca), and Verma garnet (Mn). San Carlos (USNM 111312) and Springwater (USNM 2566) olivine standards were run as unknowns throughout the analyses to monitor instrumental drift; average values are compared to accepted values from Jarosewich *et al.* (1980) in Table 3.2.

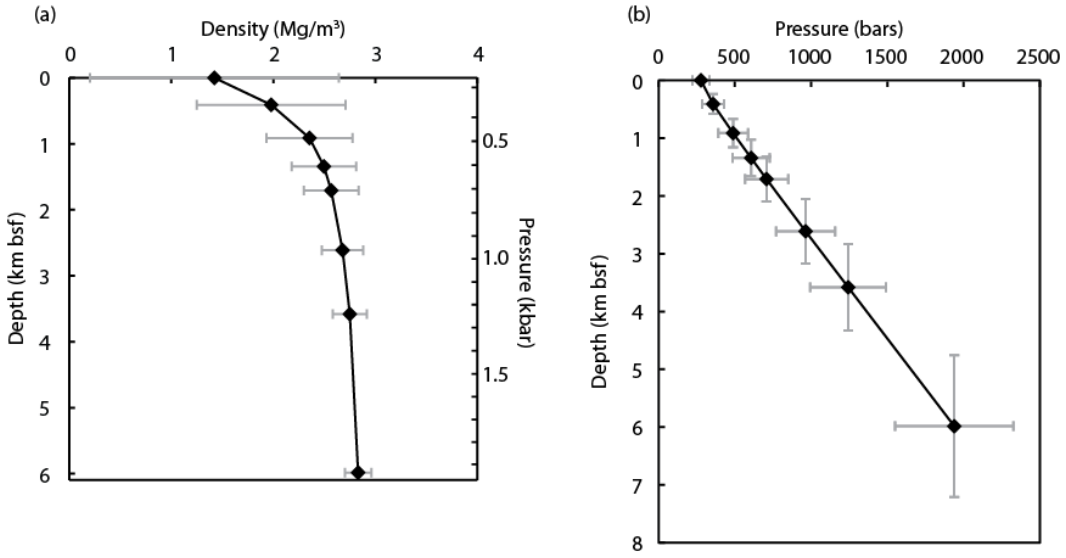

Figure 3.8. Density and pressure variations with depth. (a) Average density of overlying crust, as a function of depth within the crust (kilometers below seafloor, km bsf). Average densities calculated using the seismic velocity structure for 94.25°W from Canales *et al*. (2002) and V_p-bulk density relationship from Carlson & Herrick (1990). Pressures calculated assuming 2.75 km water depth are also given. Error bars represent ±2σ uncertainty in average density. (b) Pressure-depth relation used to calculate depths of entrapment. Error bars represent ±2σ uncertainty in saturation pressures and calculated entrapment depths.

3.11.2. Uncertainty in depths of entrapment

We use VolatileCalc (Newman & Lowenstern, 2002), which is based on the mixed CO_2 and H_2O solubility model of Dixon *et al*. (1995), to convert CO_2 and H_2O concentrations to saturation pressures. Saturation pressures calculated by VolatileCalc for tholeiitic basalts are typically within 20% of experimental pressures.

Saturation pressures are converted to depths of entrapment using an average crustal density profile constrained by seismic velocity data. Canales *et al*. (2002) determined a seismic velocity profile for 94.25°W (the "Gala-2" seismic refraction experiment). We convert seismic velocity to bulk density using the relationship determined by Carlson & Herrick (1990) from laboratory measurements. We calculate the average density of overlying crust as a function of depth, assuming that seismic velocity (and thus density) varies linearly between depths at which it is constrained (Fig. 3.8). The depth of entrapment can then be calculated from the saturation pressure and average crustal density. Uncertainties in seismic velocity (Canales *et al*., 2002), density (Carlson & Herrick, 1990), and saturation pressure are propagated through the calculation and result in relative depth uncertainties (2σ) of ~21% at 3 km below the seafloor (relative uncertainty decreases with increasing depth).

3.11.3. Diffusive loss of CO_2 from melt inclusions

Due to the relatively low solubility of CO_2 in basaltic melt, strong gradients in CO_2 concentration develop between melt inclusions and their carrier melts during magma ascent as CO_2 exsolves from the carrier melt. To assess the likelihood of diffusive loss of CO_2 from melt inclusions during or after eruption, we use the simple one-dimensional case described by Qin *et al*. (1992) and Cottrell *et al*. (2002) where a spherical melt inclusion is centered within a spherical olivine crystal, which is in contact with a carrier melt. The diffusion equation describing the concentration of CO_2 within the olivine crystal as a function of radial distance from Qin *et al*. (1992) is

$$\frac{\partial C}{\partial t} = D\left(\frac{\partial^2 C}{\partial r^2} + \frac{2}{r}\frac{\partial C}{\partial r}\right),$$

where C is the concentration of element *i*, D is the diffusivity of *i* in the olivine, r is the radial distance from the center of the inclusion, and *t* is time. The equation describing the change in the melt inclusion composition as a result of diffusive flux across the boundary between the melt inclusion and olivine crystal, also from Qin *et al*. (1992), is

$$\frac{d}{dt}\left[\frac{4}{3}\pi a^3 \rho_m C_l(t)\right] = 4\pi a^2 D \frac{\partial(\rho_c C)}{\partial r}\Big|_{r=a},$$

where *a* is the radius of the melt inclusion, ρ_c is the density of the olivine crystal, and ρ_m is the density of the melt. We use a forward in time, centered in space finite difference approximation to solve these equations with boundary conditions described below.

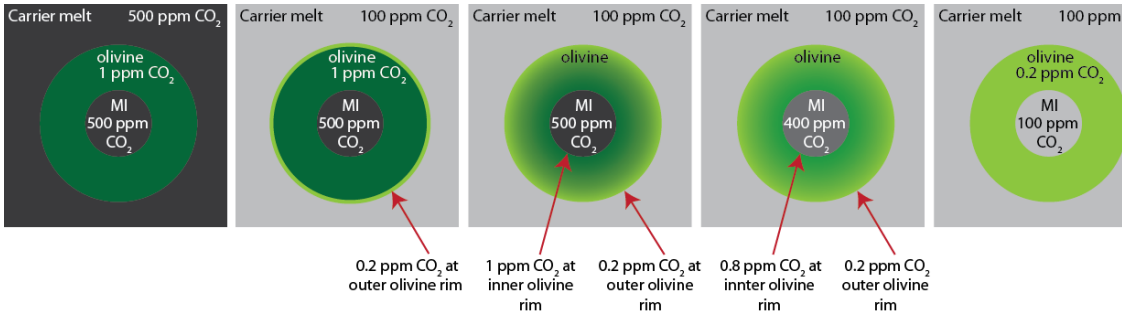

Figure 3.9. Schematic illustrating diffusive equilibration of melt inclusion with carrier melt after eruption. See text for discussion.

We assume that an olivine-hosted melt inclusion forms at some depth beneath the seafloor (see Figure 3.9). The CO_2 concentration of the melt inclusion at the time of formation (500 ppm) is equal to that of the carrier melt, and the CO_2 concentration of the host olivine crystal is in equilibrium with the melt inclusion and carrier melt. The olivine-hosted melt inclusion then ascends and is erupted on the seafloor. We assume that the carrier melt exsolves CO_2 and degases instantaneously due to the decrease in pressure at time t=0 of the diffusion model, with a new CO_2 concentration of 100 ppm. The outer rim of the olivine is kept in equilibrium with the carrier melt composition, which is held constant. The initial composition of the interior of the olivine is uniform and in equilibrium with the melt inclusion. The CO_2 concentration within the olivine is then allowed to diffusively equilibrate according to the diffusion equation. At each time step, the melt inclusion composition changes in response to diffusive flux across the boundary between the melt inclusion and host olivine, and we assume that the melt inclusion composition remains in equilibrium with the inner olivine-melt boundary.

The time required to modify the concentration of a given element in a melt inclusion is dependent on the diffusivity and compatibility of that element in the olivine (more compatible elements with higher diffusivity equilibrate more rapidly), and on the radii of the melt inclusion and host olivine (small melt inclusions in small olivine crystals equilibrate more rapidly) (Cottrell *et al.*, 2002; Qin *et al.*, 1992). We use a diffusivity of 32 $\mu m^2/yr$ (Tingle *et al.*, 1988) and an olivine-melt partition coefficient 0.002 (Keppler *et al.*, 2003).

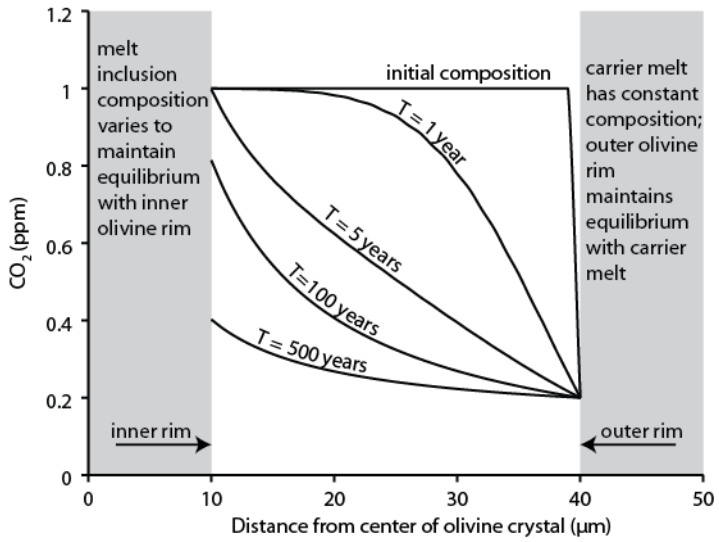

Figure 3.10. Evolution of CO_2 concentration profiles across host olivine with time. Curves are for melt inclusion (radius = 10 μm) centered within an olivine crystal (radius = 30 μm).

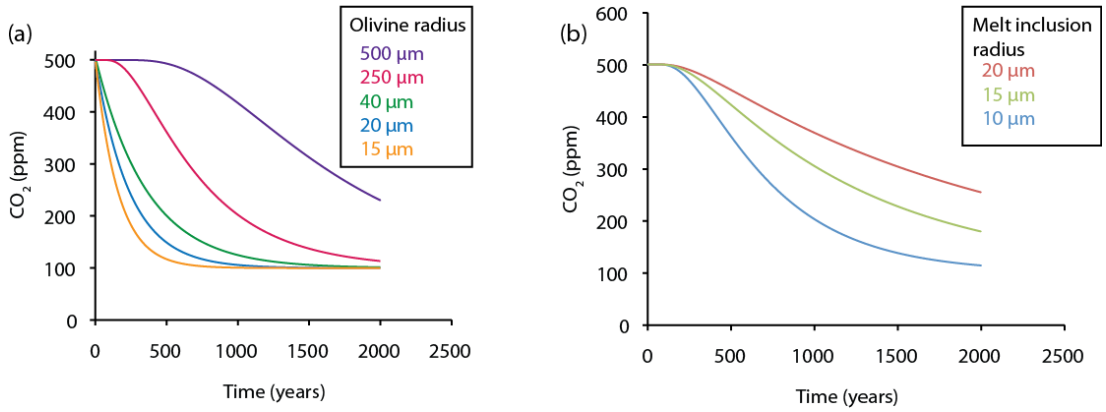

Figure 3.11. (a) Effect of varying radius of host olivine on CO_2 concentration of melt inclusion. In all cases, melt inclusion has 10 μm radius, and is centered within the host olivine. Curves are labeled with radius of host olivine. (b) Effect of varying radius of melt inclusion on CO_2 concentration of melt inclusion. In all cases, host olivine has 250 μm radius; melt inclusion is centered within host olivine. Curves are labeled with radius of melt inclusion.

We investigate varying melt inclusion and olivine radii in order to constrain timescales over which the CO_2 contents of melt inclusions are likely to be modified. Since all melt inclusions analyzed have radii > 0.1 μm, the minimum modeled melt inclusion radius is 0.1 μm. For the conservative case of a melt inclusion with radius 0.1 μm, centered within an olivine crystal with radius 0.15 μm, it takes two years for the CO_2 content of a melt inclusion to decrease even by one percent. With increasing melt inclusion radius or olivine radius, the diffusion times increase. (Figure 3.11).

Table 3.1. Sample locations and eruption depths

Sample	IGSN	Eruption	Type	Lat (°N)	Lon (°W)	Depth (m bsf)
EW56D			Dredge	2.5533	94.2383	2478
AL4597-05	JMS000041	recent	Alvin grab	2.6124	94.9313	2749
AL4598-08	JMS000053	recent	Alvin grab	2.6125	94.9522	2778
AL4598-11	JMS000056	intermediate	Alvin grab	2.6173	94.9485	2778
AL4599-03	JMS000059	oldest	Alvin grab	2.6188	94.9665	2754

Table 3.2. Standard data: averages, accepted values, and standard deviations

Basaltic glass EMPA standard analyses (all values given in wt. %)

	A99			**VG2**		
	average	accepted	std dev, n=29	average	accepted	std dev, n=28
SiO_2	50.96	50.94	0.16	50.64	50.81	0.15
TiO_2	4.13	4.06	0.06	1.88	1.85	0.03
Al_2O_3	12.47	12.49	0.04	13.99	14.06	0.04
FeO	13.40	13.30	0.07	11.78	11.84	0.05
MnO	0.19	0.15	0.01	0.21	0.22	0.01
MgO	5.09	5.08	0.02	7.05	6.71	0.03
CaO	9.29	9.30	0.03	11.21	11.12	0.03
Na_2O	2.65	2.66	0.03	2.63	2.62	0.03
K_2O	0.84	0.82	0.01	0.19	0.19	0.01
P_2O_5	0.44	0.38	0.02	0.20	0.20	0.02
S	0.02	0.01	0.01	0.15	0.13	0.00
Sum	99.49	99.19		99.93	99.75	

Olivine EMPA standard analyses (all values given in wt. %)

	San Carlos, USNM 111312			**Springwater, USNM 2566**		
	average	accepted	std dev, n=27	average	accepted	std dev, n=27
SiO_2	40.56	40.81	0.20	39.26	38.95	0.20
FeO	9.51	9.55	0.04	16.60	16.62	0.06
NiO	0.371	0.370	0.002	0.000	--	0.000
MnO	0.136	0.1	0.001	0.309	0.30	0.002
MgO	49.24	49.42	0.24	43.54	43.56	0.19
CaO	0.071	<0.05	0.001	0.000	<0.05	0.000
Sum	99.89	99.88		99.71	99.43	

Basaltic glass SIMS standard analyses (all values given in ppm)

	ALV-519-4		
	average	accepted	std dev, n=25
CO_2	160	165	7.0
H_2O	1726	1700	80
F	94	90	2.7
S	889	950	18.9
Cl	46	45	2.0

Table 3.3. Raw melt inclusion compositions, saturation pressures, and depths of entrapment

Sample	SiO2	TiO2	Al2O3	FeOT	MnO	MgO	CaO	Na2O	K2O	P2O5	H2O	CO2	F	S	Cl	Psat	Entrapment Depth	MI SIZE Length	Width	Bubble Diam.	Corr. Pressure	Corr. Sat. Depth
units	wt. %	wt. %	wt. %	wt. %	wt. %	wt. %	wt. %	wt. %	wt. %	wt. %	wt. %	ppm	ppm	ppm	ppm	bars	km bsf	µm	µm	µm	bars	km bsf
AL4597-5-01	51.00	1.40	14.65	10.83	0.20	7.70	11.97	2.35	0.15	0.14	0.25	568	190	1217	115	1201	3.4	102	92	--	--	--
AL4597-5-02	50.95	1.38	14.61	10.59	0.18	7.90	12.03	2.29	0.13	0.13	0.24	551	185	1224	92	1167	3.3	80	49	--	--	--
AL4597-5-03	51.25	1.41	14.06	12.06	0.20	7.09	11.44	2.32	0.10	0.13	0.22	481	163	1309	59	1023	2.8	138	80	--	--	--
AL4597-5-04	50.80	1.40	13.78	12.94	0.22	7.08	10.84	2.44	0.11	0.15	0.24	555	225	1260	86	1175	3.3	78	77	--	--	--
AL4597-5-05	51.15	1.41	14.72	10.37	0.18	7.90	12.06	2.31	0.15	0.13	0.22	550	179	1223	115	1165	3.3	68	54	--	--	--
AL4597-5-06	51.00	1.52	14.74	10.92	0.21	7.02	12.73	2.16	0.11	0.13	0.23	570	205	1139	92	1204	3.4	43	34	--	--	--
AL4597-5-08	51.33	1.23	14.31	11.83	0.23	7.20	11.77	2.18	0.09	0.08	0.22	617	168	1095	44	1298	3.8	83	47	--	--	--
AL4597-5-09	51.02	1.33	14.82	10.40	0.16	7.77	12.10	2.25	0.12	0.14	0.21	579	205	1223	91	1221	3.5	106	83	--	--	--
AL4597-5-10	50.93	1.42	14.79	10.39	0.21	7.71	11.97	2.22	0.16	0.10	0.22	556	197	1260	119	1176	3.4	92	37	--	--	--
AL4597-5-12	51.23	1.21	14.55	10.91	0.19	7.34	12.33	2.13	0.09	0.13	0.19	527	161	1172	55	1115	3.1	88	71	--	--	--
AL4597-5-14	50.11	1.22	16.07	9.51	0.18	7.91	12.61	2.40	0.10	0.11	0.20	547	128	1142	57	1157	3.3	65	52	--	--	--
AL4597-5-15	51.45	0.95	15.29	9.63	0.15	7.77	12.74	2.18	0.06	0.07	0.23	571	129	999	16	1207	3.5	97	63	--	--	--
AL4597-5-16	51.42	1.44	14.07	11.84	0.22	7.40	11.16	2.36	0.12	0.12	0.21	491	180	1319	62	1045	2.9	122	60	--	--	--
AL4597-5-17	51.27	1.09	14.81	10.39	0.20	7.39	12.87	2.09	0.09	0.12	0.20	528	152	1057	36	1119	3.2	66	47	--	--	--
AL4597-5-19	50.99	1.35	14.67	10.98	0.18	7.53	12.25	2.23	0.10	0.12	0.22	555	171	1133	36	1175	3.3	45	35	--	--	--
AL4597-5-20	50.99	1.29	14.61	10.25	0.20	7.78	11.98	2.31	0.13	0.12	0.20	549	209	1193	91	1162	3.3	45	26	--	--	--
AL4597-5-21	50.80	1.39	15.38	10.55	0.22	7.25	12.75	2.28	0.14	0.08	0.19	610	179	1065	89	1284	3.7	71	66	--	--	--
AL4597-5-gl	51.25	1.27	14.49	10.48	0.20	7.83	12.34	2.24	0.10	0.12	0.21	200	147	1149	62	438	0.7	--	--	--	--	--
AL4598-8-01	50.79	1.30	14.44	10.93	0.19	7.76	12.12	2.23	0.14	0.07	0.24	584	175	1214	115	1234	3.5	64	31	--	--	--
AL4598-8-02	52.27	1.37	15.27	8.92	0.17	6.93	12.95	2.29	0.11	0.12	0.22	819	154	875	59	1695	5.2	37	32	--	--	--
AL4598-8-03[a]	51.07	1.38	14.69	10.96	0.15	7.15	12.46	2.08	0.14	0.11	0.24	561	210	1242	122	--[a]	--[a]	--[a]	--[a]	--[a]	--[a]	--[a]
AL4598-8-04	51.60	1.43	13.72	12.51	0.21	7.13	11.07	2.34	0.11	0.11	0.24	578	185	1257	58	1220	3.5	143	118	--	--	--
AL4598-8-06	51.80	1.16	14.65	10.09	0.19	7.37	12.67	2.13	0.10	0.11	0.22	577	161	1120	53	1218	3.5	86	76	--	--	--
AL4598-8-07	51.04	1.41	14.32	11.93	0.22	6.97	11.95	2.22	0.14	0.12	0.21	579	174	1200	102	1221	3.5	94	54	--	--	--
AL4598-8-09	50.93	1.52	14.15	11.98	0.21	7.43	11.41	2.30	0.16	0.15	0.21	546	228	1258	123	1155	3.3	184	150	--	--	--
AL4598-8-10	51.57	1.36	14.62	10.78	0.19	6.80	12.76	2.17	0.11	0.12	0.20	540	159	1058	60	1143	3.2	64	60	--	--	--
AL4598-8-11	50.44	1.48	14.12	12.44	0.21	7.37	11.46	2.29	0.15	0.15	0.24	538	238	1299	131	1141	3.2	152	135	--	--	--
AL4598-8-12	50.62	1.41	14.05	12.64	0.21	6.60	11.82	2.26	0.15	0.14	0.22	583	254	1307	128	1230	3.5	53	37	--	--	--
AL4598-8-15	51.16	1.32	14.30	11.30	0.19	7.52	12.34	2.17	0.13	0.12	0.23	431	174	1224	81	923	2.5	206	66	--	--	--
AL4598-8-16	51.78	1.02	15.41	9.12	0.16	7.47	13.41	2.06	0.09	0.10	0.21	588	119	1031	53	1239	3.6	69	62	--	--	--
AL4598-8-17	51.45	1.18	15.04	10.20	0.16	6.95	13.12	2.06	0.12	0.12	0.22	535	159	1148	67	1134	3.2	109	56	--	--	--
AL4598-8-18	49.93	0.97	16.35	10.24	0.16	6.92	13.68	2.12	0.07	0.07	0.23	776	149	939	20	1612	4.9	96	79	--	--	--
AL4598-8-19	51.32	1.59	14.46	10.62	0.22	7.54	11.85	2.34	0.14	0.16	0.22	524	197	1154	99	1111	3.1	144	120	--	--	--
AL4598-8-gl	51.56	1.32	14.35	10.74	0.18	7.71	12.09	2.23	0.12	0.13	0.21	158	159	1170	74	346	0.4	--	--	--	--	--

Table 3.3. (continued) Raw melt inclusion compositions, saturation pressures, and depths of entrapment

Sample	SiO2	TiO2	Al2O3	FeOT	MnO	MgO	CaO	Na2O	K2O	P2O5	H2O	CO2	F	S	Cl	Psat	Entrapment Depth	MI SIZE Length	Width	Bubble Diam.	Corr. Pressure	Corr. Sat. Depth
units	wt. %	wt. %	wt. %	wt. %	wt. %	wt. %	wt. %	wt. %	wt. %	wt. %	wt. %	ppm	ppm	ppm	ppm	bars	km bsf	µm	µm	µm	bars	km bsf
AL4598-11-05	50.73	1.17	14.80	10.57	0.21	8.14	12.71	1.98	0.10	0.10	0.25	174	159	1105	81	383	0.5	68	49	--	--	--
AL4598-11-06	50.43	1.30	14.93	10.36	0.18	8.52	12.38	2.07	0.11	0.11	0.26	154	163	1123	90	340	0.3	136	118	--	--	--
AL4598-11-07	50.79	1.39	15.80	10.24	0.18	5.55	13.83	2.06	0.11	0.11	0.25	151	185	1223	98	335	0.3	37	34	--	--	--
AL4598-11-08	50.69	1.22	14.78	10.03	0.15	8.38	12.26	2.11	0.11	0.11	0.25	146	151	1108	81	324	0.3	129	113	--	--	--
AL4598-11-09	50.60	1.15	14.95	10.09	0.16	8.38	12.65	2.04	0.10	0.10	0.25	433	152	1096	83	927	2.5	83	82	--	--	--
AL4598-11-10	50.31	1.23	13.87	10.66	0.18	11.93	11.30	1.86	0.11	0.16	0.21	161	145	1150	85	354	0.4	29	26	--	--	--
AL4598-11-11	50.33	1.03	15.19	10.61	0.19	7.49	13.73	1.85	0.08	0.12	0.23	502	160	1065	70	1067	3.0	54	38	--	--	--
AL4598-11-12	50.88	1.25	14.82	9.95	0.20	8.50	12.45	2.08	0.10	0.10	0.22	505	143	1082	82	1072	3.0	95	62	--	--	--
AL4598-11-15	50.25	1.29	14.77	10.51	0.18	8.29	12.67	2.03	0.11	0.14	0.23	130	163	1113	89	288	0.0	50	34	--	--	--
AL4598-11-16	51.04	1.25	15.18	10.01	0.18	7.66	13.00	2.09	0.11	0.12	0.23	553	148	1058	57	1170	3.3	39	38	--	--	--
AL4598-11-17	50.85	1.17	14.73	10.71	0.17	7.82	12.64	2.10	0.08	0.08	0.24	502	150	1151	42	1068	3.0	57	46	--	--	--
AL4598-11-18	50.52	1.13	15.01	10.32	0.16	6.90	13.84	1.87	0.08	0.10	0.26	529	168	1090	60	1123	3.2	29	27	--	--	--
AL4598-11-20	50.31	1.08	14.85	10.12	0.17	7.78	13.28	1.90	0.09	0.07	0.24	510	160	1055	54	1084	3.0	56	52	--	--	--
AL4598-11-21	50.46	1.29	14.94	10.36	0.21	8.64	12.31	2.10	0.11	0.12	0.23	137	156	1108	88	303	0.1	72	61	--	--	--
AL4598-11-22	50.86	1.30	15.03	10.49	0.18	7.26	13.19	2.08	0.10	0.12	0.24	493	171	1167	91	1048	2.9	34	23	--	--	--
AL4598-11-23	51.25	0.88	15.67	8.34	0.17	8.74	13.78	1.92	0.04	0.05	0.23	370	98	885	11	796	2.0	82	67	--	--	--
AL4598-11-24	50.92	1.02	14.57	10.45	0.18	8.66	12.48	2.10	0.09	0.06	0.24	565	150	1019	47	1194	3.4	42	38	--	--	--
AL4598-11-gl	50.59	1.26	15.04	10.23	0.15	8.32	12.38	2.13	0.11	0.12	0.21	158	159	1170	74	346	0.4	--	--	--	--	--
AL4599-3-01	51.06	1.36	15.40	10.68	0.17	6.11	13.46	2.08	0.08	0.13	0.19	553	166	1190	65	1168	3.3	36	29	--	--	--
AL4599-3-02	50.85	1.27	15.07	10.59	0.18	8.40	12.28	2.07	0.09	0.12	0.21	486	146	1135	64	1034	2.9	87	32	--	--	--
AL4599-3-03	50.67	1.29	14.97	10.74	0.18	7.31	12.97	1.99	0.09	0.12	0.20	497	162	1150	64	1056	2.9	43	36	--	--	--
AL4599-3-04	52.98	1.02	17.76	7.23	0.11	5.98	13.61	2.37	0.03	0.11	0.19	334	93	927	1	719	1.7	36	25	--	--	--
AL4599-3-05	51.14	0.89	14.97	10.29	0.19	8.03	13.15	1.98	0.03	0.06	0.19	315	73	1000	3	680	1.6	116	65	--	--	--
AL4599-3-06	50.65	1.29	15.30	10.80	0.18	7.02	13.04	2.03	0.09	0.13	0.21	489	159	1161	70	1040	2.9	68	49	--	--	--
AL4599-3-07	50.71	1.28	14.99	10.59	0.21	8.22	12.49	2.03	0.10	0.07	0.21	499	155	1158	67	1061	3.0	48	38	--	--	--
AL4599-3-08	51.95	1.40	14.73	10.86	0.21	6.13	12.57	2.32	0.08	0.10	0.21	568	172	1255	40	1200	3.4	57	34	--	--	--
AL4599-3-11	50.57	1.27	14.85	10.68	0.18	8.27	12.20	2.08	0.10	0.08	0.19	445	133	1165	60	950	2.6	94	77	--	--	--
AL4599-3-12	50.87	1.11	14.70	10.80	0.19	7.27	12.98	2.05	0.08	0.09	0.18	554	125	1096	36	1170	3.3	69	55	--	--	--
AL4599-3-14	50.74	1.28	14.88	10.51	0.23	8.41	12.11	2.09	0.11	0.11	0.21	144	141	1142	58	317	0.2	65	43	--	--	--
AL4599-3-15	50.94	1.30	15.03	10.64	0.23	7.71	12.63	2.03	0.10	0.10	0.21	502	157	1147	64	1065	3.0	54	51	--	--	--
AL4599-3-16	50.98	1.30	14.93	10.78	0.22	7.48	12.47	2.18	0.09	0.10	0.20	515	155	1180	61	1092	3.1	50	40	--	--	--
AL4599-3-17	50.84	1.26	14.84	10.79	0.17	8.55	11.86	2.18	0.10	0.14	0.20	498	147	1149	63	1057	2.9	37	30	--	--	--
AL4599-3-18	51.26	1.05	15.02	10.50	0.19	6.87	13.41	1.92	0.06	0.09	0.21	553	131	1060	30	1170	3.3			--	--	--
AL4599-3-19	50.78	1.27	14.76	10.88	0.20	8.22	12.24	2.08	0.11	0.10	0.21	500	146	1161	62	1062	3.0	84	54	--	--	--
AL4599-3-20	50.82	1.29	14.79	10.95	0.21	7.74	12.77	1.98	0.09	0.09	0.20	409	146	1095	53	876	2.3	75	43	--	--	--
AL4599-3-21	--[b]	--[b]	--[b]	--[b]	--[b]	--[b]	--[b]	--[b]	--[b]	--[b]	0.21	522	150	1171	66	1106	3.1	135	71	--	--	--
AL4599-3-22	--[b]	--[b]	--[b]	--[b]	--[b]	--[b]	--[b]	--[b]	--[b]	--[b]	0.20	549	107	1072	35	1161	3.3	105	99	--	--	--
AL4599-3-gl	50.69	1.31	14.85	10.38	0.19	8.24	12.19	2.12	0.10	0.10	0.20	150	139	1089	54	330	0.3	--	--	--	--	--

Table 3.3. (continued) Raw melt inclusion compositions, saturation pressures, and depths of entrapment

Sample	SiO2	TiO2	Al2O3	FeOT	MnO	MgO	CaO	Na2O	K2O	P2O5	H2O	CO2	F	S	Cl	Psat	Entrapment Depth	MI SIZE Length	Width	Bubble Diam.	Corr. Pressure	Corr. Sat. Depth
units	wt. %	wt. %	wt. %	wt. %	wt. %	wt. %	wt. %	wt. %	wt. %	wt. %	wt. %	ppm	ppm	ppm	ppm	bars	km bsf	µm	µm	µm	bars	km bsf
EW56D-01	50.60	1.42	14.86	10.89	0.21	7.13	12.13	2.25	0.12	0.10	0.25	447	184	1213	90	955	2.7	82	39	--	--	--
EW56D-03	51.10	1.10	16.00	10.16	0.15	7.17	12.59	2.20	0.10	0.12	0.26	410	158	1134	62	879	2.4	38	35	--	--	--
EW56D-05	51.23	1.44	14.62	11.02	0.19	7.64	11.48	2.42	0.15	0.14	0.26	467	183	1242	91	997	2.8	150	30	--	--	--
EW56D-06	50.68	1.20	15.66	10.13	0.23	6.83	12.83	2.22	0.10	0.11	0.26	426	156	1181	63	913	2.5	61	29	--	--	--
EW56D-07	--[c]	--[c]	--[c]	--[c]	--[c]	--[c]	--[c]	--[c]	--[c]	--[c]	0.25	468	183	1276	90	998	2.8	47	36	--	--	--
EW56D-08	49.76	0.88	17.83	8.99	0.16	7.62	12.72	2.44	0.06	0.06	0.24	298	84	933	26	646	1.6	111	75	--	--	--
EW56D-10	50.84	1.45	14.82	11.43	0.21	6.72	12.29	2.29	0.12	0.12	0.23	132	174	1155	81	292	0.2	76	53	15	297	0.212
EW56D-11	50.33	1.15	15.39	11.07	0.20	7.96	11.87	2.23	0.10	0.10	0.25	405	153	1124	64	870	2.4	40	30	--	--	--
EW56D-13	50.61	1.13	16.68	9.48	0.18	7.46	12.50	2.32	0.09	0.07	0.26	366	130	1112	54	789	2.1	49	30	--	--	--
EW56D-14	51.30	1.44	14.75	11.01	0.22	7.43	12.00	2.30	0.14	0.14	0.26	486	180	1264	92	1036	3.0	47	44	--	--	--
EW56D-16	50.80	1.43	14.78	11.47	0.18	6.30	12.71	2.18	0.11	0.16	0.24	272	86	907	21	591	1.4	48	33	--	--	--
EW56D-17	49.42	0.85	17.94	9.16	0.18	7.77	12.73	2.35	0.04	0.05	0.24	557	185	1196	83	1180	3.5	66	53	--	--	--
EW56D-19	50.91	1.47	14.57	11.35	0.22	7.73	11.64	2.29	0.13	0.13	0.24	422	174	1252	95	903	2.5	40	39	--	--	--
EW56D-20	50.96	1.38	15.19	11.16	0.21	7.21	12.16	2.25	0.12	0.12	0.24	409	162	1195	81	877	2.4	68	39	--	--	--
EW56D-21	50.89	1.37	14.55	11.15	0.16	7.42	11.98	2.24	0.13	0.10	0.18	214	122	940	64	465	0.9	39	22	--	--	--
EW56D-22	51.05	1.37	14.76	11.24	0.19	7.43	11.82	2.29	0.13	0.11	0.25	276	177	1246	86	600	1.4	71	38	--	--	--
EW56D-gl	50.87	1.38	14.45	11.44	0.22	7.50	11.79	2.30	0.13	0.10	0.23	163	174	1213	81	358	0.5	--	--	--	--	--

a. Melt inclusion and vapor bubble were irregularly shaped and incompletely exposed. Sample not used in analysis.
b. Melt inclusion major elements not analyzed. No post-entrapment correction calculated.
c. Ion probe pit interfered with analysis of melt inclusion major elements. No post-entrapment correction calculated.

Table 3.4. Melt inclusions corrected for post-entrapment crystallization, with corresponding saturation pressures and depths of entrapment

Sample	SiO2	TiO2	Al2O3	FeOT	MnO	MgO	CaO	Na2O	K2O	P2O5	H2O	CO2	F	S	Cl	Psat	Entrapment Depth	Host Olivine Fo	Ol added
units	wt. %	wt. %	wt. %	wt. %	wt. %	wt. %	wt. %	wt. %	wt. %	wt. %	wt. %	ppm	ppm	ppm	ppm	bars	km bsf	mol. %	wt. %
AL4597-5-01	50.9	1.39	14.6	10.50	0.19	7.82	11.9	2.33	0.15	0.14	0.25	565	190	1219	115	1196	3.4	83	0.4
AL4597-5-02	51.0	1.38	14.6	10.26	0.18	7.93	12.0	2.29	0.13	0.13	0.24	551	186	1228	92	1167	3.3	84	0.1
AL4597-5-03	51.2	1.40	13.9	11.80	0.19	7.58	11.3	2.30	0.10	0.13	0.22	475	162	1298	58	1013	2.8	81	1.4
AL4597-5-04	51.0	1.40	13.8	12.63	0.22	7.24	10.9	2.44	0.12	0.15	0.24	557	225	1262	86	1179	3.4	79	0.4
AL4597-5-05	51.1	1.41	14.7	10.02	0.18	7.85	12.1	2.31	0.14	0.13	0.22	550	180	1230	116	1165	3.3	84	-0.1
AL4597-5-06	50.4	1.45	14.1	10.77	0.20	8.39	12.2	2.07	0.11	0.12	0.22	547	198	1101	89	1159	3.3	84	3.8
AL4597-5-09	51.0	1.32	14.7	10.12	0.16	8.02	12.0	2.24	0.12	0.14	0.21	576	205	1221	91	1217	3.5	84	0.6
AL4597-5-10	51.1	1.42	14.8	10.10	0.21	7.77	12.0	2.22	0.16	0.10	0.22	558	197	1265	120	1180	3.4	84	0.1
AL4597-5-12	51.2	1.19	14.4	10.66	0.19	7.81	12.2	2.10	0.09	0.13	0.19	521	159	1162	54	1105	3.1	83	1.3
AL4597-5-14	50.0	1.21	15.9	9.25	0.18	8.21	12.5	2.38	0.10	0.11	0.20	543	127	1138	57	1149	3.3	85	0.8
AL4597-5-15	51.3	0.94	15.2	9.35	0.15	7.97	12.7	2.17	0.06	0.07	0.23	568	129	998	16	1200	3.4	85	0.5
AL4597-5-16	51.5	1.44	14.1	11.49	0.22	7.45	11.2	2.36	0.12	0.12	0.21	492	180	1325	62	1046	2.9	81	0.1
AL4597-5-17	51.0	1.07	14.5	10.18	0.19	8.22	12.6	2.05	0.09	0.12	0.20	516	149	1038	36	1095	3.1	84	2.3
AL4597-5-19	50.8	1.33	14.4	10.70	0.18	8.02	12.1	2.19	0.10	0.12	0.21	547	170	1123	36	1159	3.3	83	1.4
AL4597-5-20	51.3	1.30	14.7	10.00	0.20	7.86	12.0	2.32	0.13	0.12	0.201	552	210	1197	91	1168	3.3	84	0.1
AL4597-5-21	50.2	1.34	14.9	10.32	0.22	8.25	12.3	2.20	0.13	0.08	0.18	590	174	1040	87	1244	3.6	84	2.8
AL4598-8-01	50.9	1.29	14.4	10.6	0.19	7.98	12.1	2.22	0.14	0.07	0.24	583	175	1213	114	1231	3.5	83	0.5
AL4598-8-02	51.8	1.32	14.7	8.8	0.17	8.16	12.5	2.21	0.11	0.12	0.21	791	149	851	57	1642	5.0	86	3.2
AL4598-8-04	51.6	1.43	13.7	12.2	0.21	7.32	11.0	2.32	0.11	0.11	0.23	575	185	1256	58	1216	3.5	80	0.5
AL4598-8-06	51.6	1.15	14.5	9.8	0.19	7.84	12.5	2.10	0.09	0.10	0.22	570	159	1111	53	1204	3.4	84	1.3
AL4598-8-07	50.7	1.37	13.9	11.7	0.21	7.91	11.6	2.16	0.13	0.12	0.21	563	171	1174	100	1192	3.4	82	2.6
AL4598-8-09	50.9	1.52	14.1	11.6	0.21	7.47	11.4	2.30	0.16	0.15	0.21	546	229	1264	123	1156	3.3	81	0.1
AL4598-8-10	51.0	1.31	14.0	10.7	0.18	8.21	12.2	2.09	0.11	0.12	0.19	518	153	1022	58	1100	3.1	84	3.9
AL4598-8-11	50.5	1.48	14.1	12.1	0.21	7.57	11.4	2.28	0.15	0.15	0.23	536	238	1299	131	1138	3.2	81	0.5
AL4598-8-12	50.4	1.36	13.6	12.6	0.20	7.93	11.4	2.19	0.14	0.14	0.22	564	246	1265	124	1194	3.4	81	3.7
AL4598-8-15	50.9	1.31	14.1	11.0	0.19	7.79	12.2	2.15	0.13	0.12	0.23	427	173	1220	81	914	2.4	82	0.8
AL4598-8-16	51.3	0.99	15.0	8.9	0.16	8.40	13.0	2.00	0.09	0.10	0.20	570	116	1009	51	1205	3.5	86	2.5
AL4598-8-17	50.9	1.14	14.5	10.1	0.15	8.28	12.6	1.98	0.11	0.12	0.21	515	154	1112	65	1095	3.1	84	3.6
AL4598-8-18	49.4	0.93	15.6	10.1	0.15	8.41	13.1	2.03	0.07	0.07	0.22	743	144	905	19	1548	4.7	85	4.1
AL4598-8-19	51.3	1.59	14.4	10.3	0.22	7.57	11.8	2.34	0.14	0.16	0.22	524	197	1158	99	1111	3.1	83	0.1

Table 3.4. (continued) Melt inclusions corrected for post-entrapment crystallization, with corresponding saturation pressures and depths of entrapment

Sample	SiO2	TiO2	Al2O3	FeOT	MnO	MgO	CaO	Na2O	K2O	P2O5	H2O	CO2	F	S	Cl	Psat	Entrapment Depth	Host Olivine Fo	Ol added
units	wt. %	wt. %	wt. %	wt. %	wt. %	wt. %	wt. %	wt. %	wt. %	wt. %	wt. %	ppm	ppm	ppm	ppm	bars	km bsf	mol. %	wt. %
AL4598-11-05	50.3	1.14	14.4	10.3	0.20	8.92	12.4	1.93	0.10	0.10	0.24	170	156	1085	80	374	0.5	85	2.2
AL4598-11-06	50.2	1.28	14.7	10.1	0.18	8.95	12.2	2.04	0.11	0.11	0.25	152	161	1114	90	336	0.3	85	1.2
AL4598-11-07	49.7	1.25	14.2	10.6	0.17	9.39	12.5	1.86	0.10	0.10	0.22	136	167	1105	88	302	0.2	85	10.5
AL4598-11-08	50.8	1.22	14.8	9.8	0.15	8.48	12.3	2.11	0.11	0.11	0.25	147	151	1111	81	325	0.3	85	0.2
AL4598-11-09	50.6	1.15	14.9	9.8	0.16	8.45	12.6	2.03	0.10	0.10	0.25	432	152	1099	83	925	2.5	85	0.2
AL4598-11-10	50.8	1.26	14.3	10.1	0.16	8.85	12.1	2.09	0.10	0.12	0.20	151	136	1081	79	331	0.3	85	6.6
AL4598-11-11	49.7	0.98	14.4	10.5	0.18	9.22	13.0	1.75	0.08	0.11	0.22	477	153	1020	67	1016	2.8	85	4.8
AL4598-11-12	50.8	1.25	14.8	9.6	0.20	8.46	12.4	2.08	0.10	0.10	0.22	505	144	1088	83	1073	3.0	85	-0.1
AL4598-11-15	50.1	1.27	14.5	10.3	0.17	8.93	12.5	1.99	0.11	0.14	0.23	128	161	1099	88	284	0.0	85	1.7
AL4598-11-16	50.5	1.20	14.6	9.8	0.17	8.91	12.5	2.01	0.10	0.11	0.22	532	144	1027	55	1128	3.2	86	3.4
AL4598-11-17	50.6	1.15	14.5	10.5	0.17	8.45	12.4	2.06	0.07	0.08	0.24	493	148	1137	41	1050	2.9	84	1.7
AL4598-11-18	50.0	1.06	14.1	10.4	0.16	9.22	13.0	1.77	0.07	0.09	0.24	498	158	1028	56	1061	3.0	85	6.2
AL4598-11-20	50.3	1.06	14.5	10.0	0.17	8.97	12.9	1.85	0.08	0.07	0.23	497	156	1027	52	1058	2.9	86	3.1
AL4598-11-21	50.3	1.28	14.9	10.0	0.21	8.58	12.3	2.09	0.11	0.12	0.23	137	157	1114	88	303	0.2	85	-0.1
AL4598-11-22	50.8	1.28	14.8	9.85	0.18	8.60	12.1	2.15	0.10	0.07	0.222	467	162	1110	87	997	2.7	85	5.4
AL4598-11-23	50.8	0.87	15.5	8.0	0.17	8.82	13.6	1.90	0.04	0.05	0.22	367	98	885	11	788	2.0	88	0.4
AL4598-11-24	50.8	1.01	14.5	10.1	0.18	8.66	12.4	2.09	0.09	0.06	0.24	562	150	1023	47	1190	3.4	85	0.1
AL4599-3-01	50.0	1.25	14.1	10.8	0.16	9.09	12.4	1.91	0.08	0.12	0.18	507	153	1100	60	1078	3.0	85	8.2
AL4599-3-02	50.5	1.26	15.0	10.2	0.18	8.38	12.2	2.05	0.09	0.12	0.21	483	146	1139	65	1027	2.8	84	0.1
AL4599-3-03	50.2	1.23	14.3	10.6	0.17	8.93	12.4	1.90	0.09	0.11	0.19	475	155	1105	62	1012	2.8	85	4.4
AL4599-3-04	51.8	0.96	16.7	7.2	0.10	8.00	12.8	2.22	0.03	0.11	0.18	314	89	883	1	677	1.6	88	5.2
AL4599-3-05	50.8	0.87	14.7	10.0	0.19	8.36	13.0	1.95	0.03	0.05	0.19	311	73	994	3	671	1.6	85	1.0
AL4599-3-06	50.0	1.23	14.5	10.7	0.17	8.85	12.4	1.93	0.09	0.12	0.19	464	152	1109	66	989	2.7	84	5.1
AL4599-3-07	50.4	1.27	14.8	10.3	0.21	8.48	12.3	2.00	0.10	0.07	0.21	493	155	1154	66	1049	2.9	85	0.8
AL4599-3-08	51.1	1.31	13.8	11.0	0.20	8.48	11.8	2.17	0.07	0.10	0.20	532	162	1181	38	1129	3.2	84	6.5
AL4599-3-11	50.5	1.26	14.7	10.4	0.18	8.53	12.1	2.06	0.10	0.08	0.19	442	133	1162	60	943	2.5	84	0.7
AL4599-3-12	50.5	1.07	14.2	10.7	0.18	8.63	12.5	1.97	0.08	0.08	0.17	534	121	1060	35	1132	3.2	84	3.7
AL4599-3-14	50.6	1.28	14.9	10.2	0.23	8.36	12.1	2.09	0.10	0.11	0.21	144	142	1148	58	316	0.2	84	-0.1
AL4599-3-15	50.5	1.26	14.6	10.4	0.22	8.58	12.3	1.97	0.09	0.10	0.20	487	154	1124	63	1037	2.9	84	2.4
AL4599-3-16	50.5	1.25	14.4	10.6	0.21	8.59	12.1	2.11	0.09	0.10	0.19	498	151	1150	59	1058	2.9	84	3.1
AL4599-3-17	50.6	1.26	14.8	10.4	0.16	8.48	11.8	2.17	0.10	0.14	0.20	496	148	1156	63	1054	2.9	84	-0.1
AL4599-3-18	50.6	0.99	14.2	10.5	0.18	8.82	12.7	1.82	0.06	0.09	0.20	523	125	1009	29	1111	3.1	85	5.3
AL4599-3-19	50.5	1.26	14.6	10.5	0.20	8.39	12.1	2.06	0.11	0.10	0.21	495	145	1160	62	1053	2.9	84	0.5
AL4599-3-20	50.3	1.25	14.4	10.7	0.20	8.60	12.4	1.92	0.09	0.09	0.19	398	143	1073	52	852	2.2	84	2.4

Table 3.4. (continued) Melt inclusions corrected for post-entrapment crystallization, with corresponding saturation pressures and depths of entrapment

Sample	SiO2	TiO2	Al2O3	FeOT	MnO	MgO	CaO	Na2O	K2O	P2O5	H2O	CO2	F	S	Cl	Psat	Entrapment Depth	Host Olivine Fo	Ol added
units	wt. %	wt. %	wt. %	wt. %	wt. %	wt. %	wt. %	wt. %	wt. %	wt. %	wt. %	ppm	ppm	ppm	ppm	bars	km bsf	mol. %	wt. %
EW56D-01	50.6	1.39	14.6	10.7	0.21	8.03	11.9	2.21	0.12	0.10	0.24	438	181	1190	89	939	2.6	83	2.4
EW56D-03	50.6	1.08	15.6	9.9	0.15	7.88	12.3	2.15	0.10	0.12	0.25	400	156	1116	61	859	2.3	84	2.0
EW56D-05	51.2	1.44	14.6	10.6	0.19	7.57	11.5	2.42	0.15	0.14	0.26	468	184	1250	92	999	2.8	82	-0.2
EW56D-06	50.4	1.17	15.2	10.0	0.23	8.02	12.4	2.15	0.10	0.11	0.25	414	152	1149	61	888	2.4	84	3.2
EW56D-08	49.5	0.86	17.6	8.7	0.16	8.02	12.5	2.40	0.06	0.05	0.24	294	84	926	25	638	1.6	86	1.1
EW56D-10	50.4	1.39	14.3	11.3	0.20	8.09	11.8	2.20	0.11	0.11	0.22	127	168	1116	78	281	0.2	82	3.8
EW56D-11	50.3	1.15	15.5	10.7	0.20	7.75	11.9	2.23	0.10	0.10	0.25	407	154	1136	65	873	2.4	83	-0.5
EW56D-13	50.2	1.10	16.3	9.2	0.17	8.12	12.2	2.27	0.08	0.07	0.25	358	128	1096	53	773	2.0	85	1.8
EW56D-14	50.9	1.41	14.5	10.7	0.22	7.92	11.8	2.25	0.14	0.14	0.25	477	178	1251	91	1018	2.9	83	1.5
EW56D-16	50.3	1.35	14.0	11.5	0.18	8.22	12.1	2.07	0.11	0.15	0.22	258	81	863	20	562	1.3	82	5.4
EW56D-17	49.1	0.83	17.7	8.9	0.18	8.23	12.5	2.31	0.04	0.05	0.24	549	183	1186	82	1163	3.4	86	1.3
EW56D-19	50.8	1.47	14.6	11.0	0.22	7.62	11.7	2.29	0.13	0.13	0.23	422	176	1261	96	904	2.5	82	-0.3
EW56D-20	50.5	1.35	14.8	10.9	0.20	7.86	11.9	2.19	0.11	0.12	0.236	399	160	1178	80	857	2.3	83	1.9
EW56D-21	50.4	1.29	13.8	11.1	0.15	9.54	11.3	2.12	0.12	0.09	0.17	202	115	891	60	441	0.8	85	5.8
EW56D-22	50.9	1.35	14.6	10.9	0.18	7.81	11.7	2.26	0.13	0.11	0.24	273	176	1238	85	593	1.4	82	1.1

Table 3.5. Olivine compositions

Sample	spot	SiO2	FeO	NiO	MnO	MgO	CaO
units		wt. %	wt. %	wt. %	wt. %	wt. %	wt. %
AL4597-05-01	MI	39.4	15.9	0.166	0.247	44.1	0.274
AL4597-05-01	rim	39.3	15.7	0.145	0.246	44.1	0.283
AL4597-05-02	MI	39.4	15.4	0.180	0.239	44.4	0.267
AL4597-05-02	rim	39.2	15.2	0.165	0.236	44.2	0.281
AL4597-05-03	MI	38.9	17.7	0.130	0.282	42.3	0.269
AL4597-05-03	rim	39.1	17.8	0.127	0.274	42.2	0.247
AL4597-05-04	MI	38.5	19.2	0.133	0.289	40.9	0.266
AL4597-05-04	rim	39.2	15.5	0.155	0.239	44.0	0.282
AL4597-05-05	MI	39.3	15.3	0.173	0.233	44.5	0.278
AL4597-05-05	rim	39.5	14.9	0.172	0.232	44.8	0.268
AL4597-05-06	MI	39.2	15.5	0.169	0.242	44.4	0.264
AL4597-05-06	rim	39.0	15.2	0.154	0.237	44.2	0.280
AL4597-05-09	MI	39.2	15.1	0.192	0.234	44.4	0.257
AL4597-05-09	rim	38.7	15.0	0.181	0.237	44.0	0.254
AL4597-05-10	MI	39.1	15.5	0.169	0.236	44.0	0.266
AL4597-05-10	rim	39.1	16.1	0.137	0.249	43.8	0.281
AL4597-05-12	MI	39.3	15.7	0.127	0.253	42.7	0.655
AL4597-05-12	rim	39.3	14.8	0.161	0.230	44.8	0.267
AL4597-05-14	MI	39.4	13.7	0.205	0.210	45.2	0.293
AL4597-05-14	rim	39.3	15.6	0.167	0.243	44.2	0.280
AL4597-05-15	MI	39.4	14.3	0.191	0.217	45.3	0.284
AL4597-05-15	rim	39.4	14.2	0.184	0.227	44.9	0.275
AL4597-05-16	MI	38.9	17.7	0.129	0.263	42.6	0.259
AL4597-05-16	rim	39.0	15.9	0.151	0.249	43.6	0.286
AL4597-05-17	MI	39.1	14.9	0.152	0.232	44.5	0.281
AL4597-05-17	rim	38.9	15.9	0.130	0.247	43.5	0.275
AL4597-05-19	MI	39.2	15.8	0.146	0.242	43.9	0.269
AL4597-05-19	rim	39.4	15.0	0.156	0.230	44.3	0.289
AL4597-05-20	MI	39.3	15.2	0.200	0.235	44.1	0.268
AL4597-05-20	rim	38.7	15.2	0.199	0.238	43.2	0.257
AL4597-05-21	MI	39.8	15.2	0.171	0.231	44.8	0.278
AL4597-05-21	rim	39.1	15.1	0.153	0.237	44.1	0.289
AL4598-08-01	MI	39.2	15.6	0.170	0.251	43.5	0.278
AL4598-08-01	rim	39.4	15.7	0.168	0.249	43.6	0.258
AL4598-08-02	MI	39.8	13.4	0.191	0.212	46.0	0.254
AL4598-08-02	rim	39.9	13.5	0.187	0.212	45.7	0.255
AL4598-08-03	MI	39.1	15.5	0.165	0.240	43.6	0.271
AL4598-08-03	rim	38.9	15.0	0.145	0.234	43.7	0.299
AL4598-08-04	MI	38.8	18.5	0.120	0.277	41.4	0.255
AL4598-08-04	rim	39.4	16.6	0.139	0.261	43.0	0.281
AL4598-08-05	MI	39.2	15.7	0.164	0.247	43.7	0.273
AL4598-08-05	rim	39.5	14.9	0.156	0.233	44.3	0.285
AL4598-08-06	MI	39.0	14.9	0.150	0.226	43.9	0.301
AL4598-08-06	rim	39.5	15.0	0.160	0.231	44.4	0.269
AL4598-08-07	MI	39.0	17.1	0.129	0.258	42.7	0.267
AL4598-08-07	rim	39.3	15.4	0.150	0.246	43.8	0.289

Table 3.5. (continued) Olivine compositions

Sample	spot	SiO2	FeO	NiO	MnO	MgO	CaO
units		wt. %	wt. %	wt. %	wt. %	wt. %	wt. %
AL4598-08-08	MI	39.0	15.8	0.142	0.243	43.6	0.270
AL4598-08-08	rim	39.0	15.3	0.152	0.237	43.9	0.304
AL4598-08-09	MI	38.7	17.6	0.177	0.274	41.9	0.254
AL4598-08-09	rim	39.3	15.4	0.159	0.238	44.1	0.270
AL4598-08-10	MI	39.4	15.5	0.147	0.247	44.1	0.300
AL4598-08-10	rim	39.5	15.5	0.147	0.248	44.2	0.304
AL4598-08-11	MI	38.8	18.0	0.183	0.276	41.8	0.259
AL4598-08-11	rim	39.3	16.1	0.174	0.247	43.6	0.279
AL4598-08-12	MI	38.7	17.9	0.180	0.276	41.7	0.261
AL4598-08-12	rim	38.3	17.6	0.173	0.266	41.6	0.246
AL4598-08-15	MI	39.1	16.4	0.129	0.252	43.3	0.275
AL4598-08-15	rim	39.4	16.3	0.134	0.257	43.7	0.279
AL4598-08-16	MI	39.4	13.1	0.179	0.201	45.7	0.283
AL4598-08-16	rim	39.0	14.9	0.149	0.235	44.0	0.278
AL4598-08-17	MI	39.4	14.7	0.162	0.224	44.6	0.287
AL4598-08-17	rim	39.1	15.3	0.148	0.246	44.1	0.281
AL4598-08-18	MI	39.3	14.6	0.193	0.221	44.8	0.279
AL4598-08-18	rim	39.2	16.0	0.140	0.248	43.9	0.266
AL4598-08-19	MI	39.1	16.0	0.173	0.247	43.6	0.263
AL4598-08-19	rim	38.4	16.2	0.141	0.255	42.7	0.260
AL4598-08-20	MI	38.9	18.1	0.182	0.277	41.9	0.251
AL4598-08-20	rim	39.0	15.5	0.149	0.238	43.5	0.282
AL4598-11-01	MI	39.3	14.4	0.242	0.227	45.0	0.288
AL4598-11-01	rim	39.5	14.0	0.199	0.220	45.2	0.289
AL4598-11-02	MI	39.5	14.0	0.216	0.213	45.4	0.279
AL4598-11-02	rim	39.2	14.1	0.209	0.216	45.0	0.297
AL4598-11-05	MI	39.4	14.1	0.197	0.217	45.3	0.290
AL4598-11-05	rim	39.3	14.1	0.211	0.217	45.3	0.309
AL4598-11-06	MI	39.6	13.8	0.205	0.215	45.5	0.289
AL4598-11-06	rim	39.5	13.9	0.208	0.211	45.4	0.276
AL4598-11-07	MI	39.5	14.1	0.202	0.222	45.3	0.293
AL4598-11-07	rim	39.7	14.1	0.203	0.217	45.2	0.288
AL4598-11-08	MI	39.5	14.0	0.189	0.217	45.1	0.285
AL4598-11-08	rim	39.3	14.0	0.204	0.216	45.2	0.289
AL4598-11-09	MI	39.5	14.1	0.198	0.211	45.4	0.297
AL4598-11-09	rim	39.5	14.2	0.205	0.215	45.4	0.290
AL4598-11-10	MI	39.5	14.1	0.193	0.221	45.2	0.277
AL4598-11-10	rim	39.4	13.8	0.203	0.211	45.3	0.274
AL4598-11-11	MI	39.6	14.0	0.219	0.216	45.5	0.288
AL4598-11-11	rim	39.6	14.1	0.209	0.218	45.4	0.289
AL4598-11-12	MI	39.6	14.0	0.191	0.217	45.6	0.289
AL4598-11-12	rim	39.5	14.1	0.209	0.217	45.2	0.280
AL4598-11-15	MI	39.4	14.0	0.202	0.207	45.1	0.279
AL4598-11-15	rim	39.4	13.8	0.205	0.215	45.1	0.300
AL4598-11-16	MI	39.7	13.6	0.204	0.210	45.6	0.286

Table 3.5. (continued) Olivine compositions

Sample	spot	SiO2	FeO	NiO	MnO	MgO	CaO
units		wt. %	wt. %	wt. %	wt. %	wt. %	wt. %
AL4598-11-16	rim	39.6	13.8	0.196	0.214	45.2	0.284
AL4598-11-17	MI	39.4	14.9	0.176	0.226	44.7	0.272
AL4598-11-17	rim	39.4	14.6	0.197	0.217	44.7	0.299
AL4598-11-18	MI	39.6	13.9	0.193	0.214	45.6	0.289
AL4598-11-18	rim	39.7	14.0	0.195	0.221	45.6	0.273
AL4598-11-19	MI	39.4	13.6	0.211	0.204	45.2	0.292
AL4598-11-19	rim	39.5	13.9	0.207	0.210	45.1	0.292
AL4598-11-20	MI	39.3	13.6	0.194	0.209	45.2	0.284
AL4598-11-20	rim	39.4	13.8	0.204	0.212	45.3	0.290
AL4598-11-21	MI	39.5	14.3	0.210	0.218	45.4	0.284
AL4598-11-21	rim	39.4	14.2	0.213	0.222	45.2	0.305
AL4598-11-22	MI	39.7	14.1	0.195	0.221	45.4	0.276
AL4598-11-22	rim	39.6	14.1	0.202	0.219	45.5	0.290
AL4598-11-23	MI	40.2	11.6	0.214	0.182	47.6	0.305
AL4598-11-23	rim	40.3	11.9	0.209	0.189	47.5	0.284
AL4598-11-24	MI	39.5	14.3	0.186	0.227	45.2	0.295
AL4598-11-24	rim	39.5	14.2	0.201	0.216	45.4	0.280
AL4599-03-01	MI	39.6	14.6	0.195	0.213	44.7	0.263
AL4599-03-01	rim	40.1	14.3	0.206	0.219	45.2	0.290
AL4599-03-02	MI	39.5	14.7	0.172	0.224	44.8	0.270
AL4599-03-02	rim	39.2	14.5	0.192	0.222	44.2	0.293
AL4599-03-03	MI	39.1	14.3	0.186	0.209	44.5	0.257
AL4599-03-03	rim	39.0	14.1	0.194	0.212	44.6	0.275
AL4599-03-04	MI	39.6	11.5	0.204	0.184	47.0	0.285
AL4599-03-04	rim	38.5	13.6	0.198	0.199	43.9	0.260
AL4599-03-05	MI	39.5	14.4	0.170	0.222	45.0	0.285
AL4599-03-05	rim	39.6	14.5	0.194	0.225	45.1	0.273
AL4599-03-06	MI	39.3	14.7	0.204	0.220	44.7	0.263
AL4599-03-06	rim	39.3	14.5	0.194	0.219	45.0	0.276
AL4599-03-07	MI	39.4	14.6	0.203	0.223	45.0	0.265
AL4599-03-07	rim	39.6	14.8	0.180	0.223	45.2	0.271
AL4599-03-08	MI	39.4	15.6	0.149	0.243	44.2	0.279
AL4599-03-08	rim	39.7	14.4	0.193	0.218	45.3	0.279
AL4599-03-09	MI	39.3	14.6	0.192	0.222	44.6	0.266
AL4599-03-09	rim	39.5	14.3	0.191	0.217	44.9	0.274
AL4599-03-11	MI	39.3	14.6	0.183	0.228	44.6	0.266
AL4599-03-11	rim	39.3	14.5	0.190	0.222	44.5	0.270
AL4599-03-12	MI	38.9	14.8	0.154	0.229	44.1	0.282
AL4599-03-12	rim	39.4	14.7	0.165	0.229	44.5	0.258
AL4599-03-14	MI	39.3	14.6	0.188	0.224	44.7	0.267
AL4599-03-14	rim	39.3	14.5	0.194	0.220	44.5	0.275
AL4599-03-15	rim	39.4	14.5	0.191	0.221	44.8	0.253
AL4599-03-15	MI	39.7	14.5	0.193	0.225	44.9	0.279
AL4599-03-16	MI	39.3	14.8	0.166	0.228	44.4	0.268
AL4599-03-16	rim	39.3	14.2	0.185	0.212	44.8	0.267

Table 3.5. (continued) Olivine compositions

Sample	spot	SiO2	FeO	NiO	MnO	MgO	CaO
units		wt. %	wt. %	wt. %	wt. %	wt. %	wt. %
AL4599-03-17	MI	39.3	14.9	0.190	0.221	44.6	0.257
AL4599-03-17	rim	39.3	14.7	0.193	0.227	44.5	0.282
AL4599-03-18	MI	39.0	14.3	0.155	0.216	44.5	0.276
AL4599-03-18	rim	39.4	14.3	0.179	0.220	44.8	0.265
AL4599-03-19	MI	39.2	15.0	0.185	0.230	44.4	0.266
AL45990-3-19	rim	38.9	14.5	0.190	0.223	44.5	0.278
AL45990-3-20	MI	39.2	14.9	0.181	0.226	44.5	0.262
AL45990-3-20	rim	39.1	14.3	0.196	0.220	44.6	0.282
EW56D-01	MI	39.1	15.8	0.175	0.239	43.6	0.278
EW56D-01	rim	39.2	16.6	0.153	0.256	43.1	0.304
EW56D-02	MI	39.0	16.5	0.155	0.253	43.0	0.303
EW56D-02	rim	39.3	16.3	0.161	0.250	43.4	0.286
EW56D-03	MI	39.5	15.1	0.194	0.228	44.5	0.265
EW56D-03	rim	39.1	16.3	0.153	0.247	43.5	0.279
EW56D-04	MI	39.5	15.3	0.160	0.237	44.1	0.278
EW56D-04	rim	39.5	15.2	0.182	0.232	44.0	0.281
EW56D-05	MI	39.3	16.3	0.154	0.246	42.6	0.426
EW56D-05	rim	39.5	16.5	0.148	0.250	43.2	0.329
EW56D-06	MI	39.4	15.0	0.182	0.226	44.5	0.277
EW56D-06	rim	39.3	16.7	0.148	0.259	43.1	0.278
EW56D-07	MI	39.3	16.0	0.168	0.245	43.6	0.275
EW56D-07	rim	39.2	16.3	0.165	0.242	43.2	0.271
EW56D-08	MI	39.8	13.5	0.226	0.208	45.8	0.298
EW56D-08	rim	39.6	15.2	0.184	0.229	44.4	0.273
EW56D-10	MI	39.0	16.4	0.159	0.254	43.1	0.260
EW56D-10	rim	39.1	16.3	0.158	0.251	42.9	0.280
EW56D-11	MI	39.4	16.3	0.169	0.251	43.5	0.271
EW56D-11	rim	39.3	16.4	0.157	0.249	43.5	0.274
EW56D-13	MI	39.9	14.0	0.218	0.210	45.6	0.273
EW56D-13	rim	39.5	16.0	0.164	0.239	43.7	0.260
EW56D-14	MI	39.4	15.9	0.171	0.239	43.8	0.265
EW56D-14	rim	39.3	16.4	0.159	0.249	43.4	0.274
EW56D-16	MI	39.1	16.4	0.154	0.251	43.3	0.269
EW56D-16	rim	38.9	16.3	0.156	0.245	43.1	0.288
EW56D-17	MI	39.7	13.4	0.231	0.199	45.8	0.276
EW56D-17	rim	39.9	13.9	0.209	0.211	45.5	0.259
EW56D-18	MI	39.4	16.5	0.154	0.257	43.5	0.268
EW56D-18	rim	39.5	15.3	0.177	0.230	44.3	0.262
EW56D-19	MI	39.5	16.6	0.148	0.249	42.4	0.531
EW56D-19	rim	39.6	16.6	0.154	0.249	43.5	0.279
EW56D-20	MI	39.2	16.2	0.166	0.244	43.5	0.272
EW56D-20	rim	38.8	16.4	0.142	0.247	42.6	0.286
EW56D-21	MI	39.5	14.2	0.206	0.223	44.9	0.273
EW56D-21	rim	38.8	15.2	0.175	0.234	43.5	0.268
EW56D-22	MI	39.3	16.0	0.168	0.241	43.7	0.259
EW56D-22	rim	39.3	16.5	0.152	0.254	43.1	0.292

Table 3.6. Parameters used in calculation and interpretation of entrapment depths and probability density functions

Location	Sample	n	Bandwidth	BW method[b]	Peak depth	Approx. dist. from vent	Seismic melt lens depth	Seismic melt lens ref.
			km		km	m		
GSC 95°W: youngest	AL4598-08	14	0.42	2σ	3.4	170		
GSC 95°W: youngest	AL4597-05	17	0.42	2σ	3.3	140		
GSC 95°W: youngest composite	AL4598-08, AL4597-05	31	0.42	2σ	3.4	140-170		
GSC 95°W: intermediate	AL4598-11	17	0.70	S	3.0	560		
GSC 95°W: oldest	AL4599-3	19	0.42	2σ	3.0	400		
GSC 95°W: composite	AL4598-08, AL4597-05, AL4598-11, AL4599-03	67	0.42	2σ	3.3	--		
GSC 94.2°W	EW56D	16	0.43	S	2.6	--	3.9	Blacic et al. 2004
EPR 9°N[a]		90	0.34	S	1.6	--	1.6	Carbotte et al., 2013
EPR 12.8°N[a]		28	0.15	S	1.6	--	1.6	Detrick et al., 1987
JFR: Cleft[a]		8	0.41	S	--[c]	--	2.1	Canales et al., 2005
JFR: Vance[a]		37	0.52	S	3.4	--	2.6	Canales et al., 2005

a. Depths from Wanless and Shaw, 2012
b. Method for calculating bandwidth: S, Silverman (as described in Rudge, 2008); 2σ, 2σ uncertainty
c. Peak not included due to small sample size (8 inclusions)

Table 3.7. Parameters used in calculation of rates of magma supply along global mid-ocean ridge system

Ridge	Location	spreading rate	crustal thickness	rate of magma supply	spreading rate reference	crustal thickness reference
		mm/yr	km	10^6 m^3/yr/km		
Cocos-Pacific	ODP Site 1256	220	5.0-5.5	1.1-1.2	Wilson et al., 2006	Hallenborg et al., 2003
East Pacific Rise	14°S	138-141	6.0-6.3	0.8-0.9	DeMets et al., 2010	Grevemeyer et al., 1998
East Pacific Rise	17-18°S	140-144	4.8-5.7	0.7-0.8	DeMets et al., 2010	Canales et al., 1998
East Pacific Rise	18-20°S	140-145	4.8-5.7	0.7-0.8	DeMets et al., 2010	Canales et al., 1998
East Pacific Rise	9-10°N	100-105	5.5-6.1	0.5-0.6	DeMets et al., 2010	Van Avendonk et al., 2001
East Pacific Rise	12-13°N	92-97	5.0-6.0	0.5-0.6	DeMets et al., 2010	Barth & Mutter, 1996
Galapagos Spreading Center	92°W	54-57	7.0-7.6	0.4	DeMets et al., 2010	Canales et al., 2002
Galapagos Spreading Center	92.5°W	54-56	6.6-7.2	0.4	DeMets et al., 2010	Canales et al., 2002
Galapagos Spreading Center	94.2°W	52-55	5.7-6.3	0.3	DeMets et al., 2010	Canales et al., 2002
Galapagos Spreading Center	95°W	52-54	5.5-6.1	0.3	DeMets et al., 2010	Canales et al., 2002
Mid-Atlantic Ridge	Reykjanes Ridge, 57°43'N	20-21	6.8-8.3	0.1-0.2	DeMets et al., 2010	Navin et al., 1998
Mid-Atlantic Ridge	Lucky Strike Segment, 37°20'	23	6.5-8.0	0.1-0.2	DeMets et al., 2010	Seher et al., 2010
Juan de Fuca Ridge	Cleft Segment	49	5.0-7.0	0.2-0.4	DeMets et al., 2010	
Juan de Fuca Ridge	Vance Segment	50	5.0-7.0	0.3-0.4	DeMets et al., 2010	

Acknowledgments

We are grateful to the captain and crew of *R/V Atlantis* cruise AT15-63, and to the *Alvin* team for their expertise in collecting the samples from 95°W used in this study. We thank B. Monteleone for assistance operating the ion microprobe, E. Hellebrand for assistance with the electron microprobe, and G. Ito for fruitful discussions. Two anonymous reviews of an earlier version of the manuscript led to substantial improvements. This research was supported by NSF grant OCE08-49813, a Denise B. Evans Fellowship, and GSA graduate student research grant 10054-13.

CHAPTER 4. MAGMATIC PROCESSES AT VARIABLE MAGMA SUPPLY ALONG THE GALÁPAGOS SPREADING CENTER: CONSTRAINTS FROM INDIVIDUAL ERUPTIVE UNITS

4.1. Abstract

Petrologic study of individual eruptive units in two locations along the Galápagos Spreading Center provides insight into how magma supply affects mid-ocean ridge magmatic systems. Low- and high-magma supply study areas at 95°W and 92°W have similar spreading rates (53 and 55 mm/yr), but differ by 30% in the time-averaged rate of magma supply (0.3×10^6 and 0.4×10^6 m^3/km/yr) as a result of varying proximity to the Galápagos hotspot. Here, we use major and trace element analyses of glass and whole rock samples, major element analyses of mineral phases, and observations of rock microstructure to characterize parental magma variability, magma reservoir processes such as fractional crystallization and mixing, and timescales of magmatic recharge relative to eruption. At the low-magma-supply study area, where magma is thought to reside intermittently at ~3 km below the seafloor, lavas are restricted to relatively unfractionated melt compositions (6.2-9.1 wt. % MgO). Magmatic evolution at this location is likely dominated by processes involving crystal-rich mush, and preserved by limited evolution in melt-dominated magma reservoirs. Eruptions at this study area appear to be closely linked to magmatic recharge; relatively evolved eruptive units consistently have compositional trends controlled by mixing of high-MgO magma with lower-MgO magma with distinct parental magmas. In contrast, at the high-magma-supply study area, where a seismically imaged melt lens is located ~1.7 km below the seafloor, fractional crystallization within a melt-rich magma reservoir causes large variations in major-element compositions with little effect on trace element concentrations or ratios. Between magmatic recharge events, resident magma fractionates, and can be repeatedly tapped by low-volume fissure eruptions. Small bodies of magma may become isolated from the larger magmatic system, allowing more extreme degrees of fractionation. An important implication of this study is that persistent melt lenses at intermediate rates of magma supply need not be "steady-state" melt lenses. Only by documenting variations in

magma composition at a given location can the temporal variability in magma reservoir properties at the scale of multiple eruptive episodes be constrained.

4.2. Introduction

The dominant control on magma supply along mid-ocean ridges is spreading rate. Full spreading rates that vary from ~5 mm/yr to 145 mm/yr correspond to variations in magma supply from 0.03×10^6 to 0.87×10^6 m^3/km/yr, assuming a constant 6 km thickness of oceanic crust. Variations in spreading rate along the global mid-ocean ridge system are accompanied by well-documented variations in crustal structure and characteristics of the volcanic eruptions that build the extrusive section of the oceanic crust.

At fast-spreading ridges, volcanic eruptions are typically smaller in volume, but occur more frequently and at higher average effusion rates, than at slower spreading ridges (Bonatti & Harrison, 1998; Perfit & Chadwick, 1998; Sinton *et al.*, 2002). Seismic data suggest that a shallow, melt-rich lens overlies a larger, more continuous region of crystal-rich mush along much of the spreading axis at fast-spreading ridges (e.g., Sinton & Detrick, 1992; Dunn *et al.*, 2000; Carbotte *et al.*, 2013). Magma residence within shallow crustal magma reservoirs promotes fractional crystallization and homogenization of parental magma compositions, leading to the eruption of dominantly aphyric lavas with widely varying degrees of fractionation (e.g., Sinton & Detrick, 1992; Rubin & Sinton, 2007). With increasing degrees of fractional crystallization, the degree of compositional heterogeneity related to parental magma composition (e.g., variability of incompatible element ratios) decreases, indicating magma homogenization concurrently with fractionation (Rubin & Sinton, 2007). Eruptions typically occur along fissures oriented parallel to the axis, and may tap compositionally zoned magma reservoirs, indicating that along-axis mixing within the magma reservoir is limited (Sinton *et al.*, 2002; Bergmanis *et al.*, 2007; Rubin *et al.*, 2009; Goss *et al.*, 2010).

At lower spreading rates, seismic studies typically do not detect axial melt lenses, although low seismic velocities throughout the lower crust indicate the presence of small fractions of melt (e.g., Detrick *et al.*, 1990; Sinton & Detrick, 1992; Dunn *et al.*, 2005). Nevertheless, magma erupted at relatively slow-spreading ridges is typically not in equilibrium with mantle compositions, indicating that it was modified within the crust

(e.g., Stolper, 1980). It is unknown whether this modification occurs during magma ascent through crystal mush, or within melt lenses that are either too small, or too intermittent, to be seismically imaged (e.g., Sinton & Detrick, 1992; Kelemen & Aharanov, 1998). Because slow-spreading ridges appear to lack steady-state melt lenses containing eruptible magma, it has been suggested that eruptions should be more closely tied to magmatic recharge in this setting (Sinton & Detrick, 1992).

Variations in magma supply can also be decoupled from spreading rate variations. At spreading ridges affected by hotspots, elevated rates of magma supply result in the production of anomalously thick oceanic crust. For example, the proximity of the Icelandic plume to the Mid-Atlantic Ridge causes crustal thickness to increase from 7.5 km at 57°45'N (Navin *et al.*, 1998) to 11 km at 62°40'N (Weir *et al.*, 2001) and 19 km at 65°45'N (Staples *et al.*, 1997), and crustal thickness may reach 46 km at the peak of plume influence (Allen *et al.*, 2002); spreading rates remain relatively constant throughout this region at 18-20 mm/yr (DeMets *et al.*, 2010). Similarly, along the Galápagos Spreading Center (GSC), the influence of the Galápagos hotspot causes crustal thickness to increase from ~5.7 km at 97°W to ~7.9 km at 91.5°W (Canales *et al.*, 2002; Detrick *et al.*, 2002), whereas spreading rates vary only from 51 to 55 mm/yr (DeMets *et al.*, 2010). In contrast, anomalously thin crust is produced at ultra-slow spreading ridges (e.g., Gakkel Ridge (Jokat *et al.*, 2003), Mohns Ridge (Klingenhöfer *et al.*, 2000), Southwest Indian Ridge (Muller *et al.*, 1999)) and near fracture zones (e.g., Detrick *et al.*, 1993). Anomalously low magma supply rates in these regions have been attributed to greater conductive cooling of the upper mantle, terminating mantle melting at greater depths (e.g., Niu & Hekinian, 1997; White *et al*., 2001).

Petrologic and geochemical studies of sample suites from individual mid-ocean ridge eruptions can yield a more nuanced understanding of magmatic conditions and the nature of spatial and temporal variability in sub-ridge magmatic systems. At two locations along the GSC with contrasting rates of magma supply, we have previously used distinctions in sediment cover, flow morphology, flow direction, and sample composition to create geologic maps of lava flow fields emplaced during individual eruptive episodes (Colman *et al.*, 2012). By documenting the mineralogy, mineral textures and compositions, and major and trace element variations among samples from

individual eruptions at each study area, we now investigate magma reservoir processes and the nature and timescales of magmatic recharge relative to eruption. At each location, we assess the relative importance of fractionation, magma mixing, crustal assimilation, and magmatic recharge in controlling erupted compositions. In particular, the eruption-scale approach allows us to document whether and how these processes vary along-axis and through time.

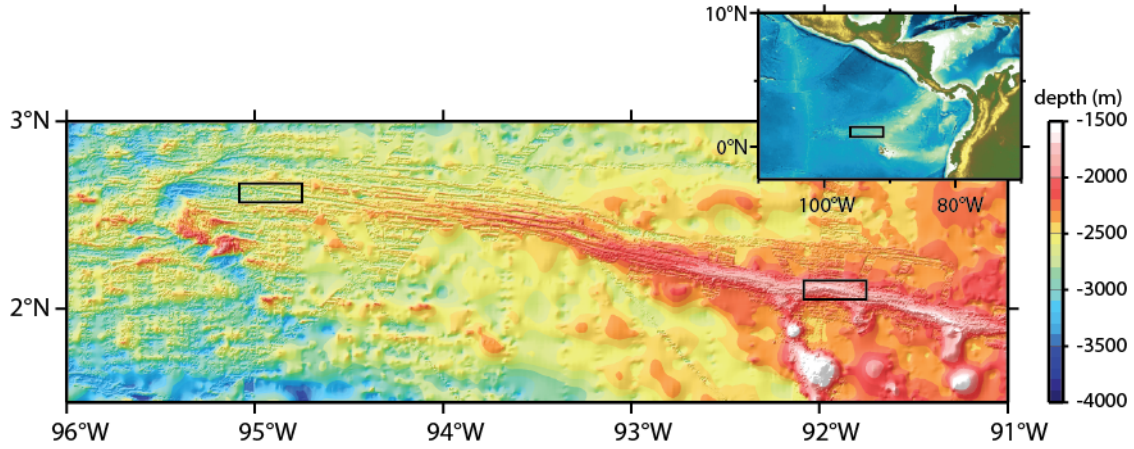

Figure 4.1. Bathymetry of western GSC, 91°-96°W (compilation of multibeam and satellite-derived bathymetry from Ryan *et al.*, 2009). Note eastward shoaling and development of axial rise spreading center morphology with proximity to the Galápagos hotspot. Maximum plume influence is observed from 91.3-92.3°W (Canales *et al.*, 2002). Black rectangles mark locations of detailed study areas. Inset, location of GSC in eastern equatorial Pacific Ocean.

4.3. Geologic setting: Galápagos Spreading Center

The GSC is an east-west-trending, intermediate-spreading-rate ridge in the eastern equatorial Pacific Ocean (Fig. 4.1). Seafloor spreading along the GSC began ~25 Ma (Hey *et al*., 1977), and has been strongly influenced by the presence of the Galápagos hot spot, which is located ~200 km to the south of the ridge near 91.5°W (e.g., Wilson & Hey, 1995). The average rate of magma supply to the crust (calculated as the product of the spreading rate and crustal thickness, after Sinton *et al.* (2003)) increases with proximity to the hotspot, from 0.26×10^6 m^3/km/yr at 97°W to 0.46×10^6 m^3/km/yr at 91°W. The increase in the rate of magma supply is indicated by thicker crust near the hotspot (Canales *et al.*, 2002), which is accompanied by shallower axial depths (Canales *et al.*, 2002), a shallower and stronger seismic melt lens reflector (Blacic *et al.*, 2004), and a transition in spreading center morphology from an axial valley to an axial high as the hotspot is approached (Sinton *et al.*, 2003).

Geochemical and isotopic variations along the western GSC show increasing enrichments of elements that are incompatible during mantle melting with proximity to the hotspot, as well as more radiogenic Sr and Pb isotope ratios, and less radiogenic Nd and Hf isotope ratios (Schilling *et al.*, 1982, 2003; Cushman *et al.*, 2004; Ingle *et al.*, 2010). These variations were attributed to mixing of varying amounts of depleted and enriched mantle end-members by Schilling *et al.* (1982, 2003). In contrast, Cushman *et al.* (2004) and Ingle *et al.* (2010) attributed these variations to lower mean extents of mantle melting near the hotspot caused by a deep zone of low-degree hydrous melting. Superimposed on variations in parental magma composition along the length of the GSC are variations in the degree of fractionation reached prior to eruption (as indicated for example by MgO content or magnitude of Sr anomaly in glass samples), with greater and more variable degrees of fractionation occurring near the hotspot (Schilling *et al.*, 1982; Cushman *et al.*, 2004; Ingle *et al.*, 2010). In addition, local variations in mantle melting and magmatic differentiation (Christie & Sinton, 1981; Schilling *et al.*, 1982; Sinton *et al.*, 1983; Christie & Sinton, 1986; Rotella *et al.*, 2009) are found in association with propagating rifts along the GSC.

4.4. Detailed study areas

This study uses samples from detailed study areas at 92°W and 95°W (Fig. 4.2) collected during the Galápagos Ridge Undersea Volcanic Eruptions Expedition in 2010 (Colman *et al.*, 2012). The 92°W study area is typical of relatively high-magma-supply regions of the GSC, with thick crust (Canales *et al.*, 2002), axial rise morphology (Sinton *et al.*, 2003), and a shallow, seismically imaged melt lens located ~1.7 km below the seafloor (Blacic *et al.*, 2004). In contrast, the spreading axis at 95°W is located within a ~300-m deep axial graben (Sinton *et al.*, 2003), and seismic studies at that location have not detected melt lens reflectors (Blacic *et al.*, 2004). However, depths of magma residence prior to the last three eruptions in this region were 3-3.4 km below the seafloor, based on saturation pressures of olivine-hosted melt inclusions (Colman et al., submitted manuscript).

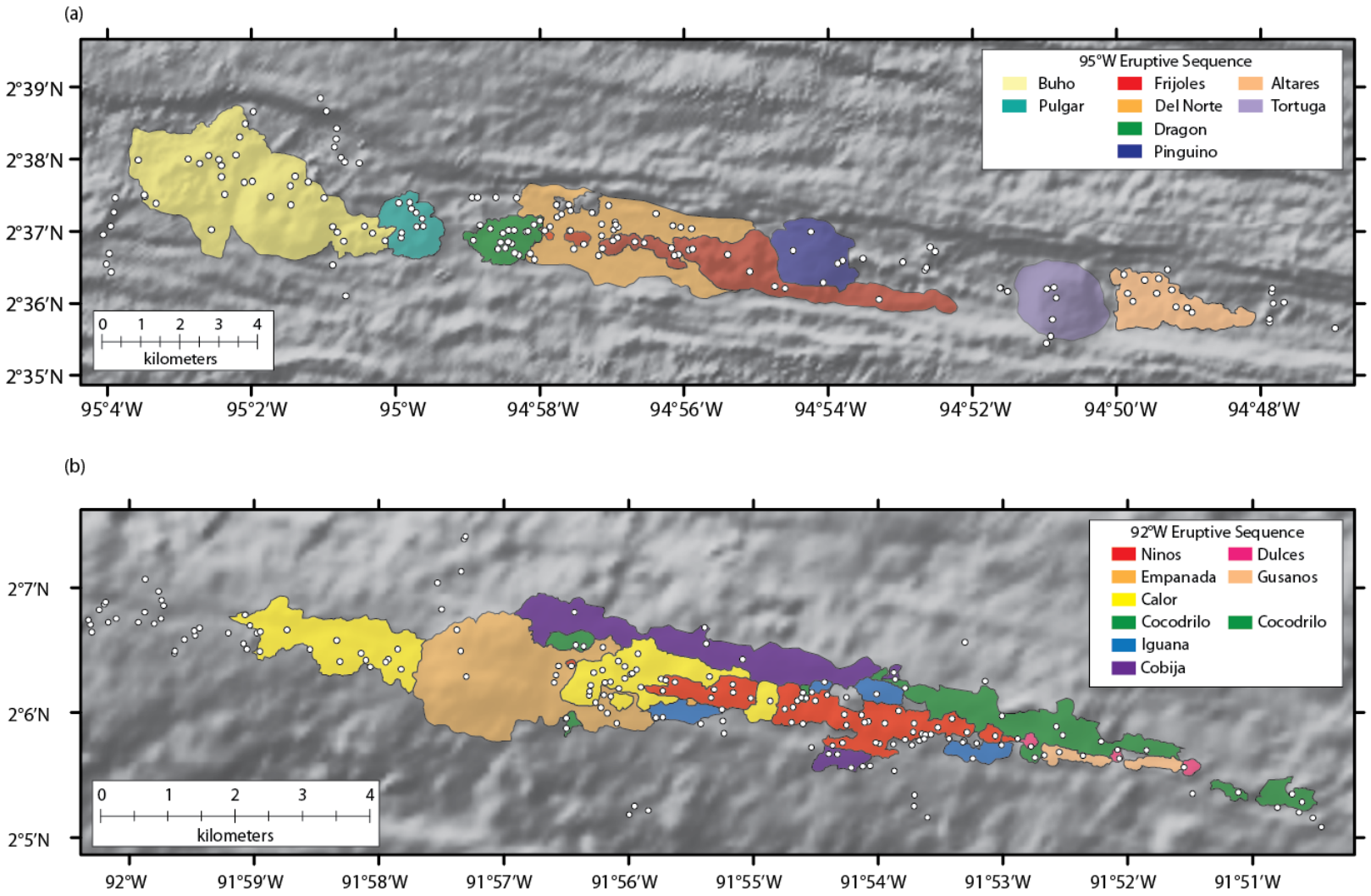
(a)
95°W Eruptive Sequence
Buho
Pulgar
Frijoles
Del Norte
Dragon
Pinguino
Altares
Tortuga
0 1 2 3 4
kilometers
2°39′N
2°38′N
2°37′N
2°36′N
2°35′N
95°4′W
95°2′W
95°W
94°58′W
94°56′W
94°54′W
94°52′W
94°50′W
94°48′W
(b)
92°W Eruptive Sequence
Ninos
Empanada
Calor
Cocodrilo
Iguana
Cobija
Dulces
Gusanos
Cocodrilo
0 1 2 3 4
kilometers
2°7′N
2°6′N
2°5′N
92°W
91°59′W
91°58′W
91°57′W
91°56′W
91°55′W
91°54′W
91°53′W
91°52′W
91°51′W

Figure 4.2. (Previous page.) Mapped eruptive units within detailed study areas at (a) 95°W, the low-magma-supply study area and (b) 92°W, the high-magma-supply study area. Relative ages of flow fields at each study area are given in legends. Eruptive units from Colman *et al*., 2012.

Within each study area, Colman *et al.* (2012) used visual observations, high-resolution bathymetry data, and sample compositions to map the most recently erupted lava flow fields. These datasets provide information about relative ages (as indicated by superposition, sediment cover, and fault density), eruption characteristics (as indicated by identification of vents, flow structures, and lava morphology), and parental magma compositions. Each mapped flow field comprises lavas that are similar in age, define coherent compositional trends, and were erupted from a spatially related set of vents (Colman *et al.*, 2012). We focus here on subsets of the eight best mapped and sampled eruptions from each study area, among which the relative age relationships are known; comparisons to the full sample set from each segment place these eruptions within the context of the region. More detailed descriptions of each flow field and the constraints on their relative ages are given in Colman *et al.* (2012).

4.4.1. Low-magma-supply study area, 95°W

In the central region of the low-magma-supply study area, a sequence of four eruptive units display diverse eruptive styles. The most recent eruption in this region emplaced the Frijoles flow field, a discontinuous chain of pillow mounds centered within the axial graben. The heights and volumes of the mounds increase towards 94°55'W, where eruptive activity apparently focused; the smallest mound rises less than 10 m above the surrounding seafloor, whereas the largest is ~250 m tall. The previous eruption emplaced the Del Norte flow field, which was erupted from a fissure to the north of the inner axial graben; lava flowed to the south and ponded within the inner axial graben via a series of channels and inflated flows. At its western edge, Del Norte overlies part of the relatively small and somewhat older Dragón pillow mound, which is centered within the inner axial graben. To the east of Del Norte and Frijoles is the Pinguino seamount. Pinguino is older than Del Norte, and likely also predates Dragón based on relative sediment cover, but the lack of contact relationships between Pinguino and Dragón precludes a definitive determination of relative ages. This eruptive sequence likely

represents several thousand years of eruptive activity at this location (Colman *et al.*, 2012).

Petrological data on four other eruptive units from this study area are included here although their ages relative to the central sequence are unknown. To the west, the Buho seamount and associated smaller pillow mounds comprise the most recent eruptive unit. An older cluster of pillow mounds make up the Pulgar flow field, which is located between Buho and Dragón. To the east of Pinguino is the Altares flow field, a cluster of pillow mounds that is somewhat elongate parallel to the spreading axis. An older seamount, Tortuga, lies immediately to the west of Altares.

4.4.2. High-magma-supply study area, 92°W

At the relatively high-magma supply study area, we focus on eight flow fields erupted over the last several hundred years (Bowles *et al.*, 2014). Active high-temperature hydrothermal vents and diffuse flow in this region attest to its continued activity at the time the samples were collected. The most recent eruption in this region emplaced the Niños flow field. Sheet flows associated with this eruption were likely erupted early in the eruption, and are overlain by a narrow pillow ridge that stretches 6.1 km discontinuously along axis. The previous eruption emplaced the Empanada flow field, which includes sheet flows, in addition to a pillow mound that is the largest eruptive edifice in the region. To the east and west of Empanada are the older Calor pillow ridges. Three other eruptive units have been partially buried by more recent eruptions and are exposed farther off-axis; in order of increasing age, these are Cocodrilo, Iguana, and Cobija.

Farther to the east, two other eruptive units appear to be relatively recent. The Gusanos flow field consists of two small pillow ridges, roughly centered on axis. Three small pillow mounds make up the Dulces flow field, also roughly centered on axis; these mounds appear to be slightly younger than Gusanos. Although direct contacts have not been observed among these eastern flow fields and the Niños, Calor, or Empanada flow fields to the west, all are known to be younger than the Cocodrilo flow field. Gusanos also is likely younger than Calor, based on the relative amounts of faulting within these flow fields.

A geomagnetic paleointensity study indicates that the Niños, Empanada, and Calor flow fields were all erupted 50-200 years ago, whereas Cobija is significantly older (~400 years old) (Bowles *et al.*, 2014). Because Dulces and Gusanos are stratigraphically younger than Cocodrilo, and Cocodrilo is younger than Cobija, the complete sequence of eight flow fields at this location must have been erupted in the last ~400 years (Bowles *et al.*, 2014).

4.5. Methods

Electron microprobe (EMP) analyses of major and minor elements from 331 glass samples were published in Colman *et al.* (2012). A representative subset of samples from each study area was selected for x-ray fluorescence (XRF) and inductively-coupled, plasma mass spectrometry (ICP-MS) analyses (84 and 43 samples, respectively). Cl contents of 26 glass samples were determined by EMP analysis. Major elements of mineral phases (olivine, plagioclase, and clinopyroxene, where present) were analyzed by EMP in selected samples from several of the eruptive units at each study area.

4.5.1. Petrography

Modal mineralogy reported in Table 4.1 is based on 1000-point counts on thin sections of a subset of samples from each study area. Mineral grains counted were ≥ 0.1 mm in size; smaller grains were counted as groundmass. Mineral modes are reported as dense rock equivalents (DRE) on a vesicle-free basis; vesicle content is reported separately. Petrographic descriptions of each thin section are provided in the supplementary material.

4.5.2. Whole-rock major and trace element analyses

Forty-one samples from 95ºW and 43 samples from 92ºW were selected for whole-rock analysis using the University of Hawai‘i Siemens 303AS XRF spectrometer. Selected samples include 2-11 samples per eruptive unit, chosen to encompass the major element compositional range of each major eruptive unit, as well as samples that lacked glassy rinds for EMP analysis. Whole rocks were crushed using a tungsten carbide-plated hydraulic rock splitter. Rock chips were then washed in distilled water and dried. Macroscopically fresh rock chips were picked, avoiding chips with alteration, rinds, and

large mineral grains, and powdered in an alumina mill. Major elements were analyzed on fused disks following methods described in Norrish & Hutton (1969), and trace elements were analyzed on pressed pellets, following methods similar to those of Chappell (1991). Reproducibility for this instrument with these methods is reported by Sinton *et al.* (2005). The dataset is provided in the supplementary material.

Table 4.1. Modal mineralogy of representative samples, based on 1000-point counts

		Phase abundances (% DRE)				
Eruptive Unit	Sample	Ol	Plag	Cpx	Groundmass	Vesicles (%)
Frijoles	AL4597-03	4.3	18.8	3.2	73.7	6.5
Frijoles	AL4597-05	1.4	9.6	2.3	86.7	0.6
Frijoles	AL4597-06	1.4	4.5	1.2	92.9	1.8
Frijoles	AL4597-08a	1.5	5.7	1.0	91.8	1.1
Frijoles	AL4597-08b	1.8	6.5	0.8	90.8	2.0
Frijoles	AL4598-01	2.5	13.9	4.1	79.5	0.5
Frijoles	AL4598-08	1.8	10.2	2.8	85.1	1.4
Altares	AL4594-02	2.4	14.1	2.5	81.1	2.7
Altares	AL4594-03	0.4	11.5	2.7	85.5	2.4
Altares	AL4594-04	3.5	11.1	1.1	84.3	1.6
Altares	AL4594-11	3.6	15.4	0.3	80.7	3.7
Buho	AL4603-13	0.6	0.8	0.0	98.6	1.0
Buho	AL4604-02	2.6	2.3	0.0	95.1	0.2
Buho	AL4604-03	3.0	2.9	0.0	94.1	6.4
Del Norte	AL4598-11	0.7	1.6	0.0	97.7	1.3
Del Norte	AL4599-08	2.0	5.0	0.0	93.0	1.2
Del Norte	AL4599-10	1.4	5.5	0.0	93.1	0.3
Dragon	AL4599-03	0.5	7.7	0.0	91.8	2.4
Dragon	AL4600-13	0.3	3.7	0.0	95.9	1.3
Pulgar	AL4604-07	1.3	12.0	0.1	86.6	0.6
Pulgar	AL4604-10	4.7	9.7	1.1	84.5	1.3
Tortuga	AL4593-05	1.7	11.0	0.0	87.3	1.6
Calor	AL4606-09	1.2	4.7	0.8	93.3	10.0
Dulces	AL4610-01	0.1	3.3	1.4	95.2	6.5
Dulces	AL4613-02	0.8	9.4	5.4	84.3	2.5
Dulces	AL4613-04	1.0	2.4	0.7	95.8	6.1
Gusanos	AL4612-02	3.7	11.0	0.0	85.3	7.6
Empanada	AL4616-02	0.7	5.9	1.8	91.5	1.8
Ninos	AL4609-02	0.0	0.0	0.0	100.0	0.6
Ninos	AL4609-09	0.0	0.0	0.0	100.0	6.1
Ninos	AL4609-11	0.2	2.4	0.0	97.4	6.6

4.5.3. Glass chlorine analyses

A subset of 26 glass samples, 21 of which were from 92ºW, was selected for Cl analysis by EMP at the University of Hawai‘i. Five points were analyzed per sample;

results were averaged. Peak and background counting times were 30 seconds each. Analyses were performed at an accelerating voltage of 15 keV, 20 nA beam current, and 10 μm beam diameter. A fluor-apatite standard (USNM 104021) was used for calibration. Reproducibility (2σ) based on repeat analyses of basaltic glass standard VG2 is 16% relative. One sample (AL4598-08) that had previously been analyzed for Cl by ion microprobe was reanalyzed for comparison; results are consistent within analytical precision. Analyses are presented in Table 4.2.

Table 4.2. Analyses of chlorine in glass samples

	Eruptive Unit	Cl (ppm)
4594-03	Altares	160
4594-11	Altares	150
4597-05	Frijoles	60
4598-08	Frijoles	90
4598-08	Frijoles	70
4598-11	Del Norte	70
4599-03	Dragon	50
4603-09	Buho	140
4604-03	Buho	160
4607-06	Empanada	890
4608-04	Empanada	880
4609-02	Ninos	1060
4609-09	Ninos	1080
4610-01	Dulces	1490
4610-09	Iguana	970
4611-08	Ninos	1000
4612-02	Gusanos	320
4612-06	Gusanos	340
4612-07	Dulces	1290
4613-02	Dulces	1260
4613-04	Dulces	1470
4614-03	Cocodrilo	490
4616-02	Empanada	1030
4616-14	Calor	590
4616-17	Cobija	410
4617-06	Lobo del Mar	560
4617-10	Calor	910
4618-04	Lagarto	240
4618-09	Lobo del Mar	500
4618-12	Lagarto	220

4.5.4. Glass trace element analyses

A subset of 2-4 samples per eruptive unit (totaling 21 samples from 95ºW and 22 from 92ºW) was selected for additional trace element analyses by ICP-MS using the University of Hawai‘i VG Element 2 mass spectrometer. Macroscopically fresh and

aphyric glass chips were picked under a stereomicroscope. Samples were washed in a sonic bath and rinsed in alcohol and distilled water. Glass chips were then dissolved in a 1:2 HF:HNO_3 solution and dried to a paste, then dissolved in 6 N HCl and dried, then dissolved in 8 N HNO_3 and dried three times, and finally dissolved in 1.5N HNO_3. Calibration was performed using rock standards BIR-1, BCR-1, and BHVO-1 at the beginning and end of each run. B, In, Tl, and Bi internal standards were used to correct for in-run drift. An in-house standard (Hawaiian basalt K1919) was run after every five samples, and was used to normalize the compositions of samples run on different days. Average values of BHVO-1 (run as an unknown) are compared with accepted values in Table 4.3; representative analyses from each study area are presented in Table 4.4. The entire dataset is provided in the supplementary material.

4.5.5. Mineral chemistry

Major and minor elements (Si, Fe, Mn, Mg, Ca, Ni) of olivine crystals were analyzed by electron microprobe at the University of Hawai‘i. Peak counting times were 100 seconds for Si, Ni, Mg, and Ca; 60 seconds for Mn; and 30 seconds for Fe. Background counting times were 90 seconds for Si, Ni, Mg, and Ca; 60 seconds for Mn; and 30 seconds for Fe. The analytical conditions for the runs (accelerating voltage of 20 keV, 200 nA beam current, and 10 μm beam diameter) generate high-precision measurements of the analyzed elements. Samples were calibrated using mineral standards San Carlos olivine (Si, Fe, Ni, Mg), Kakanui augite (Ca), and Verma garnet (Mn). San Carlos and Springwater olivine standards were run as unknowns repeatedly to monitor instrumental drift. Average values for the Springwater olivine and San Carlos olivine are compared with accepted values from Jarosewich *et al.* (1980) in Table 4.5. Ten olivine crystals were analyzed in each of 18 thin sections (13 from 95°W; five from 92°W). In most cases, three points near the crystal's core and two points near the rim were analyzed. Rim and core compositions presented in the supplementary material are averages of the rim and core analyses within each crystal, respectively. In analyses of highly skeletal olivines, we do not differentiate between cores and rims.

Table 4.3. Comparison of ICP-MS analyses of BHVO-1 standard with preferred values from GeoReM (Jochum *et al.*, 2007)

	Mean (n=5)	Std. Dev.	Acc. Val
Li	4.7	0.3	4.6
Sc	32	2	31
Cr	304	31	287
Co	45	3	45
Ni	119	10	118
Rb	9.2	0.5	9.2
Sr	394	18	396
Y	27	1	26
Zr	174	8	174
Nb	19.0	0.6	18.6
Cs	0.10	0.01	0.10
Ba	132	5	133
La	15.6	0.4	15.5
Ce	38.2	0.5	38.1
Pr	5.43	0.08	5.42
Nd	25.0	0.6	24.7
Sm	6.18	0.17	6.12
Eu	2.06	0.05	2.09
Gd	6.71	0.52	6.33
Tb	0.97	0.05	0.96
Dy	5.35	0.16	5.31
Ho	0.99	0.04	0.98
Er	2.58	0.13	2.55
Tm	0.34	0.01	0.33
Yb	1.98	0.08	2.00
Lu	0.28	0.007	0.27
Hf	4.45	0.09	4.46
Ta	1.19	0.08	1.21
Pb	2.01	0.09	2.4
Th	1.20	0.04	1.23
U	0.42	0.02	0.41

Table 4.4. Representative trace element analyses of glass from each study area, by ICP-MS.

	Buho AL4601-05	Dragon AL4600-13	Frijoles AL4597-08	Calor AL4616-14	Dulces AL4613-04	Gusanos AL4612-06	Ninos AL4611-08
Li	5.9	5.2	5.7	6.5	13.9	6.1	9.5
Sc	40.6	36.9	40.1	39.9	27.2	38.7	36.2
Cr	335	265	152	58	21	228	30
Co	46	37	38	40	26	39	39
Ni	136	88	59	42	14	67	25
Rb	2.8	1.6	2.8	10	21	7	13
Sr	99	64	78	151	134	151	140
Y	34.4	26.6	32.2	37.7	82.6	33.3	60.0
Zr	95	58	78	135	328	119	221
Nb	5.3	2.8	5.1	15.4	28.7	11.5	22.3
Cs	0.03	0.02	0.03	0.10	0.21	0.08	0.14
Ba	30	16	30	108	186	77	133
La	4.5	2.5	4.1	9.8	22.2	8.5	15.4
Ce	12.2	7.0	10.9	22.9	53.7	19.9	36.2
Pr	1.98	1.16	1.73	3.27	7.41	2.95	5.11
Nd	10.3	6.2	9.2	15.4	35.6	14.4	24.8
Sm	3.41	2.28	3.14	4.52	9.99	4.18	7.24
Eu	1.20	0.83	1.12	1.50	2.93	1.44	2.21
Gd	4.61	3.39	4.36	5.49	11.48	5.27	8.83
Tb	0.83	0.62	0.74	1.01	2.14	0.93	1.59
Dy	5.68	4.23	5.26	6.22	13.50	5.84	9.81
Ho	1.21	0.94	1.12	1.33	2.84	1.23	2.10
Er	3.68	2.77	3.45	3.86	8.44	3.57	6.06
Tm	0.56	0.42	0.53	0.58	1.29	0.53	0.92
Yb	3.51	2.67	3.23	3.99	8.70	3.42	6.27
Lu	0.53	0.41	0.51	0.57	1.27	0.52	0.91
Hf	2.50	1.62	2.28	3.37	8.01	3.19	5.50
Ta	0.27	0.34	0.26	1.00	1.53	0.80	1.41
Pb	2.48	0.27	0.38	0.78	1.69	0.76	1.14
Th	0.39	0.22	0.39	1.04	2.54	0.87	1.61
U	0.11	0.06	0.10	0.28	0.68	0.24	0.43

Table 4.5. Mineral EMP standard data: averages, accepted values, reproducibility.

Mineral EMPA standard analyses (all values given in wt. %)

San Carlos Olivine, USNM 111312				**Springwater Olivine, USNM 2566**		
	average	accepted	std dev, n=42	average	accepted	std dev, n=43
SiO_2	40.6	40.81	0.4	39.4	38.95	0.4
FeO	9.52	9.55	0.03	16.60	16.62	0.06
NiO	0.371	0.37	0.002	0.001	--	0.001
MnO	0.136	0.1	0.002	0.307	0.30	0.003
MgO	49.3	49.42	0.1	43.6	43.56	0.1
CaO	0.072	<0.05	0.002	0.000	<0.05	0.000

Diopside-2 (UCLA)				**Kakanui Augite, USNM 122142**		
	average	accepted	std dev, n=23	average	accepted	std dev, n=23
SiO_2	55.4	55.27	0.3	50.0	50.73	0.2
TiO_2	0.05	0.06	0.01	0.88	0.74	0.02
Al_2O_3	0.038	0.05	0.004	8.63	8.73	0.04
Cr_2O_3	0.006		0.005	0.16	0.15	0.01
FeO*	0.89	0.94	0.03	6.2	6.34	0.1
MnO	0.07	0.10	0.01	0.14	0.13	0.01
MgO	18.7	18.29	0.1	16.36	16.65	0.06
CaO	24.86	25.47	0.07	15.72	15.82	0.06
Na_2O	0.06	0.05	0.01	1.29	1.27	0.01
K_2O	0.002		0.001	0.00	0.00	0.00

Lake County Labradorite, USNM 115900				**Great Sitkin Island Anorthite, USNM 137041**		
	average	accepted	std dev, n=25	average	accepted	std dev, n=25
SiO_2	51.3	51.25	0.2	43.9	44.00	0.1
CaO	13.3	13.64	0.1	19.1	19.09	0.1
Al_2O_3	30.8	30.91	0.1	36.0	36.03	0.1
FeO*	0.39	0.45	0.02	0.46	0.62	0.01
Na_2O	3.71	3.45	0.07	0.52	0.53	0.02
MgO	0.10	0.14	0.01	0.010	<0.02	0.004
K_2O	0.117	0.18	0.004	0.008	0.03	0.004

Major and minor elements of plagioclase crystals (Si, Al, Fe, Mg, Ca, Na, K) were analyzed by electron microprobe at the University of Hawai‘i. Peak and background counting times were 50 seconds for Ca, Fe, and K; 30 seconds for Al and Mg; and 20 seconds for Si and Na. Analyses were performed using a 10 μm beam diameter, 15 keV accelerating voltage, and 10 nA beam current. Samples were calibrated using mineral standards anorthite (Si, Ca, Al); San Carlos olivine (Fe, Mg), and orthoclase (K). Two plagioclase standards were run as unknowns repeatedly to monitor instrumental drift. Average values for the Lake County labradorite standard (USNM 115900) and Great Sitkin Island anorthite standard (USNM 137041) are compared with accepted values from Jarosewich *et al.* (1980) in Table 4.5. Ten plagioclase crystals were analyzed in each of 12 thin sections (seven from 95°W; five from 92°W). In most cases, three points near the crystal's core and two points near the rim were analyzed. Rim and core compositions presented in the supplementary material are averages of the rim and core analyses within each crystal, respectively.

Major and minor elements (Si, Ti, Al, Cr, Fe, Mn, Mg, Ca, Na, K) of clinopyroxene crystals were analyzed by electron microprobe at the University of Hawai‘i. Peak and background counting times were 30 s for all elements. Analyses were performed using a 10 μm beam diameter, 15 keV accelerating voltage, and 15 nA beam current. Samples were calibrated using mineral standards diopside (Si), sphene glass (Ti), Kakanui augite (Al, Ca), chromite (Cr, Mg), Verma garnet (Fe, Mn), Amelia albite (Na), and orthoclase (K). Diopside and Kakanui augite standards were run as unknowns throughout the analyses to monitor instrumental drift. Average values for the Kakanui augite standard are compared with accepted values from Jarosewich *et al.* (1980) in Table 4.5. Ten clinopyroxene crystals were analyzed in each of ten thin sections (seven from 95°W; three from 92°W). In most cases, three points near the crystal's core and two points near the rim were analyzed. Rim and core compositions presented in the supplementary material are averages of the rim and core analyses within each crystal, respectively.

4.6. Results

4.6.1. Variations at each study area in the context of regional trends

Previously published major, minor, and trace element data for samples collected along the western GSC at ~ 9 km intervals between 91°W and 98°W (Cushman *et al.*, 2004; Ingle *et al.*, 2010) allow us to place samples from each study area in the context of compositional variations along the entire western GSC.

4.6.1.1. Major elements

Samples from 95°W have higher average, and less variable MgO (6.2-9.1 wt. %) than samples from 92°W (2.7-8.2 wt. %) (Fig. 4.3). FeO* (total Fe as FeO) and incompatible minor elements (TiO_2, Na_2O, K_2O, P_2O_5) increase and Al_2O_3 decreases with decreasing MgO. CaO increases with decreasing MgO until clinopyroxene joins the fractionating assemblage at ~7.9 wt. % at 95°W and ~7.4 wt. % MgO at 92°W. Below ~4 wt. % MgO, SiO_2 increases and FeO* and TiO_2 decrease with decreasing MgO. These trends are generally consistent with a crystallization sequence in which Ca-rich clinopyroxene joins olivine and plagioclase at 7.4 or 7.9 wt. % MgO, followed by Fe-Ti oxides at 4 wt. % MgO (Fig. 4.3). MgO contents decrease throughout this crystallization sequence, so that lower MgO contents correspond to greater degrees of fractionation.

Lavas sampled at both study areas are predominantly basalts, with 47-52 wt. % SiO_2. Samples with greater than 12 wt. % FeO* and 2 wt. % TiO_2, classified as Fe-Ti basalts (Byerly *et al.*, 1976), are more abundant at the high-magma-supply study area, consistent with greater average degrees of fractionation at that location (Colman *et al.*, 2012). Several basaltic andesites were also sampled at the high-magma-supply study area, though not at the low-magma-supply study area (Colman *et al.*, 2012).

Cushman *et al.* (2004) classified GSC samples as N-MORB, T-MORB, and E-MORB on the basis of K/Ti and K_2O, where N-MORB have K/Ti < 0.09, E-MORB have K/Ti > 0.15 and K_2O > 0.25 wt. %, and T-MORB are intermediate between the two groups. E-MORB compositions were only sampled east of 92.7°W, and T-MORB were only sampled east of 95.7°W (Cushman *et al.*, 2004). Although major element variations within each of these groups follow the same general trends, E-MORB have lower SiO_2

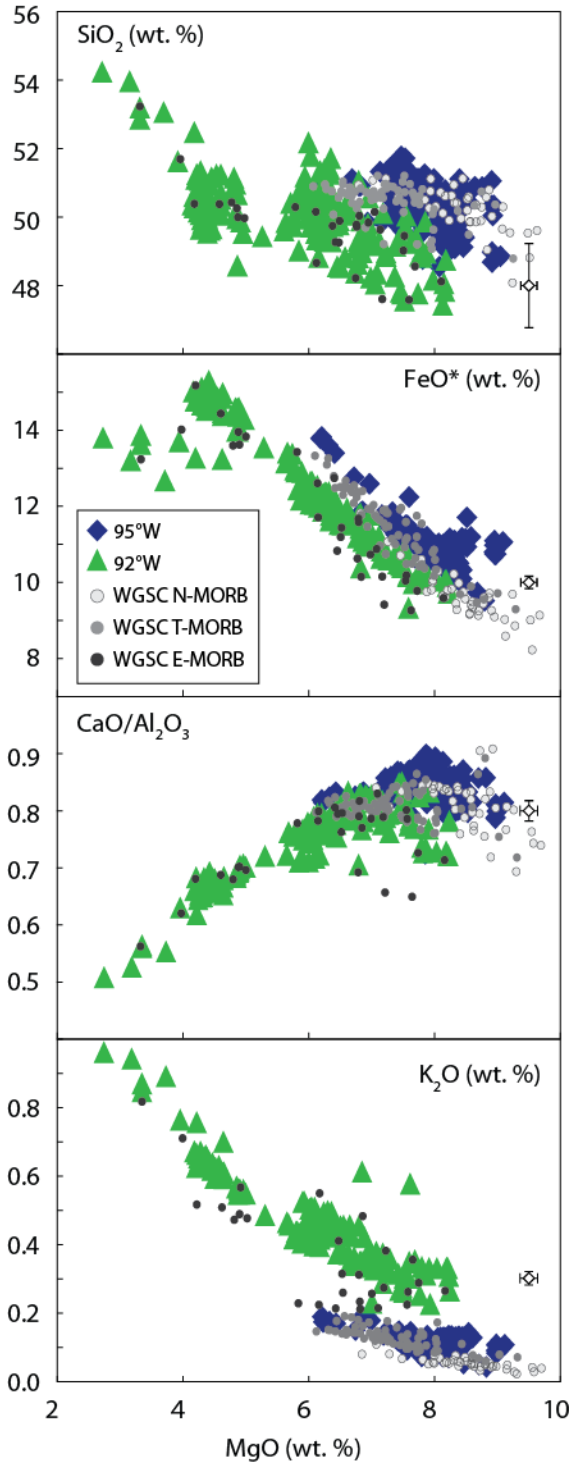

Figure 4.3. Major and minor element variations in glass samples, determined by EMP analysis. Samples from the high-magma-supply study area (triangles) have lower SiO_2 and FeO*, and higher K_2O and other incompatible elements at a given MgO content than those from the low-magma-supply study area (diamonds). There is also more variation in MgO at the high-magma-supply study area. Major element trends are generally consistent with fractionation sequences in which olivine and plagioclase are followed by Ca-rich clinopyroxene at ~7.9 wt. % MgO at 95°W, and at ~7.4 wt. % MgO at 92°W, causing observed decreases in CaO/Al_2O_3. Glass compositions of E-MORB, T-MORB, and N-MORB from the WGSC are shown for reference (data from Cushman *et al*., 2004). Analytical uncertainty (±2σ) based on repeat analyses of VG2 standard.

and FeO*, and greater Al_2O_3 and incompatible element contents at a given MgO (Fig. 4.3). Cushman *et al.* (2004) attributed these compositional differences to differences in the average extent of mantle melting, with lower extents of melting producing E-MORB. Ca-rich clinopyroxene begins to crystallize at progressively lower MgO in N-MORB, T-MORB, and E-MORB, shifting the maximum in CaO/Al_2O_3 to lower MgO (Fig. 4.3).

The compositions of samples within each of our study areas accord with the geographic distribution of compositional groups determined by Cushman *et al.* (2004), i.e., nearly all the samples collected at 95°W are T-MORB (some are N-MORB), whereas all samples from 92°W are E-MORB. E-MORB typically have the largest range in MgO, extending to values < 3 wt. %.

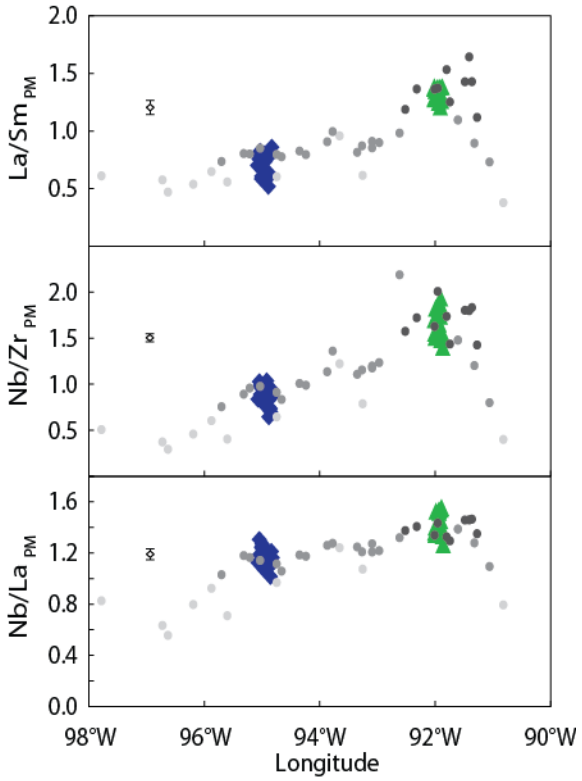

Figure 4.4. Along-axis variations in incompatible trace element ratios, comparing variability within each study area (this study) to compositions of samples along the western GSC (data from Ingle *et al.*, 2010). Symbols as in Figure 4.3. Analyses by ICP-MS on glass samples. Analytical uncertainty (±2σ) based on repeat analyses of BHVO-1 standard.

4.6.1.2. Trace elements

Ratios of highly to moderately incompatible elements are elevated at the high-magma-supply study area relative to those from the low-magma-supply study area, consistent with the regional study of Ingle *et al.* (2010) and the relative abundances of N-, T-, and E-MORB at the two study areas (Fig. 4.4). Samples are also more enriched in incompatible elements at a given MgO content at the high-magma-supply study area

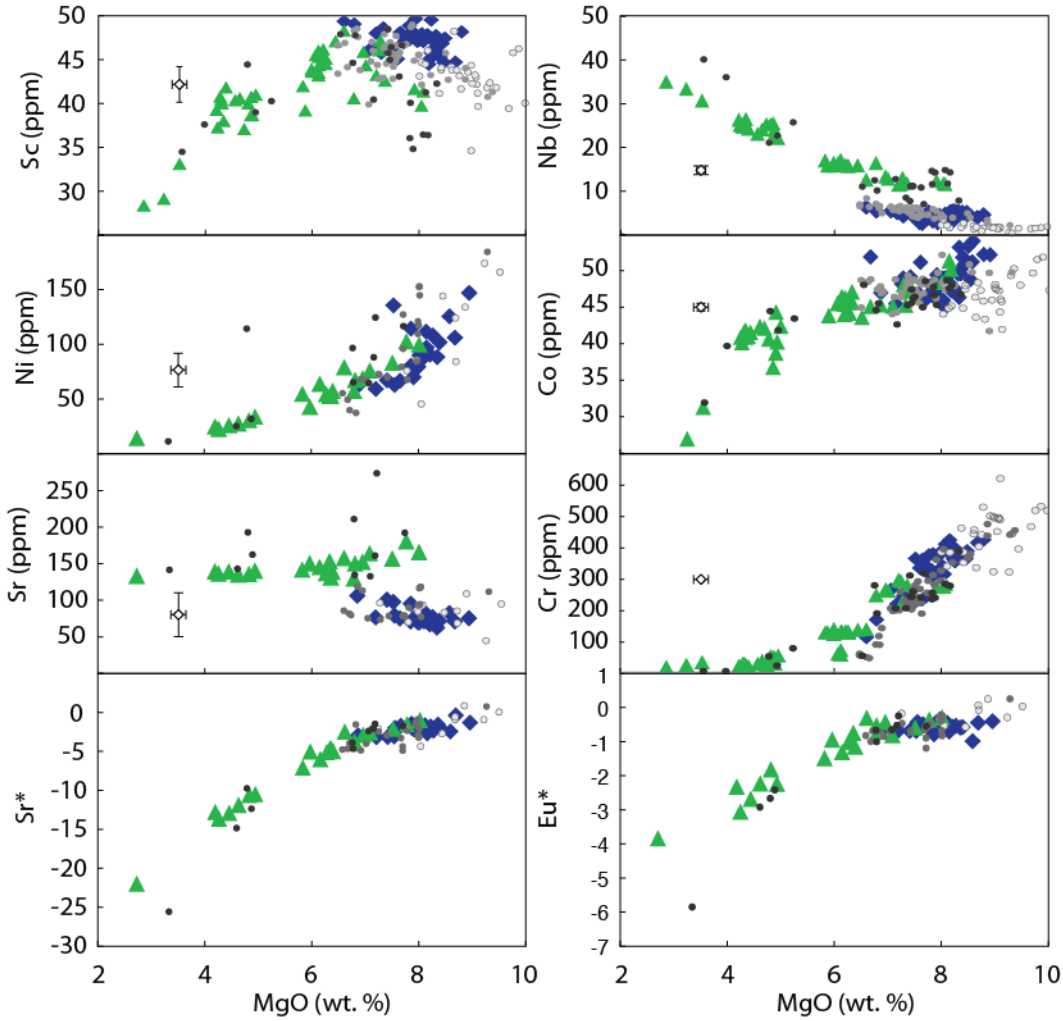

Figure 4.5. Trace element variations with MgO in each study area and in samples collected along the western GSC (data from Ingle *et al.*, 2010). Symbols as in Figure 4.3. Nb, Sc, Cr, and Co were analyzed by XRF on whole-rock powders; Ni and Sr were analyzed by ICP-MS on glass chips. Concentrations of Nb and other incompatible trace elements are elevated in samples from 92°W relative to samples from 95°W at a given MgO content, and increase with decreasing MgO. There is a maximum in Sc at ~7.5 wt. % MgO. Ni decreases with decreasing MgO. Sr is elevated in samples from 92°W, consistent with incompatible behavior during mantle melting. Sr concentrations decrease, and Sr anomalies (Sr_{PM}-(Pr_{PM}+Nd_{PM})/2) become increasingly negative, with decreasing MgO. Analytical uncertainty (±2σ) based on repeat analyses of BHVO-1 standard.

(Fig. 4.5). At both study areas, the transition metals Cr and Ni decrease with decreasing MgO; Co is relatively constant until oxides begin to crystallize, and there is a maximum in Sc at ~7.5 wt. % MgO (Fig. 4.5). High-field-strength elements, alkali and alkaline earth trace elements, and rare earth elements (REEs) generally behave incompatibly, increasing in concentration with decreasing MgO. Exceptions are Sr and Eu; Sr

concentrations decrease and Eu and Sr anomalies ($Sr^* = Sr_{PM}-(Pr_{PM}+Nd_{PM})/2$; $Eu^* = Eu_{PM}-(Sm_{PM}+Gd_{PM})/2$) become increasingly negative with continuing plagioclase fractionation at decreasing MgO at the high-magma-supply study area (Fig. 4.5).

4.6.1.3. Petrography and mineral chemistry

Samples are generally more crystal-rich and contain larger crystals at the low-magma-supply study area, consistent with regional trends along the GSC (Behn *et al.*, 2004), although nearly aphyric lava flows (<1 % crystals) have been erupted at both locations (Table 4.1) (McClinton *et al.*, submitted manuscript). Samples with > 7.9 wt. % MgO are generally olivine ± plagioclase-phyric (Fig. 4.6). Clinopyroxene is present in samples with < 6.8 wt. % MgO at 92°W, and in samples with < 7.9 wt. % MgO at 95°W, generally consistent with observations from the liquid lines of descent (Fig. 4.3).

Olivine rim compositions span a wider range at the high-magma-supply study area, extending to lower forsterite contents (Fo_{66}-Fo_{86} at 92°W; Fo_{80}-Fo_{85} at 95°W), consistent with the greater range in MgO of lavas at 92°W (Fig. 4.7). The forsterite content of olivine rims at each study area is generally consistent with that predicted to be in equilibrium with the carrier melt (Roeder & Emslie, 1970) (Fig. 4.7a). At the low-magma-supply study area, both normally and reversely zoned olivine crystals are

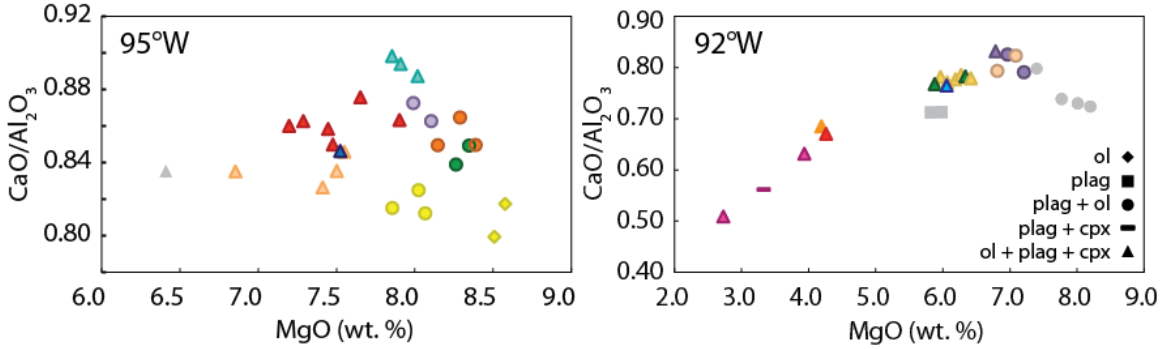

Figure 4.6. Mineral phases present in thin sections of samples from 95°W and 92°W. Colors correspond to eruptive units within each study area, as in Fig. 4.2. Gray symbols are from samples not assigned to one of the described eruptive units. Symbol shapes indicate mineral phases present. Olivine only, diamonds; plagioclase only, squares; plagioclase + olivine, circles; plagioclase + clinopyroxene, bars; plagioclase + clinopyroxene + olivine, triangles.

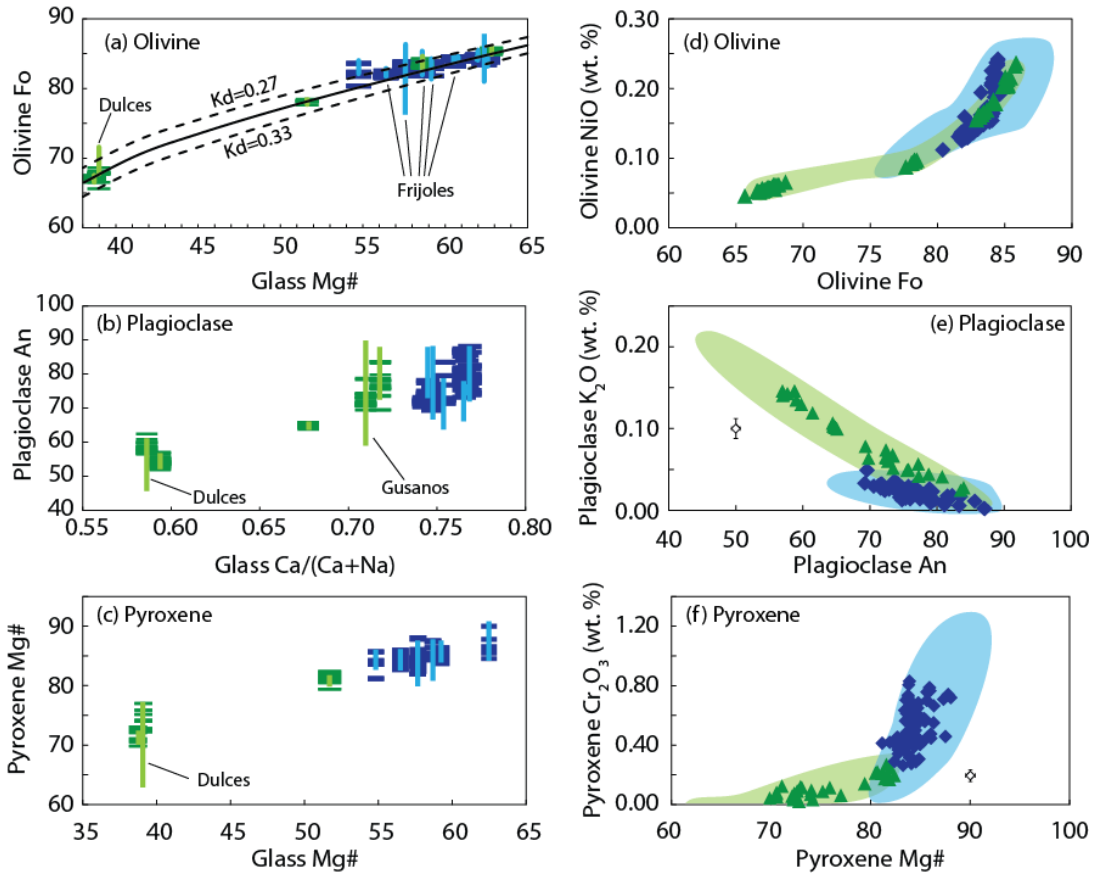

Figure 4.7. Compositions of olivine, plagioclase, and pyroxene crystals in samples from both study areas. Blue, 95°W; green, 92°W. Left panel compares mineral compositions to those of carrier melts (glass analyses from Colman *et al.*, 2012). Horizontal bars are individual analyses of crystal rims; vertical lines span the range of core compositions within each sample. (a) Forsterite content of olivine and Mg# ($Mg/(Mg+Fe^{2+})$, assuming melt Fe^{2+}/Fe^{T}=0.85 (Cottrell & Kelley, 2011) of coexisting glass; equilibrium olivine composition predicted by model of Roeder & Emslie (1970) for the Kd (molar $(Fe_{ol}/Mg_{ol})/(Fe_{liq}/Mg_{liq})$) values shown, indicated by black solid and dashed lines. (b) Anorthite content of plagioclase and Ca/(Ca+Na) of coexisting glass. (c) Mg# of pyroxene and coexisting glass. Partitioning of Fe in pyroxene between Fe2+ and Fe3+ according to the Lindsley (1983) model. Right panel, mineral minor element compositions as a function of mineral composition. Triangles, 92°W rims; diamonds, 95°W rims. Shaded fields indicate range of compositions measured in cores from each study area. Analytical uncertainty (±2σ) based on repeat analyses of mineral standards; analytical uncertainty for NiO and Fo in olivine plots is significantly smaller than symbol size.

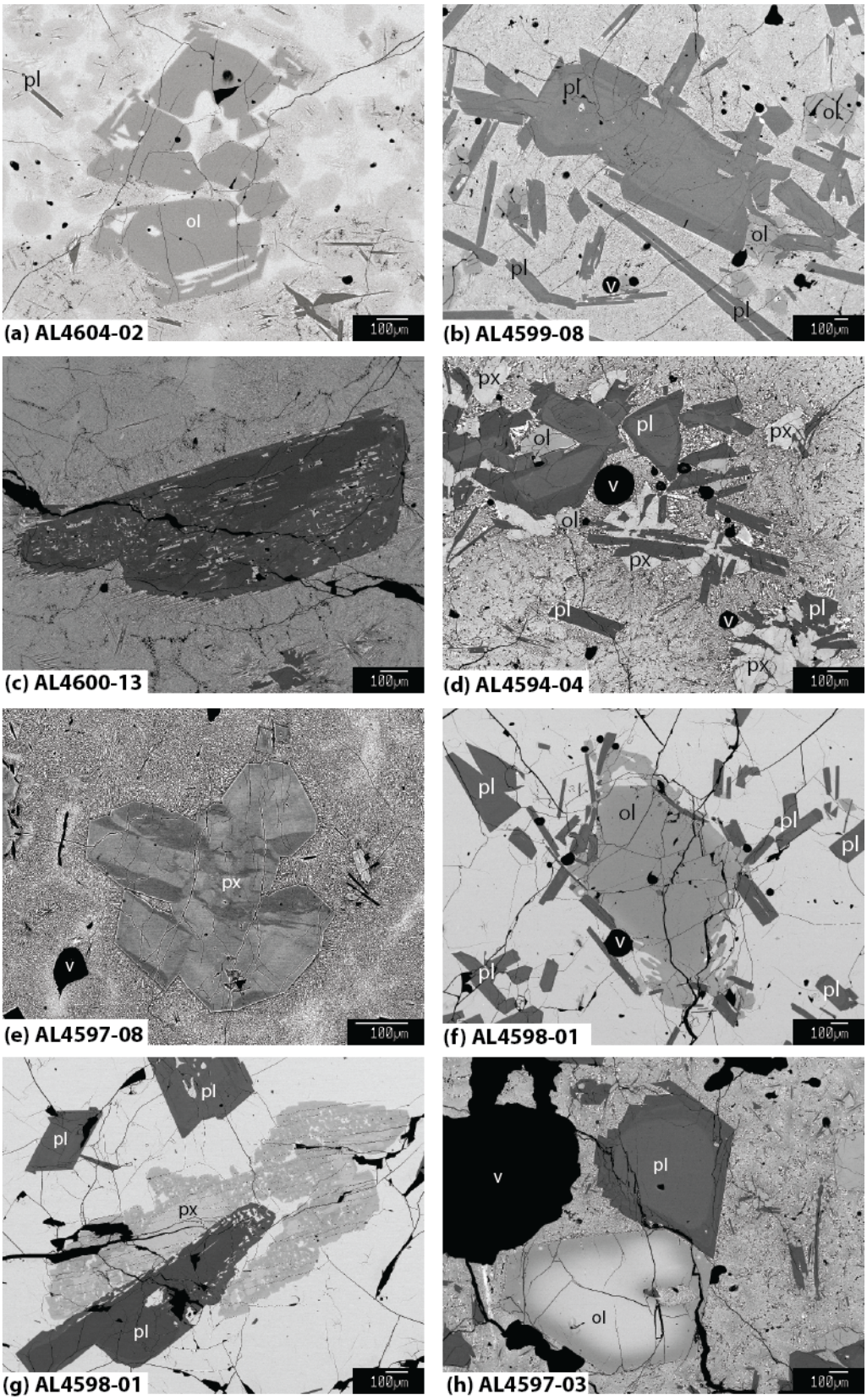
pl
ol
100μm
(a) AL4604-02
pl
ol
ol
pl
v
pl
100μm
(b) AL4599-08
100μm
(c) AL4600-13
px
ol
pl
px
v
ol
px
pl
v
pl
px
100μm
(d) AL4594-04
px
v
100μm
(e) AL4597-08
pl
ol
pl
pl
v
pl
pl
100μm
(f) AL4598-01
pl
pl
px
pl
100μm
(g) AL4598-01
v
pl
ol
100μm
(h) AL4597-03

Figure 4.8. (Previous page.) Mineral textures observed in thin sections (backscattered electron images) from low-magma-supply samples. (a) Skeletal olivine phenocrysts and plagioclase laths in glassy matrix (Buho). (b) Normally and oscillatory-zoned plagioclase and unzoned olivine in glassy matrix (Del Norte). (c) Reversely zoned, sieve-textured plagioclase with dendritic overgrowths (Dragón). (d) Intergrowths of plagioclase, sector-zoned pyroxene, and less abundant olivine (Altares). (e) Sector-zoned pyroxene (Frijoles). (f) Large, skeletal, normally zoned olivine phenocryst and smaller, blocky plagioclase (Frijoles). (g) Reversely zoned plagioclase and pyroxene with skeletal overgrowths (Frijoles). (h) Reversely zoned olivine and normally zoned plagioclase (Frijoles).

common, and morphologies range from skeletal to euhedral (Fig. 4.8). In contrast, olivine crystals within most eruptive units at the high-magma-supply study area are essentially unzoned, and typically have skeletal morphologies, locally intergrown with lath-shaped plagioclase crystals (Fig. 4.9).

Like olivine, plagioclase rim compositions are more variable, and range to more evolved compositions (lower An content), at the high-magma-supply study area (An_{53}-An_{89} at 92°W; An_{69}-An_{87} at 95°W) (Fig. 4.7b,e). At a given anorthite content, plagioclase at the high-magma-supply study area has greater K_2O, consistent with higher K/(Ca+Na) in E-MORB glasses at 92°W (Fig. 4.7e). At both study areas, plagioclase occurs with variable morphology ranging from blocky to tabular to lath-shaped (Fig. 4.8). Oscillatory zoned plagioclase also occur at both study areas, although not in every eruptive unit.

Pyroxene composition and morphology are highly variable at both study areas, and correlate less well with lava composition (Fig. 4.7c). Some pyroxenes exhibit concentric zoning (both normal and reversely zoned pyroxenes occur at both study areas); in these crystals, Mg-rich zones are relatively enriched in Cr and depleted in Ti, Al, and Fe. Other crystals are sector zoned (Fig. 4.8, 4.9); in these crystals, zones that are high in Mg are typically high in Fe, and low in Ti and Al.

4.6.2. Variations within individual eruptive units at 95°W

4.6.2.1. Compositional variations

Limited compositional variation (0.2-1.0 wt. % MgO) occurs within each of the well-sampled eruptive units at 95°W (Colman *et al.*, 2012). Because the incompatible element ratio K/Ti remains nearly constant during low to moderate degrees of fractional crystallization of basaltic magma, the range of K/Ti from ~0.07 to 0.14 at 8.5 wt % MgO

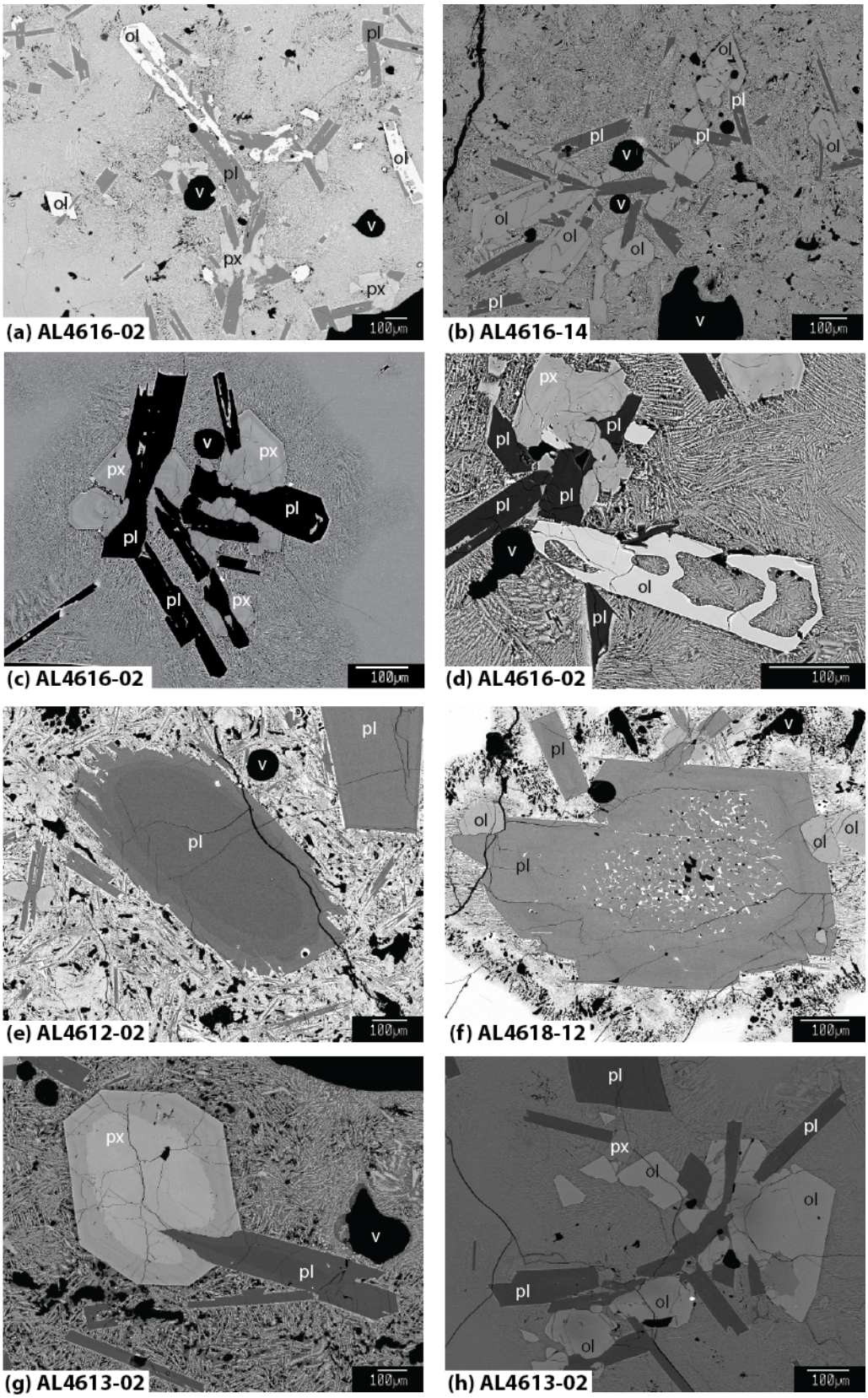
ol
pl
v
px
100µm
(a) AL4616-02
(b) AL4616-14
(c) AL4616-02
(d) AL4616-02
(e) AL4612-02
(f) AL4618-12
(g) AL4613-02
(h) AL4613-02

Figure 4.9. (Previous page.) Mineral textures observed in thin sections (backscattered electron images) from high-magma-supply samples. (a) Intergrowth of plagioclase, clinopyroxene, and skeletal olivine in glassy matrix (Empanada). (b) Intergrowth of plagioclase and olivine (Calor). (c) Intergrowth of oscillatory-zoned clinopyroxene and plagioclase (Empanada). (d) Intergrowth of plagioclase, clinopyroxene, and skeletal olivine (Empanada). (e) Reversely zoned plagioclase with dendritic overgrowth (Gusanos). (f) Large, blocky plagioclase with sieve-textured core. (g) Reversely zoned plagioclase and pyroxene (Dulces). (h) Intergrowth of normally zoned olivine and plagioclase (Dulces).

among the eruptive units requires a range of different parental magmas (i.e., melting conditions and/ or source compositions) feeding this segment (Fig. 4.10). Eruptive units with elevated K/Ti also have elevated Nb/Zr and La/Sm (Fig. 4.10). In addition to having distinct incompatible element ratios at the same high MgO, Dragón, Buho, and Del Norte also have different CaO and FeO* contents (Fig. 4.10). Many eruptive units (e.g., Dragón, Del Norte, Pulgar, Tortuga) show little variation in MgO. Buho is one notable exception, ranging from 7.5 to 8.6 wt. % MgO; over this range, there are slight increases in CaO, K_2O, and TiO_2 with decreasing MgO, but K/Ti remains constant (Fig. 4.10). Within Altares and Frijoles, CaO decreases with decreasing MgO, and K_2O, TiO_2, and most ratios of highly to moderately incompatible elements (e.g., K/Ti, La/Sm) increase significantly (Fig. 4.10).

4.6.2.2. Petrography and mineral chemistry

In contrast to the relatively limited range in major element compositions of samples from the low-magma-supply study area, petrographic differences within and among eruptive units indicate significant variations in the pre-eruptive histories of these lavas. All samples from the large Buho flow field are nearly aphyric (< 2% phenocrysts > 0.5 mm in size). Samples throughout this unit contain sparse, skeletal, olivine phenocrysts with slight normal zoning (Fo_{83-85}) (Fig. 4.8a). Plagioclase also is present in some samples, as lath-shaped crystals with swallow tails (An_{72-73}). Some older eruptive units are petrographically similar, indicating that such crystal-poor lavas are not unique to the Buho eruption, although they are relatively rare within the study area.

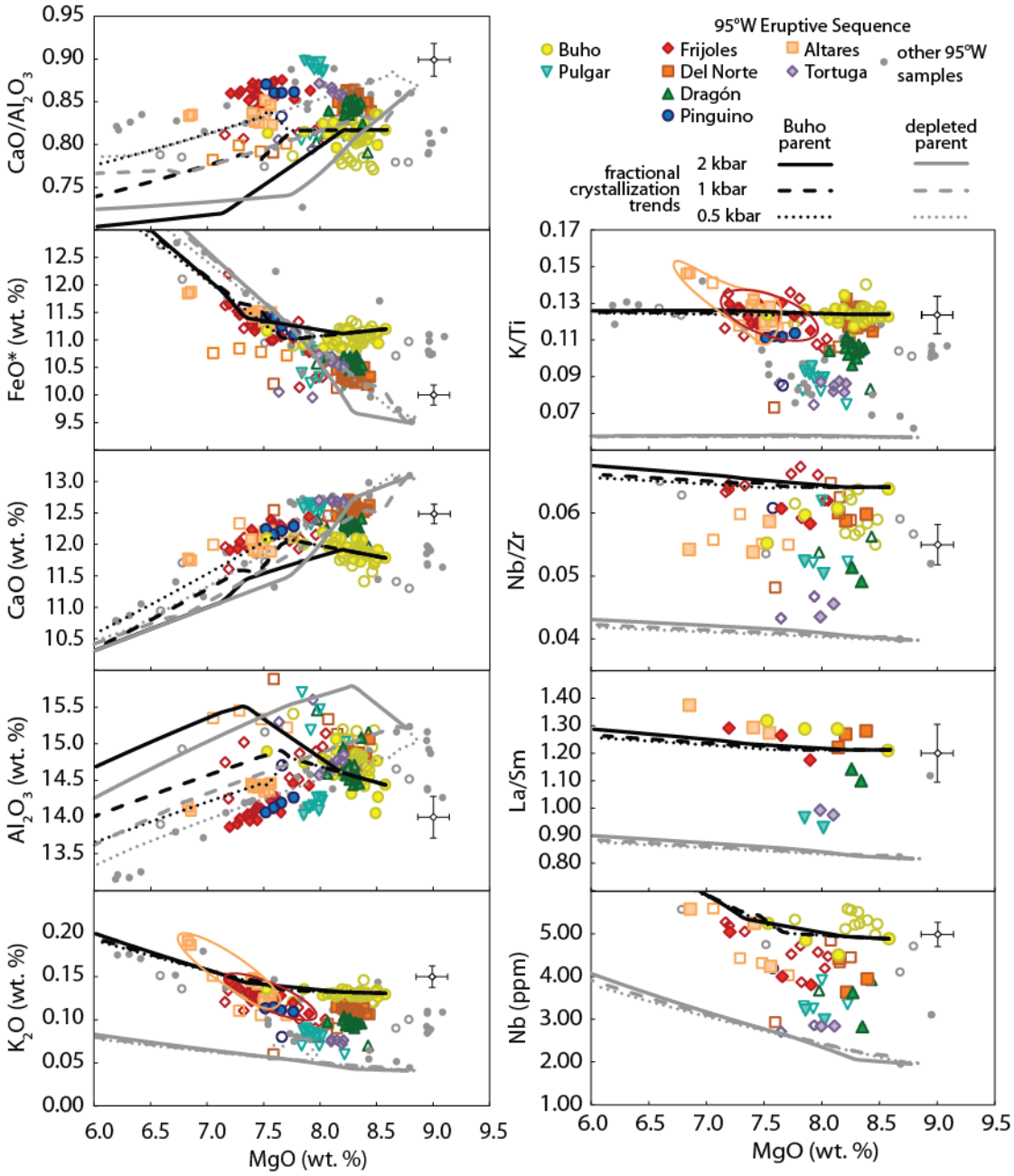

Figure 4.10. Major and trace element data for individual eruptions from 95°W. Lines show fractional crystallization trends predicted by MELTS for two different parental compositions at 0.5, 1.0, and 2.0 kbar (see text for details of MELTS modeling). Note that at 2 kbar, plagioclase crystallization is delayed to lower MgO, resulting in higher Al_2O_3 than observed in glasses. Solid symbols, glass analyses by EMP; hollow symbols, whole rock analyses by XRF. Partition coefficients used in trace element modeling are from Aigner-Torres *et al.* (2007) (plagioclase); Halliday *et al.* (1995) (clinopyroxene and olivine); and Zack & Brumm (1998) (ilmenite). Analytical uncertainty (±2σ) of based on repeat analyses of VG-2 glass standard by EMP for major and minor elements, and repeat analyses of BHVO-1 standard by ICP-MS for trace elements.

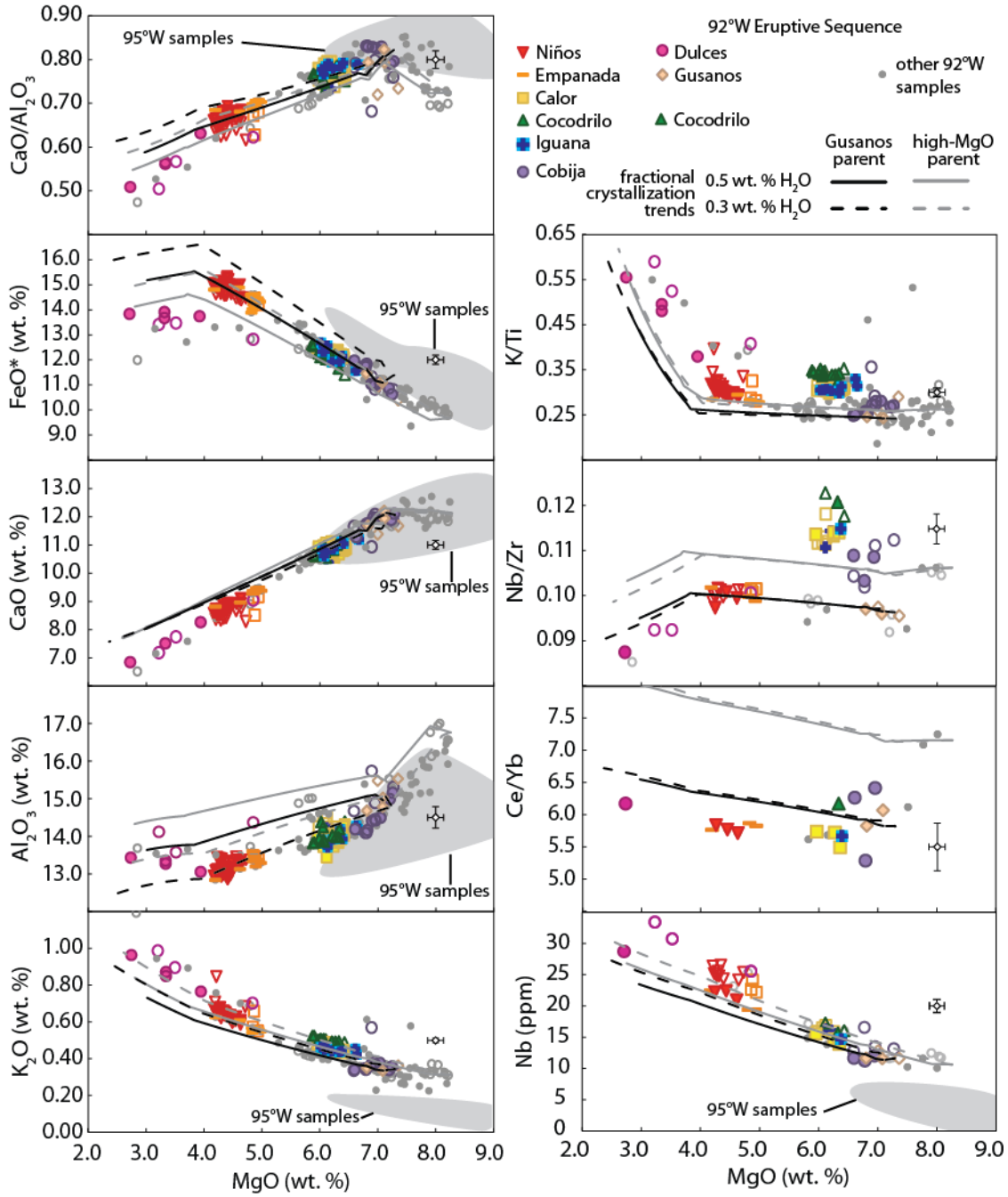

Figure 4.11. Major and trace element data for individual eruptions from 92°W. Lines show fractional crystallization trends predicted by MELTS for two different parental compositions with 0.3 and 0.5 wt. % H_2O (see text for discussion). Partition coefficients used in trace element modeling are from Aigner-Torres *et al.* (2007) (plagioclase); Halliday *et al.* (1995) (clinopyroxene and olivine); and Zack & Brumm (1998) (ilmenite). Analytical uncertainty (±2σ) of based on repeat analyses of VG-2 glass standard by EMP for major and minor elements, and repeat analyses of BHVO-1 standard by ICP-MS for trace elements.

Del Norte, Dragón, and Tortuga are olivine- and plagioclase-phyric, ranging in total phenocryst contents from 2.3 to 12.7 modal %. Olivine crystals are typically euhedral or skeletal (Fig. 4.8b) and are unzoned or slightly normally zoned (Fo_{83-86}) and range from 0.3-2.0 modal %. Plagioclase is more abundant than olivine (1.6-11.0 modal %), and is significantly more variable compositionally (An_{67-88}). Plagioclase morphologies range from relatively small, lath-shaped crystals to larger tabular crystals that typically have oscillatory concentric zonation (4.8b); dendritic overgrowths are ubiquitous on plagioclase crystals. Some plagioclase crystals have spongy textures indicating either rapid growth or partial resorption (Fig. 4.8c).

Frijoles, Altares, and Pulgar contain variable proportions of plagioclase (4.5-18.8 modal %), olivine (0.4-4.7 modal %), and clinopyroxene (0.1-4.1 modal %). These eruptive units also have the lowest MgO contents in the study area. Olivine morphologies range from skeletal to euhedral, and are commonly normally or reversely zoned (cores Fo_{76-86}; rims Fo_{80-84}) (Fig. 4.8f,h). Plagioclase morphologies are highly variable, with compositional ranges similar to those in the olivine-and plagioclase-phyric samples. Pyroxene may be normally or reversely zoned (Fig. 4.8g); some samples contain sector-zoned pyroxene crystals with irregular extinction (Fig. 8d,e), either in addition to or instead of concentrically zoned crystals.

4.6.3. Variations within individual eruptive units at 92°W

4.6.3.1. Compositional variations

At the high-magma-supply study area, the amount of compositional variation within glasses from each of the well-sampled units (range of 0.3-1.2 wt. % MgO) is similar to that at 95°W (Colman *et al.*, 2012). Some units (Cocodrilo, Iguana, and Calor) have higher incompatible element concentrations and ratios at a given MgO content than others (Gusanos, Empanada, and Niños) (Fig. 4.11). CaO and FeO* do not vary significantly among eruptive units at a given MgO (Fig. 4.11).

4.6.3.2. Petrography and mineral chemistry

Mineral phases within most eruptive units at the high-magma-supply study area (e.g., Niños, Empanada, Cobija, Calor) have simple textures indicating growth from a

melt-rich body at moderate degrees of undercooling. Although some samples are entirely aphyric, many have significant microphenocryst (0.1-0.5 mm) populations (Table 4.1). Olivine is typically skeletal (Fig. 4.9a,b,d); plagioclase is tabular or lath-shaped, and clinopyroxene typically forms intergrowths with plagioclase (Fig. 4.9c,d). Mineral phases within each sample have limited compositional range, although the compositional differences between samples from different eruptive units can be significant (Fig. 4.7).

Samples from Gusanos and Dulces are more crystal-rich (4.2-15.7 modal %) and disequilibrium textures are common. In Gusanos, olivine is typically skeletal, and is unzoned or slightly normally zoned (Fo_{83-85}). Plagioclase is normally or reversely zoned (cores An_{59-84}; rims An_{70-77}); reversely zoned crystals have skeletal overgrowths (Figs. 4.9e). Clinopyroxene is not present in samples from Gusanos, consistent with the relatively high MgO of the glass (Fig. 4.6). In Dulces, olivine crystals are typically skeletal, and are consistently slightly normally zoned (cores Fo_{68-72}; rims Fo_{66-69}) (Fig. 4.9h). Plagioclase is normally or reversely zoned (cores An_{46-60}; rims An_{57-62}) (Fig. 4.9g). In reversely zoned crystals, the core typically has a rounded, irregular margin, and is surrounded by a slightly skeletal to euhedral overgrowth. Clinopyroxene occurs both as strongly reversely zoned crystals (cores Mg# 63-66; rims Mg# 75-76) (Fig. 4.9g), and as crystals with weak oscillatory zoning (Mg# 72-77).

4.7. Discussion: Magmatic processes at 92°W and 95°W

Compositional variations within and among eruptive units at the two study areas can be used to determine the effects of variable magma supply on magma reservoir dynamics. These include the relative importance of crystal fractionation, magma mixing, assimilation of crustal material, interaction with mush zones, and recharge of the magma reservoir with new batches of magma from the mantle. In addition, the range of parental magmas that are present in each study area has implications for the nature of melting processes with distance from the Galápagos hotspot.

Table 4.6. Compositional variability at each study area

	La/Sm	Nb/Zr	Nb/Er	Ba/Y
Relative variance, 95°W	0.13	0.12	0.18	0.20
Relative variance, 92°W	0.04	0.08	0.08	0.13
Relative range, 95°W	0.47	0.45	0.60	0.67
Relative range, 92°W	0.13	0.32	0.27	0.48

4.7.1. Parental magmas and mantle melting at 92°W and 95°W

Because incompatible element ratios are affected little by fractional crystallization of basaltic magma, they can be used to assess the range of parental magma compositions in each study area (Fig. 4.12). Ratios of highly to moderately incompatible elements (e.g., La/Sm, Nb/Zr, Ba/Y) are somewhat more variable at 95°W than at 92°W, as indicated by their larger relative variance (standard deviation / mean value) and relative range ((maximum value –minimum value) / mean value) (Table 4.6). These ratios are sensitive to source composition and melting conditions; the difference in parental magma variability between our study areas could therefore reflect greater variability in parental magmas, or less effective magma homogenization at the low-magma-supply study area. Along the global mid-ocean ridge system, increasing spreading rates are correlated with decreasing variance in La/Sm and other parameters affected by melting conditions (including isotopic ratios); this trend has been attributed to greater mixing of magmas at a range of depths in the more melt-rich environments of faster spreading ridges (Rubin & Sinton, 2007; Rubin *et al.*, 2009).

Mantle melting models involving melting of a two-component mantle source have been proposed to explain compositional variations along the length of the Galápagos Spreading center. A model described by Schilling *et al.* (e.g., 2003) invokes a plume-derived component that is relatively enriched in incompatible elements, and is mixed in greater proportions with the relatively depleted ambient upper mantle with increasing proximity to the hotspot along the spreading center. In contrast, in a model described by Ito & Mahoney (2005), the plume itself contains both incompatible-element-enriched and incompatible-element-depleted components, whose relative proportions do not vary along-axis east of 96°W. Ingle *et al.* (2010) demonstrated that variations in parental magmas of T- and E-MORBs between 96°W and 92°W could be generally accounted for by melting of a two-component peridotite mantle composed of enriched veins within a depleted matrix. The melting model used by Ingle *et al*. (2010) is described in detail by Ito & Mahoney (2005).

The model used by Ingle *et al.* (2010) assumes that melts are produced within a triangular melting region beneath the ridge where mantle is ascending and is above its

solidus (e.g., Plank & Langmuir, 1992); incremental melts are separated from the residue and mixed perfectly (pooled, accumulated fractional melting). The chemically enriched component is assumed to have a higher water content, so it begins to melt at greater depths than the depleted component. Deep, hydrous melting of the enriched component contributes an additional volume of low-degree melts (Asimow & Langmuir, 2003). In this model, the plume influence is reflected in a temperature anomaly, which increases in magnitude with proximity to the hotspot (Ingle *et al.*, 2010). Additionally, buoyant flow through the deep hydrous melting regime is enhanced near the hotspot, resulting in a greater relative contribution from the enriched component in the pooled melt (Ingle *et al.*, 2010).

Ingle *et al.* (2010) found that observed variations in crustal thickness, incompatible element ratios, and radiogenic isotope ratios between 92° and 96°W could be fit best by models where the enriched component accounts for 10% of the mantle, the maximum temperature anomaly is 10-30°C, and buoyant mantle flow reaches 7.5-15 times the spreading rate at the region of maximum plume influence. In their model, the amount of enriched material in the mantle is constant along-axis, but the magnitude of the temperature anomaly and buoyant flow increase exponentially with proximity to the hotspot from background levels (no temperature anomaly and passive upwelling) at 96°W (Ingle *et al.*, 2010). Following the approach of Ingle *et al.* (2010), we investigate the range in source composition and average degree of melting required to produce the range of compositions observed in each study area. The composition of the depleted component used here is the average depleted mantle of Workman & Hart (2005) (ADM), and the enriched component is the primitive mantle (PM) of McDonough & Sun (1995), as in Ingle *et al.* (2010). Ingle *et al.* (2010) used a combination of partition coefficients from Green (1994), Johnson (1998), Salters *et al*. (2002), and Salters & Stracke (2004); we use only those of Salters & Stracke (2004) for the sake of internal consistency and because they produce smoother PM-normalized REE patterns (Fig. 4.12) than the combined partition coefficient set.

The high-magma-supply study area is near the peak of plume influence along the GSC, as defined by compositional variations (Ingle *et al.*, 2010). Mean extents of 6-7% melting using the Ingle *et al.* (2010) model produce the crustal thickness and range of

incompatible element ratios observed near 92°W (Fig. 4.13). Mean extents of melting for the low-magma-supply study area are slightly higher (~9%) despite the fact that a smaller total volume of melt is produced, because pooled melts receive less contribution from the deep, hydrous, low-degree melting regime (Fig. 4.13). Model results can account for the most incompatible-element-enriched samples from the low-magma-supply study area, but not more depleted samples (Figs. 4.12, 4.13). More depleted magmas could be produced by melting of a more depleted source composition (Ingle *et al.*, 2010), such as the depleted depleted mantle of Workman & Hart (2005) (DDM), and/or a lower proportion of the enriched material (Figs. 4.12, 4.13). More depleted magmas (and more compositional variability) could also be produced if all incremental melts are not perfectly homogenized (e.g., Plank & Langmuir, 1992; Ito & Mahoney, 2005). For example, if melts from the edges of the deep, hydrous melting region are not effectively transported to the ridge axis, the pooled magma would be less enriched in incompatible trace elements (e.g., Plank & Langmuir, 1992; Ito & Mahoney, 2005). Although these scenarios are difficult to test using trace element data, the addition of radiogenic isotope data could allow one to distinguish which are most likely.

Parental magma compositions produced by the Ingle *et al.* (2010) model (e.g., PM-normalized REEs, see Fig. 4.12) are similar to those observed in samples from each study area (i.e., light REE-enriched relative to PM at 92°W; light REE-depleted relative to PM at 95°W). In detail, slight discrepancies in the degree of melting required to produce different incompatible element ratios (Fig. 4.13) are likely related to differences between the generic depleted and enriched mantle end-members used in the model (ADM and PM) and the characteristics of the Galápagos plume. For example, elevated Nb/Er and Nb/La of samples relative to predicted compositions likely reflect greater enrichment in Nb of the Galápagos plume relative to similarly incompatible elements (e.g., La) than in the PM of McDonough & Sun (1995) (Fig. 4.13). A more detailed identification of the composition of the mantle composition in this region is beyond the scope of this study.

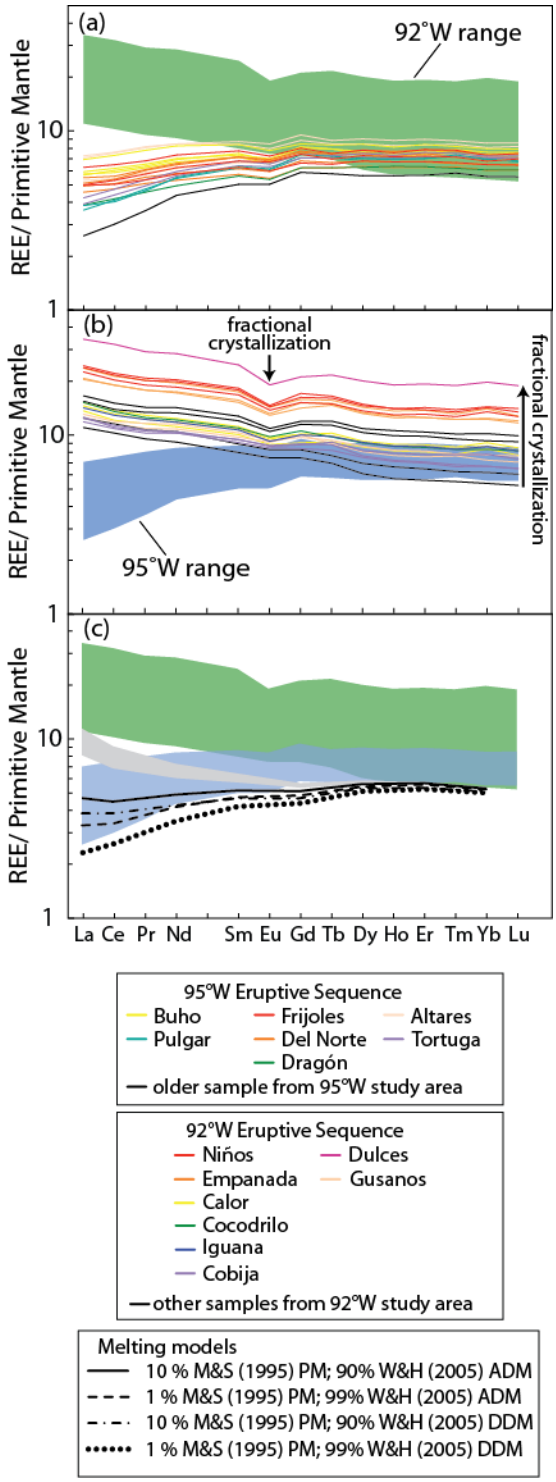

Figure 4.12. Primitive mantle-normalized REE abundances of glass samples, analyzed by ICP-MS. Colored lines represent individual sample analyses; colors correspond to eruptive units, as in Figs. 4.10 and 4.11. (a) Individual analyses from 95°W. Shaded field, range of compositions from 92°W. (b) Individual analyses from 92°W. Shaded field, range of compositions of samples from 95°W. Note that magnitude of Eu anomaly increases as REE concentrations increase, as predicted by for fractional crystallization. (c) Parental magmas produced by Ingle *et al*. (2010) mantle melting model. Grey shaded region, magmas produced at 92°W by melting of mantle with 10% PM and 90% ADM. Maximum light REE enrichment is produced by model with 10°C temperature anomaly and buoyant flow 15 times spreading rate; slightly less light REE-enriched compositions are produced by larger temperature anomaly (up to 30°C shown) and/ or less buoyant flow (as little as 7.5 times spreading rate shown). At 95°W, the magnitude of the modeled plume influence is small for all models run; variations in source composition can produce more depleted parental magmas. Black lines are compositions produced by melting of mantle with 10% PM and 90% ADM (solid line); 1% PM and 99% ADM (dashed line); 10% PM and 90% DDM (dash-dotted line); and 1% PM and 99% DDM (dotted line).

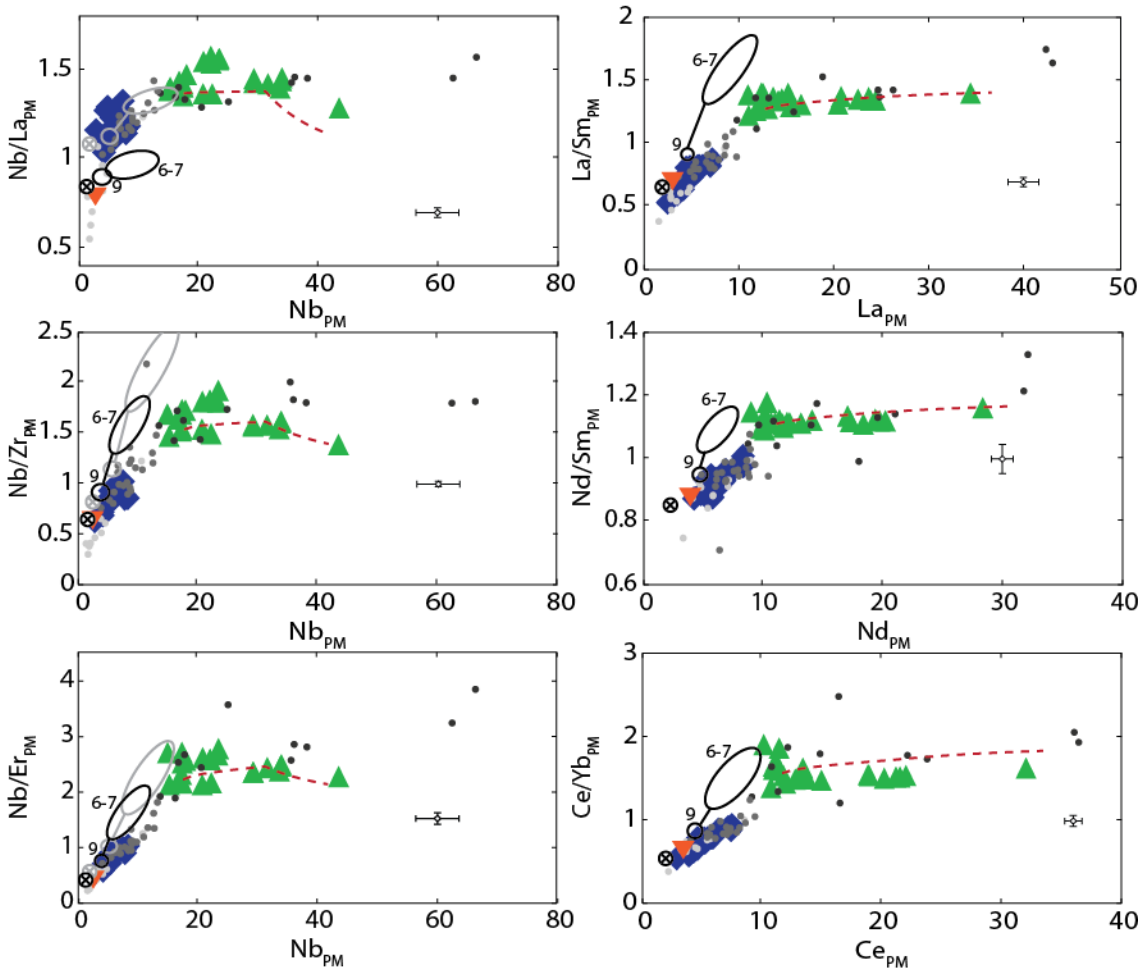

Figure 4.13. Incompatible trace element ratios of samples from each study area and samples collected along the western GSC (data from Ingle et al., 2010). Symbols as in Figure 4.3. Black lines indicate compositions produced at each study area by melting of mantle composed of 10% PM and 90% ADM, with 10-30°C temperature anomaly and buoyant flow 7.5-15 times spreading rate, as described in text. Grey lines indicate compositions produced under same conditions from a mantle whose enriched component is more enriched in Nb than the PM of McDonough and Sun (1995). Inverted triangle is produced by melting mantle with 1% PM and 99% ADM. Circle with X is composition of magma produced by accumulated fractional melting. Red dashed lines indicate fractional crystallization trends calculated using MELTS (see text for discussion). Partition coefficients used in fractional crystallization modeling are from Aigner-Torres *et al.* (2007) (plagioclase); Halliday *et al.* (1995) (clinopyroxene and olivine); and Zack & Brumm (1998) (ilmenite).

4.7.2. Fractional crystallization in upper crustal magma reservoirs at 95°W and 92°W

Major element compositional trends of most mid-ocean ridge basalts are broadly consistent with derivation by varying degrees of fractional crystallization of olivine, plagioclase, and clinopyroxene from a range of parental magmas (e.g., Grove *et al.*, 1992; Rubin & Sinton, 2007). In detail, however, magmatic histories can be more complex (e.g., Reynolds & Langmuir, 1997; Rubin *et al.*, 2001; Bergmanis *et al.*, 2007, Goss *et al.*, 2010). We calculated fractional crystallization trends using MELTS (Ghiorso & Sack, 1995; Smith & Asimow, 2005), for comparison with observed liquid lines of descent within individual eruptive units. Starting compositions were relatively high-MgO samples from each study area. Water contents were estimated based on the excellent correlation with K_2O in GSC samples (wt. % H_2O = 1.31(wt. % K_2O) + 0.09; R^2=0.96 (Cushman *et al.*, 2004)); a range of other starting water contents 0-1 wt. % H_2O) were also tested for comparison. MELTS models were run with oxygen fugacities of one and two log units below the fayalite-magnetite-quartz buffer (FMQ), and pressures appropriate for crystallization within the crust (0.5 to 2 kbar) (Figs. 4.10, 4.11).

At the low-magma-supply study area, major element variations are generally similar to those predicted by low-pressure (0.5-1 kbar) fractional crystallization at two log units below FMQ: with decreasing MgO, CaO and CaO/Al_2O_3 decrease and FeO* increases (Fig. 4.10). However, incompatible element concentrations within several eruptive units increase more rapidly with decreasing MgO than predicted by fractional crystallization, e.g., K/Ti in both Altares and Frijoles (Fig. 4.10). The prevalence of complex mineral textures (reverse and normal zoning, resorption) also cannot be explained by fractional crystallization alone.

Segment-scale compositional variations in the entire low-magma-supply study area also define patterns that are inconsistent with fractional crystallization from parental magmas with a range of incompatible element ratios. In particular, the most depleted (low K, K/Ti, La/Sm, Nb/Zr) compositions only occur at high MgO contents (8-9 wt. %

MgO) (Fig. 4.10). If the more evolved samples (6-7 wt. % MgO) were produced by simple fractional crystallization of a range of parental compositions, some should have relatively depleted compositions; only slight increases in ratios of highly to moderately incompatible elements are expected at these degrees of fractional crystallization (Fig. 4.10). The absence of low-MgO samples with low K/Ti is therefore difficult to explain and alternative explanations that couple incompatible element enrichment to differentiation can be considered (see discussion of mush zone interaction in Section 4.7.3).

At the high-magma-supply study area, major and trace element variations within the eruptive sequence Gusanos-Empanada-Niños are reasonably approximated by low-pressure (0.5-1 kbar) fractional crystallization of olivine, plagioclase, and clinopyroxene from compositionally similar parental magmas (Fig. 4.11) at two log units below FMQ. In fractional crystallization runs with Gusanos samples as parental magmas, using the water content estimated by Cushman *et al.* (2004) of 0.5 wt. % results in plagioclase crystallization beginning at lower MgO than expected based on observed mineral phases (Fig 4.6) and the MgO-Al_2O_3 covariation (Fig. 4.11); liquid lines of descent predicted by MELTS are correspondingly higher in Al_2O_3 than glass samples at low MgO. Better fits to the Al_2O_3 data are provided by reducing the starting water content to 0.3 wt. %, although this results in higher FeO than observed. During fractional crystallization at greater pressures (i.e., 2 kbar, appropriate for the mid- or lower crust), crystallization of plagioclase would also be delayed to lower MgO, causing Al_2O_3 contents to be higher than observed.

Concentrations of incompatible elements (e.g., Zr, Hf, Th, U, and REE except Eu) roughly double from Gusanos to Niños, whereas ratios of highly to moderately incompatible elements (e.g., La/Sm) increase only slightly, consistent with ~50 % fractional crystallization. Concentrations of elements that partition preferentially into one or more of the crystallizing mineral phases over the liquid (e.g., Ni into olivine and clinopyroxene; Sr into plagioclase) decrease with decreasing MgO (Fig. 4.5). Similarly, Eu and Sr anomalies become increasingly negative with decreasing MgO, as plagioclase preferentially incorporates Eu and Sr over elements that are similarly compatible during mantle melting (Fig. 4.5).

Compositions of the Calor, Cocodrilo, and Iguana eruptive units require parental magmas that are more incompatible element-enriched than other units in this segment (Fig. 4.10). Nevertheless, the magnitude of Eu and Sr anomalies within these eruptive units, which are similar to those of other samples from 92°W at the same MgO, suggest that fractional crystallization under similar conditions also dominates magmatic evolution for these units. The importance of fractional crystallization is also reflected in the low crystallinity of these samples (Table 4.1), which indicates that separation of mineral phases from residual melts is effective at the high-magma-supply study area.

The most highly evolved (lowest MgO) eruptive unit at 92°W is the Dulces basaltic andesite pillow mounds. Compositional variation within Dulces bears a resemblance to advanced fractionation of Fe-Ti oxides in addition to clinopyroxene and plagioclase ± olivine. With decreasing MgO, concentrations of incompatible major elements (Na_2O, K_2O, P_2O_5) and SiO_2 increase, and CaO and TiO_2 decrease (Fig. 4.11). However, FeO* remains essentially constant, in contrast to the decrease predicted as a result of the crystallization of Fe-Ti oxides (Fig. 4.11). Compositional variations within Dulces are thus more likely a result of mixing between moderate- and low-MgO magmas, consistent with the presence of reversely zoned plagioclase and pyroxene crystals in samples from Dulces (Fig. 4.7, 4.9).

4.7.3. Mush zone interaction at 95°W

Some of the discrepancies between fractional crystallization trends and those observed at the low-magma-supply study area may be explained by crystallization of magma within a transition zone at the margins of a melt-rich magma reservoir. We use the *in situ* crystallization model of Langmuir (1989) to simulate the effects of crystallization within the transition zone followed by mixing of some or all of the remaining melt back into a larger magma body. *In situ* crystallization may also approximate magmatic differentiation of melts moving through mush zones, which are thought to make up the volumetric majority of crust beneath mid-ocean ridge axes and mid-ocean ridge magma systems, especially those at low magma supply (e.g., Sinton & Detrick, 1992). During *in situ* crystallization, the bulk composition of the sub-liquidus crystallizing assemblage is closer to that of the liquid than in perfect fractional

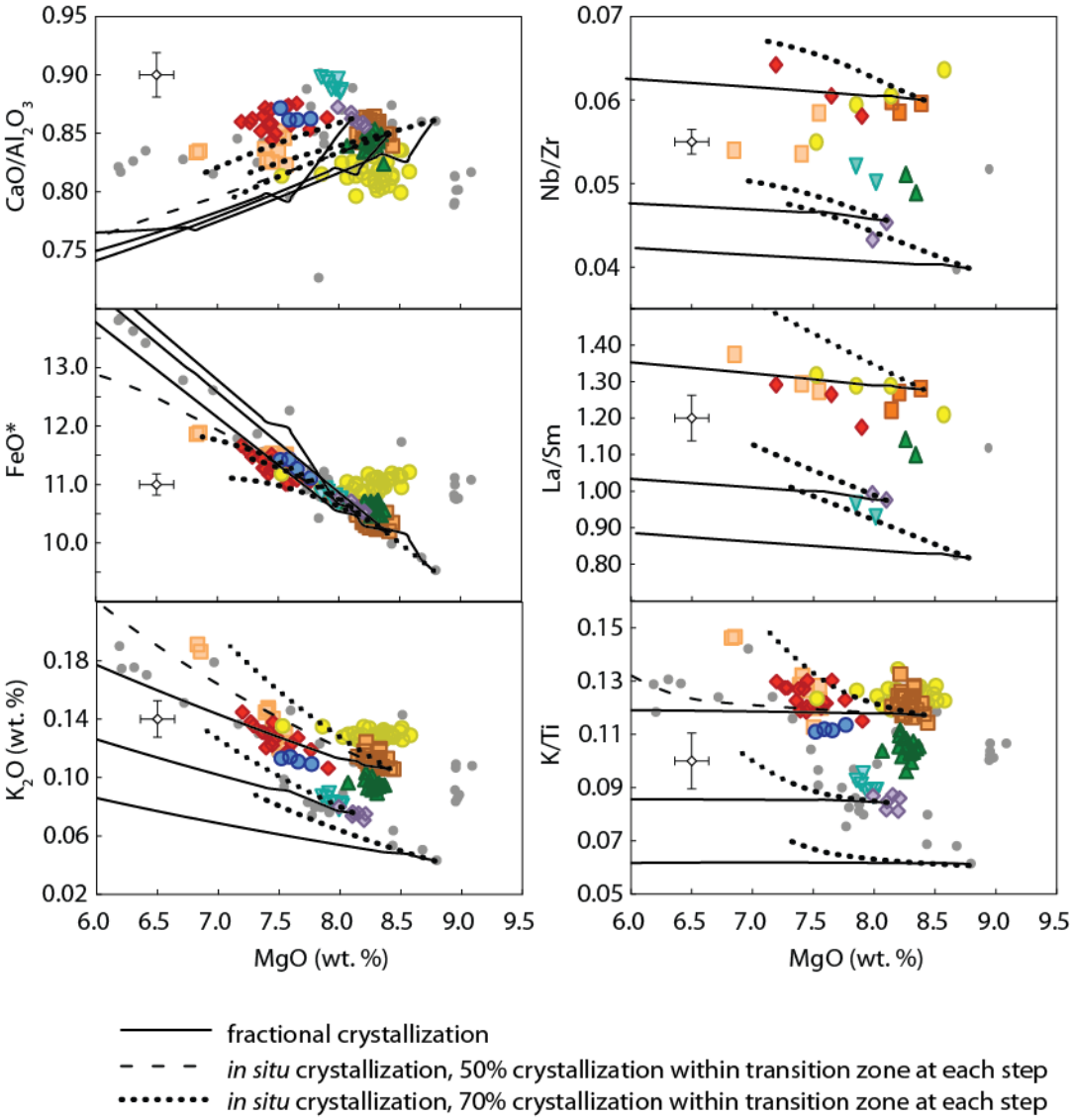

Figure 4.14. Consequences of *in situ* crystallization on differentiation trends at 95°W. Trends were calculated using MELTS, as described in text. Note the smaller changes in compatible element compositions, and larger changes in incompatible elements and ratios of highly to moderately incompatible elements, produced by *in situ* crystallization compared to fractional crystallization. Solid line, fractional crystallization; dashed line, *in situ* crystallization with 50% crystallization within the transition zone at each step; dotted line, *in situ* crystallization with 70% crystallization within the transition zone at each step. Symbols correspond to eruptive units, as in Figure 10. Error bars represent ±2σ uncertainty.

crystallization; this results in less depletion of compatible element concentrations in the liquid than predicted by fractional crystallization for a given amount of crystallization. When viewed on MgO variation diagrams the effect appears as an over-enrichment of the most incompatible elements, relative to fractional crystallization trends (Langmuir, 1989).

We model *in situ* crystallization following the step-wise approach used by Reynolds & Langmuir (1997). At all times, the transition zone where crystallization is occurring represents five percent of the total magma volume. At each step, magma is removed from the magma reservoir and undergoes 70% equilibrium crystallization (modeled using MELTS (Ghiorso & Sack, 1995; Smith & Asimow, 2005); the remaining 30% liquid is expelled and remixed into the magma reservoir. Differentiated melts produced by this process have elevated ratios of highly to moderately incompatible elements, whereas those produced by fractional crystallization have only slight increases in these ratios; if both crystallization styles operate, melt compositions will be intermediate (Fig. 4.14).

The effects of i*n situ* crystallization are much less apparent at the high-magma-supply study area, where samples from the eruptive sequence Gusanos-Empanada-Niños differentiate without associated increases in incompatible element ratios (Fig. 4.11). A transition zone in which *in situ* crystallization operates could still exist at this study area, but may represent a smaller fraction of the magmatic system and therefore have less effect on compositional variations of erupted samples.

4.7.4. Importance of assimilation at 92°W

Although most compositional and petrographic variations at the high-magma-supply study area are consistent with relatively simple, fractionation-dominated magmatic evolution, Cl increases with decreasing MgO significantly more than predicted by fractional crystallization (referred to hereafter as over-enrichment in Cl) (Fig. 4.15a). Cl behaves as a highly incompatible during mantle melting and fractional crystallization of basalt (e.g., Schilling, 1980; Michael & Schilling, 1989; Ingle *et al.*, 2010). As such, the Cl/La ratio should remain nearly constant during melting (Fig. 4.15b) and low to moderate degrees of fractionation. Samples from the low-magma-supply study area have

uniformly low Cl concentrations and Cl/La ratios. The Cl/La ratios of the most primitive samples erupted at the high-magma-supply study area are similar to those of primitive T-MORB (Fig. 4.14b), but Cl concentrations and Cl/La ratios increase more rapidly with decreasing MgO than predicted by fractional crystallization (Fig. 4.15a).

Assimilation of a Cl-rich material such as brine, amphibole, altered crust, or partial melts of altered crust has been invoked to explain over-enrichments in Cl in mid-ocean ridge basalts, andesites, and dacites (Michael & Cornell, 1998; Michael & Schilling, 1989; Coogan *et al.*, 2003; le Roux *et al.*, 2006; Wanless *et al.*, 2010, 2011). In high-SiO_2 samples from the East Pacific Rise, Wanless *et al.* (2010, 2011) also noted changes in trace elements, trace element ratios, and oxygen isotope ratios that are inconsistent with fractional crystallization, but can be explained by assimilation of partial melts of hydrothermally altered crust. Additional evidence for assimilation includes observations of partially melted xenoliths of gabbros and basaltic dikes within and below the boundary between gabbros and sheeted dikes in ophiolite sections and drill cores in oceanic crust (Coogan *et al.*, 2003; Wilson *et al.*, 2006; Gillis, 2008; France *et al.*, 2009). The base of the dike section observed in ophiolites and oceanic drill cores is typically hydrothermally altered to greenschist facies, with alteration temperatures increasing downwards; the lowermost dikes are commonly recrystallized and may be partially melted (Coogan *et al.*, 2003; Wilson *et al.*, 2006; Gillis, 2008; France *et al.*, 2009). These observations indicate that crustal materials near crustal magma reservoirs can be hydrothermally altered, and can be at least partially assimilated within the magma reservoir (e.g., Coogan *et al.*, 2003; Wilson *et al.*, 2006; France *et al.*, 2009).

Following Michael & Schilling (1989) we use the DePaolo (1981) formulation of combined assimilation and fractional crystallization (AFC) to model Cl and La variations at our high-magma-supply study area. The ratios of mass assimilated to mass crystallized (Ma:Mc) required to generate the over-enrichment in Cl observed depend on the assimilant compositions (Cl contents from Michael & Schilling, 1989). The highest-Cl material considered is brine (30 wt. % Cl), which is most likely to be present near the roof of the axial magma chamber, and could be incorporated into the magma via stoping of blocks with brine-filled pores, fractures, or fluid inclusions (Michael & Schilling, 1989; Coogan *et al.*, 2003). Only small amounts of brine (Ma:Mc 0.001-0.01) are

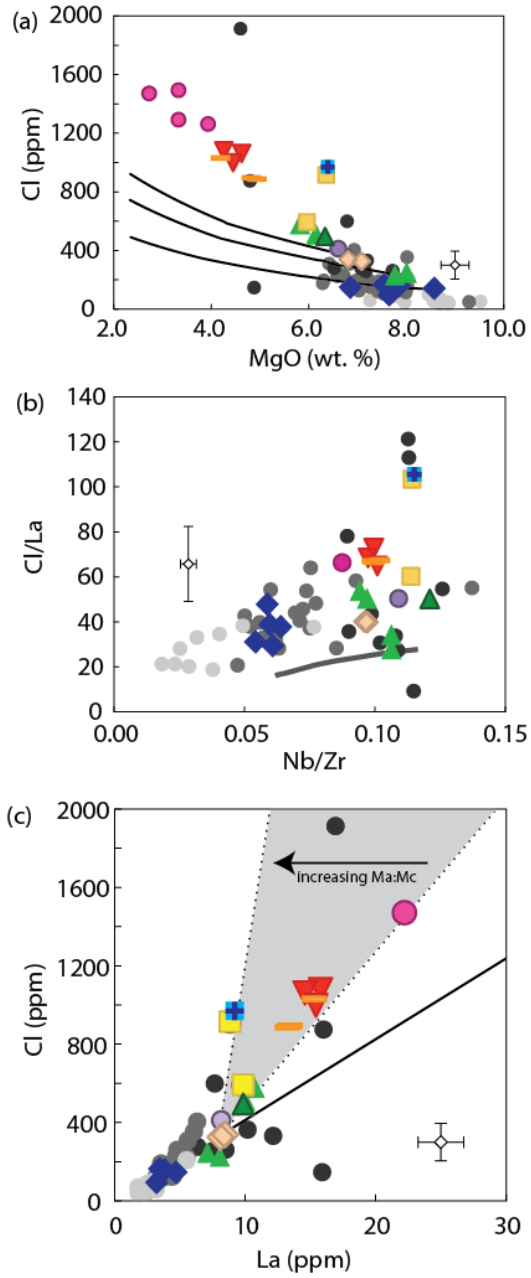

Figure 4.15. Over-enrichments in Cl. (a) Fractional crystallization trends (black lines) demonstrate that at 95°W, increases in Cl with decreasing MgO are consistent with fractional crystallization, whereas at 92°W, samples are "over-enriched" in Cl at low MgO contents. Blue X's, 95°W samples; colored symbols, 92°W samples. Gray circles, GSC N-, T-, and E-MORB (data from Cushman *et al.*, 2004 and Ingle *et al.*, 2010). (b) The lack of correlation between Cl/La and Nb/Zr in samples from 92°W demonstrates that variable degrees of enrichment in Cl relative to La are unlikely to originate in the melting process. Gray line shows parental magma compositions produced by Ingle *et al*. (2010) melting model, using range of parameters discussed in mantle melting section. Source Cl content for PM component from McDonough & Sun (1995); Cl for EDM from Salters & Stracke (2004). Note that observed enrichments in Cl/La are not predicted by this model. **(**C) Fractional crystallization and AFC trends. Solid black line, fractional crystallization trend assuming that La and Cl are equally incompatible (D_{Cl}=D_{La}=0). If D_{Cl}=0, D_{La} must be unreasonably high (0.5) to match the trend defined by samples from 92°W. Gray field bounded by dotted black lines represents compositions produced by AFC, using equations from DePaolo (1981), after Michael & Schilling (1989). For assimilation of brine (20 wt. % Cl), amphibole (0.5 wt. % Cl), and altered crust (0.1 wt. % Cl), ratios of mass assimilated to mass crystallized (Ma:Mc) are 0.001-0.01, 0.07-0.7, and 0.5->1, respectively.

required to produce even the greatest Cl over-enrichments observed at 92°W (Fig. 4.14c). Selective melting of amphibole (0.5 wt. % Cl) requires somewhat greater amounts of assimilant (Ma:Mc 0.07-0.7), and could occur via partial melting or prograde metamorphism of stoped blocks or roof material (e.g., Michael & Schilling, 1989; Gillis & Coogan, 2002). Bulk assimilation of altered crustal material (0.1 wt. % Cl) requires substantially greater masses of assimilant (Ma:Mc > 0.5), and cannot produce the highest degrees of Cl over-enrichment observed.

Assimilation of small amounts of either brine or amphibole could produce the degrees of enrichment observed in most samples (Fig. 4.15c). However, the Ma:Mc required to produce the greatest observed over-enrichments (specifically, one Calor sample and one Iguana sample with Cl/La > 100) via selective amphibole assimilation or assimilation of altered crust are unreasonably high. The significant difference in over-enrichment between the two analyzed samples from Calor (0.6 and 0.9 wt. % Cl) might reflect local variations in the amount or type of assimilated material (likely brine, in this case), despite apparently little variation in temperature and parental magma composition along axis indicated by the limited variation in MgO, K/Ti, and Nb/Zr among Calor samples (Fig. 4.11).

The lack of Cl over-enrichment at 95°W is consistent with global trends related to magma supply; at ridges with rates of magma supply too low to sustain seismically imaged melt-dominated reservoirs, Cl over-enrichments are typically not observed (Michael & Cornell, 1998). This could be due to relatively rapid ascent of these magmas through the shallower regions of the crust where Cl-enriched (i.e., hydrothermally altered) materials are most likely to be present (Michael & Schilling, 1989; Michael & Cornell, 1998).

4.7.5. Temporal and spatial variations in recharge and eruption along the GSC

At the high-magma-supply study area, on-axis eruptions are likely to be fed from the shallow, seismically imaged melt lens. Although additional melt-rich bodies could exist at greater depths within the crust, the limited nature of along-axis compositional variability suggests that mapped eruptions at this location were fed from a single magma reservoir. At the low-magma-supply study area, melt-rich magma reservoirs may be

present only intermittently. However, even at this location, erupted lavas contain > ~ 75% liquid, and although crystallinity is variable along-axis within certain units, there is little variation in melt compositions within individual eruptive units (see Section 4.6.2.1). At the low-magma-supply study area, magmatic recharge may mix with a crystal-rich mush, rather than joining a persistent melt-rich lens. Compositional differences among eruptive units within mapped eruptive sequences can be used to constrain the timing and nature of magmatic recharge to the shallow crustal magma reservoir that feeds eruptions at each study area.

In the absence of magmatic recharge, crystallization within a cooling magma reservoir will decrease the melt's MgO content, and increase incompatible element concentrations and ratios of highly to moderately incompatible elements; the magnitude of these compositional variations will be controlled by the style of crystallization (e.g., fractional, equilibrium, or *in situ*). Conversely, increases in magma temperature (indicated by increases in glass MgO content) and decreases in ratios of highly to moderately incompatible elements are unlikely to be achieved by processes occurring in the crust, and therefore require that the magmatic system was mixed with hotter and/ or more incompatible element-depleted magma. These observations can be used to determine whether or not recharge occurred between a given pair of eruptions. However, decreasing or constant MgO between eruptions does not necessarily preclude magmatic recharge; in a system where the rates of recharge and cooling and compositions of parental magmas and assimilant are constant, a steady-state can be reached where erupted magma compositions also are constant (e.g., O'Hara, 1977). Additionally, recharge of a magma that is compositionally similar to the resident magma may go undetected by these criteria.

4.7.5.1. Magmatic recharge at the low-magma-supply study area

At 95°W, magmatic recharge is required between each eruption in the eruptive sequence Pinguino-Dragón-Del Norte-Frijoles (Fig. 16). Dragón has higher MgO and is more enriched in incompatible elements than Pinguino, which is the oldest eruptive unit within the sequence. At a similar MgO content as Dragón, Del Norte is still more

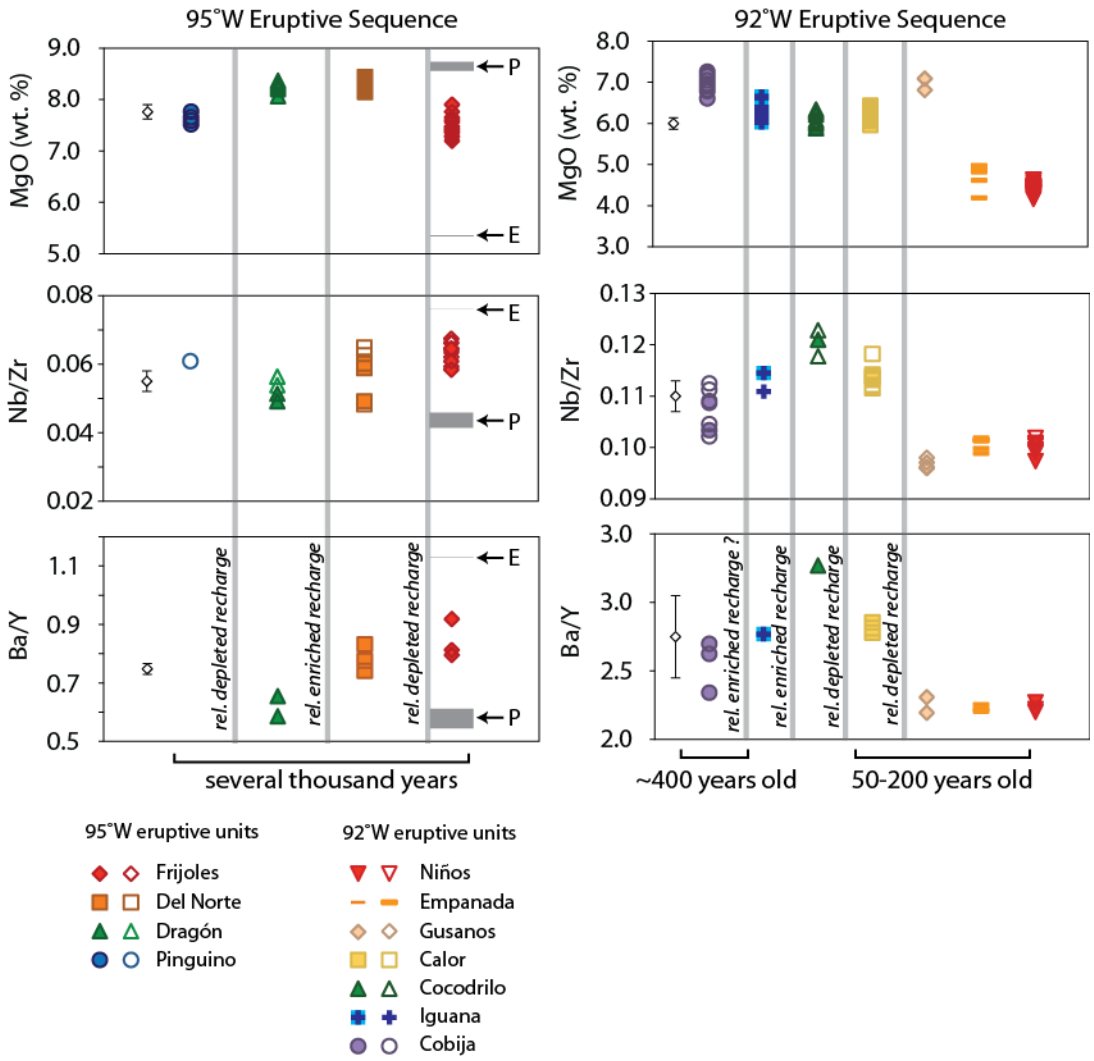

Figure 4.16. Constraints on timing of recharge events for eruptions within mapped eruptive sequences at 95°W and 92°W. Note difference in x-axis scale between low- and high-magma-supply study areas. Hollow symbols, XRF analyses of whole-rock samples. Filled symbols, ICP-MS (for Ba/Y) or EMP (for MgO) analyses of glass chips. Grey bars bracketing Frijoles compositions represent estimates of high- and low-MgO mixing end-members (see Section 4.7.6 for discussion). Error bars represent ±2σ uncertainty.

enriched in incompatible elements. Compositional variations within Frijoles indicate that it is a mixture of a relatively low-MgO, incompatible-element enriched magma and a magma with higher MgO that is also more depleted than Del Norte (see Section 4.7.6). The result that each eruption is preceded by a period of recharge from the mantle is consistent with arguments that eruptible magma is mainly only present beneath low-magma supply ridges after recharge from the mantle (Sinton & Detrick, 1992). The preservation of reverse zoning in olivine crystals requires that the period between

recharge and eruption is relatively short, supporting the speculation that recharge can trigger eruptions at low-magma-supply ridges (Sinton & Detrick, 1992).

4.7.5.2. Magmatic recharge at the high-magma-supply study area

At 92°W, chemical relations among the four oldest flow fields shown in Figure 4.16 (from oldest to youngest: Cobija, Iguana, Cocodrilo, Calor) require magmatic recharge between each of these eruptions. These eruptive units have been partially buried by later eruptions, and it is possible that additional eruptions occurred over the same interval of time that were subsequently buried. Interestingly, none of these units contains reversely zoned crystals. If recharge preceded each of these eruptions, sufficient time for magma homogenization and crystal re-equilibration or physical segregation from the melt must have elapsed between recharge-induced mixing and eruption. This result contrasts with that at low magma supply where recharge and eruption appear to be more closely linked in time.

Gusanos was most likely emplaced during the subsequent eruption. Its higher MgO and lower ratios of highly to moderately incompatible elements relative to Calor require that recharge occurred between these eruptions. Reversely zoned plagioclase crystals in samples from Gusanos also are consistent with this interpretation. In contrast, chemical relations do not require recharge before the two most recent eruptions, Empanada and Niños (average MgO decreases slightly, with variations in major and trace elements consistent with fractionation; no reversely zoned crystals have been found). MELTS-derived liquidus temperatures for glasses from each eruptive unit (Ghiorso & Sack, 1995; Smith & Asimow, 2005) indicate that compositional differences between Gusanos and Niños are associated with a decrease in magma temperature of ~ 70°C, indicating significant cooling of the magma reservoir over this interval. Most of the cooling occurred between eruption of Gusanos and Empanada. If cooling rates have been constant then a longer interval of quiescence preceded the Empanada eruption, while Ninos followed Empanada with only slight change in temperature. Since the sequence of eruptions from Calor to Ninos are constrained by paleointensity to have occurred within ~150 years of one another, cooling rates must have been greater than ~0.5°C per year,

similar to cooling rates within the upper crust of 1°C per year predicted by Maclennan *et al.* (2005).

Magmatic recharge is apparently not required to explain compositional variations among Gusanos, Empanada, and Niños; estimates of the volume erupted during this sequence can be used to assess whether the three eruptions could have been fed by magma within a reasonably sized melt lens without any recharge. Following the approach of Soule *et al.* (2007), the volume of magma removed from the magma reservoir is calculated as the sum of the eruptive volume (from Colman *et al.*, 2012) and the volume of a 1-m wide dike (Qin *et al.*, 2008) that connects the magma reservoir to the surface along the length of the eruptive fissure. If we assume that the depth of the magma reservoir has remained roughly constant over the past ~200 years while these eruptive units were being emplaced, the current magma reservoir depth of ~1.7 km (Blacic *et al.*, 2004) can be used as the height of the dike. The cumulative volume removed from the magma reservoir during this sequence is 0.19 km^3. This volume could easily have been accommodated within a melt lens that was the length of the spreading segment (~30 km (Sinton *et al.*, 2003)), 0.5-1.5 km wide (Blacic *et al.*, 2004), and 50-100 m thick (Kent *et al.*, 1993; Hussenoeder *et al.*, 1996). Even after accounting for the 50% crystallization of the melt lens indicated by compositional variations within this eruptive sequence, a melt lens that was 50-m thick after the last recharge event would contain 33% of its original melt volume after this crystallization and eruption sequence.

Observations at our study areas are consistent with predictions of the importance of recharge to eruptions at mid-ocean ridges with and without persistent melt lenses (e.g., Liu & Lowell, 2009; Fontaine *et al.*, 2011). At rates of magma supply that are high enough to maintain a melt-rich lens within the crust, tectonic spreading events cause magma to be erupted in the absence of recharge events (e.g., Sinton & Detrick, 1992). In contrast, at rates of magma supply that are insufficient to maintain a melt-rich lens, magmatic systems may be too crystal-rich to erupt much of the time, so that eruptions can only occur shortly after a magmatic recharge event; tectonic spreading events in the absence of recent recharge occur without eruption (e.g., Sinton & Detrick, 1992).

4.7.6. Magma mixing at 92°W and 95°W

Magma mixing is predicted to be an important process in mid-ocean ridge magmatic systems (e.g., Sinton & Detrick, 1992). Textural evidence of magmatic mixing at mid-ocean ridges is well-documented, particularly in plagioclase crystals in porphyritic samples from the Mid-Atlantic Ridge (Dungan & Rhodes, 1978; Rhodes *et al.*, 1979; Kuo & Kirkpatrick, 1982; Meyer & Shibata, 1990; Costa *et al.*, 2010). Plagioclase- and olivine-hosted melt inclusions have been used to constrain the compositions of mixing magmas (Dungan & Rhodes, 1978; Rhodes *et al.*, 1979), and the lack of highly evolved lava compositions erupted at slow-spreading ridges has been attributed to the importance of magma mixing in modulating erupted compositions (Dungan & Rhodes, 1978; Rhodes *et al.*, 1979; Walker *et al.*, 1979). Magma mixing also provides a mechanism for producing magmas in which clinopyroxene crystallizes before olivine, contrary to the sequence expected during low-pressure fractionation of mantle-derived mid-ocean ridge basalts (Walker et al., 1979). Although textural evidence for mixing is less common in the nearly aphyric basalts that dominate the East Pacific Rise, Bergmanis *et al.* (2007) identified mixing trends in trace element and Pb isotope ratios of individual eruptive units at 17.5°S on the East Pacific Rise.

Identification of mixing trends in glass samples is dependent on how chemically distinct the mixing magmas are, how completely they are homogenized before erupting, and how well the resulting flow field is sampled. Detailed study of mixing trends can allow the compositions and proportions of the mixing end-members to be constrained (e.g., Passmore *et al.*, 2012), whereas diffusion modeling of zoning profiles in phenocrysts of mixed magmas can be used to determine the timescales of mixing and ensuing eruption (Costa *et al.*, 2010).

Eruptive units within both of our study areas contain textural evidence for magma mixing. Nearly every eruptive unit (except Buho) at the low-magma-supply study area contains plagioclase with partially resorbed cores and/ or reverse zoning. At the high-magma supply study area, although the majority of eruptive units contain only weakly normally zoned or oscillatory zoned crystals, both Gusanos and Dulces contain reversely zoned crystals. Additionally, compositional trends within the Frijoles, Altares, and Dulces eruptive units are inconsistent with fractional crystallization (Figs. 4.10, 4.11). In

many other eruptive units (e.g., Del Norte, Dragón, Pinguino, Pulgar, Tortuga), the amount of compositional variation relative to analytical precision is insufficient to determine whether or not the intra-unit trends are consistent with fractional crystallization.

4.7.6.1. Case study: Frijoles

We focus here on Frijoles, which is exceptionally well-exposed and sampled along the length of the eruptive fissure (Fig. 4.17). Frijoles samples contain normally and reversely zoned olivine, clinopyroxene, and plagioclase crystals and show enrichments in incompatible elements and ratios of highly to moderately incompatible elements at low MgO contents, relative to those predicted by fractional crystallization of the highest-MgO Frijoles sample.

Assuming that olivine crystals within Frijoles samples are not xenocrysts randomly incorporated during ascent, the forsterite contents of the cores of normally and reversely zoned olivines can be used to constrain the compositions of the high-MgO and low-MgO mixing end-members, respectively. Using a distribution coefficient of 0.3 for Fe-Mg partitioning between olivine and melt (Roeder & Emslie, 1970), we estimate the MgO content of the magma in equilibrium with each olivine, assuming that the MgO-Mg# covariation is similar to that of other samples in Frijoles. The highest- and lowest-forsterite olivines measured (Fo_{86} and Fo_{76}) yield estimates of 8.8 and 5.3 wt. % MgO, respectively, for the composition of the mixing end-members (Fig. 4.18).

An independent constraint on mixing end-member compositions comes from K/Ti of olivine-hosted melt inclusions (data from Colman *et al.*, submitted manuscript). Although the median K/Ti of 31 melt inclusions from Frijoles is within error of the selvage glasses (median K/Ti is 0.125 and 0.123 for the melt inclusions and selvage glasses, respectively), melt inclusion K/Ti contents range to significantly higher and lower values, suggesting that the melt inclusions sampled less homogenized magmas. The negative correlation between MgO and K/Ti in Frijoles selvage glasses indicates that the high-MgO end-member had lower K/Ti than the low-MgO end-member (Fig. 4.18). By extrapolating the MgO-K/Ti covariation defined by selvage glasses to the lowest and highest K/Ti preserved in melt inclusions, we can estimate the MgO content of the

mixing end-members. The lowest and highest K/Ti melt inclusions measured (0.09 and 0.15, respectively) provide independent MgO estimates of 8.6 and 5.3 wt. %, remarkably consistent with the estimates based on olivine forsterite content (Fig. 4.18).

The range of liquidus temperatures predicted by MELTS (Ghiorso & Sack, 1995; Smith & Asimow, 2005) for high- and low-MgO end-member magmas are 1207-1210°C and 1158-1165°C, respectively. Assuming that the temperature of magma recharging the magmatic system is relatively constant, this temperature difference between the end-members indicates cooling of 50° between the two most recent recharge events in this location. The estimates of the recharged and resident magmas can also be used to compute the relative proportions of each end-member in each sample (Fig. 4.17). The mixture consistently contains at least 50% high-temperature end-member, and locally as much as 75%. Along-axis variations in the proportions of the end-members do not appear to correlate with the distribution of erupted volume; the location along the eruptive fissure where flow apparently focused is offset from the location with highest MgO and the greatest inferred proportion of relatively hot, recharged magma. Similar observations were made by Bergmanis *et al.* (2007) in the N1 flow field along the southern East Pacific Rise.

Magma mixing likely preceded eruption of many of the other eruptive units at 95°W (e.g., Altares, Del Norte, Dragón as evidenced by disequilibrium textures in plagioclase +/- pyroxene crystals). The lack of zoned olivines, more limited major element range, and higher glass MgO of Del Norte and Dragón suggests that mixing involved a greater proportion of high-MgO relative to low-MgO magma, and/or that more time elapsed between recharge and eruption, allowing melt homogenization to proceed to a greater degree and olivine crystals to re-equilibrate.

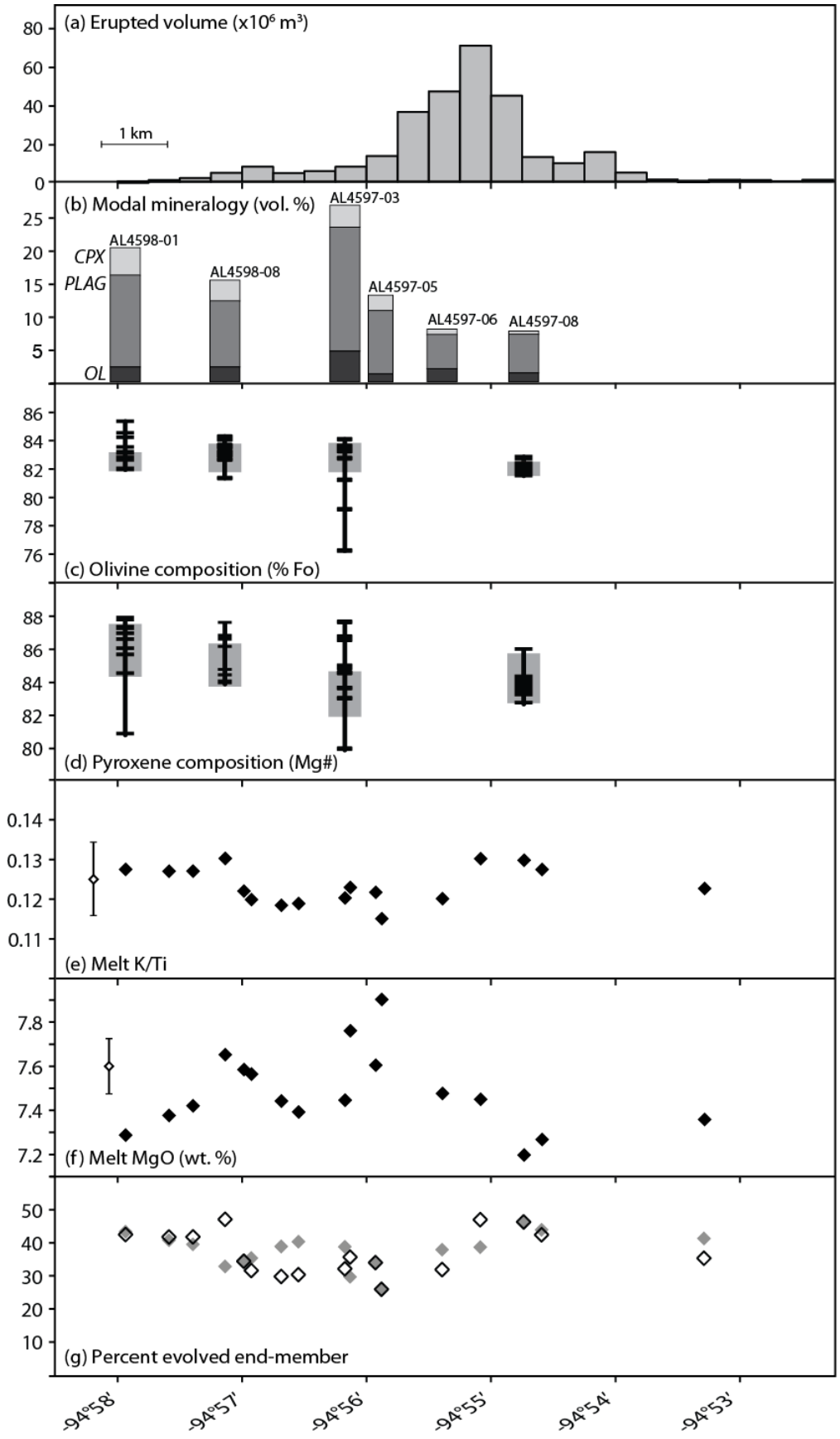
(a) Erupted volume (x10⁶ m³)
1 km
(b) Modal mineralogy (vol. %)
AL4598-01
AL4598-08
AL4597-03
AL4597-05
AL4597-06
AL4597-08
CPX
PLAG
OL
(c) Olivine composition (% Fo)
(d) Pyroxene composition (Mg#)
(e) Melt K/Ti
(f) Melt MgO (wt. %)
(g) Percent evolved end-member
-94°58'
-94°57'
-94°56'
-94°55'
-94°54'
-94°53'

Figure 4.17 (Previous page.) Along-axis variations in mineralogy, mineral chemistry, and glass composition within Frijoles eruptive unit. (a) Along-axis distribution of eruptive products within Frijoles eruptive unit, demonstrating that most lava was erupted near 95°55'W (modified from Colman *et al*., 2012). (b) Modal mineralogy. (c) Variations in Fo of olivine crystals along axis. Bars are analyses of olivine cores; gray fields are range of compositions of rims. (d) Variations in Mg# of pyroxene crystals along axis. Symbols as in (c). (e) Melt K/Ti (EMP glass analyses; data from Colman *et al*., 2012) (f) Melt MgO (EMP glass analyses, data from Colman et al., 2012). (g) Variations in proportions of mixing end-members. End-member compositions were calculated based on extreme compositions of olivine (see text for discussion). Solid symbols, based on melt MgO. Open symbols, based on K/Ti.

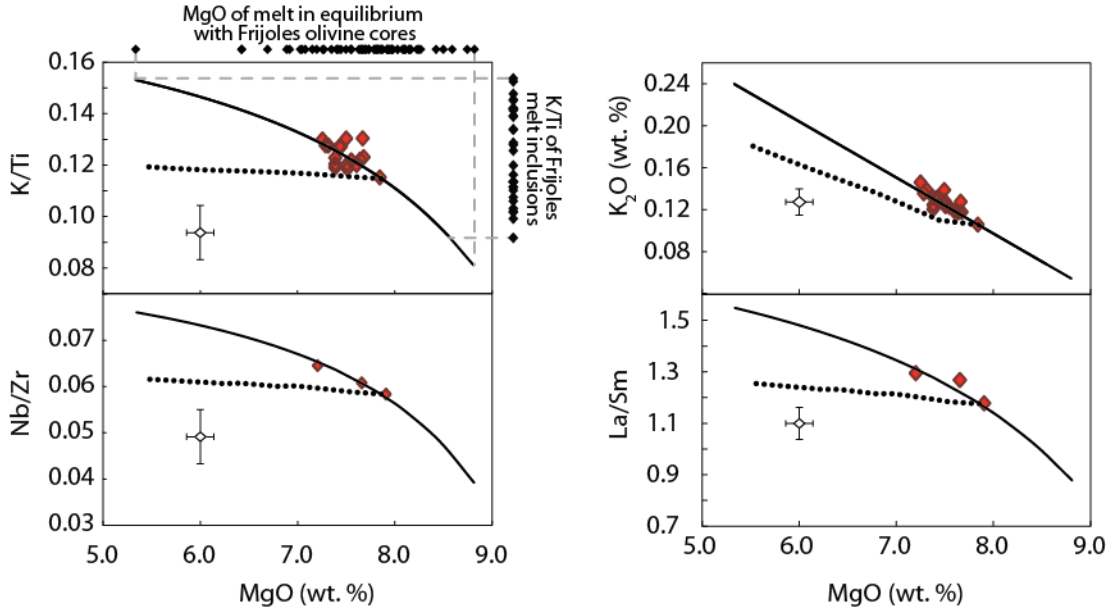

Figure 4.18. Mixing trend defined by samples from Frijoles. Red diamonds, Frijoles samples; gray circles, other samples from 95°W. Solid lines are fractional crystallization trends calculated using MELTS, using the highest-MgO sample from Frijoles as the parental magma. Dashed black line is a mixing trend between primitive and evolved mixing end-members. In plot of K/Ti vs. MgO, black diamonds demonstrate how compositions of melt inclusions and melts in equilibrium with olivine cores were used to constrain compositions of mixing end-members (see text for discussion).

4.7.6.2. Case study: Dulces

Dulces contains reversely zoned clinopyroxene and plagioclase crystals, and normally zoned olivine crystals, which can be used to place constraints on the mixing end-members. The most forsteritic olivine core measured in Dulces (Fo_{72}) is in equilibrium with a melt with 5.0 wt. % MgO (Fig. 19). A mixing line extrapolated from

the analyses of Dulces samples intersects the trend of other high-magma-supply samples near 5.0 wt. % on a range of major element plots. This analysis assumes no partial equilibration of Dulces olivines with the hybrid magma following mixing. However, if significant partial equilibration did occur (implying greater than 5.0 wt. % MgO in the MgO-rich magma), the high-MgO magma's FeO* would have been anomalously high in FeO* relative to other magmas from 92°W at a similar MgO content. Given the limited variation in FeO* at a given MgO content at 92°W (Fig. 11), this possibility seems unlikely. Therefore, minimal post-mixing re-equilibration of olivine crystals within Dulces implies a limited time period between mixing and eruption. The inferred composition of the high-MgO mixing end-member is similar to that of Empanada lavas. Dulces is also similar in age to Empanada (50-200 years old (Bowles *et al.*, 2014)), based on relatively little sediment cover and the fact that both eruptive units are younger than Cocodrilo. Although an absolute age for Dulces has not been determined, this eruptive unit was likely also erupted within the past 50-200 years.

It is more difficult to constrain the composition of the low-MgO end-member based on the reversely zoned plagioclase and pyroxene crystals, because of the relatively poor correlations between MgO and the anorthite content of plagioclase or Mg# of pyroxene. The low-MgO magma must have had < 2.7 wt. % MgO, however, as this is the most evolved glass composition analyzed from the Dulces flow field. Inncreasing P_2O_5 with decreasing MgO among samples from Dulces suggests that apatite has not begun to crystallize in the low-MgO mixing end-member. Apatite is present in an andesite sample with 1.2 wt. % MgO from 85°W on the GSC (Fornari *et al.*, 1983; Perfit & Fornari, 1983); if apatite stability is similar at 92°W, the low-MgO mixing end-member is not likely to have less than ~1.2 wt. % MgO. Similarities in incompatible element ratios of Dulces with Gusanos, Empanada, and Niños are consistent with the low-MgO mixing end-member having been derived from a similar parental magma (Fig. 11). This magma may have become isolated from the larger volume of the melt lens, allowing it to cool and fractionate to a greater extent. Thus the mixing trend within Dulces may record lateral injection of magma into a cooler, more crystal-rich portion of the sub-axial melt lens. MELTS-derived liquidus temperatures for magmas with 2.7 and 5.0 wt. % MgO are

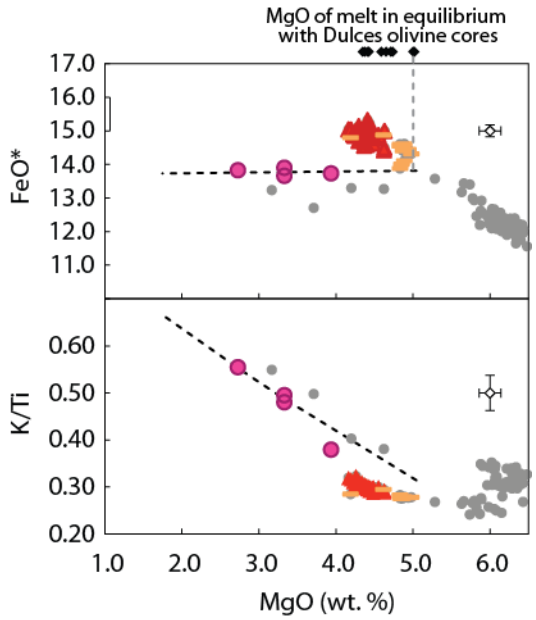

Figure 19. Mixing trend within Dulces. Note that if the high-MgO mixing end-member had > 5 wt. % MgO, its FeO* content would have to be higher than in other magmas with similar MgO for the mixing trend to pass through samples from Dulces.

1070°C and 1120°C, respectively, which could reflect the along-axis variability of temperatures and degrees of fractionation within the magma reservoir.

4.8. Conclusions

At the low-magma-supply study area, where magma is thought to reside intermittently at ~3 km below the seafloor, lavas are restricted to relatively unfractionated melt compositions (6.2-9.1 wt. % MgO). Magmatic evolution at this location is likely dominated by processes involving crystal-rich mush, and preserved by limited evolution in melt-dominated magma reservoirs. Eruptions at this study area appear to be closely linked to magmatic recharge; relatively evolved eruptive units consistently have compositional trends controlled by mixing of high-MgO magma with lower-MgO magma with distinct parental magmas. Between eruptions, mush-zone processes, as simulated by *in situ* crystallization, appear to be important in controlling magma compositions. Although no melt lens has been detected by seismic studies at this location, some melt is apparently able to remain in the crust between eruptions and mix with fresh batches of magma.

In contrast, at the high-magma-supply study area, where a seismically imaged melt lens is located ~1.7 km below the seafloor, fractional crystallization within a melt-rich magma reservoir causes large variations in major-element compositions with little

effect on trace element concentrations or ratios. Between magmatic recharge events, resident magma fractionates, and can be repeatedly tapped by low-volume fissure eruptions. Small bodies of magma may become isolated from the larger magmatic system, allowing more extreme degrees of fractionation. These may be remobilized by lateral injection of magma during diking events, allowing the eruption of highly evolved magmas.

An important implication of this study is that persistent melt lenses at intermediate rates of magma supply need not be "steady-state" melt lenses. At 92°W, the seismic melt lens reflector is strong and nearly continuous along the ridge axis (Blacic *et al.*, 2004). Nevertheless, differences in the compositions of lava erupted over the past several hundred years indicate that temperatures within the melt lens have varied by up to 100°C (1070-1170°C). If the last three eruptions occurred without intervening magmatic recharge, as suggested by the systematic decrease in MgO and limited variation in incompatible element ratios, there must have been a significant decrease in the volume of the melt lens over this limited time period as well. Only by documenting variations in magma composition at a given location can the temporal variability in magma reservoir properties at the scale of multiple eruptive episodes be constrained.

4.9. Appendix: Petrographic descriptions of thin samples

4.9.1. 95°W study area

AL4594-02 (Altares). Olivine-, plagioclase-, and clinopyroxene-phyric basalt. Clear, light brown glassy margin grades to spherulitic interior. Vesicles are round (0.2-1 mm) or irregularly shaped (< 1.5 mm). Olivine is typically skeletal (< 0.2 mm) and occurs as lone crystals or in clusters or intergrowths with plagioclase. Plagioclase is lath-shaped, blocky, or tabular. Some blocky crystals have oscillatory concentric zoning. Dendritic overgrowths are common. Some tabular crystals have boxy cellular rims. Clinopyroxene forms sector-zoned crystals (< 0.5 mm) that are commonly intimately intergrown with plagioclase laths. Clinopyroxene also occurs as euhedral or rounded crystals (< 1.5 mm), often simply twinned, either alone or poikilitically enclosing tabular plagioclase crystals.

AL4594-03 (Altares). Olivine-, plagioclase-, and clinopyroxene-phyric basalt. Clear, light brown glassy margin grades to spherulitic interior. Vesicles are round (0.2-0.4 mm) or irregularly shaped (may be several mms). Olivine is euhedral to skeletal (commonly < 1.5 mm; rarely up to 4 mm). Olivine occurs alone or in intergrowths with plagioclase. Plagioclase is lath-shaped, blocky, or tabular. Some blocky and tabular crystals have oscillatory concentric zoning. Plagioclase occurs alone, in clusters of plagioclase, or in intergrowths with clinopyroxene or olivine. Clinopyroxene forms sector-zoned crystals (0.1-0.5 mm) that are commonly intergrown with plagioclase laths. Clinopyroxene also rarely forms euhedral crystals without sector zoning (0.4-1.2 mm).

AL4594-04 (Altares). Olivine-, plagioclase-, and clinopyroxene-phyric basalt. Clear, light brown glassy margin grades to spherulitic interior. Vesicles are round (0.1-0.5 mm). Olivine (< 1 mm) is typically euhedral to slightly skeletal, and may have dendritic overgrowths. Plagioclase morphology is highly variable, including laths, tabular, and blocky crystals. Plagioclase also occurs as irregular clusters of blocky crystals, and commonly has oscillatory zoning. Some plagioclase crystals also have spongy cellular or boxy cores. Large (1-2 mm) clinopyroxene crystals may be euhedral or have rounded margins, and commonly have blocky or tabular plagioclase inclusions (fully surrounded). Smaller clinopyroxene crystals (typically < 0.5 mm) are sector-zoned and form intergrowths with plagioclase laths.

AL4594-11 (Altares). Olivine-, plagioclase-, and clinopyroxene-phyric basalt. Clear, light brown glassy margin with abundant microlites grades to microcrystalline interior. Vesicles are round (0.1-0.2 mm) to slightly irregularly shaped (< 0.4 mm). Olivine (< 2 mm) is euhedral to highly skeletal. Plagioclase morphology ranges from laths to tabular or blocky crystals. Larger crystals are commonly oscillatory zoned and may have spongy or boxy cellular cores or rims. Plagioclase often occurs as irregular clusters of blocky or tabular crystals up to 3 mm in diameter. Clinopyroxene typically occurs as sector-zoned crystals (typically < 0.6 mm) intergrown with plagioclase laths, but also occurs as lone, euhedral crystals (< 0.4 mm).

AL4601-06 (Buho). Sparsely olivine-phyric basalt. Clear, light brown glassy margin grades to devitrified interior. Rare vesicles are round (0.1-0.5 mm). Olivine (< 1 mm) is skeletal or euhedral, and sometimes has dendritic overgrowths.

AL4603-09 (Buho). Sparsely olivine-phyric basalt, glassy throughout sample. Vesicles are round (0.4-1 mm). Glass is clear, and light brown in color, with rare round vesicles. Olivine skeletal to euhedral, typically < 0.5 mm.

AL4603-13 (Buho). Sparsely olivine- and plagioclase-phyric glassy basalt. Clear, light brown glass grades to spherulitic interior. Vesicles are round (0.1-0.6 mm) or irregularly shaped (typically elongate, < 2.5 mm long). Olivine is skeletal to euhedral, equant, typically < 0.5 mm. Plagioclase microphenocrysts are less abundant, forming highly elongate laths up to 1 mm long, with swallow tails.

AL4604-02 (Buho). Sparsely olivine- and plagioclase-phyric glassy basalt. Clear, light brown glass grades to microcrystalline interior. Vesicles are small and round (0.1-0.2 mm). Olivine is skeletal to euhedral, equant, typically < 0.8 mm, and may have dendritic overgrowths. Plagioclase microphenocrysts are common but smaller, forming laths up to 0.4 mm long. Interior contains abundant plagioclase microlites.

AL4604-03 (Buho). Olivine- and plagioclase- phyric basalt. Clear, light brown glass grades to spherulitic interior. Vesicles are round (< 0.5 mm) or irregularly shaped (typically elongate, and < 1 mm long). Olivine crystals are typically skeletal (< 1 mm) and occur as lone crystals, in clusters, or intergrown with plagioclase. Plagioclase forms lath-shaped crystals and, rarely, tabular crystals. Dendritic overgrowths are common.

AL4597-03 (Frijoles). Olivine-, plagioclase-, and clinopyroxene-phyric basalt. Clear, light brown glassy margin grades to microcrystalline interior. Vesicles are round (0.1-0.8 mm) or irregularly shaped (< 1.5 mm). Olivine (up to 3 mm; commonly < 1 mm) is euhedral or slightly skeletal and occurs alone or intergrown with plagioclase. Plagioclase morphology is highly variable, including laths, tabular, and blocky crystals. Dendritic

overgrowths (swallowtails) are rare. Plagioclase also occurs as glomerocrysts with cumulate textures; in these clusters, there may be 120 degree crystal contacts (dihedral angles?) indicating an approach to textural equilibration. Plagioclase also occurs as xenocrysts (up to 6 mm long). Oscillatory zoning is common. Clinopyroxene morphology is also highly variable. Clinopyroxene occurs as medium-sized euhedral crystals, often with a simple twin (?) (< 1 mm), sometimes poikilitically surrounding small, tabular (blocky?) plagioclase crystals. Other, typically smaller clinopyroxene crystals, are sector-zoned and intergrown with plagioclase. The plagioclase is often arranged so as to radiate outward from the center of the clinopyroxene, with plagioclase laths widening outward, indicating the co-precipitation of the phases. Clinopyroxene also rarely occurs as nearly euhedral crystals up to 2 mm with small, crystallographically oriented exsolution lamellae of low-Ca pyroxene.

AL4597-05 (Frijoles). Olivine-, plagioclase-, and clinopyroxene-phyric basalt. Clear, light brown glassy margin grades to spherulitic interior. Vesicles are round (0.1-0.4 mm) or slightly irregularly shaped (< 0.4 mm). Olivine (up to 2 mm, commonly < 0.5 mm) is euhedral or slightly skeletal. Plagioclase occurs as laths, tabular and blocky crystals. Dendritic overgrowths (swallowtails) are rare. Oscillatory zoned crystals are relatively rare, but present. Some of the larger crystals (~1 mm) have boxy cellular rims. Clinopyroxene occurs as euhedral crystals (< 1.5 mm) that may contain (or partially contain) small (< 0.4 mm), tabular plagioclase inclusions. Clinopyroxene also occurs as sector-zoned crystals (< 1 mm), typically intergrown with lath-shaped plagioclase. This thin section contains what appear to be fragments of a disaggregated olivine-plagioclase-clinopyroxene-phyric mush. Where they are in contact with glass, olivine and clinopyroxene crystals have rounded margins, whereas plagioclase crystals have irregular, angular margins. The rims of clinopyroxene crystals commonly have a spongy cellular texture.

AL4597-06 (Frijoles). Olivine-, plagioclase, and clinopyroxene-phyric basalt. Clear, light brown glassy margin grades to microcrystalline interior. Vesicles are round (0.1-0.5 mm) or irregularly shaped (< 0.6 mm). Olivine occurs as euhedral to skeletal crystals (< 1

mm), typically alone. Some olivine crystals have dendritic overgrowths at the Plagioclase ranges from laths to blocky to tabular; dendritic overgrowths (swallowtails) are rare, but present. Clinopyroxene occurs as sector-zoned crystals (< 0.5 mm) that are typically intergrown with plagioclase laths. Larger euhedral to subhedral clinopyroxene crystals (up to 2 mm) typically lack sector zoning, often have simple twins, and may poikilitically enclose small, blocky (?) plagioclase crystals.

AL4597-08 (Frijoles). Olivine-, plagioclase-, and clinopyroxene-phyric basalt. Clear, light brown glassy margin grades to microcrystalline interior. Vesicles are round (0.1-0.5 mm) or irregularly shaped (< 2.5 mm). Olivine crystals (typically < 0.5 mm; rarely up to 2 mm) are skeletal and may form loose clusters or intergrowths with plagioclase laths. Plagioclase occurs as laths or as tabular crystals, and may form clusters of either purely plagioclase or plagioclase-olivine intergrowths. Oscillatory zoning and dendritic overgrowths (swallowtails) are both rare. Clinopyroxene occurs as sector-zoned crystals (<1 mm), commonly intergrown with plagioclase laths. Clinopyroxene only rarely occurs without sector zoning, in simply twinned crystals intergrown with tabular plagioclase.

AL4598-01 (Frijoles). Olivine-, plagioclase-, and clinopyroxene-phyric basalt. Clear, light brown glass throughout is locally devitrified in contact with crystals. Vesicles are round (0.1-1 mm) or slightly irregularly shaped (< 1.2 mm). Olivine (< 2 mm) is euhedral to skeletal, and typically occurs alone. Plagioclase morphology ranges from lath-shaped to tabular to blocky. Concentrically zoned plagioclase crystals are rare. Blocky and tabular plagioclase crystals sometimes form large clusters (up to 3 mm). Clinopyroxene commonly occurs as blocky, euhedral to subhedral crystals (< 2 mm). Sector-zoned clinopyroxene also can form intergrowths with plagioclase. Clinopyroxene also rarely occurs as irregularly-shaped crystals with a fine boxy cellular texture.

AL4598-08 (Frijoles). Olivine-, plagioclase-, and clinopyroxene-phyric basalt. Clear light brown glass throughout is locally devitrified in contact with crystals. Vesicles are round (1-4 mm) or slightly irregularly shaped (<0.8 mm). Olivine occurs as euhedral to skeletal (rarely dendritic) crystals (< 2 mm). Plagioclase forms lath-shaped, tabular, or blocky

crystals that typically lack dendritic overgrowths (swallowtails). Clinopyroxene forms blocky crystals (up to 4 mm) with euhedral or somewhat rounded margins that poikilitically enclose tabular plagioclase crystals. Sometimes these crystals have rims where lath-shaped plagioclase crystals are abundant. Clinopyroxene also occurs as smaller (< 0.5 mm) sector-zoned crystals intergrown with lath-shaped plagioclase.

AL4598-11 (Del Norte). Olivine- and plagioclase-phyric glassy basalt. Clear, light brown glass is locally devitrified against crystals. Vesicles are round (< 0.6 mm). Olivine crystals are small (< 0.5 mm) and euhedral to slightly skeletal; olivine forms lone crystals and intergrowths with plagioclase laths. Plagioclase form lath-shaped crystals or blocky or tabular crystals. Some larger crystals (1-2 mm) have spongy cellular cores and/ or concentric oscillatory zoning. Plagioclase occurs as lone crystals, in intergrowths with olivine, or as clusters of blocky crystals. Small dendritic overgrowths (swallowtails) are present on some elongate crystals.

AL4599-05 (Del Norte). Olivine-, plagioclase, and clinopyroxene-phyric basalt. Clear, light brown glass is present throughout thin section. Vesicles are round (< 0.5 mm). Olivine typically occurs as euhedral crystals (< 1 mm), sometimes with small dendritic overgrowths. Rare larger olivine crystals (up to 2 mm) are more irregularly shaped and sometimes occur intergrown with large, blocky plagioclase. Plagioclase occurs as blocky or tabular crystals, and rarely as lath-shaped crystals. Plagioclase typically forms clusters in which crystals may be aligned, or more randomly oriented. Concentric oscillatory zoning is common, and cellular regions occasionally occur either in the rim (typically boxy) or the cores (typically spongy). Clinopyroxene crystals (0.5-2 mm) are anhedral, with well-rounded or more irregular margins and commonly have a spongy cellular texture. Euhedral clinopyroxene crystals are not present. The clinopyroxene crystals with irregular margins contain abundant embayments and/ or melt inclusions.

AL4599-08 (Del Norte). Olivine- and plagioclase-phyric glassy basalt. Clear, light brown glass grades to spherulitic interior. Vesicles are round (0.1-0.5 mm) or irregularly shaped (typically elongate, <1.5 mm long). Olivine crystals are larger than in AL4598-11 (up to

1 mm) and euhedral to highly skeletal. Olivine forms lone crystals, intergrowths with plagioclase laths, or clusters (several mm across) composed of smaller plagioclase and olivine crystals (typically < 0.5 mm). Plagioclase occurs as laths or as tabular or blocky crystals (up to 2 mm long). Concentric oscillatory zoning is common in blocky plagioclase crystals. Dendritic overgrowths (swallowtails) are common on plagioclase crystals.

AL4599-10 (Del Norte). Olivine- and plagioclase-phyric basalt. Clear, light brown glass grades to spherulitic interior. Vesicles are round (typically 0.2-0.6 mm). Olivine (up to 1 mm, but typically < 0.5 mm) occurs as euhedral crystals, sometimes with small dendritic overgrowths. Olivine forms lone crystals or in intergrowths with plagioclase. Plagioclase occurs as lath-shaped, blocky, or tabular crystals, and commonly forms clusters. Elongate crystals commonly have dendritic overgrowths. Rare plagioclase crystals with a pervasive spongy cellular texture are also present. Concentric oscillatory zoning is common.

AL4599-03 (Dragón). Olivine- and plagioclase-phryic basalt. Clear, light brown glass grades to spherulitic interior. Vesicles are round (< 0.5 mm) or irregularly shaped (may be several mm across). Olivine (0.2-1 mm) is euhedral and occurs as lone crystals or intergrown with plagioclase. Plagioclase is typically tabular or blocky, and more rarely occurs as lath-shaped crystals. Oscillatory concentric zoning is common. Dendritic overgrowths are common on elongate crystals. Some of the larger, blocky plagioclase crystals contain abundant melt inclusions in the core. Rare plagioclase crystals with a pervasive boxy cellular texture are also present.

AL4600-13 (Dragón). Sparsely olivine- and plagioclase-phyric basalt. Clear, light brown glass grades to spherulitic interior. Vesicles are round (0.1-1 mm) or slightly irregular (typically < 0.5 mm long). Olivine is typically < 0.5 mm and euhedral to slightly skeletal. Olivine forms lone crystals, clusters, and intergrowths with plagioclase. Plagioclase occurs as laths, tabular, or blocky crystals. Elongate crystals commonly have dendritic

overgrowths (swallowtail morphology). Some blocky plagioclase crystals have spongy cellular cores or boxy cellular rims.

EW65D (Pinguino). Olivine-, plagioclase, and clinopyroxene-phyric basalt. Clear, light brown glass grades to microcrystalline interior. Vesicles are round to slightly irregular in shape (0.1-0.4 mm). Olivine occurs as euhedral to highly skeletal crystals (< 1 mm), as lone crystals or in intergrowths with plagioclase. Plagioclase is lath-shaped, blocky, or tabular. Some elongate crystals have well-developed dendrites (swallowtails)(?) or hopper morphology. Oscillatory concentric zoning is common. Clinopyroxene forms sector-zoned crystals (< 0.4 mm), often in intergrowths with plagioclase.

AL4604-05 (Pulgar). Olivine-, plagioclase, and clinopyroxene-phyric basalt. Clear, light brown glass grades to spherulitic interior. Vesicles are round (0.1-0.6 mm) or irregularly shaped (typically elongate, < 2 mm). Olivine is euhedral to highly skeletal (< 2 mm) and occurs alone, in clusters, or intergrown with plagioclase. Plagioclase is lath-shaped, tabular, or blocky. Tabular and blocky crystals commonly have oscillatory concentric zoning, and more rarely have spongy or boxy cellular cores. Clinopyroxene is rare (< 1 mm), occurring as simply twinned crystals with rounded margins and abundant plagioclase laths intergrown in the outer rim.

AL4604-07 (Pulgar). Olivine-, plagioclase, and clinopyroxene-phyric basalt. Clear, light brown glass grades to microcrystalline interior. Vesicles are round (typically 0.1-0.5 mm; up to 1 mm) or irregularly shaped (typically elongate, < 0.5 mm long). Olivine forms skeletal crystals (< 2 mm), commonly intergrown with plagioclase. Plagioclase is present as lath-shaped, tabular, and blocky crystals, commonly in clusters or intergrowths with olivine or clinopyroxene. Oscillatory concentric zoning is common. Clinopyroxene forms small (0.1-0.5 mm), sector-zoned crystals with irregular margins, typically intergrown with plagioclase.

AL4604-08 (Pulgar). Olivine-, plagioclase-, and clinopyroxene-phyric basalt. Clear, light brown, glassy rim grades to microcrystalline interior. Vesicles are round (0.1-1.2 mm) or

irregularly shaped (< 0.2 mm). Olivine is euhedral to skeletal (< 1.6 mm) and occurs alone, in clusters, or intergrown with plagioclase. Plagioclase is lath-shaped, blocky, or tabular, and also occurs as intergrowths of plagioclase grains with cumulate textures. Some elongate plagioclase crystals have dendritic overgrowths. Many blocky and tabular crystals have oscillatory concentric zoning. Plagioclase crystals with spongy cores are rare, but present. Clinopyroxene is relatively rare, and forms small (< 0.2 mm), sector-zoned crystals intergrown with plagioclase laths. Clinopyroxene also occurs as larger (< 2 mm), crystals (not sector-zoned) with rounded exteriors, sometimes poikilitically enclosing elongate plagioclase crystals.

AL4604-10 (Pulgar). Olivine-, plagioclase-, and clinopyroxene-phyric basalt. Clear, light brown, glassy rim grades to microcrystalline interior. Vesicles are round (0.2-0.5 mm) or irregularly shaped (<1.5 mm). Olivine is skeletal , up to 2 mm, and may form clusters with tabular plagioclase crystals. Plagioclase may be lath-shaped, blocky, or tabular, and also occurs as large cluster of plagioclase crystals (< 3 mm). Concentrically zoned plagioclase crystals are common. Clinopyroxene is the least abundant phase, and forms sector-zoned crystals intergrown with plagioclase laths (< 1 mm) or occurs alone as euhedral to anhedral crystals (< 1 mm).

AL4593-05 (Tortuga). Olivine- and plagioclase-phyric basalt. Clear, light brown glass grades to microcrystalline interior. Vesicles are round (0.1-0.6 mm) or irregularly shaped (typically elongate, < 1 mm long). Olivine (< 2.5 mm) ranges from euhedral to highly skeletal, and occurs as lone crystals or in clusters or intergrowths with plagioclase. Plagioclase is lath-shaped, blocky, or tabular. Plagioclase occurs alone, in clusters several mm wide of plagioclase, or in clusters with olivine. Many blocky crystals have an irregularly shaped core (often spongy) mantled by a euhedral rim.

AL4593-09 (Tortuga). Olivine- and plagioclase-phyric basalt. Clear, light brown glass is locally devitrified against crystal margins. Vesicles are round (0.1-0.3 mm). Olivine (< 1 mm) ranges from euhedral to highly skeletal, and occurs as lone crystals or in clusters or intergrowths with plagioclase. Plagioclase is lath-shaped, blocky, or tabular. Plagioclase

occurs alone or in clusters with olivine. Some blocky plagioclase crystals have spongy cellular cores.

AL4599-06 (pre- Del Norte flow field). Olivine-, plagioclase, and clinopyroxene-phyric basalt. Clear, light brown glass grades to microcrystalline interior. Vesicles are round or slightly irregularly shaped (0.1-0.6 mm). Olivine is euhedral to slightly skeletal (< 2 mm). Plagioclase is lath-shaped, tabular, or blocky. Concentric oscillatory zoning is common. Many plagioclase crystals have an irregularly shaped core, mantled by a euhedral rim. Clinopyroxene is abundant, and occurs both as sector-zoned crystals intergrown with plagioclase (typically < 0.5 mm) and as larger crystals (< 2 mm) lacking sector-zoning that commonly have a simple twin and sometimes form clusters with plagioclase.

4.9.2. 92°W Low-magma-supply study area

AL4606-09 (Calor). Olivine-, plagioclase-, and clinopyroxene-phyric basalt. Light brown glass grades to microcrystalline interior. Vesicles are round (0.1-1 mm) or irregularly shaped (typically elongate, up to several mm). Olivine is skeletal (typically < 0.5 mm long; rarely up to 1 mm) and commonly occurs in loose clusters with plagioclase and clinopyroxene. Plagioclase predominantly occurs as laths with swallowtail or hopper morphology, and rarely as larger (2 mm), tabular, rounded crystals. Clinopyroxene is sector-zoned and occurs in clusters with plagioclase +/- olivine.

AL4608-07 (Calor). Olivine-, plagioclase-, and clinopyroxene-phyric basalt. Light brown glass grades to microcrystalline interior. Vesicles are round (0.1-0.6 mm) or irregularly shaped (typically elongate, up to several mm). Olivine is skeletal (< 0.4 mm) and commonly occurs in loose clusters with plagioclase +/- clinopyroxene. Plagioclase forms lath-shaped crystals with swallowtail or hopper morphology. Clinopyroxene is sector-zoned and occurs in clusters with plagioclase +/- olivine.

AL4611-07 (Calor). Olivine-, plagioclase-, and clinopyroxene-phyric basalt. Light brown glass grades to microcrystalline interior. Vesicles are round (0.1-1.2 mm) or irregularly

shaped (typically elongate, up to several mm). Olivine is skeletal (< 0.4 mm) and commonly occurs in loose clusters with plagioclase and clinopyroxene. Plagioclase forms lath-shaped crystals with swallowtail or hopper morphology. Clinopyroxene is sector-zoned and commonly occurs in clusters with plagioclase +/- olivine.

AL4616-09 (Calor). Olivine-, plagioclase-, and clinopyroxene-phyric basalt. Light brown glass grades to microcrystalline interior. Vesicles are round (0.1-0.6 mm) or irregularly shaped (typically elongate, up to several mm). Olivine is skeletal (< 0.6 mm) and commonly occurs in clusters with plagioclase and clinopyroxene. Plagioclase forms lath-shaped crystals with swallowtail or hopper morphology. Clinopyroxene is sector-zoned (typically < 0.4 mm) and commonly occurs in clusters with plagioclase +/- olivine.

AL4616-14 (Calor). Olivine-, plagioclase-, and clinopyroxene-phyric basalt. Light brown glass grades to microcrystalline interior. Vesicles are round (0.1-0.4 mm) or irregularly shaped (up to several mm). Olivine is skeletal (< 1 mm) and commonly occurs in clusters or intergrowths with plagioclase. Plagioclase is typically lath-shaped with swallowtail or hopper morphology. Clinopyroxene is sector-zoned (< 0.5 mm) and occurs alone or in intergrowths with plagioclase.

AL4610-06 (Cangrejo). Olivine- and plagioclase-phyric basalt. Light brown glass grades to microcrystalline interior with abundant plagioclase microlites. Vesicles are small and round (< 0.2 mm) or larger and more irregularly shaped (up to several mm). Olivine is present as a microlite (< 0.1 mm) and rarely as large, euhedral crystals (< 1.5 mm). Plagioclase occurs as lath-shaped crystals and as larger, tabular or blocky euhedral crystals with oscillatory concentric zoning, some of which have boxy cellular cores.

AL4610-14 (Cangrejo). Plagioclase-phryic basalt. Light brown glass grades to spherulitic interior. Vesicles are round (0.1-1.5 mm) or ovoid. Olivine is present as a microlite (< 0.1 mm) and rarely as slightly larger skeletal crystals (< 0.2 mm). Plagioclase occurs as small lath-shaped crystals and as larger, tabular or blocky euhedral crystals, some of which have oscillatory concentric zoning.

AL4611-03 (Cobija). Olivine-, plagioclase-, and clinopyroxene-phyric basalt. Light brown glass grades to devitrified interior. Vesicles are round (0.1-0.8 mm) or irregularly shaped (typically < 2 mm). Olivine forms skeletal crystals (< 0.4 mm), sometimes intergrown with plagioclase. Plagioclase is lath-shaped, commonly with swallowtail or hopper morphology. Clinopyroxene is sector-zoned (< 0.4 mm) and occurs alone or in intergrowths with plagioclase.

AL4615-08 (Cobija). Olivine- and plagioclase-phyric basalt. Light brown glass grades to microcrystalline interior. Vesicles are round (0.1-0.6 mm) or irregularly shaped (up to several mm). Olivine is skeletal (typically < 0.6 mm) and occurs alone or in intergrowths with plagioclase. Plagioclase is lath-shaped, sometimes with swallowtail or hopper morphology.

AL4616-17 (Cobija). Olivine- and plagioclase-phyric basalt. Light brown glass grades to microcrystalline interior. Vesicles are round (0.1-1 mm) or irregularly shaped (up to several mm). Olivine is skeletal (< 0.4 mm) and occurs alone or in intergrowths with plagioclase. Plagioclase is typically lath-shaped with swallowtail or hopper morphology. Plagioclase also occurs as larger (up to several mm), blocky crystals with rounded or irregular margins.

AL4613-06 (Cocodrilo). Olivine-, plagioclase-, and clinopyroxene-phyric basalt. Light brown glass is locally devitrified in contact with crystals. Vesicles are round (0.1-1 mm) or slightly irregular in shape. Olivine is skeletal (< 0.6 mm) and occurs alone or in intergrowths with plagioclase. Plagioclase occurs as lath-shaped crystals, sometimes with swallowtail or hopper morphology. Clinopyroxene is sector-zoned (< 0.6 mm) and occurs alone or in intergrowths with plagioclase.

AL4614-03 (Cocodrilo). Olivine-, plagioclase-, and clinopyroxene-phyric basalt. Light brown glass grades to microcrystalline interior. Vesicles are round (0.1-0.3 mm) or irregularly shaped (up to several mm). Olivine is skeletal (< 1 mm) and occurs alone or

intergrown with plagioclase. Plagioclase typically forms laths, sometimes with swallowtail or hopper morphology. Plagioclase also occurs rarely as blocky euhedral crystals. Clinopyroxene is sector-zoned (< 0.4 mm), and is typically intergrown with plagioclase.

AL4610-01 (Dulces). Plagioclase- and clinopyroxene-phyric basaltic andesite. Light brown glass grades to microcrystalline interior. Vesicles are round (0.1-1 mm) or irregularly shaped. Plagioclase is lath-shaped or blocky. Blocky crystals commonly have rounded core mantled by euhedral rims. Clinopyroxene is typically sector-zoned.

AL4613-02 (Dulces). Olivine-, plagioclase-, and clinopyroxene-phyric basalt. Light red-brown glass grades to microcrystalline interior. Vesicles are round (0.1-1 mm) or irregularly shaped (typically < 1 mm). Olivine is skeletal (< 0.6 mm) and commonly is intergrown with plagioclase. Plagioclase is lath-shaped or blocky. Some crystals have a rounded core mantled by a euhedral rim. Swallowtail morphology is common. Clinopyroxene occurs mainly as sector-zoned crystals, commonly intergrown with plagioclase. Clinopyroxene is less commonly present as reversely zoned crystals with a rounded core mantled by a euhedral rim.

AL4613-04 (Dulces). Olivine-, plagioclase- and clinopyroxene-phyric basaltic andesite. Light brown glass grades to microcrystalline interior. Vesicles are round (0.1-1.6 mm) or slightly irregular in shape. Olivine is rare, but occurs as skeletal crystals (< 0.4 mm). Plagioclase is lath-shaped, commonly with dendritic overgrowths (swallowtail morphology). Plagioclase also occurs rarely as blocky crystals, sometimes with rounded cores mantled by euhedral or skeletal rims. Clinopyroxene is abundant, commonly sector zoned (< 0.4 mm). Pigeonite is also present.

AL4616-02 (Empanada). Olivine-, plagioclase-, and clinopyroxene-phyric basalt. Red-brown grades to devitrified interior. VESICLES Olivine is skeletal (typically elongate, < 0.8 mm) and is commonly intergrown with plagioclase. Plagioclase is lath-shaped, with

swallowtail or hopper morphology. Clinopyroxene is sector-zoned (< 0.4 mm) and is commonly intergrown with plagioclase.

AL4612-02 (Gusanos). Olivine- and plagioclase-phyric basalt. Light brown glass grades to microcrystalline interior. Vesicles are round (0.1-0.5 mm) or, more commonly, irregularly shaped (several mm). Olivine is skeletal (typically < 1 mm; rarely up to 1.5 mm) and is almost always intergrown with plagioclase. Plagioclase is lath-shaped, tabular, or blocky (up to 2 mm). Many of the tabular and blocky crystals have concentric oscillatory zoning; some have boxy cellular rims. Some of the larger olivine and plagioclase crystals form clusters with associated devitrified glass in regions where the surrounding groundmass is microcrystalline.

AL4612-06 (Gusanos). Olivine- and plagioclase-phyric basalt. Light brown glass grades to microcrystalline interior. Vesicles are round (0.1-0.8 mm) or irregularly shaped (up to several mm). Olivine is skeletal (elongate, < 1 mm), and is typically intergrown with plagioclase. Plagioclase is lath-shaped, tabular, or blocky. Dendritic overgrowths are common. Many of the tabular and blocky crystals have concentric oscillatory zoning; some have boxy cellular rims.

AL4610-09 (Iguana). Aphyric basalt. Light brown glass grades to microcrystalline interior. Vesicles are round (< 0.3 mm) or irregularly shaped (up to several mm). Acicular plagioclase microlites dominate over skeletal olivine microlites in the interior.

AL4615-16 (Iguana). Olivine-, plagioclase-, and clinopyroxene-phyric basalt. Light brown glass grades to microcrystalline interior. Vesicles are round (< 1 mm) or irregularly shaped (up to several mm). Olivine is skeletal (< 0.2 mm). Plagioclase is lath-shaped, often with swallowtail morphology. Clinopyroxene is sector-zoned (< 0.2 mm).

AL4618-02 (Lagarto). Olivine- and plagioclase-phyric basalt. Light brown glass grades to microcrystalline interior. Vesicles are round (< 0.3 mm) or irregularly shaped (up to several mm). Olivine occurs rarely as large, equant crystals (< 1 mm) in clusters with

tabular plagioclase. Plagioclase is blocky or tabular, sometimes with spongy cellular cores or oscillatory concentric zoning. Olivine and plagioclase are also present as microlites.

AL4618-04 (Lagarto). Olivine- and plagioclase-phyric basalt. Light brown glass grades to microcrystalline interior. Vesicles are round (0.1-0.5 mm) or irregularly shaped (up to several mm). Olivine is skeletal (< 0.8 mm) and typically is intergrown with plagioclase. Plagioclase is lath-shaped, tabular, or blocky. Dendritic overgrowths are present on some crystals. Blocky and tabular crystals commonly have oscillatory concentric zoning.

AL4618-12 (Lagarto). Olivine- and plagioclase-phyric basalt. Light brown glass is locally devitrified in contact with crystals. Vesicles are round (< 0.6 mm). Olivine is skeletal (< 0.6 mm) and typically is intergrown with plagioclase. Plagioclase is lath-shaped, tabular, or blocky. Dendritic overgrowths are present on some crystals. Blocky and tabular crystals commonly have oscillatory concentric zoning, and less commonly have spongy cores.

AL4617-04 (Lobo del Mar). Plagioclase-phyric basalt. Light brown glass grades to devitrified interior. Vesicles are round (<0.2 mm) or irregularly shaped (up to several mm). Some crystals are euhedral (sometimes with dendritic overgrowths), while other have rounded margins. Some crystals have spongy cellular cores. Some crystals have rounded cores mantled by euhedral rims. Plagioclase is the only microlite phase; abundant plagioclase microlites are well aligned in the interior, but are absent in the glassy outer rim.

AL4617-06 (Lobo del Mar). Plagioclase-phyric basalt. Light brown glass grades to devitrified interior. Vesicles are round or irregularly shaped (< 0.2 mm). Larger pipe vesicles are also present. Plagioclase is tabular or blocky. Many plagioclase have interesting disequilibrium textures. Some crystals have rounded or spongy cellular cores mantled by euhedral rims; other crystals have concentric oscillatory zoning. Plagioclase

is the only microlite phase; abundant plagioclase microlites are well aligned in the interior, but are absent in the glassy outer rim.

AL4609-02 (Ninos). Glassy, aphyric basalt. Light brown glass throughout, with small, sparse, incipient microlites. Vesicles are round (< 0.2 mm).

AL4609-09 (Ninos). Sparsely olivine- and plagioclase-phyric basalt. Red-brown glass grades to microcrystalline interior. Vesicles are round (< 1.5 mm) or irregularly shaped. Olivine is skeletal (< 0.4 mm). Plagioclase is lath-shaped. Clinopyroxene is also present as a microlite.

AL4614-05 (Ninos). Aphyric basalt. Red-brown glass grades to microcrystalline interior. Vesicles are round (< 1 mm) or irregularly shaped (up to several mm). Olivine, plagioclase, and clinopyroxene are present as microlites and rarely as microphenocrysts (< 0.2 mm).

AL4614-06 (Ninos). Aphyric basalt. Red-brown glass is locally devitrified. Vesicles are round (< 1 mm). Plagioclase microlites are very rare, but present, in addition to rare rounded plagioclase and olivine microphenocrysts (< 0.2 mm).

ACKNOWLEDGMENTS

We thank Eric Hellebrand for assistance with the electron microprobe, XRF analyses, and helpful conversations; Chuck Fraley for assistance with XRF analyses; Doug Pyle, Denys Vonderhaar, and Greg Ravizza for assistance obtaining ICP-MS data; JoAnn Sinton for the preparation of thin sections; Kristina Taylor and Emilie Grau for assistance with sample preparation, and Julia Hammer and Mike Mottl for discussion. Garrett Ito provided the scripts for the mantle melting model used in Section 4.7.1. This work was funded by NSF grant OCE08-49813 and a Denise B. Evans graduate fellowship in oceanography.

CHAPTER 5. CONCLUSIONS

5.1. Summary

Results presented in this dissertation provide insight into the effects of variable rates of magma supply on eruption style (Chapter 2), depths of magma residence (Chapter 3), and sub-axial magmatic processes prior to eruption (Chapter 4), as summarized in Table 5.1. Studying the products of individual eruptive episodes (the eruption-scale approach) allows temporal variability in eruption characteristics and magma reservoir properties to be constrained, providing a more complete understanding of the range of conditions that is possible at a given rate of magma supply. Characterizing anomalous eruptions in addition to more typical eruptive behavior is important to understanding magmatic systems, particularly at relatively low rates of magma supply, where magma reservoirs are apparently not present in a steady state.

At 92°W, where the time-averaged rate of magma supply is relatively high (0.4×10^6 m^3/km/yr), a melt lens has been seismically imaged at ~1.7 km beneath the seafloor (Blacic *et al.*, 2004). This melt lens is likely persistent in time as well as in space (present at depths of 1-2 km along much of the spreading axis east of 92.5°W (Blacic *et al.*, 2004)), although fluctuations in its temperature are apparent in the widely variable MgO content of erupted lavas (2.7-8.4 wt. %). Variations in MgO can be explained by fractional crystallization within the melt lens. There also is evidence for assimilation of hydrothermally altered crustal material within the shallow melt lens. Frequent eruptions (at least eight in the last 400 years (Bowles *et al.*, 2014)) tap magmas with varying parental magmas, indicating frequent replenishment of the melt lens. Magmatic recharge apparently does not precede every eruption, however. Eruptions at 92°W tend to be small (0.002-0.13 km^3), occur at relatively high effusion rates, and commonly are fissure fed, consistent with predictions for the effects of shallow melt lens depth on eruption rate and edifice morphology.

Magma reservoirs at the low-magma-supply 95°W study area are likely dominated by crystal-rich mush, consistent with the lack of seismically observed melt lens reflectors at any location west of 94.3°W (Blacic *et al.*, 2004). Before the last three eruptions at 95°W, however, magma residence depths were relatively consistent at 3-3.4 km below the seafloor. This suggests that there is a preferred magma residence depth,

even at rates of magma supply too low to sustain a persistent shallow, seismically detectable melt lens. Melt-rich eruptible magma is likely only present shortly after magmatic recharge, and many eruptions contain evidence of mixing between compositionally distinct magmas. Eruptions at 95°W are larger in volume (0.09-1.3 km^3), and occur less frequently, than at 92°W. Eruptions occur at lower average effusion rates, typically producing irregular clusters of pillow mounds or larger flat-topped axial seamounts. Between magmatic recharge events, magma evolution within the mush zone results in elevated incompatible element contents with decreasing temperature or MgO, relative to those predicted for fractional crystallization.

Table 5.1. Summary of effects of magma supply on magma reservoirs and eruption characteristics

	Low-magma-supply, 95°W	High-magma-supply, 92°W
Eruptive volume	Relatively large (0.09-1.3 km^3)	Relatively small (0.002-0.13 km^3)
Eruptive style	Lower average effusion rates; eruption from point sources	Higher average effusion rates; eruption along fissures
Seismically imaged melt lens	None present	Strong reflector, continuous along-axis
Magma residence depths	3-3.4 km below seafloor	~1.7 km below seafloor
Eruption temperatures	1130-1220°C	1060-1210°C
Assimilation of hydrothermally altered material		Affects compositions of erupted lavas
Mush-melt interaction	Affects compositions of erupted lavas	
Frequency of magmatic recharge	Precedes each eruption	Some eruptions not preceded by recent recharge events

5.2. Future work

Having documented variations in major and trace element glass and whole rock chemistry and major element compositions of mineral phases, the sequences of mapped eruptive units can be used for more detailed studies of specific parameters related to magma reservoirs and eruptive processes, or more detailed studies of conditions at a specific time (represented by an individual lava flow field). Additionally, the eruption-scale approach can be applied at other locations in order to better constrain the global systematics of variations in mid-ocean ridge behavior. Several potential directions for further work are outlined below.

5.2.1. Evaluation of magma reservoir depth as a control on eruptive style (effusion rate and edifice morphology)

There is significant variability in eruptive edifice morphology among mapped eruptions at 95°W, including large, flat-topped axial seamounts (Buho, Pinguino, Tortuga), smaller and more irregularly shaped clusters of pillow mounds (Dragón, Pulgar), and fissure-fed eruptions that alternately ponded within the axial graben (Del Norte) or built pillow ridges (Frijoles). Effusion rates inferred from lava morphology are also variable, ranging from relatively high effusion rates during the earlier phases of the Del Norte eruption, when sheet flows were emplaced, to the much more common low effusion rates associated with pillow lavas. In addition, eruptive volumes at 95°W span roughly an order of magnitude, from 0.09 to 1.3 km^3. These characteristics contrast with those at 92°W, where fissure-fed eruptions are more common, and the single axial seamount is significantly smaller than those at 95°W.

Various controls on eruptive style, edifice morphology, and eruptive volume have been proposed, including magma reservoir depths (e.g., Smith & Cann, 1992) and dike widths (e.g., Head *et al.*, 1996). Smith & Cann (1992) presented a model in which the heights of flat-topped seamounts are controlled by the depths of the magma reservoir; seamounts 100-m (e.g., Empanada), 200-m (e.g., Pinguino) and 300-m tall (e.g., Tortuga) are predicted to be fed from magma reservoirs at depths of 2.0 km, 2.9 km and 3.7 km, respectively. A systematic study of magma residence depth prior to eruption, as recorded by volatile element saturation pressures of olivine-hosted melt inclusions, could help constrain models of mid-ocean ridge eruption dynamics. Effusion rates inferred from lava morphology are known to generally increase with decreasing magma reservoir depths, but a predictive model for this relationship does not exist presently. Questions to address include whether there is a correlation between reservoir depth and lava effusion rate, edifice morphology, height, and/ or volume. Additional constraints on the magma reservoir depth at 95°W would also better constrain the spatial and temporal variability of magma reservoir depths at this relatively low-magma-supply location.

5.2.2. Magmatic evolution in mush-dominated magma reservoirs

Although crystal-rich mush is thought to dominate the magma reservoir at the low-magma-supply study area, its effects on erupted compositions have not been sufficiently explored. The *in situ* crystallization model used in Section 4.7.3 represents an approach to modeling mush-melt interactions in which sub-liquidus equilibrium crystallization dominates. An alternative is to consider the effects of disequilibrium melt-rock interactions during migration of melts through the lower crust, as recorded in gabbro textures and mineral compositions (e.g., Lissenberg & Dick, 2008). Further constraints on the compositions of melts coexisting with crystals in mush zones could be obtained by analyzing trace element compositions of zoned phenocryst cores, which likely record residence within a crystal-rich mush. Costa *et al.* (2010) used this approach to constrain the MgO of interstitial melts in mush zones (via measurements of MgO in plagioclase).

Another unanswered question is the extent to which recharge magma is modified by interactions with resident mineral phases (reaction or dissolution) as it mixes with resident mush. In the treatment of mixing between relatively high- and low-MgO end-members in the Dulces and Frijoles eruptive units, mixing was assumed to be a binary process between two liquids. The presence of crystals with strong resorption textures and zonation indicates that mineral-melt reactions also occur during the mixing process, although the magnitude of their effect on melt compositions has not been determined.

5.2.3. Timescales of magma mixing and eruption

Sinton & Detrick (1992) suggested that at relatively low rates of magma supply, magmatic recharge is closely linked in time to eruption, and may even trigger eruptions. Several eruptive units have variations in glass composition and mineral chemistry and textures indicative of magma mixing shortly prior to eruption (e.g., Frijoles, Altares, Dulces). In others, such as Gusanos, Del Norte, and Dragón, compositional variations are more limited and, although reversely zoned plagioclase crystals are present, olivine is normally zoned or unzoned. The timing of magma recharge relative to eruption could be constrained by modeling of diffusion profiles for both olivine and plagioclase, so that timescales of magma recharge relative to eruption could be compared between the two study areas and among eruptions at a given study area. This approach has been applied to

samples from the Mid-Atlantic Ridge and Costa Rica Rift, where timescales between mush remobilization and eruption were typically less than one year (Costa *et al.*, 2010).

5.2.4 Constraints on mantle composition and melting processes along axis

As indicated in Section 4.7.1, the specific composition of the mantle beneath both the plume-influenced regions of the GSC and beyond the limits of plume influence, west of 95.5°W, have not been determined precisely. A more detailed analysis of how these mantle compositions differ could yield insight into the origin and nature of the Galápagos plume. The combination of detailed sample sets at 95°W and 92°W and more widely spaced samples along the length of the GSC constrain both the variability at a given location and the larger trends related to proximity to the Galápagos hotspot. Ideally, existing geochemical data would be combined with isotopic data for the detailed study areas, in order to constrain both trace element and isotopic variability at these locations.

In addition, the range of compositions observed at both 92°W and 95°W is greater than predicted by the simplified model of Ingle *et al.* (2010), which incorporates constant proportions of two primary lithologies along axis, and complete extraction and pooling of all melts from the subaxial melting regime. The extent to which the extended range of compositions reflects incomplete pooling or different mantle compositions along axis has yet to be determined.

5.2.5. Applying the eruption-scale approach at lower rates of magma supply

Applying the eruption-scale approach to additional mid-ocean ridge locations with different rates of magma supply would extend the observations made here. At several locations with very high rates of magma supply (~0.7×10^6 m^3/km/yr) along the southern East Pacific Rise, the most recent eruptions have been identified, mapped, and sampled (Sinton *et al.*, 2002), but similar studies are lacking at lower rates of magma supply. A magma supply rate of ~0.3×10^6 m^3/km/yr appears to be a threshold below which persistent melt lenses in the crust are not viable; the GSC at 95°W is just below this threshold. We have attributed many of the differences between study areas at 95°W and 92°W to the presence of a persistent melt-rich lens only at 92°W. At 97°W, seamounts are even more common than at 95°W (Behn *et al.*, 2004), and lavas are

restricted to higher Mg# (51-62 at 97°W (Cushman *et al.*, 2004); 44-62 at 95°W). Thus significant differences exist between 95°W and locations farther to the west, beyond the limit of hotspot influence, which suggest systematic differences in eruption characteristics and magma reservoirs also occur at even lower rates of magma supply.

REFERENCES

Aigner-Torres, M., Blundy, J., Ulmer, P. & Pettke, T. (2007). Laser ablation ICPMS study of trace element partitioning between plagioclase and basaltic melts: an experimental approach. *Contributions to Mineralogy and Petrology* **153**, 647-667.

Allen, R. M., Nolet, G., Morgan, W. J., Vogfjörd, K., Nettles, M., Ekström, G., Bergsson, B., Erlendsson, P., Foulger, G., Jakobsdóttir, S., Julian, B. R., Pritchard, M., Ragnarsson, S. & Stefánsson, R. (2002). Plume-driven plumbing and crustal formation in Iceland. *Journal of Geophysical Research* **107**.

Argus, D. F., Gordon, R. G. & DeMets, C. (2011). Geologically current motion of 56 plates relative to the no-net-rotation reference frame. *Geochemistry Geophysics Geosystems* **12**, Q11001, doi:10.1029/2011GC003751.

Asimow, P. D. & Ghiorso, M. S. (1998). Algorithmic modification extending MELTS to calculate subsolidus phase relations. *American Mineralogist* **83**, 1127-1131.

Asimow, P. D. & Langmuir, C. H. (2003). The importance of water to oceanic mantle melting regimes. *Nature* **421**, 815-820.

Auzende, J.-M., Ballu, V., Batiza, R., Bideau, D., Charlou, J. L., Cormier, M. H., Fouquet, Y., Geistdorfer, P., Lagabrielle, Y., Sinton, J. & Spadea, P. (1996). Recent tectonic, magmatic, and hydrothermal activity on the East Pacific Rise between 17 and 19 S: Submersible observations. *Journal of Geophysical Research* **101***,* 17995-18010.

Ballard, R. D. & van Andel, T. H. (1977). Morphology and tectonics of the inner rift valley at lat 36°50'N on the Mid-Atlantic Ridge. *Geological Society of America Bulletin* **88**, 507-530.

Barth, G.A. & Mutter, J. (1996). Variability in oceanic crustal thickness and structure: Multichannel seismic reflection results from the northern East Pacific Rise. *Journal of Geophysical Research* **101**, 17951-17975.

Behn, M. D., Sinton, J. M. & Detrick, R. S. (2004). Effect of the Galápagos hotspot on seafloor volcanism along the Galápagos Spreading Center (90.9-97.6°W). *Earth and Planetary Science Letters* **217**, 331-347.

Behn, M. D., Buck, W. R. & Sacks, I. S. (2006). Topographic controls on dike injection in volcanic rift zones. *Earth and Planetary Science Letters* **246**, 188-196.

Bergmanis, E. C., Sinton, J. & Rubin, K. H. (2007). Recent eruptive history and magma reservoir dynamics on the southern East Pacific Rise at 17°30'S. *Geochemistry Geophysics Geosystems* **8**, Q12O06, doi:10.1029/2007GC001742.

Bialas, R. W., Buck, W. R. & Qin, R. (2010). How much magma is required to rift a continent? *Earth and Planetary Science Letters* **292**, 68-78.

Blacic, T. M., Ito, G., Canales, J. P., Detrick, R. S. & Sinton, J. (2004). Constructing the crust along the Galapagos Spreading Center 91.3°-95.5°W: Correlation of seismic layer 2A with axial magma lens and topographic characteristics, *Journal of Geophysical Research* **109**, B10310, doi:10.1029/2004JB003066.

Bonatti, E. & Harrison, C. G. A. (1988). Eruption style of basalt in oceanic spreading ridges and seamounts: effect of magma temperature and viscosity. *Journal of Geophysical Research* **93**, 2967-2980.

Bonatti, E., Ligi, M., Brunelli, D., Cipriani, A., Fabretti, P., Ferrante, V., Gasperini, L. & Ottolini, L. (2003). Mantle thermal pulses below the Mid-Atlantic Ridge and temporal variations in the formation of oceanic lithosphere. *Nature* **423**, 499-505.

Bowles, J., Gee, J. S., Kent, D. V., Bergmanis, J. & Sinton, J. (2005). Cooling rate effects on paleointensity estimates in submarine basaltic glass and implications for dating young flows. *Geochemistry Geophysics Geosystems* **6**, Q07002, doi:10.1029/204GC000900.

Bowles, J., Gee, J. S., Kent, D. V., Perfit, M. R., Soule, S. A. & Fornari, D. J. (2006). Paleointensity applications to timing and extent of eruptive activity, 9°-10°N East Pacific Rise. *Geochemistry Geophysics Geosystems* **7**, Q06006, doi:10.1029/2005/GC001141.

Bowles, J. A., Ab Fatah, A., Colman, A., McClinton, J. T. , Sinton, J. M., White, S. M. & Rubin, K. H. (2011). Geomagnetic paleointensity constraints on eruption timing at the Galápagos Spreading Center. Abstract V53D-2657 presented at 2011 Fall Meeting, AGU.

Bowles, J., Colman, A., McClinton, T., Sinton, J., White, S. & Rubin, K. (2014). Eruptive timing and 200-year episodicity at 92°W on the hotspot-influenced Galapagos Spreading Center derived from geomagnetic paleointensity. *Geochemistry Geophysics Geosystems.* doi:10.1002/2014GC005315.

Bown, J. W. & White, R. S. (1994). Variation with spreading rate of oceanic crustal thickness and geochemistry. *Earth and Planetary Science Letters* **121**, 435-449.

Bruce, P. M. & Huppert, H. E. (1989). Thermal control of basaltic fissure eruptions. *Nature* **342**, 665-667.

Bucholz, C.E., Gaetani, G.A., Behn, M.D. & Shimizu, N. (2013). Post-entrapment modification of volatiles and oxygen fugacity in olivine-hosted melt inclusions. *Earth and Planetary Science Letters* **374**, 145-155. doi: 10.1016/j.epsl.2013.05.033.

Buck, R.W., Carbotte, S.M. & Mutter, C.Z. (1997). Controls on extrusion at mid-ocean ridges. *Geology* **25**, 935-938.

Buck, W. R., Einarsson, P. & Brandsdottir, B. (2006). Tectonic stress and magma chamber size as controls on dike propagation: Constraints from the 1975-1984 Krafla rifting episode. *Journal of Geophysical Research* **111**, B12404, doi:10.1029/2005JB003879.

Byerly, G. R., Melson, W. G. & Vogt, P. R. (1976). Rhyodacites, andesites, ferrobasalts and ocean tholeiites from the Galápagos Spreading Center. *Earth and Planetary Science Letters* **30***,* 215-221.

Canales, J.P., Detrick, R.S., Bazin, S., Harding, A.J. & Orcutt, J.A. (1998). Off-axis crustal thickness across and along the East Pacific Rise within the MELT area. *Science* **280**, 1218-1221.

Canales, J. P., Detrick, R. S., Lin, J., Collins, J. A. & Toomey, D. R. (2000). Crustal and upper mantle seismic structure beneath the rift mountains and across a nontransform offset at the Mid-Atlantic Ridge (35ºN). *Journal of Geophysical Research **105***, 2699-2719.

Canales, J. P., Ito, G., Detrick, R. S. & Sinton, J. (2002). Crustal thickness along the western Galápagos Spreading Center and the compensation of the Galápagos hotspot swell. *Earth and Planetary Science Letters* **203**, 311-327.

Canales, J.P., Detrick, R.S., Carbotte, S.M., Kent, G.M., Diebold, J.B., Harding, A., Babcock, J., Nedimović, M.R. & van Ark, E. (2005). Upper crustal structure and axial topography at intermediate spreading ridges: Seismic constraints from the

southern Juan de Fuca Ridge. *Journal of Geophysical Research* **110**, 1-27. doi:10.1029/2005JB003630.

Carbotte, S., Mutter, C., Mutter, J. & Ponce-Correa, G. (1998). Influence of magma supply and spreading rate on crustal magma bodies and emplacement of the extrusive layer: Insights from the East Pacific Rise at lat 16°N. *Geology* **26**, 455-458.

Carbotte, S. M., Marjanović, M., Carton, H., Mutter, J. C., Canales, J. P., Nedimović, M. R., Han, S. & Perfit, M. R. (2013). Fine-scale segmentation of the crustal magma reservoir beneath the East Pacific Rise. *Nature Geoscience* **6**, 866-870.

Caress, D. W., Clague, D. A., Paduan, J. B., Martin, J. F., Dreyer, B. M., Chadwick, W. W., Denny, A. & Kelley, D. S. (2012). Repeat bathymetric surveys at 1-metre resolution of lava flows erupted at Axial Seamount in April 2011. *Nature Geoscience* **5***,* 483-488, doi:10.1038/ngeo1496.

Carlson, R.L. & Herrick, C.N. (1990). Densities and porosities in the oceanic crust and their variations with depth and age. *Journal of Geophysical Research* **95**, 9153-9170.

Chadwick, W. W., & Embley, R. W. (1994). Lava flows from a mid-1980s submarine eruption on the Cleft segment, Juan de Fuca Ridge, *Journal of Geophysical Research* **99**, 4761-4776.

Chadwick, W. W., Embley, R. W. & Fox, C. G. (1995). SeaBeam depth changes associated with recent lava flows, CoAxial segment, Juan de Fuca Ridge: Evidence for multiple eruptions between 1981-1993, *Geophysical Research Letters* **22**, 167-170.

Chadwick, W. W., Embley, R. W. & Shank, T. M. (1998). The 1996 Gorda Ridge eruption: geologic mapping, sidescan sonar, and SeaBeam comparison results. *Deep-Sea Research II* **45**, 2547-2569.

Chappell, B. W. (1991). Trace element analysis of rocks by x-ray spectrometry. *Advances in X-Ray Analysis* **34**, 263-276.

Christie, D. M. & Sinton, J. M. (1981). Evolution of abyssal lavas along propagating segments of the Galapagos Spreading Center. *Earth and Planetary Science Letters* **56***,* 321-335.

Christie, D. M. & Sinton, J. M. (1986). Major element constraints on melting, differentiation, and mixing of magmas from the Galapagos 95.5°W propagating rift system. *Contributions to Mineralogy and Petrology* **94**, 274-288.

Clague, D. A., Dreyer, B. M., Paduan, J. B., Martin, J. F., Chadwick, W. W., Caress, D. W., Portner, R. A., Guilderson, T. P., McGann, M. L., Thomas, H., Butterfield, D. A., Embley, R. W. (2013). Geologic history of the summit of axial seamount, Juan de Fuca Ridge. *Geochemistry Geophysics Geosystems* **14** doi:10.1002/ggge.20240.

Colin, A., Faure, F. & Burnard, P. (2012). Timescales of convection in magma chambers below the Mid-Atlantic ridge from melt inclusions investigations. *Contributions to Mineralogy and Petrology* **164**, 677-691. doi:10.1007/s00410-012-0764-2.

Colman, A., Sinton, J.M., White, S.M., McClinton, J.T., Bowles, J.A., Rubin, K.H., Behn, M.D., Cushman, B., Eason, D.E., Gregg, T.K.P., Gronvöld, K., Hidalgo, S., Howell, J., Neill, O. & Russo, C. (2012). Effects of variable magma supply on mid-ocean ridge eruptions: Constraints from mapped lava flow fields along the Galápagos Spreading Center. *Geochemistry Geophysics Geosystems* **13**, Q08014. doi:10.1029/2012GC004163.

Coogan, L. A., Mitchell, N .C. & O'Hara, M. J. (2003). Roof assimilation at fast spreading ridges: An investigation combining geophysical, geochemical, and field evidence. *Journal of Geophysical Research* **108**. doi:10.1029/2001JB001171.

Costa, A., Caricchi, L., Bagdassarov, N. (2009). A model for the rheology of particle-bearing suspensions and partially molten rocks. *Geochemistry Geophysics Geosystems* **10**, Q03010, doi:10.1029/2008GC002138.

Costa, F., Coogan, L. A., Chakraborty, S. (2010). The time scales of magma mixing and mingling involving primitive melts and melt-mush interaction at mid-ocean ridges. *Contributions to Mineralogy and Petrology* **159**, 371-387.

Cottrell, E., Kelley, K.A. (2011). The oxidation state of Fe in MORB glasses and the oxygen fugacity of the upper mantle. *Earth and Planetary Science Letters* **305**, 270-282.

Cottrell, E., Spiegelman, M. & Langmuir, C. H. (2002). Consequences of diffusive reequilibration for the interpretation of melt inclusions. *Geochemistry Geophysics Geosystems* **3**. doi:10.1029/2001GC000205.

Cowie, P. A., Scholz, C. H., Edwards, M. & Malinverno, A. (1993). Fault strain and seismic coupling on mid-ocean ridges. *Journal of Geophysical Research* **98**, 17911-17920.

Crisp, J. A. (1984). Rates of magma emplacement and volcanic output. *Journal of Volcanology and Geothermal Research* **20**, 177-348.

Curewitz, D., & Karson, J. A. (1998). Geological consequences of dike intrusion at mid-ocean ridge spreading centers. In: Buck, W. R., Delaney, P. T., Karson, J. A. & Lagabrielle, Y. (eds.) *Faulting and Magmatism at Mid-ocean Ridges.* American Geophysical Union, 117-136.

Cushman, B., Sinton, J., Ito, G. & Dixon, J. E. (2004). Glass compositions, plume-ridge interaction, and hydrous melting along the Galápagos Spreading Center, 90.5°W to 98°W. *Geochemistry Geophysics Geosystems* **5**, Q08E17, doi:10.1029/2004GC000709.

Danyushevsky, L.V., Sokolov, S. & Falloon, T.J. (2002). Melt inclusions in olivine phenocrysts: Using diffusive re-equilibration to determine the cooling history of a crystal, with implications for the origin of olivine-phyric volcanic rocks. *Journal of Petrology* **43**, 1651-1671.

DeMets, C., Gordon, R.G. & Argus, D.F. (2010). Geologically current plate motions. *Geophysical Journal International* **181**, 1-80.

DePaolo, D. J. (1981). Trace element and isotopic effects of combined wallrock assimilation and fractional crystallization. *Earth and Planetary Science Letters* **53**, 189-202.

Detrick, R.S., Buhl, P., Vera, E., Mutter, J., Orcutt, J., Madsen, J. & Brocher, T. (1987). Multi-channel seismic imaging of a crustal magma chamber along the East Pacific Rise. *Nature* **326**, 35-41.

Detrick, R.S., Mutter, J.C., Buhl, P. & Kim, I.I. (1990). No evidence from multichannel reflection data for a crustal magma chamber in the MARK area on the Mid-Atlantic Ridge. *Nature* **346**, 61-64.

Detrick, R. S., White, R. S. & Purdy, G. M. (1993). Crustal structure of North Atlantic Fracture Zones. *Reviews of Geophysics* **31**, 439-458.

Detrick, R.S., Sinton, J.M., Ito, G., Canales, J.P., Behn, M., Blacic, T., Cushman, B., Dixon, J.E., Graham, D.W. & Mahoney, J.J. (2002). Correlated geophysical, geochemical, and volcanological manifestations of plume-ridge interaction along the Galápagos Spreading Center. *Geochemistry Geophysics Geosystems* **3**. doi:10.1029/2002GC000350.

Dixon, J. & Stolper, E. 1995. An experimental study of water and carbon dioxide solubilities in mid-ocean ridge basaltic liquids. Part II: Applications to degassing. *Journal of Petrology* **36**, 1633-1646.

Dixon, J., Stolper, E. & Holloway, J. (1995). An experimental study of water and carbon dioxide solubilities in mid-ocean ridge basaltic liquids, Part I: Calibration and solubility models. *Journal of Petrology* **36**, 1607-1631.

Dungan, M. A. & Rhodes, J. M. (1978). Residual glasses and melt inclusions in basalts from DSDP Legs 45 and 46: Evidence for magma mixing. *Contributions to Mineralogy and Petrology* **67**, 417-431.

Dunn, R.A. & Forsyth, D.W. (2007). Crust and lithospheric structure—Seismic structure of mid-ocean ridges. In: Romanowicz, B., Dziewonski, A.M. (eds.) *Treatise on Geophysics, v. 1: Seismology and Structure of the Earth*. Elsevier, 419-443.

Dunn, R. A., Toomey, D. R. & Solomon, S. C. (2000). Three-dimensional seismic structure and physical properties of the crust and shallow mantle beneath the East Pacific Rise at 9°30'N. *Journal of Geophysical Research* **105**, 23537-23555.

Dunn, R. A., Lekić, V., Detrick, R. S. & Toomey, D. R. (2005). Three-dimensional seismic structure of the Mid-Atlantic Ridge (35°N): Evidence for focused melt supply and lower crustal dike injection, *Journal of Geophysical Research* **110**, B09101.

Dziak, R. P. & Fox, C. G. (1999). The January 1998 earthquake swarm at Axial Volcano, Juan de Fuca Ridge, Hydroacoustic evidence for seafloor volcanic activity. *Geophysical Research Letters* **26**, 3425-3428.

Eason, D. E. & Sinton, J. M. (2009). Lava shields and fissure eruptions of the Western Volcanic Zone, Iceland: Evidence for magma chambers and crustal interaction.

Journal of Volcanology and Geothermal Research **186***,* 331-348, doi:10.1016/j.jvolgeores.2009.06.009.

Ebinger, C., Ayele, A., Keir, D., Rowland, J., Yirgu, G., Wright, T., Belachew, M. & Hamling, I. (2010). Length and timescales of rift faulting and magma intrusion: The Afar rifting cycle from 2005 to present. *Annual Review of Earth and Planetary Science* **38**, 437-464, doi:10.1146/annurev-earth-040809-152333.

Embley, R., Chadwick, W. W., Perfit, M. R. & Baker, E. T. (1991). Geology of the northern Cleft segment, Juan de Fuca Ridge: Recent lava flows, sea-floor spreading, and the formation of megaplumes. *Geology* **19**, 771-775.

Embley, R. W., Chadwick, W. W., Clague, D. & Stakes, D. (1999). The 1998 eruption of Axial Volcano: Multibeam anomalies and seafloor observations. *Geophysical Research Letters* **26***,* 3425-3428.

Embley, R. W., Chadwick, W. W., Perfit, M. R., Smith, M. C. & Delaney, J. R. (2000). Recent eruptions on the CoAxial segment of the Juan de Fuca Ridge: Implications for mid-ocean ridge accretion processes. *Journal of Geophysical Research* **105***,* 16501-16525.

Faure, F. & Schiano, P. (2004). Crystal morphologies in pillow basalts: implications for mid-ocean ridge processes. *Earth and Planetary Science Letters* **220**, 331-344. doi:10.1016/S0012-821X(04)00057-3.

Faure, F. & Schiano, P. (2005). Experimental investigation of equilibration conditions during forsterite growth and melt inclusion formation. *Earth and Planetary Science Letters* **236**, 882-898. doi:10.1016/j.epsl.2005.04.050.

Ferguson, D. J., Barnie, T. D., Pyle, D. M., Oppenheimer, C., Yirgu, G., Lewi, E., Kidane, T., Carn, S. & Hamling, I. (2010). Recent rift-related volcanism in Afar, Ethiopia. *Earth and Planetary Science Letters* **292**, 409-418, doi:10.1016/j.epsl.2010.02.010.

Fontaine, F. J., Olive, J.-A., Cannat, M., Escartin, J. & Perol, T. (2011). Hydrothermally-induced melt lens cooling and segmentation along the axis of fast- and intermediate-spreading centers. *Geophysical Research Letters* **38**, L14307. doi:10.1029/2011GL047798.

Fornari, D. J. & Perfit, M. R. (1983). Geochemical studies of abyssal lavas recovered by DSRV *Alvin* from Eastern Galapagos Rift, Inca Transform, and Ecuador Rift 1. Major element variations in natural glasses and spacial distribution of lavas. *Journal of Geophysical Research* **88**, 10519-10529.

Fornari, D.J. (2003). A new deep-sea towed digital camera and multi-rock coring system, *Eos Transactions American Geophysical Union* **84***,* 69-76, doi:10.1029/2003EO080001.

Fornari, D., Tivey, M., Schouten, H., Perfit, M., Yoerger, D., Bradley, A., Edwards, M., Haymon, R., Scheirer, D., Von Damm, K., Shank, T. & Soule, A. (2004). Submarine lava flow emplacement at the East Pacific Rise 9°50'N: Implications for uppermost ocean crust stratigraphy and hydrothermal fluid circulation. In: German, C. R., Lin, J. & Parson, L. M. (eds.) *Mid-Ocean Ridges: Hydrothermal Interactions between the Lithosphere and the Oceans.* American Geophysical Union, 187-217.

Fox, C. G. (1999). In situ ground deformation measurements from the summit of Axial Volcano during the 1998 volcanic episode. *Geophysical Research Letters* **26**, 3437-3440.

Fox, C. G., Murphy, K. M. & Embley, R. W. (1988). Automated display and statistical analysis of interpreted deep-sea bottom photographs. *Marine Geology* **78**, 199-216.

Fox, C. G., Radford, W. E., Dziak, R. P., Lau, T.-K., Matsumoto, H. & Schreiner, A. E. (1995). Acoustic detection of a seafloor spreading episode on the Juan de Fuca Ridge using military hydrophone arrays. *Geophysical Research Letters **22***, 131-134

France, L., Ildefonse, B. & Koepke, J. (2009). Interactions between magma and hydrothermal system in Oman ophiolite and in IODP Hole 1256D: Fossilization of a dynamic melt lens at fast spreading ridges. *Geochemistry Geophysics Geosystems* **10***,* Q10019, doi:10.1029/2009GC002652.

Fundis, A., Soule, S., Fornari, D. J. & Perfit, M. R. (2010). Paving the seafloor: Volcanic emplacement processes during the 2005-2006 eruption at the fast-spreading East

Pacific Rise, 9º50'N. *Geochemistry Geophysics Geosyst*ems **11**, Q08024, doi:10.1029/2010GC003058.

Gaetani, G. A. & Watson, T. L. (1998). The influence of water on melting of mantle peridotite. *Contributions to Mineralogy and Petrology* **131**, 323-346.

Gaetani, G.A. & Watson, E.B. (2000). Open system behavior of olivine-hosted melt inclusions. *Earth and Planetary Science Letters* **183**, 27-41.

Gaetani, G.A. & Watson, E.B. (2002). Modeling the major-element evolution of olivine-hosted melt inclusions. *Chemical Geology*. **183**, 25-41.

Ghiorso, M. S. & Sack, R. O. (1995). Chemical mass transfer in magmatic processes. IV. A revised and internally consistent thermodynamic model for the interpolation and extrapolation of liquid-solid equilibria in magmatic systems at elevated temperatures and pressures. *Contributions to Mineralogy and Petrology* **199**, 197-212.

Gillis, K. M. (2008). The roof of an axial magma chamber: A hornfelsic heat exchanger. *Geology* **36**, 299-302.

Gillis, K. M. & Coogan, L. (2002). Anatectic migmatites from the roof of an ocean ridge magma chamber. *Journal of Petrology* **43**, 2075-2095.

Giordano, D., Russell, J. K. & Dingwell, D. B. (2008). Viscosity of magmatic liquids: A model. *Earth and Planetary Science Letters* **271**, 123-134, doi:10.1016/j.epsl.2008.03.038.

Goldstein, S. & Luth, R.W. (2006). The importance of cooling regime in the formation of melt inclusions in olivine crystals in haplobasaltic melts. *Canadian Mineralogist* **44**, 1543-1555.

Goss, A. R., Perfit, M. R., Ridley, W. I., Rubin, K. H., Kamenov, G. D., Soule, S. A., Fundis, A. & Fornari, D. J. (2010). Geochemistry of lavas from the 2005-2006 eruption at the East Pacific Rise, 9°46'N-9°56'N: Implications for ridge crest plumbing and decadal changes in magma chamber compositions. *Geochemistry Geophysics Geosystems* **11**, doi:10.1029/2009GC002977.

Green, T. H. (1994). Experimental studies of trace-element partitioning applicable to igneous petrogenesis—Sedon 16 years later. *Chemical Geology* **117**, 1-36.

Gregg, T, K. P. & Fink, J. H. (1995). Quantification of submarine lava-flow morphology through analog experiments. *Geology* **23**, 73-76.

Gregg, T.K.P. & Fornari, D.J. (1998). Long submarine lava flows: Observations and results from numerical modeling. *Journal of Geophysical Research* **103**, 27517-27531.

Gregg, T. K. P., Fornari, D. J., Perfit, M. R., Haymon, R. M. & Fink, J. H. (1996). Rapid emplacement of a mid-ocean ridge lava flow on the East Pacific Rise at 9º46'-51'N. *Earth and Planetary Science Letters* **144**, E1-E7.

Grevemeyer, I., Weigel, W. & Jennrich, C. (1998). Structure and ageing of oceanic crust at 14°S on the East Pacific Rise. *Geophysical Journal International* **135**, 573-584.

Griffiths, R. W. & Fink, J. A. (1992). Solidification and morphology of submarine lavas; a dependence on extrusion rate. *Journal of Geophysical Research* **97**, 19729-19737.

Grönvold, K., Halldorsson, S. A., Sigurdsson, G., Sverrisdottir, G. & Oskarsson, N. (2008). The Krafla magma system—Isotopic constraints, presented at IAVCEI General Assembly.

Grove, T. L., Kinzler, R. J. & Bryan, W. B. (1992). Fractionation of mid-ocean ridge basalt (MORB). In: Morgan, J. P., Blackman, D. K. & Sinton, J. M. (eds.) *Mantle Flow and Melt Generation at Mid-Ocean Ridges*. American Geophysical Union, 281-310.

Hallenborg, E., Harding, A. & Kent, G.M. (2003). Seismic structure of 15 Ma oceanic crust formed at an ultrafast spreading East Pacific Rise: Evidence for kilometer-scale fracturing from dipping reflectors. *Journal of Geophysical Research* **108**. doi:10.1029/2003JB002400.

Halliday, A. N., Lee, D.-C., Tommasini, T., Davies, G. R., Paslick, C. R., Fitton, J. G. & James, D. E. (1995). Incompatible trace elements in OIB and MORB and source enrichment in the sub-oceanic mantle. *Earth and Planetary Science Letters* **133**, 379-395.

Harris, A. J. L., Murray, J. B., Aries, S. E., Davies, M. A., Flynn, L. P., Wooster, M. J., Wright, R. & Rothery, D. A. (2001). Effusion rate trends at Etna and Krafla and

their implications for eruptive mechanisms. *Journal of Volcanology and Geothermal Research* **102***,* 237-270.

Hartley, M., Maclennan, J., Edmonds, M. & Thordarson, T. (2014). Reconstructing the deep CO_2 degassing behaviour of large basaltic fissure eruptions. *Earth and Planetary Science Letters* **393**, 120-131.

Haymon, R. M., Fornari, D. J., Von Damm, K. L., Lilley, M. D., Perfit, M. R., Edmond, J. M., Shanks, W. C., Lutz, R. A., Grebmeier, J. M., Carbotte, S., Wright, D., McLaughlin, E., Smith, M., Beedle, N. & Olson, E. (1993). Volcanic eruption of the mid-ocean ridge along the East Pacific Rise crest at 9º45-52'N: Direct submersible observations of sea-floor phenomena associated with an eruption event in April, 1991. *Earth and Planetary Science Letters* **119**, 85-101.

Head, J. W., Wilson, L. & Smith, D. (1996). Mid-ocean ridge eruptive vent morphology and substructure: Evidence for dike widths, eruption rates, and evolution of eruptions and axial volcanic ridges. *Journal of Geophysical Research* **101**, 28265-28280.

Hey, R. (1977). Tectonic evolution of the Cocos-Nazca spreading center. *Geological Society of America Bulletin* **88**, 1404-1420.

Hey, R. N., Kleinrock, M. C., Miller, S. P., Atwater, T. M. & Searle, R. C. (1986). Sea Beam/ Deep-Tow investigation of an active oceanic propagating rift system, Galápagos 95.5°W. *Journal of Geophysical Research* **91**, 3369-3393.

Hooft, E.E. & Detrick, R.S. (1993). The role of density in the accumulation of basaltic melts at mid-ocean ridges. *Geophysical Research Letters* **20**, 423-426.

Hooft, E. E., Schouten, H. & Detrick, R. S. (1996). Constraining crustal emplacement processes from the variation in seismic layer 2A thickness at the East Pacific Rise. *Earth and Planetary Science Letters* **142**, 289-309.

Hooft, E.E.E., Detrick, R.S. & Kent, G.M. (1997). Seismic structure and indicators of magma budget along the Southern East Pacific Rise. *Journal of Geophysical Research* **102**, 27319-27340.

Hussenoeder, S. A., Collins, J. A., Kent, G. M., Detrick, R. S. & TERA Group. (1996). Seismic analysis of the axial magma chamber reflector along the southern East

Pacific Rise from conventional reflection profiling. *Journal of Geophysical Research* **101**, 22087-22105.

Ingle, S., Ito, G., Mahoney, J. J., Chazey, W., Sinton, J., Rotella, M. & Christie, D. M. (2010). Mechanisms of geochemical and geophysical variations along the western Galápagos Spreading Center. *Geochemistry Geophysics Geosystems* **11**, Q04003, doi: 10.1029/2009GC002694.

Ito, G., & Behn, M. D. (2008). Magmatic and tectonic extension at mid-ocean ridges: 2. Origin of axial morphology. *Geochemistry Geophysics Geosystems* **9**, Q09O12, doi:1029/2008GC001970.

Ito, G. & Mahoney, J. J. (2005). Flow and melting of a heterogeneous mantle: 1. Method and importance to the geochemistry of ocean island and mid-ocean ridge basalts. *Earth and Planetary Science Letters* **230**, 29-46.

Jarosewich, E.J., Nelen, J. A. & Norberg, J. A. (1980). Reference samples for electron microprobe analysis. *Geostandards Newsletter* **4**, 257-258.

Jochum, K. P., Nohl, U., Herwig, K., Lammel, E., Stoll, B. & Hofmann, A. W. (2007). GeoReM: A new geochemical database for reference materials and isotopic standards. *Geostandards and Geoanalytical Research* **29**, 333-338.

Johnson, K. T. M. (1998). Experimental determination of partition coefficients for rare earth and high-field-strength elements between clinopyroxene, garnet, and basaltic melt at high pressures. *Contributions to Mineralogy and Petrology* **133**, 60-68.

Jokat, W., Ritzmann, O., Schmidt-Aursch, M. C., Drachev, S., Gauger, S. & Snow, J. (2003). Geophysical evidence for reduced melt production on the Arctic ultraslow Gakkel mid-ocean ridge. *Nature* **423**, 962-965.

Kappel, E. S. & Ryan, W. B. F. (1986). Volcanic episodicity and a non-steady state rift valley along northeast Pacific spreading centers: Evidence from Sea MARC I. *Journal of Geophysical Research* **91**, 13925-13940.

Kelemen, P.B. & Aharanov, E. (1998). Periodic formation of magma fractures and generation of layered gabbros in the lower crust beneath oceanic spreading ridges. In: Buck, W.R., Delaney, P.T., Karson, J.A., Lagabrielle, Y. (eds.) *Faulting and Magmatism at Mid-Ocean Ridges*. American Geophysical Union, 267-289.

Kent, A.J.R. (2008). Melt inclusions in basaltic and related volcanic rocks. *Reviews in Mineralogy and Geochemistry* **69**, 273-331.

Kent, G. M., Harding, A. J. & Orcutt, J. A. (1993). Distribution of magma beneath the East Pacific Rise between the Clipperton Transform and the 9°17'N Deval from forward modeling of common depth point data. *Journal of Geophysical Research* **98**, 13945-13969.

Keppler, H., Wiedenbeck, M. & Shcheka, S. S. (2003). Carbon solubility in olivine and the mode of carbon storage in the Earth's mantle. *Nature* **424**, 414-416.

Klein, E. M. & Langmuir, C. H. (1987). Global correlations of ocean ridge basalt chemistry with axial depth and crustal thickness. *Journal of Geophysical Research* **92**, 8089-8115.

Kleinrock, M. C., & Hey, R. N. (1989). Detailed tectonics near the tip of the Galápagos 95.5°W propagator: How the lithosphere tears and a spreading axis develops. *Journal of Geophysical Research* **94**, 13801-13838.

Klingelhöfer, F., Géli, L., Matias, L., Steinsland, N. & Mohr, J. (2000). Crustal structure of a super-slow spreading centre: a seismic refraction study of Mohns Ridge, 72°N. *Geophysical Journal International* **141**, 509-526.

Kohut, E. & Nielsen, R.L. (2004). Melt inclusion formation mechanisms and compositional effects in high-An feldspar and high-Fo olivine in anhydrous mafic silicate liquids. *Contributions to Mineralogy and Petrology* **147**, 684-704. doi:10.1007/s00410-004-0576-0.

Kuo, L.-C. & Kirkpatrick, R. J. (1982). Pre-eruption history of phyric basalts from DSDP Legs 45 and 46: Evidence from morphology and zoning patterns in plagioclase. *Contributions to Mineralogy and Petrology* **79**, 13-27.

Kuzmin, D.V. & Sobolev, A.V. (2004). Boundary layer contribution to the composition of melt inclusions in olivine. *Geochimica Cosmochimica Acta* **68**, A544.

Langmuir, C. H. (1989). Geochemical consequences of *in situ* crystallization. *Nature* **340**, 199-205.

Laubier, M., Gale, A. & Langmuir, C. (2012). Melting and crustal processes at the FAMOUS Segment (Mid-Atlantic Ridge): New insights from olivine-hosted melt

inclusions from multiple samples. *Journal of Petrology* **53**, 665-698. doi:10.1093/petrology/egr075.

Le Roux, P. J., Shirey, S. B., Hauri, E. H., Perfit, M. R. & Bender, J. F. (2006). The effects of variable sources, processes and contaminants on the composition of northern EPR MORB (8-10°N and 12-14°N): Evidence from volatiles (H_2O, CO_2, S) and halogens (F, Cl). *Earth and Planetary Science Letters* **251**, 209-231.

LeBas, M. J. & Streckeisen, A. L. (1991). The IUGS systematics of igneous rocks, *Journal of the Geological Society of London* **148**, 825-833.

Le Voyer, M., Asimow, P.D., Mosenfelder, J.L., Guan, Y., Wallace, P.J., Schiano, P., Stolper, E.M. & Eiler, J.M. (2014). Zonation of H2O and F concentrations around melt inclusions in olivines. *Journal of Petrology* **55**, 685-707. doi:10.1093/petrology/egu003.

Lissenberg, C. J. & Dick, H. J. B. (2008). Melt-rock reaction in the lower oceanic crust and its implications for the genesis of mid-ocean ridge basalt. *Earth and Planetary Science Letters* **271**, 311-325.

Liu, L. & Lowell, R. P. (2009). Models of hydrothermal heat output from a convecting, crystallizing, replenished magma chamber beneath an oceanic spreading center. *Journal of Geophysical Research* **114**, B02102. doi: 10.1029/2008JB005846.

Lloyd, A.S., Plank, T., Ruprecht, P., Hauri, E.H. & Rose, W. (2012). Volatile loss from melt inclusions in pyroclasts of differing sizes. *Contributions to Mineralogy and Petrology* **165**, 129-153. doi:10.1007/s00410-012-0800-2.

Lockwood, J. P., Dvorak, J. J., English, T.T., Koyanagi, R. Y., Okamura, A. T., Summers, M. L. & Tanigawa, W. R. (1987). Mauna Loa 1974-1984: a decade of intrusive and extrusive activity. *United States Geological Survey Professional Paper 1350*, 537-570.

Maclennan, J. (2008). Concurrent mixing and cooling of melts under Iceland. *Journal of Petrology* **49***,* 1931-1953, doi:10.1093/petrology/egn052.

Maclennan, J., Hulme, T. & Singh, S. (2005). Cooling of the lower oceanic crust. *Geology* **33**, 357-366.

McClinton, J. T., White, S. M., Sinton, J. M. & Colman, A. (2011). Effects of magma supply on seafloor construction: insights from contrasting volcanic features along

the Galápagos Spreading Center, 95W and 92W. Abstract V53D-2650 presented at 2011 Fall Meeting, AGU.

McClinton, J.T., White, S.M. & Sinton, J.M. (2012). Neuro-fuzzy classification of submarine lava flow morphology. *Photogrammetric Engineering and Remote Sensing* **78**, 605-616.

McClinton, T., White, S. M., Colman, A. & Sinton, J. M. (2013). Reconstructing lava flow emplacement processes at the hot spot-affected Galápagos Spreading Center, 95°W and 92°W. *Geochemistry Geophysics Geosystems* **14**. doi:10.1002/ggge.20157.

McClinton, J. T., White, S. M., Colman, A., Rubin, K. H. & Sinton, J. M. The role of crystallinity and viscosity in the formation of submarine lava flow morphology. Submitted to *Bulletin of Volcanology*, 2014

McDonough, W. F. & Sun, S.-s. (1995). The composition of the Earth. *Chemical Geology* **120**, 223-253.

McKenzie, D. & Bickle, M. J. (1988). The volume and composition of melt generated by extension of the lithosphere. *Journal of Petrology* **29**, 625-679.

Meyer, P. S. & Shibata, T. (1990). Complex zoning in plagioclase feldspars from ODP Site 648. *Proceeding of the Ocean Drilling Program, Scientific Results* **106/109**, 123-142.

Meyer, J. D. & White, S. M. (2007). Lava morphology mapping by expert system classification of high-resolution side-scan sonar imagery from the East Pacific Rise, 9°-10° N, *Marine Geophysical Researches **28,*** doi: 10.1029/2006GC001327.

Michael, P. J. & Cornell, W. C. (1998). Influence of spreading rate and magma supply on crystallization and assimilation beneath mid-ocean ridges: Evidence from chlorine and major element chemistry of mid-ocean ridge basalts. *Journal of Geophysical Research* **103**, 18325-18356.

Michael, P. J. & Schilling, J.-G. (1989). Chlorine in mid-ocean ridge magmas: Evidence for assimilation of seawater-influenced components. *Geochimica et Cosmochimica Acta* **53**, 3131-3143.

Mitchell, N. C. (1998). Sediment accumulation rates from Deep Tow profiler records and DSDP Leg 70 cores over the Galápagos spreading center. In: Cramp, A., MacLeod, C. J., Lee, S. V. & Jones, E. J. W. (eds.) *Geological Evolution of Ocean Basins: Results from the Ocean Drilling Program*. Geological Society of London, 199-209.

Mix, A. C., Pisias, N. G., Zahn, R., Rugh, W., Lopez, C. & Nelson, K. (1991). Carbon 13 in Pacific deep and intermediate waters, 0-370 Ka: Implications for ocean circulation and Pleistocene CO_2. *Paleoceanography* **6**, 205-226.

Muller, M. R., Minshull, T. A. & White, R. S. (1999). Segmentation and melt supply at the Southwest Indian Ridge. *Geology* **27**: 867-870.

Navin, D. A., Peirce, C. & Sinha, M. C. (1998). The RAMESSES experiment—II. Evidence for accumulated melt beneath a slow spreading ridge from wide-angle refraction and multichannel reflection seismic profiles, *Geophysical Journal International* **135**, 746-772.

Newman, S. & Lowenstern, J. B. (2002). VolatileCalc: a silicate melt-H_2O-CO_2 solution model written in Visual Basic for excel. *Computers and Geosciences* **28**, 597-604.

Niu, Y. & Hékinian, R. (1997). Spreading-rate dependence of the extent of mantle melting beneath ocean ridges. *Nature* **285**, 326-329.

Norrish, K. & Hutton, J. T. (1969). An accurate X-ray spectrographic method for the analysis of a wide range of geological samples, *Geochimica et Cosmochimica Acta* **33***,* 431-541.

O'Hara, M. J. (1977). Geochemical evolution during fractional crystallization of a periodically refilled magma chamber. *Nature* **266**, 503-507.

O'Hara, M. J. (1985). Importance of the "shape" of the melting regime during partial melting of the mantle. *Nature* **314**, 58-62.

Passmore, E., Maclennan, J., Fitton, G. & Thordarson, T. (2012). Mush disaggregation in basaltic magma chambers: Evidence from the AD 1783 Laki eruption. *Journal of Petrology* **53**, 2593-2623.

Peirce, C., Gardiner, A. & Sinha, M. (2005). Temporal and spatial cyclicity of accretion at slow-spreading ridges—evidence from the Reykjanes Ridge. *Geophysical Journal International* **163**, 56-78.

Perfit, M. R. & Fornari, D. J. (1983). Geochemical studies of abyssal lavas recovered by DSRV *Alvin* from Eastern Galapagos Rift, Inca Transform, and Ecuador Rift 2. Phase chemistry and crystallization history. *Journal of Geophysical Research* **88**, 10530-10550.

Perfit, M. R. & Chadwick, W. W.(1998). Magmatism at mid-ocean ridges: constraints from volcanological and geochemical investigations. In: Buck, W.R., Delaney, P.T., Karson, J.A., Lagabrielle, Y. (eds.) *Faulting and Magmatism at Mid-Ocean Ridges*. American Geophysical Union, 59-116.

Phipps Morgan, J. & Chen, Y.J. (1993a) The genesis of oceanic crust: Magma injection, hydrothermal circulation, and crustal flow. *Journal of Geophysical Research* **98**, 6283-6297.

Phipps Morgan, J. & Chen, Y.J. (1993b). Dependence of ridge-axis morphology on magma supply and spreading rate. *Nature* **364**, 706-708.

Plank, T. & Langmuir, C. H. (1992). Effects of the melting regime on the composition of the oceanic crust. *Journal of Geophysical Research* **97**, 19749-19770.

Plank, T., Spiegelman, M., Langmuir, C. H. & Forsyth, D. W. (1995). The meaning of "mean F": Clarifying the mean extent of melting at ocean ridges. *Journal of Geophysical Research* **100**, 15045-15052.

Portnyagin, M., Almeev, R., Matveev, S., Holtz, F. (2008). Experimental evidence for rapid water exchange between melt inclusions in olivine and host magma. *Earth Planetary Science Letters* **272**, 541-552. doi:10.1016/j.epsl.2008.05.020.

Purdy, G. M., Kong, L. S. L., Christeson, G. L. & Solomon, S. C. (1992). Relationship between spreading rate and the seismic structure of mid-ocean ridges. *Nature* **355**, 815-817.

Qin, Z., Lu, F. & Anderson, A.T. (1992). Diffusive reequilibration of melt and fluid inclusions. *American Mineralogist* **77**, 565-576.

Qin, R. & Buck, W. R. (2008). Why meter-wide dikes at oceanic spreading centers? *Earth and Planetary Science Letters* **265**, 466-474.

Reynolds, J. R. & Langmuir, C. H. (1997). Petrological systematics of the Mid-Atlantic Ridge south of Kane: Implications for ocean crust formation. *Journal of Geophysical Research* **102**, 14915-14946.

Rhodes, J. M., Dungan, M. A., Blanchard, D. P. & Long, P. E. (1979). Magma mixing at mid-ocean ridges: Evidence from basalts drilled near 22°N on the Mid-Atlantic Ridge. *Tectonophysics* **55**, 35-61.

Richter, D. H., Eaton, J. P., Murata, K. J., Ault, W. A. & Krivoy, H. L. (1973). Chronological narrative of the 1959-1960 eruption of Kilauea volcano, Hawaii, *US Geol. Surv. Prof. Paper 537-E*, 1-73.

Robinson, C. J., Bickle, M. J., Minshull, T. A., White, R. S. & Nichols, A. R. L. (2001). Low degree melting under the Southwest Indian Ridge: the roles of mantle temperature, conductive cooling and wet melting. *Earth and Planetary Science Letters* **188**, 383-398.

Roeder, P. L. & Emslie, R. F. (1970). Olivine-liquid equilibrium. *Contributions to Mineralogy and Petrology* **29**, 275-289.

Rotella, M. D., Sinton, J. M., Mahoney, J. J. & Chazey, W. (2009). Geochemical evidence for low magma supply and inactive propagation at the Galápagos 93.25° overlapping spreading center. *Geochemistry Geophysics Geosystems* **10**, Q09005, doi:10.1029/2009GC002445.

Rubin, K. H. & Sinton, J. M. (2007). Inferences on mid-ocean ridge thermal and magmatic structure from MORB compositions. *Earth and Planetary Science Letters* **260**, 257-276.

Rubin K. H., J. D. Macdougall, & Perfit, M. R. (1994). ^{210}Po-^{210}Pb dating of recent volcanic eruptions on the sea floor. *Nature* **368**, 841-844.

Rubin, K. H., Smith, M. C., Perfit, M. R., Christie, D. M. & Sacks, L. F. (1998). Geochronology and geochemistry of lavas from the 1996 North Gorda Ridge eruption. *Deep-Sea Research Part II* **45**, 2571-2597.

Rubin, K. H., Smith, M. C., Bergmanis, E. C., Perfit, M. R., Sinton, J. M. & Batiza, R. (2001). Geochemical heterogeneity within mid-ocean ridge lava flows: insights into eruption, emplacement and global variations in magma generation. *Earth and Planetary Science Letters* **188**, 349-367.

Rubin, K. H., Perfit, M. R., Fornari, D. J., Soule, S. A., Tolstoy, M. & Waldhauser, F. (2006). Geochronology and composition of the 2005-06 volcanic eruptions of the

East Pacific Rise, 9°46'-56'N, *EOS Transactions American Geophysical Union* **87**(52), Fall Meet. Suppl., Abstract V23B-0602.

Rubin, K. H., Tolstoy, M., Fornari, D. J., Dziak, R. P., Soule, S. A., Waldhauser, F., Von Damm, K. L. (2008). Integrating radiometric, geophysical and thermal signals of volcanic unrest and eruption in 2005-06 at 9deg 50'N EPR, *Eos Transactions American Geophysical Union* **89**(53), Fall Meeting Supplement, Abstract B23F-07.

Rubin, K. H., Sinton, J. M., Maclennan, J. & Hellebrand, E. (2009). Magmatic filtering of mantle compositions at mid-ocean-ridge volcanoes. *Nature Geoscience* **2**, 321-328.

Rubin, K. H., Soule, S. A., Chadwick, W. W., Fornari, D. J., Clague, D. A., Embley, R. W., Baker, E. T., Perfit, M. R., Caress, D. W. & Dziak, R. P. (2012). Volcanic eruptions in the deep sea. *Oceanography* **25**, 142-157, doi:10.5670/oceanog.2012.12.

Rudge, J.F. (2008). Finding peaks in geochemical distributions: A re-examination of the helium-continental crust correlation. *Earth and Planetary Science Letters* **274**, 179-188. doi:10.1016/j.epsl.2008.07.021.

Ryan, W.B.F., Carbotte, S. M., Coplan, J. O., O'Hara, S., Melkonian, A., Arko, R. Weissel, R. A., Ferrini, V. Goodwillie, A., Nitsche, F., Bonczkowski, J. & Zemsky, R. (2009). Global Multi-Resolution Topography synthesis. *Geochemistry Geophysics Geosystems* **10**, Q03014, doi:10.1029/2008GC002332.

Saal, A. E., Hauri, E. H., Langmuir, C. H. & Perfit, M. R. (2002). Vapour undersaturation in primitive mid-ocean ridge basalt and the volatile content of Earth's upper mantle. *Nature* **419**, 451-455.

Saemundsson, K. & Kröflukerfisins. (1991). In Gardarson, A. & Einarsson, Á. (eds.) *The Nature of Lake Mývatn* (in Icelandic). edited by A. Gardarson and Á. Einarsson. Icelandic Natural Science Society, 2-95.

Salters, V. J. M. & Stracke, A. (2004). Composition of the depleted mantle. *Geochemistry Geophysics Geosystems* **5**, Q05004, doi:10.1029/2003GC000597.

Salters, V. J. M., Longhi, J. E. & Bizimis, M. (2002). Near mantle solidus trace element partitioning at pressures up to 3.4 GPa. *Geochemistry Geophysics Geosystems* **3**. doi:10.1029/2001GC000148.

Schilling, J.-G. (1973). Iceland mantle plume: Geochemical evidence along the Reykjanes Ridge. *Nature* **242**, 565-571.

Schilling, J.-G., Bergeron, M. B., Evans, R. & Smith, J. V. (1980). Halogens in the mantle beneath the North Atlantic. *Philosophical Transactions of the Royal Society of London A* **297**, 147-178.

Schilling, J.-G., Kingsley, R. H. & Devine, J. D. (1982). Galapagos hot spot-spreading center system 1. Spatial petrological and geochemical variations (83°W-101°W). *Journal of Geophysical Research* **87**, 5593-5610.

Schilling, J.-G., Fontignie, D., Blichert-Toft, J., Kingsley, R. & Tomza, U. (2003). Pb-Hf-Nd-Sr isotope variations along the Galápagos Spreading Center (101°W-83°W): Constraints on the dispersal of the Galápagos mantle plume. *Geochemistry Geophysics Geosystems* **4**, doi:10.1029/2002GC000495.

Seher, T., Crawford, W.C., Singh, S.C., Cannat, M., Combier, V. & Dusunur, D. (2010). Crustal velocity structure of the Lucky Strike segment of the Mid-Atlantic Ridge at 37°N from seismic refraction measurements. *Journal of Geophysical Research* **155**, B03103. doi:10.1029/2009JB006650.

Shaw, A.M., Behn, M.D., Humphris, S.E., Sohn, R.A. & Gregg, P.M. (2010). Deep pooling of low degree melts and volatile fluxes at the 85°E segment of the Gakkel Ridge: Evidence from olivine-hosted melt inclusions and glasses. *Earth and Planetary Science Letters* **289**, 311-322. doi:10.1016/j.epsl.2009.11.018.

Singh, S. C., Crawford, W. C., Carton, H., Seher, T., Combier, V., Cannat, M., Canales, J. P., Düsünür, D., Escartin, J. & Miranda, J. M. (2006). Discovery of a magma chamber and faults beneath a Mid-Atlantic Ridge hydrothermal field. *Nature* **442**, 1029-1032.

Sinha, M.C., Navin, D.A., MacGregor, L.M., Constable, S., Peirce, C., White, A., Heinson, G. & Inglis, M.A. (1997). Evidence for accumulated melt beneath the slow-spreading Mid-Atlantic Ridge. *Philosophical Transactions: Mathematical, Physical and Engineering Sciences* **355**, 233-253.

Sinton, J. M. & Detrick R. S. (1992). Mid-ocean ridge magma chambers, *Journal of Geophysical Research* **97**, 197-216.

Sinton, J. M., Wilson, D. S., Christie, D. M., Hey, R. N., & Delaney, J. R. (1983). Petrologic consequences of rift propagation on oceanic spreading ridges. *Earth and Planetary Science Letters* **62**, 193-207.

Sinton, J. M., Bergmanis, E., Rubin, K., Batiza, R., Gregg, T. K. P., Grönvold, K., Macdonald, K. C. & White, S. M. (2002). Volcanic eruptions on mid-ocean ridges: New evidence from the superfast spreading East Pacific Rise, 17°-19°S, *Journal of Geophysical Research* **107**(B6), doi:10.1029/2000JB000090.

Sinton, J., Detrick, R., Canales, J. P., Ito, G. & Behn, M. (2003). Morphology and segmentation of the western Galápagos Spreading Center, 90.5°-98°W: Plume-ridge interaction at an intermediate spreading ridge. *Geochemistry Geophysical Geosystems* **4**, 8515, doi:10.1029/2003GC000609.

Sinton, J., Grönvold, K. & Sæmundsson, K. (2005). Postglacial eruptive history of the Western Volcanic Zone, Iceland. *Geochemistry Geophysics Geosystems* **6**, Q12009, doi:10.1029/2005GC001021.

Small, C. & Sandwell D. T. (1989). An abrupt change in ridge axis gravity with spreading rate. *Journal of Geophysical Research* **94**, 17383-17392.

Smith, P. M. & Asimow, P. D. (2005). Adiabat_1ph: A new public front-end to the MELTS, pMELTS, and pHMELTS models. *Geochemistry Geophysics Geosystems* **6**, Q02004, doi:10.1029/2004GC000816.

Smith, D. K. & Cann, J. R. (1992). The role of seamount volcanism in crustal construction at the Mid-Atlantic Ridge (24-30N). *Journal of Geophysical Res*earch **97**, 1645-1658.

Soule, S. A., Fornari, D. J., Perfit, M. R. & Rubin, K. H. (2007). New insights into mid-ocean ridge volcanic processes from the 2005-06 eruption of the East Pacific Rise, 9°46'-56'N, *Geology* **35**, 1079-1082, doi:10.1130/G23924A.1.

Soule, S.A., Nakata, D.S., Fornari, D.J., Fundis, A.T., Perfit, M.R. & Kurz, M.D. (2012). CO2 variability in mid-ocean ridge basalts from syn-emplacement degassing: Constraints on eruption dynamics. *Earth and Planetary Science Letters*. **327-328**, 39-49. doi:10.1016/j.epsl.2012.01.034.

Stakes, D. S., Perfit, M. R., Tivey, M. A., Caress, D. W., Ramirez, T. & Maher, N. (2006). The Cleft revealed: Geologic, magnetic, and morphologic evidence for construction of upper oceanic crust along the southern Juan de Fuca Ridge. *Geochemistry Geophysics Geosystems* **7**, Q04003, doi:10.1029/2005GC001038.

Staples, R. K., White, R. S., Brandsdóttir, B., Menke, W., Maguire, P. K. H. & McBride, J. H. (1997). Färoe-Iceland Ridge Experiment 1. Crustal structure of northeastern Iceland. *Journal of Geophysical Research* **102**, 7489-7866.

Stolper, E. (1980). A phase diagram for mid-ocean ridge basalts: Preliminary results and implications for petrogenesis. *Contributions to Mineralogy and Petrology* **74**, 13-27**.**

Thorarinsson, S., Steinthórsson, S., Einarsson, Th, Kristmannsdóttir, H. & Oskarsson, N. (1973). The eruption on Heimaey, Iceland. *Nature* **241**, 372-375.

Tingle, T. N., Green, H. W. & Finnerty, A. A. (1988). Experiments and observations bearing on the solubility and diffusivity of carbon in olivine. *Journal of Geophysical Research* **93**, 15289-15304.

Tolstoy, M., Cowen, J. P., Baker, E. T., Fornari, D. J., Rubin, K. H., Shank, T. M., Waldhauser, F., Bohnenstiehl, D. R., Forsyth, D. W., Holmes, R. C., Love, B., Perfit, M. R., Weekly, R. T., Soule, S. A. & Glazer, B. (2006). A sea-floor spreading event captured by seismometers. *Science* **314**, 1920-1922, doi:10.1126/science.1133950.

Toplis, M.J. (2005). The thermodynamics of iron and magnesium partitioning between olivine and liquid: criteria for assessing and predicting equilibrium in natural and experimental systems. *Contributions to Mineralogy and Petrology* **149**, 22-39. doi:10.1007/s00410-004-0629-4.

van Andel, T. H. & Ballard, R. (1979). The Galápagos Rift at 86°W: 2. volcanism, structure, and evolution of the rift valley. *Journal of Geophysical Research* **84**, 5390-5406.

Van Avendonk, H.J.A., Harding, A.J. & Orcutt, J.A. (2001). Contrast in crustal structure across the Clipperton transform fault from travel time tomography. *Journal of Geophysical Research* **106**, 10961-10981.

Vona, A., Romano, C., Dingwell, D. B. & Giordano, D. (2011). The rheology of crystal-bearing basaltic magmas from Stromboli and Etna. *Geochimica et Cosmochimica Acta* **75**, 3214-3236, doi:10.1016/j.gca.2011.03.031.

Wadge, G. (1981). The variation of magma discharge during basaltic eruptions. *Journal of Volcanology and Geothermal Research* **11**, 139-168.

Walker, D., Shibata, T. & DeLong, S. E. (1979). Abyssal tholeiites from the oceanographer fracture zone II. Phase equilibria and mixing. *Contributions to Mineralogy and Petrology* **70**, 111-125.

Wanless, V. D., Perfit, M. R., Ridley, W. I. & Klein, E. (2010). Dacite petrogenesis on mid-ocean ridges: Evidence for oceanic crustal melting and assimilation. *Journal of Petrology* **51**, 2377-2410.

Wanless, V. D., Perfit, M. R., Ridley, W. I., Wallace, P. J., Grimes, C. B. & Klein, E. M. (2011). Volatile abundances and oxygen isotopes in basaltic to dacitic lavas on mid-ocean ridges: The role of assimilation at spreading centers, *Chemical Geology* **287**, 54-65.

Wanless, V.D. & Shaw, A.M. (2012). Lower crustal crystallization and melt evolution at mid-ocean ridges. *Nature Geoscience* **5**, 651-655. doi:10.1038/NGEO1552.

Weir, N. R. W., White, R. S., Brandsdóttir, B., Einarsson, P., Shimamura, H., Shiobara, H. & RISE Fieldwork Team. (2001). Crustal structure of the northern Reykjanes Ridge and Reykjanes Peninsula, southwest Iceland. *Journal of Geophysical Research* **106**, 6347-6368.

White, R. S., McKenzie, D. & O'Nions, R. K. (1992). Oceanic crustal thickness from seismic measurements and rare earth element inversions. *Journal of Geophysical Research* **97**, 19683-19715.

White, R. S., Minshull, T. A., Bickle, M. J. & Robinson, C. J. (2001). Melt generation at very slow-spreading oceanic ridges: Constraints from geochemical and geophysical data. *Journal of Petrology* **42**, 1171-1196.

White, S. M., Macdonald, K. C. & Sinton, J. M. (2002). Volcanic mound fields on the East Pacific Rise, 16°-19°S: Low effusion rate eruptions at overlapping spreading centers for the past 1 Myr. *Journal of Geophysical Research* **107**, B10, 2240, doi:10.1029/2001JB000483.

White, S. M., Meyer, J. D., Haymon, R. M. & Macdonald, K. C. (2008). High-resolution surveys along the hot spot-affected Galápagos Spreading Center: 2. Influence of magma supply on volcanic morphology. *Geochemistry Geophysics Geosystems* **9**, Q09004, doi:10.1029/2008GC002036.

White, S. M., Mason, J. L., Macdonald, K. C., Perfit, M. R., Wanless, V. D. & Klein, E. M. (2009). Significance of widespread low effusion rate eruptions over the past two million years for delivery of magma to the overlapping spreading centers at 9°N East Pacific Rise. *Earth and Planetary Science Letters* **280**, 175-184.

Whitehead, J. A. & Helfrich, K. R. (1991). Instability of flow with temperature-dependent viscosity: A model of magma dynamics. *Journal of Geophysical Research* **96**, 4145-4155.

Wilson, D. S. & Hey, R. N. (1995). History of rift propagation and magnetization intensity for the Cocos-Nazca spreading center. *Journal of Geophysical Research* **100**, 10041-10056.

Wilson, D. S., Teagle, D. A. H., Alt, J. C., Banerjee, N. R., Umino, S., Miyashita, S., Acton, G. D., Anma, R., Barr, S. R., Belghoul, A., Carlut, J., Christie, D. M., Coggon, R. M., Cooper, K. M., Cordier, C., Crispini, L., Rodriquez Durand, S., Einaudi, F., Galli, L., Gao, Y., Geldmacher, J., Gilbert, L. A., Hayman, N. W., Herrero-Bervera, E., Hirano, N., Holter, S., Ingle, S., Jiang, S., Kalberkamp, U., Kerneklian, M., Koepke, J., Laverne, C., Lledo Vasquez, H. L., Maclennan, J., Morgan, S., Neo, N., Nichols, H. J., Park, S.-H., Reichow, M. K., Sakuyama, T., Sano, T., Sandwell, R., Scheibner, B., Smith-Duque, C. E., Swift, S. A., Tartarotti, P., Tikku, A. A., Tominaga, M., Veloso, E.A., Yamasaki, T., Yamazaki, S. & Ziegler, C. (2006). Drilling to gabbro in intact ocean crust. *Science* **312**, 1016-1020.

Workman, R. K. & Hart, S. R. (2005). Major and trace element composition of the depleted MORB mantle (DMM). *Earth and Planetary Science Letters* **231** 53-72.

Wright, T. J., Sigmundsson, F., Pagli, C., Belachew, M., Hamling, I. J., Brandsdóttir, B., Keir, D., Pedersen, R., Ayele, A., Ebinger, C., Einarsson, P., Lewi, E. & Calais, E. (2012). Geophysical constraints on the dynamics of spreading centres from rifting episodes on land. *Nature Geoscience* **5**, 243-250, doi:10.1038/NGEO1428.

Zack, T. & Brumm, R. (1998). Ilmenite/ liquid partition coefficients of 26 trace elements determined through ilmenite/ clinopyroxene partitioning in garnet pyroxene. In: Gurney, J. J., Gurney, J. L., Pascoe, M. D. & Richardson, S. H. (eds.) *7th International Kimberlite Conference*. Red Roof Design, 986-988.

Zhang, Y., Ni, H. & Chen, Y. (2010). Diffusion data in silicate melts. *Reviews in Mineralogy and Geochemistry* **72**, 311-408.

Zhang, Y. & Ni, H. (2010). Diffusion of H, C, and O components in silicate melts: *Reviews in Mineralogy and Geochemistry* **72**, 311-408.